SYSTEM PERFORMANCE UNDER MULTIHAZARD ENVIRONMENT

A Dissertation

Presented to the Faculty of the Graduate School

of Cornell University

in Partial Fulfillment of the Requirements for the Degree of

Doctor of Philosophy

by

Cagdas Kafali

January 2008

SYSTEM PERFORMANCE UNDER MULTIHAZARD ENVIRONMENT

Cagdas Kafali, Ph.D.

Cornell University 2008

Natural hazards such as earthquakes, tropical and extratropical storms, tornadoes, floods and droughts are known for their destructive impacts on life, economy and environment. Although it is not possible to completely avoid damage due to such disasters, it may be possible to minimize their devastating effects by enhancing resilience in communities, that is, by reducing failure probability of infrastructural systems, consequences of system failures, and time to recovery. System failure probability and recovery time can be reduced by increased system performance through retrofitting and rehabilitation. However, due to limited resources and budget constraints, it is important to identify the most critical systems and prioritize their mitigation with the objective of minimizing the expected losses due to natural hazards. These decisions are based on performance level for a service and cost estimates. In addition to current hazard-specific vulnerability methods, a multihazard approach is necessary for assessing the long-term impact of mitigation strategies on system vulnerability, ensuring that strategies implemented to mitigate one hazard do not amplify the vulnerability to another hazard, and evaluating the relative importance of various hazards.

This study presents a new methodology for (1) assessing performance of structural/nonstructural systems subjected to multiple hazards during their lifetime and (2) identifying a strategy from a collection of design alternatives that is optimal in some sense. System performance is measured by the total lifetime losses and the system fragility, that is, the probability that a system response exceeds a critical value subjected to a hazard event specified by its intensity and other parameters. Accordingly, fragility

is a surface with support the defining parameters of a hazard. The methodology is based on site hazard analysis, system fragility analysis and capacity and cost estimation.

The proposed methodology is probabilistic in nature since (1) the intensity and arrival time of different hazards, such as earthquakes and hurricanes, (2) the loads acting on the system due to a hazard event, such as, ground accelerations and wind velocities, and (3) some of the system characteristics, are generally uncertain. Consequently, probabilistic models are developed for characterizing natural hazards occurring at a given site at single/multiple points. These models specify (1) the random arrival times of individual events at a site during a reference time, (2) the random properties of the hazards under considerations at these times, and (3) the random loads acting on the system due to each event. For a system in a multihazard environment the occurrence of both individual and coincidental hazard events are considered. We present two methods for estimating system fragility, crossing theory of stochastic processes and Monte Carlo simulation.

The proposed models are implemented in computer programs and the life-cycle risk analysis methodology is illustrated through numerical examples. In the first example MCEER West Coast Demonstration Hospital is analyzed to identify an optimal rehabilitation strategy with respect to total life-cycle losses using the concepts of seismic activity matrix and fragility surfaces. It is shown that proposed retrofitting alternatives do not change the mean value of the life-cycle costs significantly, however, the probability of exceeding large costs is lower for the retrofitted systems. The second example discusses the case of a typical offshore platform under earthquake and hurricane hazards. This example demonstrates how different hazards can be dominant at different reliability levels. The last example presents a method for selecting an optimal maintenance policy for a deteriorating system by minimizing the total life-cycle cost such that system reliability at any given time is greater than a specified level.

BIOGRAPHICAL SKETCH

Cagdas Kafali was born to Naime and Aydin Kafali on March 18, 1976, in Mersin, Turkey. After graduating from Lycée de Galatasaray in 1994 he entered Bogazici University, in the Department of Civil and Environmental Engineering, and received his B.S. degree in 1999. He then moved to the United States and started his graduate studies at Case Western Reserve University, where he received his M.S. degree in Structural Engineering in 2001, under the supervision of Professor Art Huckelbridge. Following his graduation he entered Cornell University and started working towards his Ph.D. degree with Professor Mircea Grigoriu. He is currently working at AIR Worldwide Corporation, a leading risk modeling and technology firm specializing in risks associated with natural and man-made catastrophes, weather and climate, as a research engineer.

To my mother Naime Kafalı and my father Aydın Kafalı.

ACKNOWLEDGEMENTS

This dissertation could not have been completed without the help and support of many individuals. I would first like to thank Professor Mircea Grigoriu for his excellent supervision and patience. I believe he is the best possible example that a student could have during his or her graduate studies. I would also like to thank my committee members, Professors Katerina Papoulia and Gennady Samorodnitsky, for their technical advice and comments on my work. Thanks goes to Dr. Rich Fields, my office mate through the toughest years of my graduate studies at Cornell, and to Dr. John Emery, Dr. Keith Kesner and Dr. Matt Rouse, my first house mates and colleagues who introduced me the American way of life, from deer hunting and fishing to thanksgiving dinners and poker nights. I would also like to thank my class mates Colin Lautz and Rohit Gupta for introducing me the other side of America, the West Side, jazz music and vegan chocolate cake.

During my studies at Cornell I had a wonderful time with the Turkish community in Ithaca and made many good friends. First, I would like to thank the advisors of the Turkish Student Association at Cornell, Professors Teoman Pekoz and Peter Kuniholm and our presidents Dr. Umut Cetin, Hakan Bas, Nilay Yilmaz and Bahar Bolukbasi, for their time and support to create a productive Turkish community at Cornell. Thanks also goes to all members of the Turkish community, my good friends Baskan, Cunyor, Akbas, Safak, Gizem, Gokhan, Ecehan, Banu, Haluk, Secer Riza Orkun Keskin, Ibrahim, Cagla, Yesim, Demirhan, my teammates from Istanbulls, our two time Cornell Intramural Soccer Champion team, Hakan, Mutty, Arin, Can Baba, Can Erdogan, Eren, Eren, Melih, Bob, Aycan, and our beautiful supporters, Nilay, Derya, Firdevs, Merve, Bahar and Nazli.

Finally, I am grateful to my mother Naime, my father Aydin, my sisters Eylul, Ezgi, Ege, Elsen, my brother Candas and my dear love Nilay, for their support,

encouragement, and understanding.

This work was supported primarily by the Earthquake Engineering Research Center Program of the National Science Foundation under NSF Award Number EEC-9701471 to the Multidisciplinary Center for Earthquake Engineering Research. This support is also gratefully acknowledged.

TABLE OF CONTENTS

LIST OF TABLES

LIST OF FIGURES

Chapter 1
Introduction

1.1 Overview

Natural hazards of geological origin such as earthquakes and volcanic eruptions or of meteorological origin such as hurricanes, tornadoes, floods and droughts are known for their destructive impacts on human life, economy and environment. The four principal natural disasters in terms of losses, earthquakes, windstorms, floods and droughts, have claimed almost two million lives since 1900 [42]. The financial cost of all global disasters in 1980's was estimated to be $120 billion in 1990 US dollars [42]. Developing countries are more vulnerable to natural disasters due to poverty, illiteracy and lack of infrastructure development. Although it is not possible to completely avoid damage due to such disasters, it is however possible to minimize their devastating effects by enhancing resilience in communities, that is, by reducing (1) system (such as hospitals, lifelines) failure probabilities, (2) consequences of system failures, and (3) time to recovery [24]. Earthquakes and hurricanes have been given high priority in efforts to enhance community disaster resistance because of their potential for producing high losses and extensive community disruption. Accordingly, earthquakes and wind and wave hazards caused by hurricanes are considered in this study.

Earthquakes can have devastating effects on poorly constructed superstructures and infrastructures resulting in very high life and economic losses. The 1999 Armenia Earthquake resulted in 1,200 life losses, 200,000 people without shelter and $500 million in damage [170]. The 1999 Turkey earthquakes resulted in more than 17,000 life losses, 250,000 people without shelter, approximately 214,000 residential and

30,000 business units with structural damage [178, 170], and economic losses of $16 billion [168]. The 1999 Chi-Chi Earthquake in Taiwan claimed 23,000 lives, resulted in 100,000 people without shelter and caused economic losses of $16 billion [170]. Thousands of structures were damaged or destroyed by the 1994 Northridge Earthquake, and total direct losses were estimated at more than $20 billion [168]. In the 1995 Kobe Earthquake more than 6,000 people were killed and the total losses exceeded $16 billion [170].

Earthquakes have also the potential to disrupt lifeline systems. For example, electrical power outages were reported during the 1999 Taiwan, the 1999 Turkey, the 1995 Kobe, and the 1994 Northridge earthquakes [107, 168, 137, 111]. Extensive damage to transportation routes and gas distribution systems was also reported after the Kobe and Northridge earthquakes, respectively [41, 111]. Lifeline damage can have detrimental effects on emergency response activities. For example, loss of water delayed emergency response to (1) several of the gas-caused fires following the Northridge Earthquake [26] and (2) earthquake-triggered hazardous material releases following the Turkey earthquakes [165].

Extreme winds resulting from, for example, tropical and extratropical storms, tornadoes and severe thunderstorms, can also cause very high life and economic losses due to their devastating effects on poorly constructed buildings and other infrastructure, as well as on offshore structures [91, 83, 28, 143]. In this study we focus on extreme winds caused by tropical storms, that is, storms that originate, generally, within latitudes 5 and 20 (hence the name tropical) deriving their energy from the heat released by the condensation of water vapor. Hurricanes, typhoons and tropical cyclones are types of tropical storms with wind speeds exceeding a certain threshold, and named according to their geographical locations, respectively, America, Far East and Australia and Indian Ocean. In the United States hurricanes represent a major threat to the communities in the

east coast and the Gulf of Mexico. The average economic losses caused by hurricanes in the U.S. have been estimated to be approximately $2 billion a year [154]. Hurricane Katrina mostly impacting Louisiana and Mississippi in 2005 was considered to be one of the most deadly and costly disasters in U.S. history resulting in 1,836 life losses and over $81 billion total damage [106]. Hurricane Andrew impacting Florida and Louisiana in 1992 caused economic losses in the order of $30 billion [92]. Hurricanes also bring torrential rain which often causes severe flooding problems. For instance the November 12, 1970 cyclone that hit Bangladesh killed almost half a million people, mostly washed into the sea by surges and water waves [113].

Strong waves and surges of the sea due to tropical storms also pose severe threat to offshore structures and lives and property in low areas along coastlines. Offshore structures can be subjected to extremely hostile environmental conditions caused by strong winds and waves. In 2005 Hurricane Katrina damaged or destroyed 30 oil platforms and caused the closure of nine refineries [93]. Also, in 1980 the structural failure of the mobile ring Alexander Kielland in the Ekofisk field in the North Sea resulted in 123 life losses and in 1961 the collapse of Texas Tower No.4 off the New Jersey coast took 28 lives [143]. Furthermore, the suction of the low-pressure centers of the hurricanes can cause storm surges of less than one meter in height. When the direction of the strong winds of hurricanes are onshore they can result in larger surges. This phenomenon is called a wind tide. A wind tide coinciding with a normal tide at a particular location can create very large surges, reaching as high as seven meters.

Engineering communities contribute to natural hazard mitigation by setting codes and standards for the design and rehabilitation of infrastructural systems and also by constructing them according to such codes and standards. The adoption of appropriate codes for designing new structures and retrofitting the older ones can help minimize loss of life and property during natural hazards. In earthquake engineering field

code/stantard development activities have mostly centered around impacts on buildings and lifeline systems [81]. In the United States adoption and enforcement of seismic building codes is left to the discretion of each state, with the exception of some seismic requirements for federal buildings. The state of California, for example, has adopted the Uniform Building Code [89], which requires designing buildings for the 1 in 475-year earthquake event. However, some local communities in the state may choose to following stricter codes, such as the International Building Code [90], which requires the design of new buildings for the 1 in 2475-year event. Each state has adopted various seismic construction standards for new buildings, however, the problem remains for older structures. For the lifeline systems in the U.S., the Technical Council on Lifeline Earthquake Engineering develops guidelines and standards for the seismic design and construction of lifelines. For example, lifeline vulnerability functions and estimates of time required to restore damaged facilities are provided in the ATC-25 report "Seismic Vulnerability and Impact of Disruption of Lifelines in the Conterminous United States" [9]. Engineering design codes also exist to insure that buildings and structures are constructed to withstand particular wind speeds depending on the climatic characteristics of each region. The design wind speeds have been updated over the years, and in general the new codes require the use of higher design wind speeds [36]. In the United States, for example, American Society of Civil Engineers (ASCE) provides the guidelines for the design and calculation of wind loads in the design standard ASCE 7 "Minimum Design Loads for Buildings and Other Structure" [6].

The need to move beyond the current hazard-specific vulnerability assessment methods toward a broader approach that considers the collective impact of different hazards on urban areas is being repeatedly called for [35, 138, 81, 52]. Multihazard risk analysis of a system deals with the assessment of the system performance under multiple random loads caused by natural and/or man-made hazards, some of which may

occur simultaneously. A multiple-hazard approach is necessary for (1) assessing the long-term impact of mitigation strategies on community vulnerability and (2) ensuring that strategies implemented to mitigate one hazard do not amplify the vulnerability to another hazard. A formal multihazard evaluation methodology can also help assess the relative importance of the various hazards, for example, earthquake and wind [81]. In the U.S. the Multihazard Mitigation Council, established by the National Institute of Building Sciences, works to reduce direct and indirect losses resulting from natural and other hazards by promoting improved multihazard risk mitigation strategies, guidelines, and practices. The Federal Emergency Management Agency under contract with the National Institute of Building Sciences has recently developed HAZUS-MH, a nationally applicable standardized methodology and software program that estimates potential losses from earthquakes, floods, and hurricane winds.

Accordingly, in this study, we focus on the effects of seismic and hurricane hazards, in addition to their combined effect, on the performance of structural/nonstructural systems.

1.2 Objectives of the study

The main goals of this study are (1) developing a methodology for assessing performance of structural/nonstructural systems subjected to multiple hazards during their lifetimes and (2) identifying a rational strategy from a collection of design alternatives for increasing the resilience of these systems. System performance is measured by the total losses incurred during system's lifetime and by system fragility, that is, the probability that a system response exceeds a critical value subjected to a hazard event of known intensity. The methodology is based on (i) site hazard analysis, (ii) system fragility analysis and (iii) capacity and cost estimation. The methodology

is probabilistic in its nature since (1) the intensity and arrival time of different hazards, such as earthquakes and hurricanes, (2) the loads acting on the system due to a hazard event, such as, seismic ground accelerations and wind velocities, and (3) some of the system characteristics, are generally uncertain.

Figure 1.1 shows a schematic chart summarizing the life-cycle loss estimation

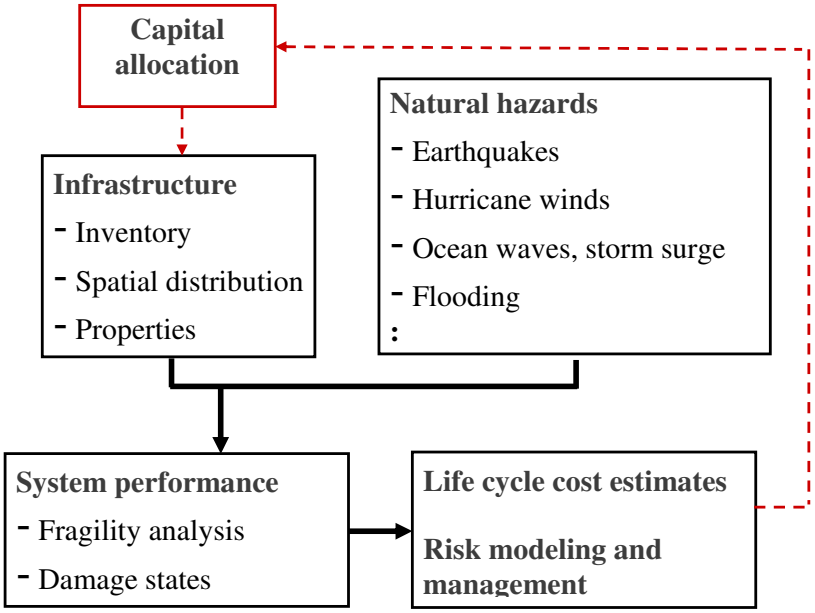

Figure 1.1: General methodology.

methodology. For a given infrastructural system we first characterize relevant hazards at the system site. Next, we assess the performance of the system by fragility analysis, delivering the probabilities that the system enters different damage states, for example, low, moderate or extensive, under a hazard event of given intensity. Finally, estimates of costs, referred to as life cycle costs, are derived using fragility information and financial models. The results from a life-cycle loss analysis can be used for capital allocation decision making, such as, identifying an optimal retrofitting technique for structural/nonstructural systems from a collection of design alternatives [96, 60, 24, 25], or for determining the relative importance of different hazards [17].

Probabilistic lifetime hazard models are used to specify the random arrival times of individual hazard events at a site during a reference time and the random properties of the hazards under considerations. The loads acting on a structure for a given hazard event are generally time varying. However, the structural response to these time varying loads may be static or dynamic depending on the frequency content of the load and the dynamic characteristics of the resisting structural system. To characterize the loads on a structure due to natural hazards and the structural response to these loads the following steps are needed: (1) establishing the natural hazard activity in the vicinity of the structure from available information, (2) estimating the loads on the structure due to the possible hazards, and (3) calculating system response. A deterministic or a stochastic approach can be followed for the above procedure. In this study a stochastic approach is used to characterize the probability law of the load processes acting on a structure. A natural hazard event at a site, such as seismic ground acceleration or wind velocity, is characterized by a random process with a probability law derived from measurements and/or analytical models. System fragility, the probability that the system is in an undesired damage state, is plotted against the parameters characterizing natural hazards which completely define the probability law of the hazard at the system site.

1.3 Outline

The three main parts of the methodology described above, namely, hazard, system fragility and life-cycle loss analyses, are addressed in Chapters 2, 3 and 4, respectively. The following briefly summarizes the content of each chapter.

Chapter 2 defines the natural hazards addressed in this study, presents probabilistic models characterizing these random events and their random occurrences in time, discusses Monte Carlo algorithms for generating samples of such hazards, and provides

an approach for characterizing multiple hazards at a given site.

Chapter 3 focuses on the relationship between the random load acting on a system due to a given hazard event and the response of this system. More specifically, the main objective of this chapter is to calculate system fragility, that is, the probability that the system response leaves a safe set in a given time if subjected to a natural hazard event of specified intensity. If a safe set of the system response is associated with a system damage state, fragility becomes a function that describes the probability of exceedance of this damage state, given a hazard intensity. The damage state corresponding to a safe set can represent, for example, slight, moderate, extensive damage of the system.

Chapter 4 covers three examples focusing on the life-cycle performance and loss estimation. The first example presents the overall life-cycle loss estimation methodology using a realistic hospital system under seismic hazard. Seismic fragilities for structural and nonstructural systems and estimates of losses and recovery times are obtained corresponding to different rehabilitation alternatives. In the second example a methodology is presented for assessing performance of a system under multihazard environment. The methodology is illustrated by examining a simple model of an offshore structure subjected to seismic and hurricane hazards. The last example provides a probabilistic model for selecting an optimal maintenance strategy for deteriorating systems using reliability constraints. In this example the overall objective is to develop an optimal maintenance policy such that the probability of total life-cycle cost exceeding a critical value is minimized given the system functions at the required performance level during its lifetime.

Finally, Chapter 5 outlines conclusions of the study and proposes possible future areas of research.

Chapter 2
Hazard definitions and models

In this chapter earthquakes, tropical storms and ocean waves are defined and their causes and mechanisms are discussed in Section 2.1, probabilistic models characterizing these random events are presented in Section 2.2, probabilistic models for their random occurrences in time are presented in Section 2.3, Monte Carlo algorithms for generating samples of such hazards are discussed in Section 2.4, numerical example are provided in Section 2.5, and a multihazard approach at a given site is discussed in Section 2.6.

2.1 Hazard definitions

This section briefly describes the seismic, wind and wave hazards and their causes and mechanisms.

2.1.1 Seismic hazard

The word earthquake describes ground shaking events and ruptures at the Earth's surface. Earthquakes are caused by a sudden energy release in the Earth's crust creating seismic waves. Earthquakes may occur naturally, for example, due to the movement of tectonic plates or the movement of magma in volcanoes, or as a result of human activities, for example, due to nuclear tests. Most earthquakes occurring naturally are related to the Earth's tectonic nature. The earth's surface is broken into seven large and many small moving plates [177]. These plates, each about 50 miles thick, move relative to one another an average of a few inches a year. Three types of movement are recognized at the boundaries between plates: convergent, divergent and transform-fault

[177]. At convergent boundaries, plates move toward each other and collide. Where an oceanic plate collides with a continental plate, the oceanic plate tips down and slides beneath the continental plate forming a deep ocean trench. An example of this type of movement, called subduction, occurs at the boundary between the oceanic Nazca Plate and the continental South American Plate. Where continental plates collide, they form major mountain systems such as the Himalayas. At divergent boundaries, plates move away from each other such as at the Mid-Atlantic Ridge. Where plates diverge, hot, molten rock rises and cools adding new material to the edges of the oceanic plates. This process is known as sea-floor spreading. At transform-fault boundaries, plates move horizontally past each other. The San Andreas Fault zone is an example of this type of boundary where the Pacific Plate on which Los Angeles sits is moving slowly northwestward relative to the North American Plate on which San Francisco sits. The slow motion of the plates is caused by the heat in the Earth's mantle and planetary core. The heat causes the rock under the earth to become liquid magma, on which the plates are able to move. Plate boundaries grind past each other, creating frictional stress. When the frictional stress exceeds a critical value, called local strength, a sudden failure occurs. The boundary of tectonic plates along which failure occurs is called the fault plane. When the failure at the fault plane results in a violent displacement of the Earth's crust, the energy is released and seismic waves are radiated, thus causing an earthquake. The majority of tectonic earthquakes originate at depths not exceeding tens of miles. In subduction zones, where older and colder oceanic crust descends beneath another tectonic plate, earthquakes may occur at much greater depths, up to five hundred miles. Deep focus earthquakes are another phenomenon associated with a subducting slab. These are earthquakes that occur at a depth at which the subducted lithosphere should no longer be brittle, due to the high temperature and pressure. Earthquakes may also occur in volcanic regions and are caused by the movement of magma in volcanoes.

Such earthquakes can be an early warning of volcanic eruptions.

When an earthquake fault ruptures, it causes two types of deformation, static and dynamic. Static deformation is the permanent displacement of the ground due to the event. The two general types of vibrations produced by earthquakes are surface waves, which travel along the Earth's surface, and body waves, which travel through the Earth [176]. Body waves are of two types, compressional and shear. Both types pass through the Earth's interior from the focus of an earthquake to distant points on the surface, but only compressional waves travel through the Earth's molten core. Because compressional waves travel at great speeds, at speeds between 1.5 and 8 kilometers per second in the Earth's crust, and ordinarily reach the surface first, they are often called primary waves or simply P waves. Shear waves do not travel as rapidly through the Earth's crust and mantle as do compressional waves, usually at 60% to 70% of the speed of P waves, and because they ordinarily reach the surface later, they are called secondary or S waves. P waves shake the ground in the direction they are propagating, while S waves shake perpendicularly or transverse to the direction of propagation. Surface waves usually have the strongest vibrations and probably cause most of the damage done by earthquakes.

An earthquake's underground point of initial ground rupture is called its focus or hypocenter. The better-known term epicenter means the point at ground level directly above this. Earthquake magnitude is a logarithmic measure of earthquake size. In simple terms, this means that at the same distance from the earthquake, the shaking will be 10 times as large during a magnitude 5 earthquake as during a magnitude 4 earthquake. A common magnitude measure is called the moment magnitude, which is based on the moment of the earthquake, which is equal to the rigidity of the earth times the average amount of slip on the fault times the amount of fault area that slipped. The intensity, as expressed by the Modified Mercalli Scale, is a subjective measure that

describes how strong a shock was felt at a particular location. Specific local geological, geomorphological, and geostructural features can induce high levels of shaking on the ground surface even from low-intensity earthquakes. This effect is called site or local amplification. It is principally due to the transfer of the seismic motion from hard deep soils to soft superficial soils and to effects of seismic energy focalization owing to typical geometrical setting of the deposits.

An earthquake's destructiveness depends on many factors. In addition to magnitude and the local geologic conditions, these factors include the focal depth, the distance from the epicenter, and the design of buildings and other structures. The extent of damage also depends on the density of population and construction in the area shaken by the quake.

2.1.2 Wind hazard

Hurricanes, typhoons, cyclones, and so on are different names for the same type of severe storm occurring in different geographical regions. Those occurring in the North Atlantic, the Caribbean Sea, the Gulf of Mexico, and the Western part of the South Pacific are called hurricanes. Those encountered in the Far East, more specifically in the South Sea and Pacific Northwest are called typhoons. Those in the Indian Ocean, Arabian Sea and the Bay of Bengal are called cyclones. In the following discussion they will all be referred to as hurricanes.

A hurricane is a large funnel-shaped storm with a wide top of the order of 1,000 km in diameter and a narrow bottom of the order of 300 to 500 km in diameter [113]. The height of the storm is of the order of 10 to 15 km. The center part of a hurricane with a diameter around 30 km is called the eye, the boundary of the eye is called the wall. The eye region is absent of rain and strong winds, while the wall is a region packed with high winds and intense rain. Due to the Coriolis force generated by the Earth's rotation,

hurricanes in the Northern Hemisphere always rotate in the counterclockwise direction. In contrast, hurricanes in the Southern Hemisphere rotate clockwise. Hurricanes are generated by low-pressure centers above the ocean at low latitudes and move away from the equatorial regions toward higher latitudes. They derive their energy from the latent heat released by the condensation of water vapor contained in hurricanes. As the moisture in a hurricane is lost through the rain, new moisture is fed into the hurricane due to intense evaporation from the ocean caused by the low pressure and high wind in the hurricane. This mechanism perpetuates and strengthens hurricanes over the ocean. However, as soon as a hurricane has reached land, it dies down due to the lack of moisture and increased surface resistance to wind. Therefore, hurricane winds are strong only over the ocean and in adjacent coastal areas, within approximately 100 kilometers of coastlines. The lifespan of a hurricane is of the order of one to three weeks, averaging about 10 days [113]. The air outside a hurricane eye circles around the eye and spirals inward at low heights with increasing speed toward the eye. Upon reaching the wall, the air rushes upward to large heights. The it spirals outward from the upper region of the hurricane. The wind speed in a hurricane reaches a maximum at the wall. The speed decreases rapidly and linearly from the wall to the center of the eye. It decreases more gradually outward from the wall. The maximum wind speeds of hurricanes have been grossly overestimated in the past. Based on severe damage caused by hurricanes many meteorologists and engineers used to think that hurricanes could have surface winds speeds higher than 100 m/sec (224 mph). However, it is now widely accepted that hurricane surface wind speed may never exceed 90 m/sec (200 mph). The storm, or translational, speed of a hurricane is the speed at which the center of a hurricane moves. This should not be confused with the wind speed in the hurricane. The wind speed is often much higher than the storm speed. Normally, the storm speed is between 5 to 50 km/hr.

As in the case of most other types of winds the wind speed in a hurricane decreases with decreasing height, reaching zero velocity at ground level to satisfy the no-slip condition of fluid mechanics. What is normally referred to as the surface wind is the wind speed not at the surface but rather near the surface, measured by anemometers mounted normally at a height of 10 m above ground. Except for very tall structures the surface wind speed is what is encountered by structures.

Hurricanes occur most frequently in the late summer when the ocean water temperature has reached a maximum. The winter is almost entirely absent of hurricanes.

2.1.3 Wave hazard

Ocean waves are produced by the wind. The faster the wind, the longer the wind blows, and the bigger the area over which the wind blows, the bigger the waves. If the wind suddenly begins to blow steadily over a smooth sea three different physical processes begin. First, the turbulence in the wind produces random pressure fluctuations at the sea surface, which produces small waves with wavelengths of a few centimeters. Next, the wind acts on the small waves, causing them to become larger. Wind blowing over the wave produces pressure differences along the wave profile causing the wave to grow. The process is unstable because, as the wave gets bigger, the pressure differences get bigger, and the wave grows faster. The instability causes the wave to grow exponentially. Finally, the waves begin to interact among themselves to produce longer waves [166].

2.2 Event models

Probabilistic models, referred to as event models, are developed for seismic, wind and wave events occurring at single/multiple points at a given site. A natural hazard

event at a site, such as seismic ground acceleration or wind or wave velocity, is characterized by a random process with a probability law derived from measurements and/or analytical models.

Monte Carlo algorithms presented in Sections 2.4.1 and 2.4.2 can be used for generating samples of ground accelerations, wind and wave velocities at single/multiple points at a given site, based on their probability laws presented in this section. Numerical examples are provided in Section 2.5.1.

2.2.1 Seismic hazard

The earthquake strong motion at a site can be modeled by a kinematic or a stochastic method [74]. The kinematic method is used to obtain ground motions at the site due to an earthquake from a fault with specific dimensions and orientation in a known geologic setting [74]. In this method a slip function on a fault plane is used to represent the rupture process and empirical Green's functions are used to model propagation effects [72, 172, 21, 37, 103]. The elastodynamic representation theorem [3] is used to compute the earthquake strong motion at the site. Accordingly, this approach is useful for site specific simulations. In the stochastic method, earthquake motion at the site is modeled as a random process with a spectrum that is either empirical, for example, band-limited white-noise [34, 151], Kanai-Tajimi type of spectrum [102, 167], or Clough-Penzien type of spectrum [32]; or a spectrum that is based on a physical model, for example, single corner frequency model [22, 23], two corner frequency model [10], or the specific barrier model [130, 131, 127]. The intent of the stochastic method to strong motion simulation is to capture the essential characteristics of high-frequency motion at an average site at a distance r from an average earthquake event of a specified magnitude m. In other words, the accelerograms artificially generated using the stochastic method do not represent any specific earthquake but embody certain

average properties of past earthquakes of a given magnitude. Seismological models are generally used in the stochastic method to estimate the seismic motion at a site as a function of source strength, attenuation of seismic waves due to propagation path between the source and the site, and wave amplification due to site effects [76, 18, 82, 10, 158, 159, 140, 126, 171, 136, 19]. However, other stochastic models are also available, for example, empirical models [84, 124, 141], time series models [124, 53, 33, 38, 104], and models delivering response spectrum compatible ground motions [67, 134, 132, 174, 175, 105, 160, 57].

To investigate the seismic response of spatially distributed systems, such as bridges and pipelines, ground motion models for multiple points at a site are required. The earthquake strong motion at multiple points can be modeled using the methods developed for single point modeling together with spatial correlation models. A stationary model has been developed for seismic waves, which are stochastic in time and space, propagating in a homogeneous two dimensional medium by Shinozuka and Deodatis [146]. Developments in [146] have been extended in [147] to model the near field ground motions due to a seismic source to include stochastic waves propagating through a 3D layered half space with lateral non-homogeneities. A nonstationary stochastic vector process with evolutionary power spectral densities was considered in [43, 77] to model correlated ground accelerations at a collection of sites. A simulation algorithm for a stationary Gaussian random process model representing seismic ground accelerations at multiple points was introduced by Zerva [188]. Several spatial variability models [78, 114, 116, 115, 77, 125, 2] and simulation schemes were examined in [189]. A method for generating time series, representing nonstationary seismic ground acceleration at multiple points compatible with the observed wave propagation properties, can be found in [125].

We characterize seismic ground acceleration at a site as a random process with

a probability law derived from a seismological model based on the source model developed by Papageorgiou and Aki [130, 131, 127], namely the specific barrier model, and measurements of actual ground motions records. The specific barrier model is selected for the quantitative description of heterogenous rupture because it (i) is free of ambiguities caused by the stress parameter in the commonly used simple single frequency model, (ii) is fully consistent with the important (salient) features of the more complex theoretical models of rupture and observed source spectra, (iii) provides the most complete description for the faulting processes that are responsible for the generation of the high frequencies and also clearly describes how to distribute the seismic moment on the fault plane, and (iv) is applicable to both near-fault and far-field regions, which allows consistent ground motion simulations over the entire frequency range and for all distances of engineering interest, [127, 128, 129]. The specific barrier model has been recently calibrated for (i) shallow crustal earthquakes in active regions (interplate earthquakes, for example, those of California), (ii) earthquakes of regions characterized by active tectonic extension, for example, Basin and Range Province, and (iii) for earthquakes of intraplate regions, for example, eastern North America [73, 75]. More explanations on the specific barrier model, and other source models are provided in Appendix A.

In this section Gaussian and non-Gaussian ground acceleration models for single/multiple points at a given site are introduced.

2.2.1.1 Single point models

The seismic ground acceleration at a single point at a given site, generated by a seismic event with moment magnitude m and source-to-site distance r, is modeled by a zero-mean nonstationary process $X(t)$ of the form

$$X(t) = e(t)\, Y(t), \quad 0 \leq t \leq \tau, \tag{2.1}$$

where τ is the total duration of the seismic event defined by the specific barrier model [130, 131, 127, 75], $e(t)$ is a deterministic modulation function given by [142, 74]

$$e(t) = e_1\, t^{e_2}\, \exp(-e_3 t), \quad 0 \leq t \leq \tau, \tag{2.2}$$

with $e_2 = 1.2531$, $e_1 = (13.5914/\tau)^{e_2}$, and $e_3 = 5\, e_2/\tau$, and $Y(t)$ is a zero-mean stationary Gaussian/non-Gaussian process with a prescribed probability law based on the specific barrier model and statistical properties of recorded free field ground acceleration time histories.

2.2.1.1.1 Gaussian model: A zero-mean nonstationary Gaussian model for the seismic ground acceleration can be defined by Equation 2.1 in which $Y(t)$ is a zero-mean stationary Gaussian process with one-sided spectral density function

$$g_{YY}(\omega) = \begin{cases} \dfrac{1}{2\pi\tau}|a(\omega; m, r)|^2 & , \quad 0 \leq \omega \leq \bar{\omega} \\ 0 & , \quad \omega > \bar{\omega} \end{cases} \tag{2.3}$$

where ω is the frequency in rad/sec, $\bar{\omega}$ is a cut-off frequency that is selected such that $\int_0^{\bar{\omega}} g_{YY}(\omega)d\omega \simeq \int_0^{\infty} g_{YY}(\omega)d\omega$, and

$$|a(\omega; m, r)| = k\, q(\omega, m) d(\omega, r) p(\omega) b(\omega), \quad 0 \leq \omega \leq \bar{\omega}, \tag{2.4}$$

is the Fourier amplitude spectrum of the ground acceleration at the site, in which, k is a scaling factor, $q(\omega, m)$ is the acceleration source spectrum modeled by the specific barrier model, $d(\omega, r)$ is the attenuation function, $p(\omega)$ is the high frequency cut-off filter, and $b(\omega)$ is a function which defines local soil effects [130, 131, 127, 75, 74]. The frequency content of $X(t)$ in Equation 2.1 does not change in time since its spectral density is time invariant. The modulation function in Equation 2.2 and the spectral density function in Equation 2.3 completely define the probability law of the seismic ground acceleration process $X(t)$ at a site, and is a function of the earthquake moment magnitude m, the source-to-site distance r, and the site soil type.

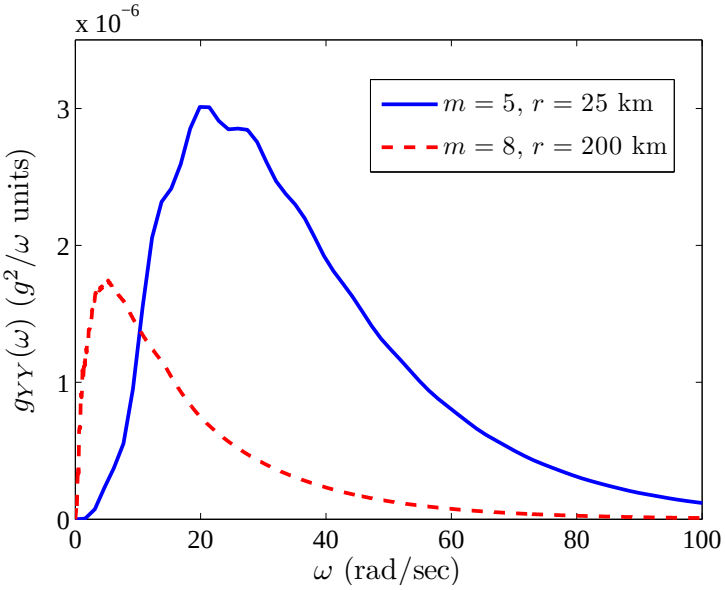

Figure 2.1: Spectral density of $Y(t)$ for different (m, r).

Figure 2.1 shows the spectral density function of $Y(t)$ at a site in California on generic soil (NEHRP site class D, [56]), for ($m = 5, r = 25$ km) and ($m = 8, r = 200$ km). The plots in Figure 2.1 show that the frequency content of the seismic ground acceleration depends strongly on the values of m and r. Figure 2.2 shows the spectral densities for two sites in California, one on generic soil and the other one on generic hard rock, corresponding to NEHRP site classes D and A [56], respectively, for an earthquake with ($m = 6, r = 100$ km). Figure 2.2 shows that a site with a softer soil will have a larger spectral density compared to a site located on a stiffer soil or rock. This increase in the spectral densities is a result of the frequency dependent site amplification function $b(\omega)$ in Equation 2.4.

2.2.1.1.2 Non-Gaussian translation model: This section extends the model for the seismic ground acceleration at single point presented in Section 2.2.1.1.1 to account for the non-Gaussian character of actual seismic acceleration records.

Statistics of the actual ground acceleration records show that the strong ground

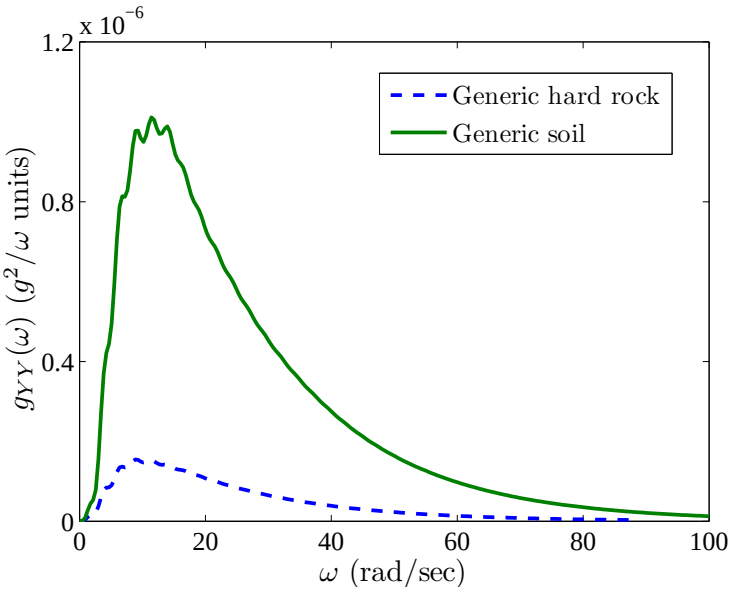

Figure 2.2: Spectral density of $Y(t)$ for different soil classes.

motion part of the seismic ground acceleration records has kurtosis coefficient in the range $(4.0, 6.5)$ (see Appendix B). Figure 2.3 shows the dependence of the kurtosis coefficient on soil conditions (the relationship between the USGS [133] and NEHRP [56] site classes is provided in Table B.4 in Appendix B). These statistics suggest that the marginal probability density function of the seismic ground acceleration have heavier tails than normal density and therefore seismic ground acceleration can not be modeled as a Gaussian process, which has kurtosis 3.

The student-t density is proposed to model the marginal density of the stationary non-Gaussian ground acceleration process. Accordingly, $Y(t)$ in Equation 2.1 is a translation process with one-sided spectral density function given by Equation 2.3 and marginal density function

$$f(x) = \frac{\Gamma\left(\frac{c+1}{2}\right)}{b\sqrt{\pi c}\,\Gamma\left(\frac{c}{2}\right)}\left[1+\frac{(\frac{x}{b})^2}{c}\right]^{-\frac{c+1}{2}}, \quad x \in \mathbb{R}, \tag{2.5}$$

where $b,\ c > 0$ are some constants; constant c is also called the degree of freedom of the distribution. Student-t is not the only density that can be used but it is consistent

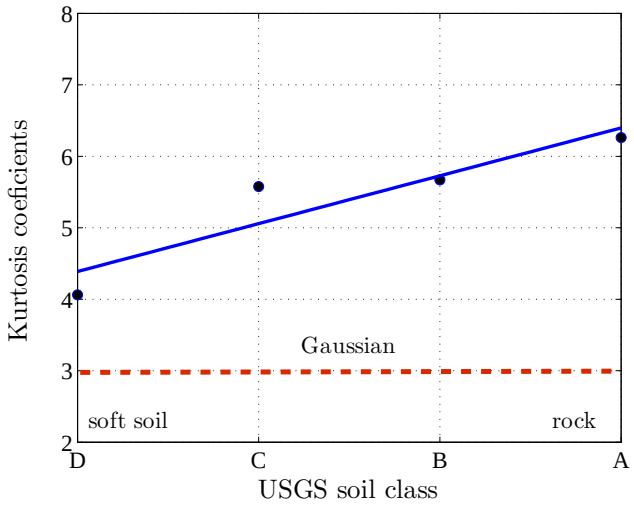

Figure 2.3: Change in the kurtosis coefficient with USGS soil class.

with the available information. This density is very flexible and can cover a broad range of values for variance and kurtosis coefficient. Figure 2.4 shows the marginal density

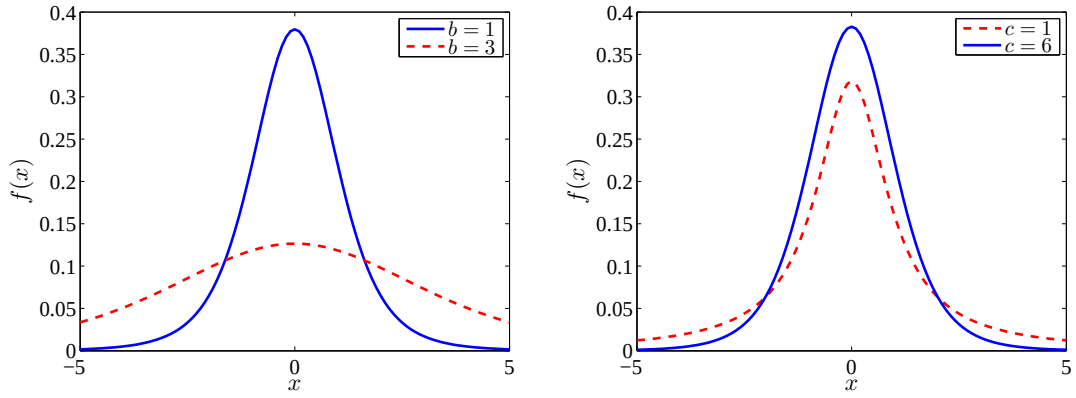

(a) (b)

Figure 2.4: Student-t density.

function in Equation 2.5 for (a) $c = 5$ and two values of b, 1 and 3, and (b) $b = 1$ and two values of c, 6 and 1. The kurtosis coefficient corresponding to the marginal density

in Equation 2.5 is

$$\gamma_4 = 3\left[\frac{(c-2)^2\Gamma(\frac{c}{2}-2)}{4\Gamma(\frac{c}{2})}\right] \tag{2.6}$$

and can match virtually any values. Figure 2.5 shows the kurtosis coefficient as a

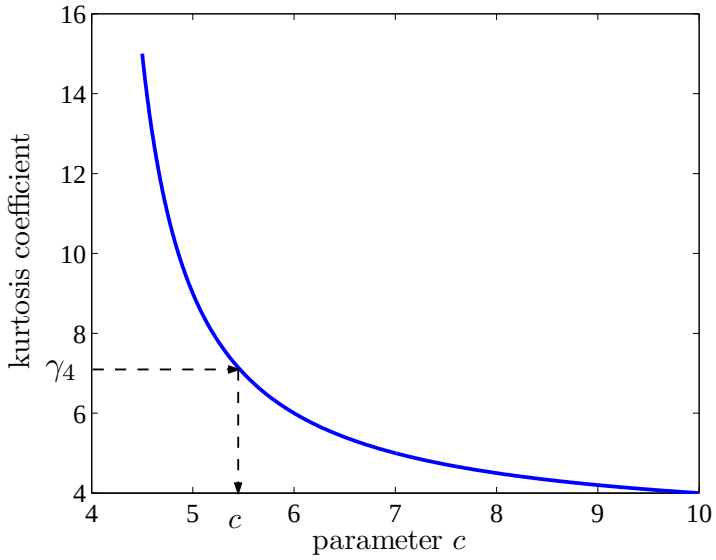

Figure 2.5: Kurtosis coefficient vs parameter c.

function of the parameter c of the marginal density in Equation 2.5.

The memoryless transformation model proposed for $Y(t)$ has the form

$$Y(t) = F^{-1} \circ \Phi(G(t)), \tag{2.7}$$

where (i) $F(y) = \int_{-\infty}^{y} f(x)dx$, in which $f(x)$ is the marginal density in Equation 2.5, (ii) $G(t)$ is the Gaussian image of $Y(t)$ with mean zero and spectral density function approximated by $g_{YY}(\omega)/\sigma_Y^2$, in which $g_{YY}(\omega)$ is the spectral density function of $Y(t)$ in Equation 2.3 and $\sigma_Y^2 = \int_0^\infty g_{YY}(\omega)d\omega$ is the variance of $Y(t)$, and (iii) $\Phi(\cdot)$ is the cumulative distribution function of a standard normal random variable. The transformation is called memoryless because the non-Gaussian process $Y(t)$ at an arbitrary instant t depends only on the value of its Gaussian image $G(t)$. We note that the

translation process $Y(t)$ has the marginal distribution F since F and Φ are monotonic functions with no atoms so that

$$P(Y(t) \leq y) = P(F^{-1} \circ \Phi(G(t)) \leq y) = P(G(t) \leq \Phi^{-1}(F(y))) = F(y) \qquad (2.8)$$

for all values of y, therefore $Y(t)$ can follow an arbitrary marginal distribution. The approximation of the density function of $G(t)$ in Equation 2.7 by $g_{YY}(\omega)/\sigma_Y^2$ is based on the observation that the difference between the scaled covariance function in the non-Gaussian space, $\zeta(\tau) = EY(t+\tau)Y(t)/EY(t)^2$, and the corresponding one in the Gaussian space, $\rho(\tau) = EG(t+\tau)G(t)$, are not significant for a broad range of values of the covariance function of $Y(t)$ so that the scaled target spectral density function $g_{YY}(\omega)/\sigma_Y^2$ can be used as a first order approximation of the spectral density function of $G(t)$ ([69], Section 3.1).

Calibration of the stationary non-Gaussian ground acceleration process $Y(t)$ is performed as follows. First, the kurtosis coefficient of $Y(t)$ in Equation 2.1 is determined from the soil condition at the site of interest using Figure 2.3. Then, the degree of freedom c of the marginal density of $Y(t)$ in Equation 2.5 delivering the targeted kurtosis coefficient is obtained using Equation 2.6 (Figure 2.5). Finally, the parameter b of the marginal density of $Y(t)$ in Equation 2.5 is obtained by matching the variance of $Y(t)$ obtained from its spectral density function in Equation 2.3.

Nonstationarity can be introduced by modulating the non-Gaussian signal $Y(t)$ using the envelop function defined in Equation 2.2. The nonstationary non-Gaussian ground acceleration is given by the Equation 2.1 with $Y(t)$ in Equation 2.7.

2.2.1.2 Multiple point models

The seismic ground acceleration at n points at a given site, located far from a seismic source (see illustration in Figure 2.6) and generated by a seismic event with moment magnitude m and source-to-site distance r, is modeled by a zero-mean $\mathbb{R}^n$-

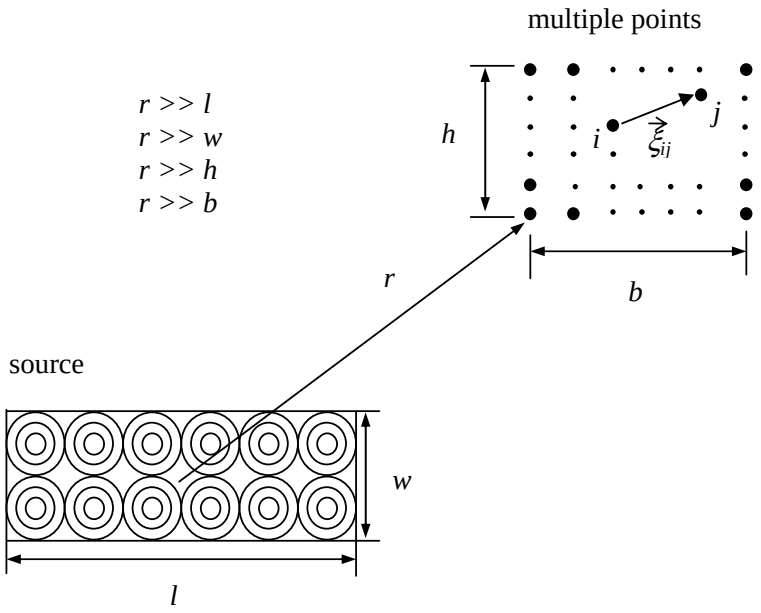

Figure 2.6: Illustration of multiple points.

valued stochastic process of the form

$$\boldsymbol{X}(t) = (\ldots, X_i(t) = e(t)\, Y_i(t), \ldots), \quad i = 1, \ldots, n, \quad 0 \leq t \leq \tau, \tag{2.9}$$

where (i) τ is the total duration of the seismic event defined in Equation 2.1, (ii) $e(t)$ is a deterministic modulation function given by Equation 2.2, and (iii) $\boldsymbol{Y}(t) = (\ldots, Y_i(t), \ldots), i = 1, \ldots, n$, is a zero-mean stationary Gaussian/non-Gaussian vector process with a prescribed probability law based on the specific barrier model and statistical properties of recorded free field ground acceleration time histories. We note that the modulating function $e(t)$ does not depend on the local soil conditions hence it is the same for all points at the site in the far field.

2.2.1.2.1 Gaussian model: A zero-mean nonstationary Gaussian model for the seismic ground accelerations at n points at a site located far from a seismic source (Figure 2.6) can be defined by Equation 2.9 in which $\boldsymbol{Y}(t) = (\ldots, Y_i(t), \ldots)$, $i = 1, \ldots, n$, is an $\mathbb{R}^n$-valued zero-mean stationary Gaussian process with prescribed

second-moment characteristics. Besides the (auto) spectral density functions at individual points given by Equation 2.3, cross spectral density functions are required to completely characterize Gaussian vector process $\boldsymbol{Y}(t)$. Complex valued cross spectral density function between points i and j is given by

$$g_{Y_iY_j}(\omega) = \gamma(\omega, \vec{\xi}_{ij})\sqrt{g_{Y_iY_i}(\omega)g_{Y_jY_j}(\omega)}, \quad 0 \leq \omega \leq \bar{\omega}, \tag{2.10}$$

in which $g_{Y_iY_i}(\omega)$ and $g_{Y_jY_j}(\omega)$ are the one-sided spectral density functions (Equation 2.3) of the stationary ground acceleration processes $Y_i(t)$ and $Y_j(t)$ at points i and j, respectively, and $\gamma(\omega, \vec{\xi}_{ij})$ is a frequency dependent function quantifying the spatial variability between the two points, that is, a coherency function, where $\vec{\xi}_{ij}$ is the separation vector between points i and j, as illustrated in Figure 2.6.

The coherency function in [78] is used in this study. Accordingly,

$$\gamma(\omega, \vec{\xi}_{ij}) = \rho(\omega, \vec{\xi}_{ij})\, e^{-\sqrt{-1}\omega d}, \quad 0 \leq \omega \leq \bar{\omega}, \tag{2.11}$$

in which

$$\rho(\omega, \vec{\xi}_{ij}) = A \exp\left(\frac{-2|\vec{\xi}_{ij}|(1 - A + aA)}{a\theta(\omega)}\right) \tag{2.12}$$

$$+ (1 - A) \exp\left(\frac{-2|\vec{\xi}_{ij}|(1 - A + aA)}{\theta(\omega)}\right),$$

$$\theta(\omega) = k\left(1 + \left(\frac{|\,\omega\,|}{2\pi f_0}\right)^b\right)^{(-1/2)}, \tag{2.13}$$

$$d = \frac{\vec{V}.\,\vec{\xi}_{ij}}{|\,\vec{V}\,|^{\,2}}, \tag{2.14}$$

where $\vec{V}$ is the apparent velocity vector whose direction coincides with the direction of the site from the source, and parameters $A,\ a,\ k,\ f_0,\ b$ are estimated using event 20 of SMART-I seismograph array located in Lotung, Taiwan [78]. The spatial correlation function $\rho(\omega, \vec{\xi}_{ij})$ in Equation 2.11 given by Equations 2.12 and 2.13 models the decay

of coherency (incoherence) between ground motions at two points located along a straight line in a particular direction. The parameters in $\rho(\omega, \vec{\xi}_{ij})$ were obtained by aligning (shifting) actual ground motions records relative to one another. Note that $\rho(\omega, \vec{\xi}_{ij}) = \rho(-\omega, \vec{\xi}_{ij})$ and $\rho(\omega, \vec{\xi}_{ij}) = \rho(\omega, \vec{\xi}_{ji})$. Dependence of $\rho(\omega, \vec{\xi}_{ij})$ on the separation distance only, and not on the actual location, implies the homogeneity of the random field. The phase component $e^{-\sqrt{-1}\omega d}$ was added to the model to obtain the true (unaligned) motions at the points which are generally related to the approximately constant apparent velocity of propagation the seismic waves. This coherency function describes a homogeneous, non-isotropic, space-time random field. More explanations on the coherence model in Equation 2.11 and other models are provided in Appendix C.

The modulation function in Equation 2.2, the spectral density function in Equation 2.3 and the coherency function in Equation 2.11 completely define the probability law of the seismic ground acceleration process $\boldsymbol{X}(t)$ at multiple points at a site located far from a seismic source, and is a function of the earthquake moment magnitude m, the source-to-site distance r, and the local soil types. We note that the modulating function $e(t)$ in Equation 2.2 does not depend on the local soil conditions hence it is the same for all points at the site in the far field.

2.2.1.2.2 Non-Gaussian translation model: The Gaussian model for seismic ground accelerations at multiple points proposed in Section 2.2.1.2.1 is extended to account for the non-Gaussian character of these time series presented in Section 2.2.1.1.2.

A memoryless transformation model for the seismic ground accelerations at n points at a site located far from a seismic source can be defined by Equation 2.9 in which

$$Y_i(t) = F_i^{-1} \circ \Phi(G_i(t)), \quad i = 1, \ldots, n, \tag{2.15}$$

where (i) $F_i(y) = \int_{-\infty}^{y} f_i(x)dx$, in which $f_i(x)$ is the marginal density given in

Equation 2.5, (ii) $G_i(t)$ is the Gaussian image of $Y_i(t)$ with mean zero and spectral density function $g_{Y_iY_i}(\omega)/\sigma^2_{Y_i}$, in which $g_{Y_iY_i}(\omega)$ is the spectral density function of $Y_i(t)$ in Equation 2.3 and $\sigma^2_{Y_i} = \int_0^\infty g_{Y_iY_i}(\omega)d\omega$ is the variance of $Y_i(t)$, (iii) and $\Phi(\cdot)$ is the cumulative distribution function of a standard normal random variable. The components $G_i(t)$, $i = 1, \ldots, n$, in Equation 2.15 have marginal distributions F_i and correlation functions

$$\zeta_{ij}(\tau) = EG_i(t+\tau)G_j(t) = \int_{-\infty}^{\infty}\int_{-\infty}^{\infty} f_i(u)f_j(v)\phi(u, v; \rho_{ij}(\tau))dudv, \qquad (2.16)$$

where $i, j = 1, \ldots, n$ and $\phi(\cdot, \cdot; \rho_{ij})$ denotes the density of a two dimensional normal variable with mean zero, variance one and correlation coefficient ρ_{ij}, which can be obtained from the cross spectral density given in Equation 2.10 using the Wiener-Khintchine formulas ([164], Section 2.4.2).

The translation process

$$\boldsymbol{Y}(t) = \boldsymbol{F}^{-1} \circ \boldsymbol{\Phi}(\boldsymbol{G}(t)), \qquad (2.17)$$

with components in Equation 2.15, (i) is stationary if the underlying Gaussian process $\boldsymbol{G}(t) = (\ldots, G_i(t), \ldots), i = 1, \ldots, n$, is stationary, (ii) can follow any marginal distributions, and (iii) its correlation functions ζ_{ij} are completely defined by the distributions F_i and the covariance functions $\rho_{ij}(\tau)$, $i, j = 1, \ldots, n$. The functions ζ_{ij} and F_i cannot be selected arbitrarily, they must be such that the solutions ρ_{ij} of Equation 2.16 are covariance functions [69]. The non-Gaussian vector process $\boldsymbol{Y}(t)$ is defined by the second-moment characteristics of $\boldsymbol{G}(t)$, and the mapping $\boldsymbol{F}^{-1} \circ \boldsymbol{\Phi}(\cdot)$.

Calibration of the stationary non-Gaussian ground acceleration vector process $\boldsymbol{Y}(t)$ is performed as in Section 2.2.1.1.2 for each of its components $Y_i(t)$, $i = 1, \ldots, n$.

Nonstationarity can be introduced as in Section 2.2.1.2.1, by modulating the non-Gaussian signals $\boldsymbol{Y}(t)$ using the envelop function defined in Equation 2.2. The nonstationary non-Gaussian ground acceleration is given by the Equation 2.9 with $\boldsymbol{Y}(t)$ in Equation 2.17.

2.2.2 Wind hazard

The following longitudinal wind velocity model is based on horizontally homogeneous flows over a sufficiently large horizontal site of uniform roughness. The derivations are based on the assumption that the flow in the free atmosphere is geostrophic, that is, the wind flow is a steady horizontal motion of air along straight, parallel contours in an unchanging contour field, and also means that there is no friction and that the flow is straight with no curvature. These assumptions do not hold in the region of highest winds of a mature hurricane ([154], Section 2.4.3). However, it was shown that the mean wind profiles differ only insignificantly from the logarithmic profile that is used in the below-derivations for elevations from around 10 to 400 m ([154], Section 2.4.3), and accordingly the American National Standard A58.1 [5] does not differentiate between profiles of tropical storms such as hurricanes, cyclones, and extratropical storms.

Most winds are produced by severe storms such as hurricanes, tornadoes, thunderstorms, downbursts and so on. We will focus on hurricanes only in this study. However, other type of extreme winds can be modeled in a similar way.

2.2.2.1 Single point model

The (longitudinal) wind velocity at a point above the ground surface in a given direction is generally resolved into a temporal mean value over a certain duration, that is, a mean wind speed, and a stationary fluctuating part parallel to the direction of the mean wind. It follows from the definition of the mean value that the mean wind speed depends on the averaging time. As the length of the averaging time decreases the maximum mean speed corresponding to that length increases. The averaging time for determining the wind loads on structures ranges from seconds to an hour [113]. A relationship between the wind speeds averaged over different time intervals is provided

in ([154], Section 2.3.6). For example, wind speeds averaged over one minute at 10 m above ground over open terrain near a coastline can be converted to mean hourly wind speeds via multiplication of the original data by the factor 1/1.24 [122]. The fluctuating part of the wind is mainly caused by the turbulence of the wind flow and generally modeled by a zero-mean stationary Gaussian process with a prescribed spectral density function [154].

The wind velocity in direction $\bar{\theta}$ at a point 10 m above surface on an open terrain has the form

$$V^*(t) = \bar{v} + V(t), \quad 0 \leq t \leq \tau, \tag{2.18}$$

where τ is the total duration of strong winds in a typical storm ranging between 10 minutes to 1 hour ([154], Section 2.3.3) and assumed to be 1 hour in this study, $\bar{v}$ is the hourly mean wind velocity at this point along the direction $\bar{\theta}$, and $V(t)$ is the fluctuating component modeled by a zero-mean stationary Gaussian process with one-sided spectral density function [154, 101]

$$g_{VV}(\omega) = \begin{cases} \dfrac{200\kappa x \bar{v}^2}{\omega(1+50x)^{5/3}}, & , \quad 0 \leq \omega \leq \bar{\omega} \\ 0 & , \quad \omega > \bar{\omega}, \end{cases} \tag{2.19}$$

in which $\omega = 2\pi f$, f is the frequency in Hertz, $\bar{\omega}$ is a cut-off frequency as defined in Equation 2.3, $x = 10\omega/(2\pi\bar{v})$ is the Monin coordinate, and $\kappa = k/\ln(10/z_0)$ is called the surface drag coefficient, in which, z_0 is the roughness length and k is called von Kármán's constant which is generally assumed to be 0.4 [154]. For an open terrain $z_0 = 0.035$ m delivering $\kappa \simeq 0.005$. The spectral density function in Equation 2.19 assumes that the variation of the wind speed with height follows the logarithmic law ([154], Section 2.3.3).

Figure 2.7 shows the one-sided spectral density function in Equation 2.19 of $V(t)$ for two values of $\bar{v}$, 20 and 40 m/sec, over an open terrain. For wind flow over water surface the surface drag coefficient κ is a function of the mean wind speed $\bar{v}$ with the

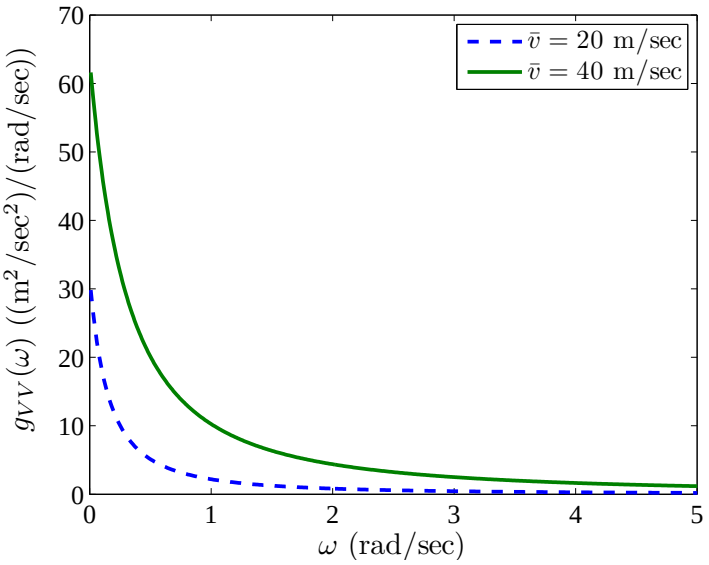

Figure 2.7: One-sided spectral density of $V(t)$.

form [154]

$$\kappa = 0.0015 \left[1 + \exp\left(-\frac{\bar{v} - 12.5}{1.56}\right)\right]^{-1} + 0.00104. \tag{2.20}$$

The logarithmic profile overestimates the wind speeds below three wave heights; above three wave heights, the influence of waves on the wind profile is negligible ([154] Section 2.2.3).

The spectral density given in Equation 2.19 is a very good representation of wind velocity spectra in the high frequency range and may be conservatively assumed to be valid for $x > 0.2$, moreover, the response of most of land-based structures and non-compliant offshore structures does not depend significantly on the shape of the spectrum in the lower frequency range ([154], Section 2.3.3). Accordingly, the spectral density function in Equation 2.19 can be used in the analysis of such structures. On the other hand, for a structure with a low fundamental frequency of vibration, such as a compliant offshore platform, Equation 2.19 may result in an overestimation of structural response and should be used with caution.

Consider two sites each with uniform surface roughness and let the roughness

lengths for the two terrains be $z_{0,1}$ and $z_{0,2}$, and the shear velocities be $u_{*,1}$ and $u_{*,2}$. Denote by $\bar{v}_1$ and $\bar{v}_2$ the mean wind speeds at a certain hight at these sites. The mean wind speed will be lower over the rougher site ([154], Section 2.3.5). Suppose that we have measurements of mean wind speeds $\bar{v}_1$ at one site and we need respective values of $\bar{v}_2$ at the other site. A similarity model provides a relationship between the wind speeds in different surface roughness regimes. Accordingly, the shear velocities $u_{*,1}$, $u_{*,2}$ and roughness lengths $z_{0,1}$, $z_{0,2}$ satisfy ([154], Section 2.3.5)

$$\frac{u_{*,1}}{u_{*,2}} = \left(\frac{z_{0,1}}{z_{0,2}}\right)^{0.0706}. \tag{2.21}$$

For example, suppose that we have measurements of mean hourly speed in meters per second at 10 m above ground over open terrain near a coastline and we need corresponding mean wind speeds at 10 m above water surface. The roughness lengths for open terrain and water surface are $z_{0,1} = 0.035$ m and $z_{0,2} = 10/\exp(0.4/\sqrt{\kappa})$ with κ in Equation 2.20, respectively. The logarithmic law can be used to relate the shear velocity $u_{*,i}$ to the mean speed $\bar{v}_i$ by $\bar{v}_i = 2.5u_{*,i}\ln(10/z_{0,i})$, for $i = 1, 2$, corresponding to wind flow over open terrain and water surface, respectively. Given the mean wind speed over open terrain $\bar{v}_1$ we first obtain $u_{*,1}$ using the logarithmic law and $z_{0,1} = 0.035$ m, then using the similarity model in Equation 2.21 we solve for $\bar{v}_2$ satisfying Equation 2.20 and the logarithmic law simultaneously. Figure 2.8 shows the relationship between mean wind speed $\bar{v}_1$ over open terrain, and $\bar{v}_2$ over water at 10 m above the surface. The mean speed is larger over water surface.

Although Equation 2.18 gives the wind velocity at 10 m above the ground surface, for high wind speeds such as are assumed in structural design (of the order of 20 m/sec or more), it is reasonable to apply Equation 2.19 throughout the height range of interest ([154], Section 2.3.3), which is the case in this study.

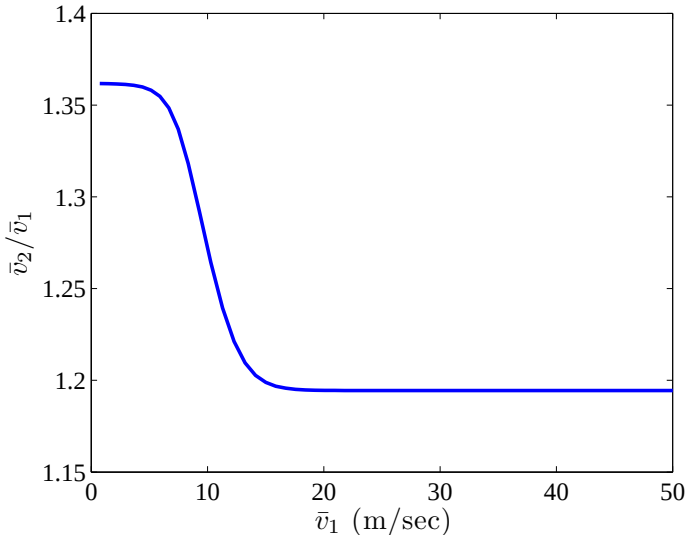

Figure 2.8: Relationship between mean wind speeds over water and open terrain.

2.2.2.2 Multiple point model

An $\mathbb{R}^n$-valued zero-mean stationary Gaussian vector process can be used to model the wind velocities at n points at a site. Besides the (auto) spectral density functions at individual points given by Equation 2.19, cross spectral density functions are required to completely characterize the Gaussian vector process. A coherency function can be used to define the cross spectral density function between points i and j, $i, j = 1, \ldots, n$, as in Section 2.2.1.2.1.

A coherency function between the (longitudinal) wind velocity fluctuations at two points i and j can be assumed to be [40]

$$\gamma(\omega) = \exp\left(-\frac{\omega}{2\pi}\frac{\left[c_z^2(z_i - z_j)^2 + c_y^2(y_i - y_j)^2)\right]^{1/2}}{\left[\bar{v}_i - \bar{v}_j\right]/2}\right), \quad 0 \le \omega \le \bar{\omega}, \tag{2.22}$$

where c_z and c_y are exponential decay coefficients in the vertical z and horizontal y directions, respectively, and (y_i, z_i) and (y_j, z_j) are the coordinates of points i and j, and $\bar{v}_i$ and $\bar{v}_j$ are the mean wind speeds at points i and j, respectively. This model assumes that the line connecting the two points is perpendicular to the direction of the

mean wind. It has been suggested that it is reasonable to assume $c_z = 10$ and $c_y = 16$ from a structural design viewpoint [108, 109].

2.2.3 Wave hazard

It is commonly assumed that the temporal variation of the water surface elevation at a particular location, caused by wind flow over the surface, can be modeled by a stationary Gaussian random process [143]. The Pierson-Moskowitz spectrum [135] is commonly used at present [143] to characterize the water surface elevation, and depends on the mean wind speed $\bar{v}$ at that location.

2.2.3.1 Single point model

A wave theory can be used to relate the kinematics of water particles below the sea surface to the water surface elevation. Stochastic description of water particle kinematics are generally limited to the linear wave theory [17], although several other theories with various degrees of refinement are also available.

Consider two dimensional water waves propagating over a smooth undisturbed depth d and a Cartesian coordinate system (x, s) with x measured in the direction of wave propagation and s measured upwards from the sea bed (see illustration in Figure 2.9). It is assumed that waves propagate in the positive x direction with water particles moving up and down in s direction, there is no underlying current and the free surface is uncontaminated. Water is taken to be incompressible and inviscid and the flow to be irrotational. Figure 2.9 indicates the general form of such a wave train at time t with wave height $H(t)$ which is the vertical distance from trough to crest, wave length l which is the distance between successive crests, wave period T which is the time interval between successive crests passing a particular point, wave angular frequency $\omega = 2\pi/T$ and wave number $k = 2\pi/l$. Accordingly, the free surface elevation $\eta(x, t)$ at location

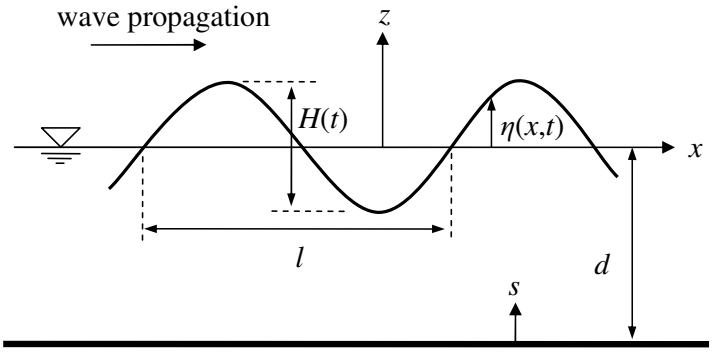

Figure 2.9: Progressive wave train.

x measured from still water level $z = 0$, or $s = d$, is [143]

$$\eta(x,t) = \frac{H(t)}{2}\cos(kx - \omega t), \quad 0 \le t \le \tau, \tag{2.23}$$

where τ is the total duration of strong winds inducing the waves given in Equation 2.18. This theory gives the water particle velocity $U(x,s,t)$ at time t at a point with coordinates (x,s) and the linear dispersion relationship as follows

$$U(x,s,t) = \omega\,\eta(x,t)\frac{\cosh(ks)}{\sinh(kd)}, \tag{2.24}$$

$$\omega^2 = kg\tanh(kd), \tag{2.25}$$

where $\eta(x,t)$ is given by Equation 2.23.

The free surface elevation $\eta(x,t)$ in Equation 2.23 is commonly modeled by a zero-mean stationary Gaussian process with one-sided spectral density function given by the Pierson-Moskowitz spectrum [135]. In the development of the Pierson-Moskowitz spectrum it was assumed that if the wind blew steadily for a long time over a large area, the waves would come into equilibrium with the wind. This is the concept of a fully developed sea. Measurements of water surface elevation over large areas of the North Atlantic were used to obtain a spectrum of a fully developed sea. First, wave data corresponding to steady wind were selected. Then, the wave spectra for various wind

speeds were calculated and it was found that the spectra of the water surface elevation $\eta(x,t)$ were of the form

$$g_{\eta\eta}(\omega) = \begin{cases} \dfrac{\alpha g^2}{\omega^5}\,\exp\left(-\dfrac{\beta g^4}{\bar{v}^4\omega^4}\right) & , \quad 0 \le \omega \le \bar{\omega} \\ 0 & , \quad \omega > \bar{\omega} \end{cases} \tag{2.26}$$

where $\omega = 2\pi f$, f is the wave frequency in Hertz, $\bar{\omega}$ is a cut-off frequency as defined in Equation 2.3, g is the acceleration of gravity in m/sec, $\alpha = 0.0081$, $\beta = 0.74$, and $\bar{v}$ is the mean wind speed at a height of 10 m above the sea surface. In the original work in [135] the wave spectrum in Equation 2.26 is a function of the mean wind speed at a height of 19.5 m above the sea surface (measurements were obtained from anemometers located at that elevation on the weather ships). However, for air flow over water, wind speeds do not increase as much with height as they do on land because of low surface roughness, so that the mean wind speeds at a height of 10 and 19.5 m above the sea surface can be assumed equal [166].

The spectral density function of water particle velocity $U(t)$ at the water surface $z = 0$ in deep waters is obtained from Equations 2.23, 2.24 and 2.26 as

$$g_{UU}(\omega) = \begin{cases} \dfrac{\alpha g^2}{\omega^3}\,\exp\left(-\dfrac{\beta g^4}{\bar{v}^4\omega^4}\right) & , \quad 0 \le \omega \le \bar{\omega} \\ 0 & , \quad \omega > \bar{\omega} \end{cases} \tag{2.27}$$

noting that $\sinh(kd) \simeq \cosh(kd)$ for deep water so that Equations 2.23 and 2.24 yield $U(t) = U(x,d,t) = \omega\eta(x,t)\cosh(kd)/\sinh(kd) = \omega\eta(x,t)$ for $s = d$, hence $g_{UU}(\omega) = \omega^2 g_{\eta\eta}(\omega)$. Figure 2.10 shows the one-sided spectral density function of $U(t)$ for two values of $\bar{v}$, 20 and 40 m/sec, obtained using Equation 2.27. In general, the spectral density function of the horizontal velocity in Equation 2.24 of a water particle at a distance s from the sea bed has the form

$$g_{UU}(\omega; s) = \omega^2 \frac{\cosh^2(ks)}{\sinh^2(kd)} g_{\eta\eta}(\omega), \tag{2.28}$$

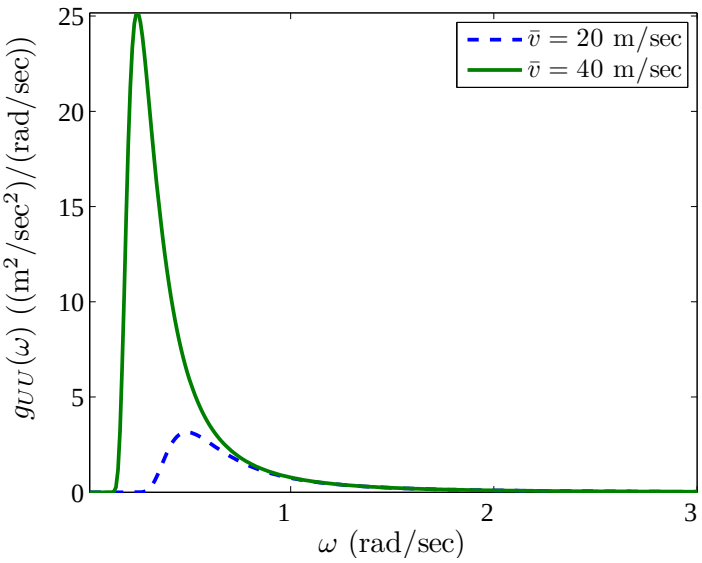

Figure 2.10: One-sided spectral density of $U(t)$.

with $g_{\eta\eta}(\omega)$ and k in Equations 2.26 and 2.25, respectively.

The spectral density function in Equation 2.27, for the water particle velocity $U(t)$ at a given point, is along the direction $\bar{\theta}$ of the mean wind speed $\bar{v}$. However, in general, the free surface elevation in a random sea is caused by waves with different frequencies ω, wave numbers k and directions θ. Accordingly, the spectrum of the free surface elevation is a function of arguments ω, k and θ. A three dimensional spectrum is redundant to a certain extent since it may be possible to exploit the linear dispersion relationship between k and ω to effect a reduction from three arguments to two. This reduction is only an approximation, particularly for the higher frequencies, on account of nonlinear interactions between various wave components [143]. The spectrum depending on ω and θ is referred to as a directional spectrum. In general a directional spectrum $\tilde{g}_{\eta\eta}(\omega, \theta)$ of the free surface elevation is separated in two parts

$$\tilde{g}_{\eta\eta}(\omega, \theta) = g_{\eta\eta}(\omega)h(\omega, \theta), \quad 0 \leq \omega \leq \bar{\omega}, \tag{2.29}$$

where $g_{\eta\eta}(\omega)$ is a unidirectional spectrum such as the one given in Equation 2.26 and

$h(\omega, \theta)$ is directional spreading function, which is not necessarily independent of ω. In the special case of unidirectional random waves propagation in the principal wave direction $\bar{\theta}$, the directional spreading function is given in terms of the Dirac delta function $\delta(\cdot)$ as $h(\theta) = \delta(\theta - \bar{\theta})/(2\pi)$. Various expressions for $h(\omega, \theta)$ are provided in the literature and outlined in ([143], Section 7.3.4). A commonly used directional spreading function is

$$h(\theta) = \frac{1}{2\sqrt{\pi}} \frac{\Gamma(s+1)}{\Gamma(s+1/2)} \cos^{2q}((\theta - \bar{\theta})/2), \quad -\pi \leq \theta \leq \pi, \tag{2.30}$$

where q is a parameter controlling the degree of spread and $\Gamma(\cdot)$ is the Gamma function. Figure 2.11 shows the directional spreading function $h(\theta)$ in Equation 2.30 for $q = 1$

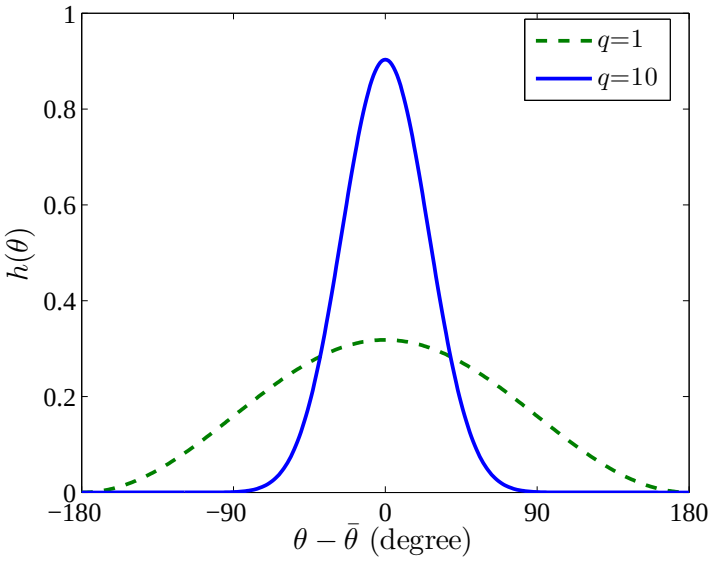

Figure 2.11: Directional spreading function $h(\theta)$.

and $q = 10$. In case where the directional spreading function is taken to be independent of frequency and the principal wave direction is a constant independent of frequency, the principal force direction will be equal to the principal wave direction.

Wind flow over the water surface also generates a current in the principal wind

direction $\bar{\theta}$ with velocity [17]

$$u_0(s) = c\,\frac{s}{d}\,\bar{v}, \tag{2.31}$$

where $u_0(s)$ is the velocity of the current at a distance s from the bottom of the sea (Figure 2.9), $c \in [0.01, 0.05]$ is a constant and $\bar{v}$ is the mean wind speed at a height of $z = 10$ m above the sea surface. Hence, the total water particle velocity at a point of coordinates (x, s) is given by

$$U^*(x, s, t) = u_0(s) + U(x, s, t), \quad 0 \le t \le \tau, \tag{2.32}$$

with $u_0(s)$ in Equation 2.31, $U(x, s, t)$ in Equation 2.24, and τ in Equation 2.18.

2.2.3.2 Multiple point model

An $\mathbb{R}^n$-valued zero-mean stationary Gaussian vector process can be used to model the water particle velocities at n points on a submerged structure. Besides the (auto) spectral density functions at individual points given by Equation 2.27, cross spectral density functions are required to completely characterize the Gaussian vector process.

The one-sided cross spectrum between wave velocities $U_i(t)$ and $U_j(t)$ at points i and j with coordinates (x_i, s_i) and (x_j, s_j), respectively, in the direction of wave propagation, can be assumed to be [153]

$$g_{U_iU_j}(\omega) = \omega^2 g_{VV}(\omega)\lambda(\omega, s_i, s_j)\exp\left[-\sqrt{-1}k(x_i - x_j)\right], \quad 0 \le \omega \le \bar{\omega}, \tag{2.33}$$

in which $gVV(\omega)$ is the one-sided spectral density of wind velocity defined in Equation 2.19, k is the wave number which can be determined from the linear dispersion relationship in Equation 2.25, $k = \omega^2/g$ in deep waters, and

$$\lambda(\omega, s_i, s_j) = \frac{\cosh(ks_i)\cosh(ks_j)}{\sinh^2(kd)}, \tag{2.34}$$

where d is the water depth.

2.3 Lifetime models

Probabilistic models, referred to as lifetime models, are developed for the single point natural hazards at a given site discussed in Sections 2.2.1.1, 2.2.2.1 and 2.2.3.1. The lifetime model of a natural hazard specifies (1) the random arrival times, $T_1, T_2, \ldots$, of individual events at a site during a reference time τ, and (2) the random properties of the hazards under considerations at $T_1, T_2, \ldots$. A lifetime probabilistic model of a natural hazard is defined by (1) activity matrix at the site (defined below), (2) probability law of the individual events, such as the ones discussed in Sections 2.2.1.1, 2.2.2.1 and 2.2.3.1, for earthquake, wind and wave events, respectively, and (3) a reference time τ.

Monte Carlo algorithms presented in Section 2.4.3 can be used for generating samples of lifetime seismic, wind and wave hazards at a given site during a reference time τ. A lifetime hazard sample consists of the arrival times of individual events and the properties defining their probability law. Numerical examples are provided in Section 2.5.1.

2.3.1 Activity matrix

An activity matrix of a natural hazard at a given site delivers the annual rate of occurrence for events of this hazard corresponding to various properties. We plot activity matrices against the properties which completely define the probability law of the hazard at the site.

Consider a hazard at a site with defining properties quantified by a set of parameters $(\Phi_1, \ldots, \Phi_d)$, $d \geq 1$. For example, the seismic hazard at a site is completely defined by $d = 2$ parameters, $\Phi_1 =$ earthquake moment magnitude M, and $\Phi_2 =$ source-to-site distance R (Section 2.2.1), and the plot of mean annul rate of occurrence of earthquakes for all (M, R) at the site is called the site seismic activity matrix [96].

Similarly, the wind and wind-induced wave hazards at a site are completely defined by Φ_1 = mean wind velocity $\bar{V}$, and Φ_2 = principal wind direction $\bar{\Theta}$, that is, the direction of the predominant winds in a storm (Sections 2.2.2 and 2.2.3). Consider a partition in bins of the possible values of $(\Phi_1, \ldots, \Phi_d)$, and let $\nu_{i_1 \ldots i_d}$ denote the yearly rate of occurrence of events with parameters $(\Phi_1, \ldots, \Phi_d)$ in bins $i_1, \ldots, i_d$ denoted by $\{\Phi_1 \in \text{bin-}i_1, \ldots, \Phi_d \in \text{bin-}i_d\}$, respectively. The activity matrix delivers the annual rate of occurrence $\nu_{i_1 \ldots i_d}$ for events with properties $(\phi_{1,i_1}, \ldots, \phi_{d,i_d})$, in which $\phi_{k,l}$ is the mid-value of bin-l for parameter k.

2.3.2 Event arrivals

The average number of events per year irrespective of the values of $(\Phi_1, \ldots, \Phi_d)$ is

$$\nu = \sum_{i_1, \ldots, i_d} \nu_{i_1 \ldots i_d} \, . \tag{2.35}$$

We assume that the events occur in time according to a homogeneous Poisson counting process $\{N(\tau), \tau \geq 0\}$ of intensity ν so that

$$P(N(\tau) = n) = \frac{(\nu\tau)^n}{n!} \exp(-\nu\tau), \quad n = 0, 1, 2, \ldots . \tag{2.36}$$

We note several properties of homogeneous Poisson counting process $\{N(\tau), \tau \geq 0\}$. First, the inter-arrival times $T_k - T_{k-1}$, $k = 1, \ldots, N(\tau)$, $T_0 = 0$, are independent exponential random variables with rate ν since $P(T > \tau) = P(N(\tau) = 0) = \exp(-\nu\tau)$. Second, conditional on $N(\tau) = n$, the unordered Poisson events $\{s_1, s_2, \ldots, s_n\}$ occurring in $(0, \tau)$ have the probability density function $1/\tau^n$. Therefore, the unordered Poisson events are independent and uniformly distributed on $(0, \tau)$ conditional on $N(\tau) = n$. Accordingly, there are two ways of generating samples of $\{T_k\}$, $k = 1, \ldots, N(\tau)$. The first method is based on the first property above. Samples of inter-arrival times are generated consecutively using their conditional

distributions as long as the generated Poison events remain in $(0, \tau)$ ([69], Section 4.6). The second method uses the second property. In this case we first generate a sample n of the Poisson counting process $\{N(\tau), \tau \geq 0\}$, then we generate n independent samples of uniform distribution on $(0, \tau)$ which correspond to the Poisson events in $(0, \tau)$ ([69], Section 4.6).

Figure 2.12 illustrates a sample of a natural hazard consisting of events E_i with

Figure 2.12: A sample of lifetime hazard.

arrival times T_i, $i = 1, \ldots, N(\tau)$, at a site in time $(0, \tau)$.

Although the Poisson model, by its time-independent event-occurrence assumption, is not necessarily the best model for random occurrence of rare natural hazards, for example, hurricanes occur most frequently in the late summer when the ocean water temperature has reached a maximum, the winter is almost entirely absent of hurricanes [113, 110], it is still widely used for many natural-hazard assessments [52, 184] and can be used as a benchmark for comparisons with other more sophisticated models. Accordingly, in this study, it is assumed that the Hurricane can only occur between August 1st and October 31st in a given year, on the other hand, earthquakes can occur at any given time.

2.3.3 Event properties

Properties of each event E_i in Figure 2.12, $i = 1, \ldots, N(\tau)$, characterizing its probability law, are assigned using the joint probability density function of the parameters $(\Phi_1, \ldots, \Phi_d)$ defining them, which can be approximated in discrete form by

$$P[\Phi_1 \in \text{bin-}i_1, \ldots, \Phi_d \in \text{bin-}i_d] = \nu_{i_1 \ldots i_d}/\nu, \tag{2.37}$$

where $P[\Phi_1 \in \text{bin-}i_1, \ldots, \Phi_d \in \text{bin-}i_d]$ is the probability of an event having parameters $(\phi_{1,i_1}, \ldots, \phi_{d,i_d})$, in which $\phi_{k,l}$ is the mid-value of bin-l for parameter k, $\nu_{i_1 \ldots i_d}$ is the annual rate of occurrence of an event with parameters $(\phi_{1,i_1}, \ldots, \phi_{d,i_d})$ delivered by the activity matrix at the site (Section 2.3.1), and ν in given by Equation 2.35. The events E_i, $i = 1, \ldots, N(\tau)$, are independent identically distributed random variables with the probability density function given in Equation 2.37, and the total number of events $N(\tau)$ in $(0, \tau)$ follows a Poisson distribution with constant annual rate ν.

2.3.4 Seismic hazard

The seismic hazard at a site is completely defined by earthquake moment magnitude m, and source-to-site distance r (Section 2.2.1). The United States Geological Survey (USGS) provides realizable values of earthquake moment magnitude m and source-to-site distance r at each zip code in the United States, and mean yearly rates, ν_{ij} of earthquakes with moment magnitude m_i and source-to-site distance r_j [180]. Details on the calculations of mean yearly rates for all possible (m, r) at a given site can be found in [179]. Figure 2.13 shows the seismic activity matrix for Los Angeles, California, normalized by $\nu = \sum_{i,j} \nu_{ij} = 0.95$, that is, the joint probability density function of $(\Phi_1 = M, \Phi_2 = R)$ in Equation 2.37. Given that an earthquake occurs at a site, the probability that it has parameters (m_i, r_j) is ν_{ij}/ν.

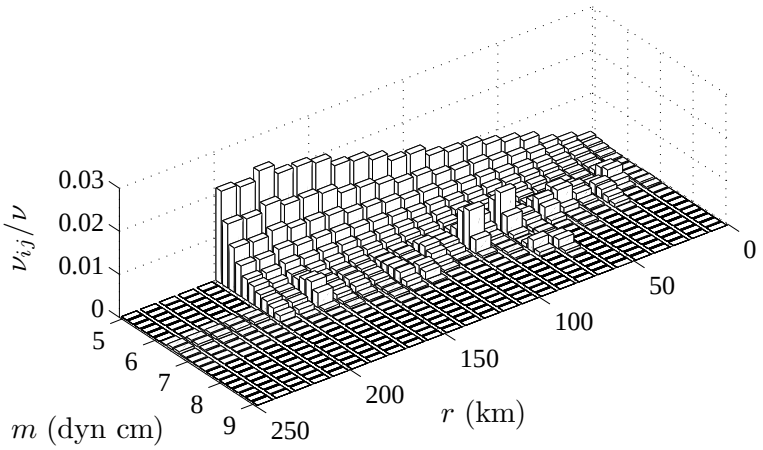

Figure 2.13: Normalized seismic activity matrix for Los Angeles.

2.3.5 Wind and wave hazards

Wind effects on structures and components depend not only on the magnitude of the wind speeds, but on the associated wind directions as well. A joint probability distribution of extreme wind speeds and directions is required to completely define the wind forces on structures, however, so far no credible models for such distributions have been proposed in the literature ([154], section 3.4). In the absence of such models wind effects and their probability distributions may be estimated from the available recorded data or simulated results. In hurricane-prone regions such estimates can be obtained from wind speed data generated by Monte Carlo simulation on the basis of climatological information on hurricane storms for each of the 16 principal compass directions ([154], Section 3.3).

The National Institute of Standards and Technology (NIST) provides (i) hurricane wind speed data generated by Monte Carlo simulation for each 16 compass directions and (ii) estimated mean annual rate of occurrence of hurricanes, at 56 mileposts located at distances of 50 nautical miles along the Gulf and Atlantic coasts of the United States [122]. Figure 2.14 shows the location of mileposts in NIST database. For a given

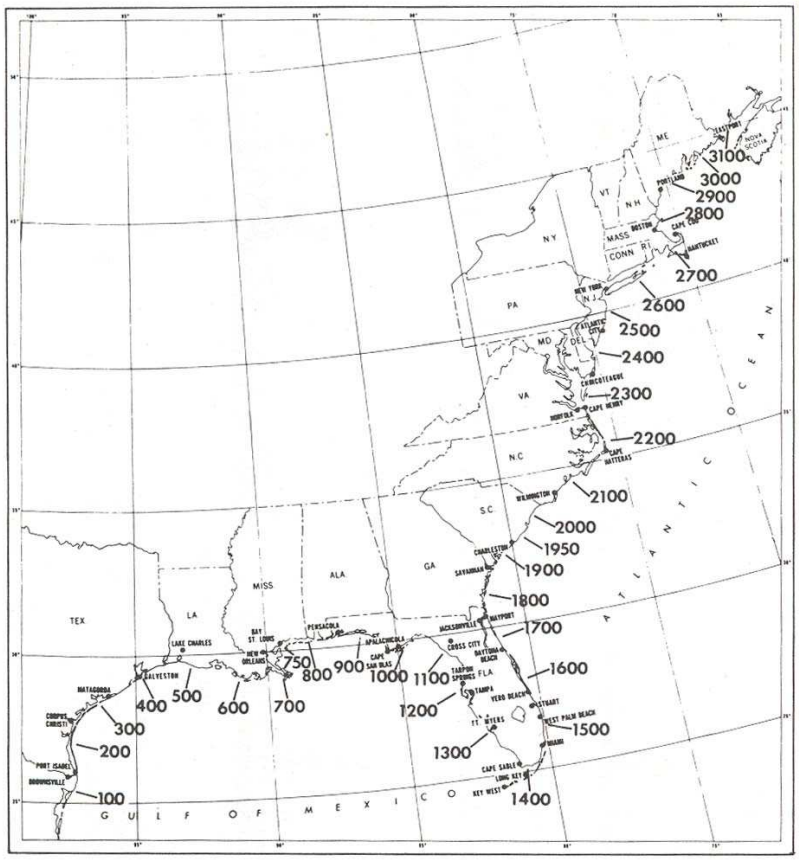

Figure 2.14: Milepost locations [154].

milepost, the data consists of (i) estimated annual rate of occurrence of hurricanes at this milepost and (ii) 1-minute wind speeds in knots at 10 m above open terrain near the coastline in 16 specified directions, beginning with North-Northeast and moving clockwise to North, for a total of 999 simulated hurricanes. The respective mean hourly wind speeds in meters per second at 10 m above ground over open terrain near the coastline can be obtained via multiplication by the factor 0.4146 (Section 2.2.2.1). Figure 2.15 shows the mean hourly wind speeds and corresponding directions for the first simulated hurricane at milepost-150.

The procedure followed by NIST to obtain extreme wind speeds in hurricane prone regions is based on a comprehensive and effective approach to the modeling of

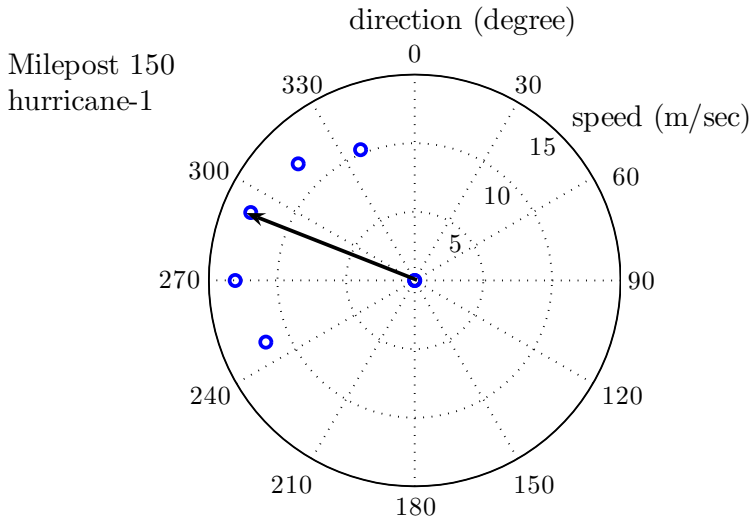

Figure 2.15: Wind speeds and directions for hurricane-1 at milepost-150.

extreme wind probabilities at a site on the basis of information on typical hurricane characteristics developed in [139]. This approach was subsequently applied in [15], where extreme wind speeds associated with hurricanes were estimated on the basis of the climatological and physical models described in [154]. Some important details of these models relevant to this study are provided here. Estimates of the probabilities of occurrence of hurricane wind speeds were obtained in [15] by assuming each of the area adjoining 56 mileposts to be hit by 1000 hurricanes. The hurricane frequency of occurrence was modeled by a Poisson process with a constant rate. The climatological characteristics of the hurricanes were determined by Monte Carlo simulation from the respective probabilistic models as fitted to historical data. The maximum wind speed at a site for a given hurricane is obtained as follows. First, the hurricane track, that is the footprint of the eye of the hurricane, and the characteristics defining the intensity of the hurricane along its track are generated at a sufficiently large number of positions (locations) along its track. For each position of the hurricane the climatological characteristics used in conjunction with the physical models to define a wind field so that the wind speed at the site of interest is calculated. The largest among these speeds is the

maximum wind speed caused by the hurricane at the site.

For simplicity, in this study, we assume that a hurricane can be represented by the maximum hourly mean wind speed $\bar{v}$ in any direction and a corresponding principal, or predominant, wind direction $\bar{\theta}$. The principal wind direction $\bar{\theta}$ is defined here as a weighted average of the wind directions corresponding to non-zero wind speeds. We use an average direction rather than the direction corresponding to the maximum wind speed to account for the directions with non-zero wind speeds. Our assumption that a hurricane can be represented by ($\bar{v}$,$\bar{\theta}$) can be justified by the data in [122], which shows that the directions corresponding to non-zero wind speeds are similar for most of the simulated hurricanes in all mileposts (see, for example, Figure 2.15). The mean wind speed $\bar{v}$ and its direction $\bar{\theta}$ for each simulated hurricane at a given milepost are obtained using the NIST database [122] as follows.

Let $\boldsymbol{v}$ be an $\mathbb{R}^{16}$-valued vector whose coordinates $\{v_i\}$, $i = 1, \ldots, 16$, denote wind speeds in 16 directions of a hurricane at a site (milepost). The corresponding wind directions are at angles $\theta_i = 22.5^0(i-1)$, $i = 1, \ldots, 16$, where θ_1 corresponds to North. The NIST database [122] consists of 999 such vectors for each of the 56 mileposts. Denote by $(\tilde{v}_1, \ldots, \tilde{v}_n)$, $n \leq 16$, the non-zero readings extracted from $(v_1, \ldots, v_{16})$. For example, v_1 is not included in $(\tilde{v}_1, \ldots, \tilde{v}_n)$ if 0 and $\tilde{v}_1 = v_1$ if $v_1 \neq 0$. Denote by $(\tilde{\theta}_1, \ldots, \tilde{\theta}_n)$ the directions corresponding to $(\tilde{v}_1, \ldots, \tilde{v}_n)$. The hurricane wind speed $\bar{v}$ and its direction $\bar{\theta}$ are

$$\bar{v} = \max(\tilde{v}_1, \ldots, \tilde{v}_n), \tag{2.38}$$

$$\bar{\theta} = \arctan\left(\frac{x}{y}\right) + \phi, \tag{2.39}$$

where $x = \sum_{j=1}^{n} w_j \sin(\tilde{\theta}_j)$, $y = \sum_{j=1}^{n} w_j \cos(\tilde{\theta}_j)$, in which $w_j = \tilde{v}_j^2 / \sum_{k=1}^{n} \tilde{v}_k^2$, $j = 1, \ldots, n$, are some weights assigned to each direction $\tilde{\theta}_j$, and ϕ equals 0, 180, 360 and 180 degrees for $(x > 0, y > 0)$, $(x < 0, y < 0)$, $(x \geq 0, y < 0)$ and

$(x \leq 0, y > 0)$, respectively. The weights w_j, $j = 1, \ldots, n$ are assigned such that (i) they are proportional to the square of the wind speed since the wind force acting on a structure is proportional to the square of the wind speed as well [154], (ii) $w_j > 0$ for $j = 1, \ldots, n$, and (iii) $\sum_{j=1}^{n} w_j = 1$. For example, for the hurricane shown in Figure 2.15 $\bar{v} = 13.0793$ m/sec and $\bar{\theta} = 289.5413^0$ (shown with the arrow on the plot). Hence, 999 pairs of $(\bar{v}, \bar{\theta})$ can be obtained, corresponding to 999 simulated hurricanes, at each milepost.

The wind activity matrix at a site (milepost) can be constructed from (i) a histogram of $(\bar{V}, \bar{\Theta})$ obtained from 999 pairs of $(\bar{v}, \bar{\theta})$ calculated following the above procedure, and (ii) the estimated mean annual rate of occurrence of hurricanes at the site provided in the NIST database [122]. Figure 2.16 shows the wind activity matrix for milepost-

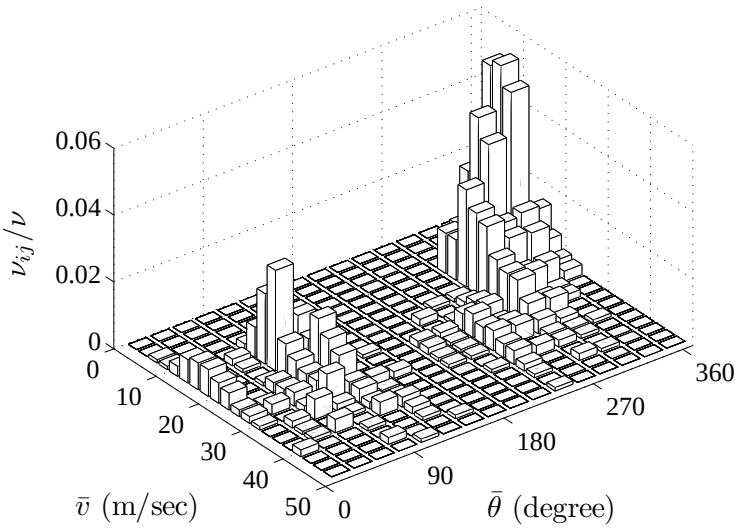

Figure 2.16: Normalized wind activity matrix for milepost-150.

150, normalized by $\nu = \sum_{i,j} \nu_{ij} = 0.325$, that is, the joint probability density function of $(\Phi_1 = \bar{V}, \Phi_2 = \bar{\Theta})$ in Equation 2.37. Given that a hurricane occurs at a site, the probability that it has parameters $(\bar{v}_i, \bar{\theta}_j)$ is ν_{ij}/ν.

As in the seismic hazard model in Section 2.3.4, the hurricane events are independent

identically distributed random variables with the probability density function given in Equation 2.37, and the total number of events $N(\tau)$ in $(0, \tau)$ follows a Poisson distribution with constant annual rate ν. However, unlike the seismic hazard model in which earthquakes may occur at any given time in a year, hurricanes occur most frequently in the late summer when the ocean water temperature has reached a maximum, the winter is almost entirely absent of hurricanes [113]. For simplicity we assume that hurricanes in the Atlantic basin only occur from August 1st trough October 31st at a constant mean rate. Our assumption that the hurricanes only occur from August trough October in the Atlantic is based on the fact that the Atlantic basin shows a very peaked season from August through October, with 78% of the tropical storm days, 87% of the minor (Saffir-Simpson Scale [155] categories 1 and 2) hurricane days, and 96% of the major (Saffir-Simpson Scale categories 3, 4 and 5) hurricane days occurring in this time period [110].

The lifetime model presented for hurricane wind hazard is also used for ocean waves since, in this study, we are also interested in wave hazard on structures and human life induced by tropical storms. The wind activity matrix in Section 2.3.5 provides realizable values of $(\bar{v}, \bar{\theta})$ at a site near the coastline over an open terrain. The respective mean wind speeds over water surface at the system site can be calculated using the similarity model in Section 2.2.2.1 providing a relationship between wind speeds in different surface roughness regimes. Figure 2.8 shows the relationship between the hourly mean wind speeds over open terrain and water surface, at 10 m above the surface.

Hence, the wind activity matrix at an offshore site, characterizing completely the wave hazard to the system at the site, can be obtained directly from that of a nearby onshore site by adjusting the mean wind speeds according to Figure 2.8.

2.4 Monte Carlo simulation

Monte Carlo algorithms are presented for generating samples of (1) single/multiple point events due to seismic, wind and wave hazards with respective probabilistic models discussed in Sections 2.2.1, 2.2.2 and 2.2.3, and (2) lifetime natural hazard scenarios, using the probabilistic models discussed in Section 2.3.

2.4.1 Single point events

Monte Carlo algorithms are presented for generating samples of a hazard event at a single point modeled by stationary/nonstationary Gaussian and non-Gaussian processes. First, realizations of the stationary Gaussian process are obtained using its parametric representation. This representation consists of superpositions of harmonics that have random amplitudes and deterministic phases. For the non-Gaussian model, first realizations of its Gaussian image are generated using the same procedure, then these realizations are translated using a memoryless transformation [69]. Nonstationarity is introduced by modulating the Gaussian/non-Gaussian signals using an appropriate envelop function.

2.4.1.1 Gaussian model

Let $G(t)$ be a zero-mean, real-valued, stationary Gaussian process with a spectral density function $g_{GG}(\omega)$ defined on the frequency interval $(0, \bar{\omega})$, such as the ones in Equations 2.3, 2.19 and 2.27, for seismic ground acceleration, wind velocity and wave particle velocity, respectively. The process $G(t)$ has the spectral representation

$$G(t) = \int_0^{\bar{\omega}} [\cos(\omega t)\, dU(\omega) + \sin(\omega t)\, dV(\omega)], \tag{2.40}$$

where $U(\omega)$ and $V(\omega)$ are zero-mean, real-valued, independent Gaussian processes with orthogonal increments and increment variances $E[dU^2(\omega)] = E[dV^2(\omega)] = g_{GG}(\omega)d\omega$.

An approximate spectral representation of $G(t)$ can be obtained discretizing its spectral density. Let $(\alpha_{r-1}, \alpha_r),\ r = 1, \ldots, q$, with $\alpha_0 = 0$ and $\alpha_q = \bar{\omega}$, be a partition of the frequency band $(0, \bar{\omega})$ in q non-overlapping intervals of length $\Delta\omega_r = \alpha_r - \alpha_{r-1}$ and denote by $\{\omega_r\}$, $r = 1, \ldots, q$, the midpoints of these frequency intervals. Define a discrete approximation of order q of $G(t)$ as

$$G^{(q)}(t) = \sum_{r=1}^{q} \sigma_r \ (A_r \cos \omega_r t + B_r \sin \omega_r t) \tag{2.41}$$

where A_r and B_r, $r = 1, \ldots, q$ are independent zero-mean, unit-variance Gaussian random variables and

$$\sigma_r^2 = \int_{\alpha_{r-1}}^{\alpha_r} g_{GG}(\omega)\, d\omega \simeq g_{GG}(\omega_r)\Delta\omega_r. \tag{2.42}$$

It can be shown that $G^{(q)}(t)$ approaches to $G(t)$ in the mean square sense as $q \to \infty$; and that the covariance function of $G^{(q)}(t)$ converges to that of $G(t)$. The model $G^{(q)}(t)$ is periodic with period π/ω_1 hence samples longer than π/ω_1 provide same information as samples with length π/ω_1.

Nonstationarity can be introduced by modulating the stationary record using an appropriate envelop function, such as the one given in Equation 2.2 for seismic ground motions.

2.4.1.2 Non-Gaussian translation model

First the underlying Gaussian image $G^{(q)}(t)$ of the non-Gaussian process $Z^{(q)}(t)$ is generated following Section 2.4.1.1. Then the Gaussian record $G^{(q)}(t)$ is translated to the non-Gaussian space by

$$Z^{(q)}(t) = F^{-1} \circ \Phi\left(G^{(q)}(t)\right). \tag{2.43}$$

The parameters of the student-t distribution F are selected to match the target statistics from the data. The inversion of the student-t distribution is performed numerically using

MATLAB. Nonstationarity can be introduced by modulating the stationary record using an appropriate envelop function.

2.4.2 Multiple point events

Monte Carlo algorithms are presented for generating samples of a hazard event at multiple points modeled by stationary/nonstationary Gaussian and non-Gaussian vector processes. The algorithm is similar to the single point case presented in Section 2.4.1.

2.4.2.1 Gaussian model

Let $\boldsymbol{G}(t)$ be an n-dimensional, wide-sense stationary vector process with real-valued components of mean zero and covariance functions; $c_{G_kG_l}(\tau) = E[G_k(t)G_l(t+\tau)]$, $k, l = 1, \ldots, n$. The spectral density functions $s_{G_kG_l}(\omega)$ of $\boldsymbol{G}(t)$ and the covariance functions $c_{G_kG_l}(\tau)$ are related by the Wiener-Khintchine relationships,

$$s_{kl}(\omega) = \frac{1}{2\pi} \int_{-\infty}^{\infty} e^{-j\omega\tau} c_{kl}(\tau)\, d\tau, \tag{2.44}$$

$$c_{kl}(\tau) = \int_{-\infty}^{\infty} e^{j\omega\tau}\, s_{kl}(\omega) d\omega, \tag{2.45}$$

where $k, l = 1, \ldots, n$ and $j = \sqrt{-1}$. $\boldsymbol{G}(t)$ can be represented by the spectral representation method as

$$\boldsymbol{G}(t) = \int_0^{\infty} [\cos\, \omega t\, d\boldsymbol{U}(\omega) + \sin\, \omega t\, d\boldsymbol{V}(\omega)], \tag{2.46}$$

where $\boldsymbol{U}(\omega)$ and $\boldsymbol{V}(\omega)$ are processes with zero-mean and orthogonal increments satisfying the conditions

$$E[U_k(\omega)] = E[V_k(\omega')] = 0, \tag{2.47}$$

$$E[dU_k(\omega) dU_l(\omega')] = E[dV_k(\omega) dV_l(\omega')] = \delta(\omega - \omega')\, b_{kl}(\omega)\, d\omega,$$

$$E[dU_k(\omega) dV_l(\nu)] = -E[dV_k(\omega) dU_l(\omega')] = \delta(\omega - \omega')\, h_{kl}(\omega)\, d\omega,$$

where $b_{kl}(\omega) = s_{kl}(\omega) + s_{kl}(-\omega)$, $h_{kl}(\omega) = -\sqrt{-1}\,[s_{kl}(\omega) - s_{kl}(-\omega)]$, and $k, l = 1, \ldots, n$. For a Gaussian process, the processes $\boldsymbol{U}(\omega)$ and $\boldsymbol{V}(\omega)$ are Gaussian.

A discrete approximation of order q, $\boldsymbol{G}^{(q)}(t)$, of $\boldsymbol{G}(t)$ can be obtained using the spectral representation method as follows: Let $(0, \bar{\omega}_k)$ be the bandwidth of the component $G_k(t)$, k=1,...,n. The bandwidth of $\boldsymbol{G}(t)$ is $(0, \bar{\omega})$, in which $\bar{\omega} = \max_{1 \le k \le n}\{\bar{\omega}_k\}$. If a component $G_k(t)$ has power over the entire frequency range, a cutoff frequency $\bar{\omega}_k < \infty$ can be selected such that $\int_{-\bar{\omega}_k}^{\bar{\omega}_k} s_{kk}(\omega) \simeq \int_{-\infty}^{\infty} s_{kk}(\omega)$. Let $(\alpha_{r-1}, \alpha_r),\ r = 1, \ldots, q$, with $\alpha_0 = 0$ and $\alpha_q = \bar{\omega}$, be a partition of the frequency band $(0, \bar{\omega})$ in q non-overlapping intervals of length $\Delta\omega_r = \alpha_r - \alpha_{r-1}$ and denote by $\{\omega_r\}$, $r = 1, \ldots, q$, the midpoints of these frequency intervals. Define $\boldsymbol{G}^{(q)}(t)$ as

$$\boldsymbol{G}^{(q)}(t) = \sum_{r=1}^{q} (\boldsymbol{A}_r \cos \omega_r t + \boldsymbol{B}_r \sin \omega_r t) \tag{2.48}$$

which is a discrete approximation of order q of $\boldsymbol{G}(t)$. The zero mean Gaussian vector $\{\boldsymbol{A}_r, \boldsymbol{B}_r\}$, $r = 1, \ldots, q$, has the covariances

$$E[A_{r,k} A_{p,l}] = E[B_{r,k} B_{p,l}] = \delta_{rp} \int_{\alpha_{r-1}}^{\alpha_r} b_{kl}(\omega)\, d\omega \simeq \delta_{rp}\, b_{kl}(\omega_r)\, \Delta\omega_r, \tag{2.49}$$

$$E[A_{r,k} B_{p,l}] = -E[B_{r,k} A_{p,l}] = \delta_{rp} \int_{\alpha_{r-1}}^{\alpha_r} h_{kl}(\omega)\, d\omega \simeq \delta_{rp}\, h_{kl}(\omega_r)\, \Delta\omega_r,$$

in which δ_{rp} is 1 if $r = p$, and 0 otherwise, b_{kl} and h_{kl} are defined by Equation 2.47, and $k, l = 1, \ldots, n$ and $r, p = 1, \ldots, q$.

It can be shown that $\boldsymbol{G}^{(q)}(t)$ approaches to $\boldsymbol{G}(t)$ in the mean square sense as $q \to \infty$; and that the covariance functions of $\boldsymbol{G}^{(q)}(t)$ converge to those of $\boldsymbol{G}(t)$ assuming that $\boldsymbol{G}(t)$ has a bounded frequency band $[0, \bar{\omega}]$. Hence $\boldsymbol{G}^{(q)}(t)$ has nearly the same second-moment properties as $\boldsymbol{G}(t)$ for sufficiently large q.

Samples of the nonstationarity Gaussian vector process may be obtained from the samples of the corresponding stationary process by modulating each of its component by an appropriate modulation function, such as the one in Equation 2.2 for seismic ground motions.

2.4.2.2 Non-Gaussian translation model

Similar to the non-Gaussian model for single point case, first the Gaussian image $\boldsymbol{G}^{(q)}(t)$ of the non-Gaussian vector process $\boldsymbol{Z}^{(q)}(t)$ is generated following Sections 2.4.2.1 and then it's translated by

$$\boldsymbol{Z}^{(q)}(t) = (\ldots,\ Z_i^{(q)}(t) = F_i^{-1} \circ \Phi\left(G_i^{(q)}(t)\right),\ \ldots), \quad i = 1, \ldots, n. \tag{2.50}$$

The parameters of the student-t distribution F are selected to match the target statistics from the data. Nonstationarity can be introduced by modulating the stationary record using an appropriate envelop function.

2.4.3 Lifetime hazard

Samples of the lifetime seismic hazard at a site can be generated directly following the procedure outlined below. However, in order to generate samples of the lifetime wind and/or wave hazards at a site caused by a hurricane the procedure outlined below should be slightly modified to account for the fact that hurricanes only occur in summer. This issue is addressed at the end of this section.

Consider a natural hazard at a site during a reference time τ. The lifetime model developed in Section 2.3.2 specifies (1) the random arrival times T_k, $k = 1, \ldots, N(\tau)$, of events E_k at this site in $(0, \tau)$ (see Figure 2.12), and (2) the random properties of each event E_k, $k = 1, \ldots, N(\tau)$. In our model $\{N(\tau), \tau \geq 0\}$ is a homogeneous Poisson counting process during the time interval $(0, \tau)$ with a mean yearly arrival rate ν.

There exists several methods for generating samples of $\{T_k, N(\tau)\}$ ([69], Section 4.6). The method used here is based on the property that the unordered homogeneous Poisson events in a time interval $(0, \tau)$, conditional on $N(t)$, are independent and have

a uniform distribution

$$F(u) = \begin{cases} 0.0, & u \leq 0 \\ u/\tau, & 0 \leq u \leq \tau \\ 1.0, & u \leq \tau, \end{cases} \tag{2.51}$$

on $(0, \tau)$. The simulation method based on this property has two steps. First, a sample n of the Poisson counting process $\{N(\tau), \tau \geq 0\}$ has to be generated. The inverse transform method ([69], Section 4.1) and the probability in Equation 2.36 can be used to obtain this sample of the Poisson counting process. Second, we need to generate n independent samples of distribution F defined by Equation 2.51. The resulting n samples constitute a realization of the Poisson events $\{T_k\}$ in $(0, \tau)$.

Properties of each event E_k, that is, independent samples of $(\Phi_1, \ldots, \Phi_d)$, $k = 1, \ldots, N(\tau)$, are assigned using the joint probability density function in Equation 2.37 of the parameters $(\Phi_1, \ldots, \Phi_d)$ defining them. The activity matrix of the hazard at site, normalized by the mean annual rate ν, is a discrete approximation to the joint probability density function and is used here to assign the parameters $(\Phi_1, \ldots, \Phi_d)$ of each event E_k, $k = 1, \ldots, N(\tau)$, in a hazard sample (see Figure 2.12).

In Section 2.3.5 it was assumed that hurricanes in the Atlantic basin only occur from August trough October with a constant mean rate, that is, they occur during 1/4 of a year. Accordingly, the above procedure is modified for generating samples of hurricane hazard at a site. The first step above, that is, generating a sample n of the Poisson counting process $\{N(\tau), \tau \geq 0\}$ with mean annual rate ν, remains the same. In the next step, we generate n independent samples of a uniform distribution over $(0, \tau/4)$. The resulting n samples constitute a realization of the Poisson events $\{\tilde{T}_k\}$, $k = 1, \ldots, n$, in $(0, \tau/4)$. The final step is to obtain the arrival time T_k of event E_k, $k = 1, \ldots, n$, corresponding to $\tilde{T}_k$. The mapping from $\tilde{T}_k$ to T_k, $k = 1, \ldots, n$, as illustrated in Figure 2.17, is $T_k = [4\tilde{T}_k] + 7/12 + \delta$, in which, $[4\tilde{T}_k]$ is the integer part of

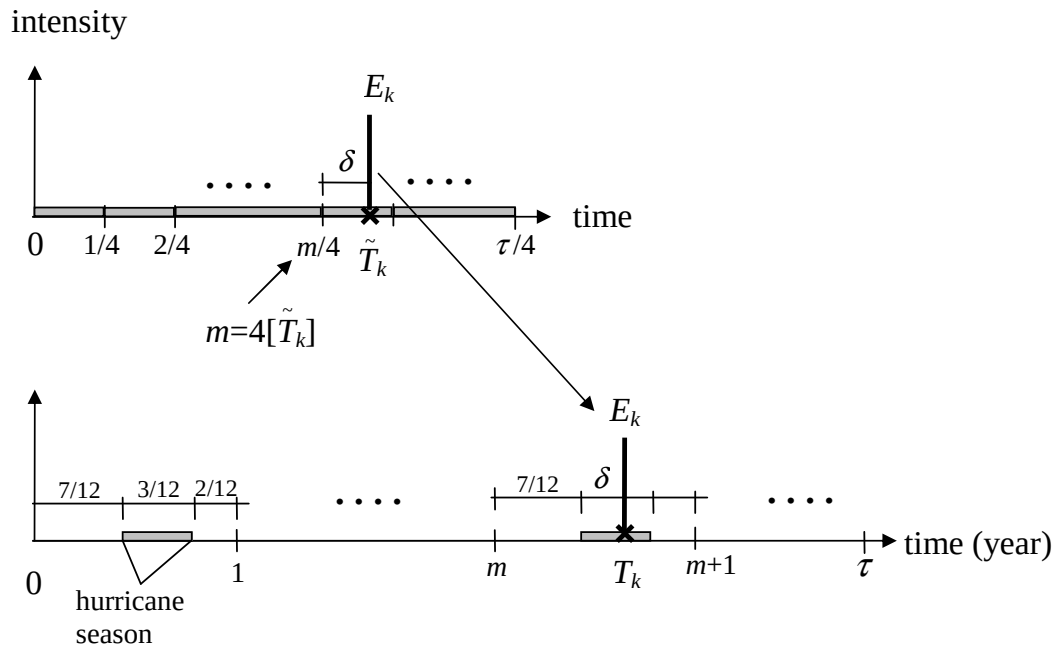

Figure 2.17: Generation of hurricane arrival times.

$4\tilde{T}_k$, $\delta = \tilde{T}_k - [4\tilde{T}_k]/4$, and $k = 1, \ldots, N(\tau)$.

2.5 Examples

Samples of lifetime natural hazard scenarios, specifying the random arrival times of individual events at a site during a reference time τ and the random properties of the events under considerations, are generated using the probabilistic models in Section 2.3 and Monte Carlo algorithms in Section 2.4.3, for seismic, wind and wave hazards. Also, time history records of ground accelerations and wind/wave velocities are generated at single/multiple points for a given event in a sample of the lifetime natural hazard scenario using the respective probabilistic models in Section 2.2 and Monte Carlo algorithms in Sections 2.4.1 and 2.4.2, for seismic, wind and wave hazards.

2.5.1 Seismic hazard

Samples of lifetime seismic hazard at a site can be generated using Monte Carlo algorithms presented in Section 2.4.3. For example, Figure 2.18 shows part of a sample

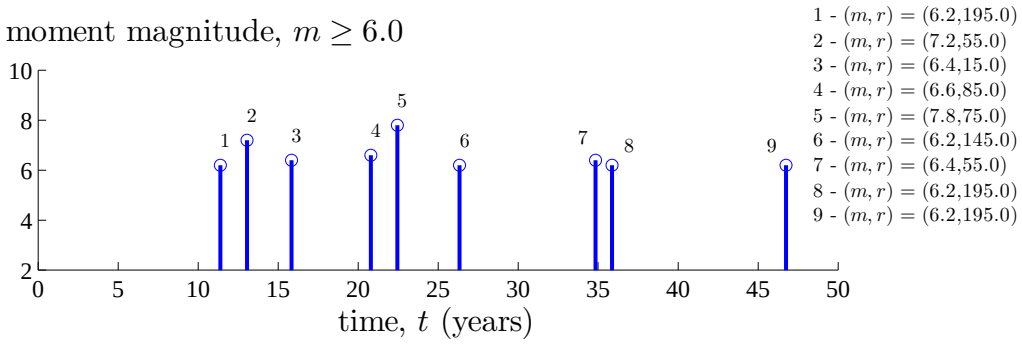

Figure 2.18: A hypothetical sample of the seismic hazard for Los Angeles.

of seismic hazard scenario for Los Angeles, California over a lifetime of 50 years. The actual sample has 51 events, but just for presentation purposes only the earthquakes with $m \geq 6.0$ are shown in Figure 2.18.

Gaussian and non-Gaussian ground acceleration time histories at single/mutliple points in Los Angeles can be generated for each event in Figure 2.18 using Monte Carlo algorithms presented in Section 2.4. For example, the samples of the ground acceleration processes below correspond to event-2 in Figure 2.18 with moment magnitude, $m = 7.2$ and source to site distance, $r = 55$ km, resulting in a ground motion duration of 20.63 sec and one-sided spectral density function in Figure 2.19.

2.5.1.1 Single point

Gaussian and non-Gaussian ground acceleration time histories are generated at a single point at the site Figure 2.18 following the Monte Carlo algorithm presented in Section 2.4.1. First, stationary ground acceleration samples are generated and then

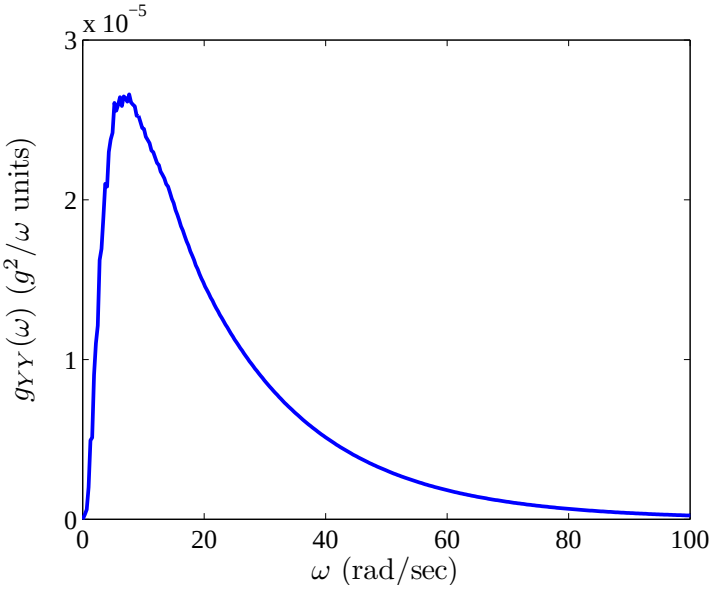

Figure 2.19: Spectral density of ground acceleration from event-2.

corresponding nonstationary samples are calculated using the modulation function given by Equation 2.2 for both Gaussian and non-Gaussian models. Figures 2.20 and 2.21

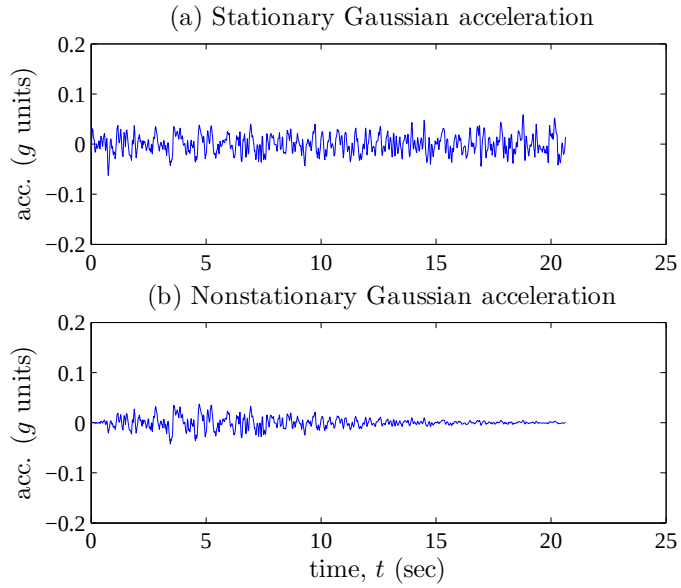

Figure 2.20: Gaussian ground accelerations on USGS class-A soil.

show the stationary/nonstationary Gaussian ground accelerations on USGS class A and

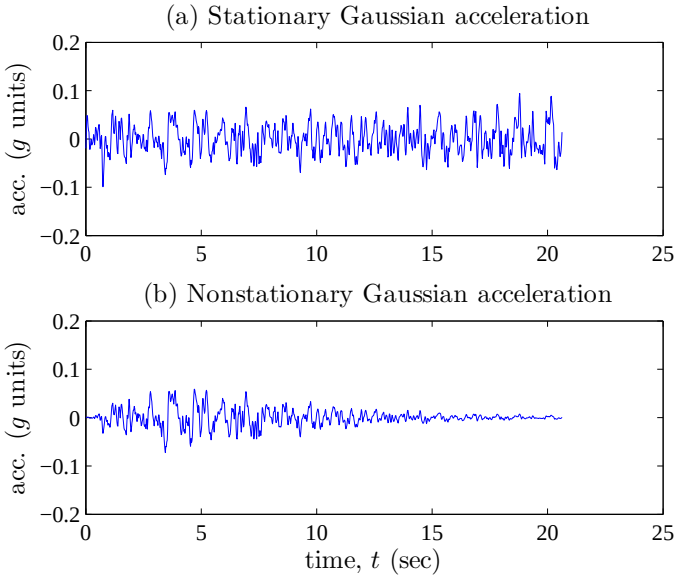

Figure 2.21: Gaussian ground accelerations on USGS class-C soil.

C soils, representing hard rock and generic soil, respectively. Ground accelerations are higher for USGS class-C soil, since spectral densities for softer soil are larger than those for stiffer soil or rock (Figure 2.2). Figures 2.22 and 2.23 show the

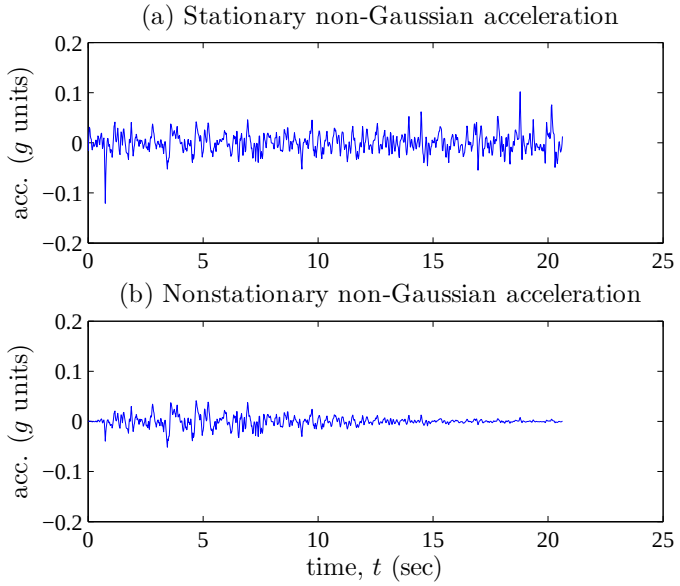

Figure 2.22: Non-Gaussian ground accelerations on USGS class-A soil (γ_4=6.26).

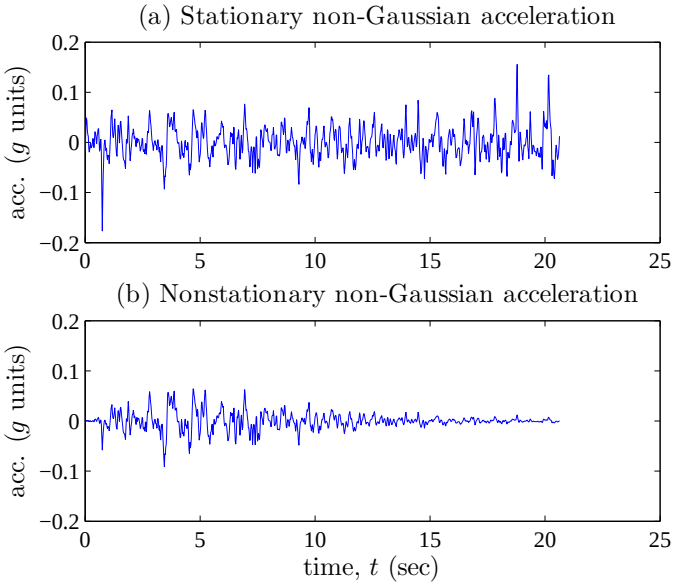

Figure 2.23: Non-Gaussian ground accelerations on USGS class-C soil (γ_4=5.58).

stationary/nonstationary non-Gaussian ground accelerations on USGS class-A and C soils, respectively. Table 2.1 shows the parameters of the student-t density function in

Table 2.1: Student-t parameters.

	Parameters	
Soil type	b	c
USGS class-A	0.0131	5.8405
USGS class-C	0.0214	6.3256

Equation 2.5 for the selected soil types and earthquake. Again, ground accelerations are higher for USGS class-C soil, since spectral density for class-C soil is larger than that of class-A soil.

2.5.1.2 Multiple points

Monte Carlo algorithms presented in Section 2.4.2 are used to generate samples of stationary Gaussian ground accelerations at multiple points at the site in Figure 2.18. Corresponding non-Gaussian samples are then calculated using Equation 2.17. Nonstationarity is introduced to Gaussian and non-Gaussian samples by Equation 2.9 using the modulation function in Equation 2.2.

Seismic strong ground accelerations are generated at points selected at 50 m in both directions in a 500x500 m^2 area. The coherence function is given by Equation 2.11 with parameters $A = 0.736$, $a = 0.147$, $k = 5120\,\text{m}$, $f_0 = 1.09\,\text{Hz}$, $b = 2.78$ [78]. The apparent velocity vector $\vec{V}$ in Equation 2.14 has magnitude $|\vec{V}| = 500$ m/sec and its direction θ coincides with the direction of the site from the source as shown in Figure 2.24 (a). We chose $\theta = 0$ for this example. Figures 2.25 and 2.26 show

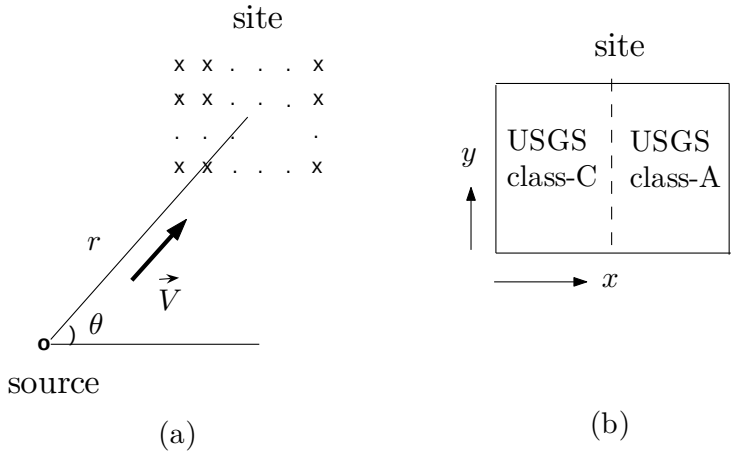

Figure 2.24: Illustration of the site.

the Gaussian ground accelerations at $t = 5$ sec for homogeneous soil (USGS class-C) and for inhomogeneous soil (USGS classes A and C, see Figure 2.24-b), respectively. Again, ground accelerations are higher for USGS class-C soil. Figures 2.27 and 2.28

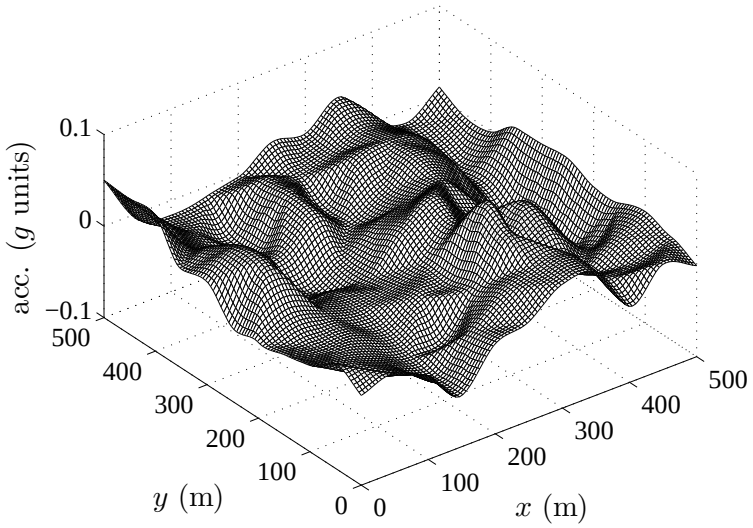

Figure 2.25: Gaussian ground accelerations at $t = 5$ sec on homogeneous soil (USGS class-C).

show the non-Gaussian ground accelerations at $t = 5$ sec on a homogeneous soil (USGS class-C) and for inhomogeneous soil (USGS classes A and C), respectively.

2.5.1.3 Comparison of Gaussian and non-Gaussian ground motions

Differences between the Gaussian and non-Gaussian ground acceleration samples can be assessed by Figures 2.20 and 2.22, Figures 2.21 and 2.23, Figures 2.25 and 2.27, and Figures 2.26 and 2.28. The samples in these pairs of figures correspond to processes with the same second-moment properties. Since non-Gaussian ground accelerations have higher kurtosis coefficients the peak ground accelerations (PGA) are higher compared to those obtained using Gaussian models. Figures 2.29 and 2.30 show the tails of the PGA's obtained using Gaussian and non-Gaussian models, for class-A and class-C soils, respectively. The parameters of the student-t density function for the selected soil types and earthquake are shown in Table 2.1. Figures 2.31 and 2.32 show the normalized histograms of PGA's for the same cases. The figures show

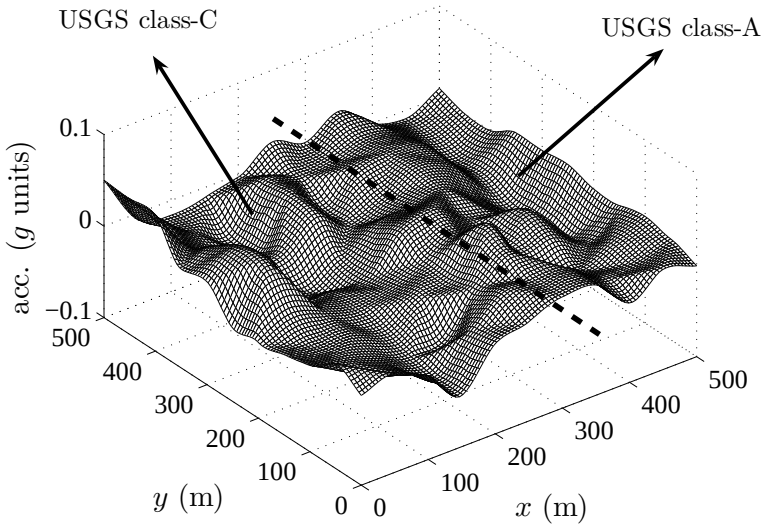

Figure 2.26: Gaussian ground accelerations at $t = 5$ sec on inhomogeneous soil (USGS classes A and C).

that the Gaussian models can underpredict the PGA and other ground acceleration characteristics.

2.5.2 Wind and wave hazards

Samples of lifetime hurricane hazard at a site can be generated using Monte Carlo algorithms presented in Section 2.4.3. For example, Figure 2.33 shows part of a sample of wind hazard scenario in milepost-150 over a lifetime of 50 years. The actual sample has 18 events, but just for presentation purposes only the winds with $\bar{v} \geq 20.0$ m/sec are shown in Figure 2.33.

Wind and wave velocity time histories at an offshore site located near milepost 150 can be generated for each hurricane event in Figure 2.33 at single/mutliple points using Monte Carlo algorithms presented in Section 2.4. For example, the samples of the wind and wave velocity processes below correspond to event-6 in Figure 2.33 with mean wind speed, $\bar{v} = 32.8$ m/sec and principal direction, $\bar{\theta} = 202.5$ degrees, assuming a

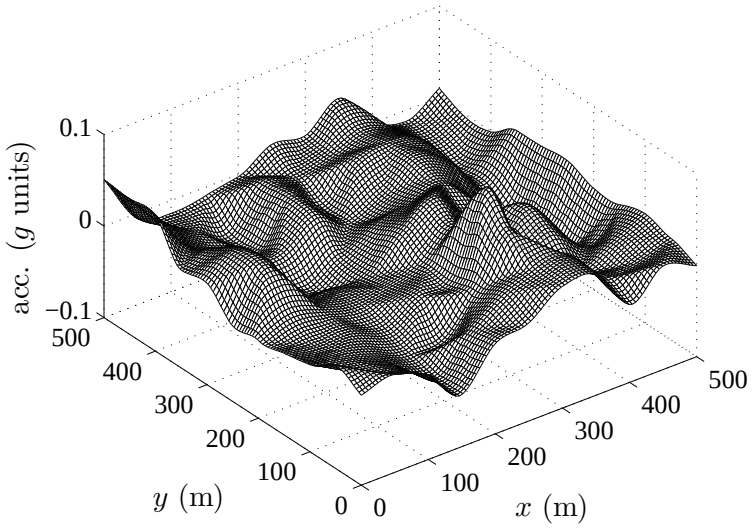

Figure 2.27: Non-Gaussian ground accelerations at $t = 5$ sec on homogeneous soil (USGS class-C, γ_4=5.58).

total duration of 1 hr (Section 2.2.2.1).

Figure 2.34 shows the one-sided spectral density function in Equation 2.19 of the fluctuating component of the wind velocity $V(t)$ in Equation 2.18. Figure 2.35 shows a sample of the wind velocity $V^*(t)$ given by Equation 2.18 with the spectral density function in Figure 2.34.

Figure 2.36 shows the one-sided spectral density function in Equation 2.27 of water particle velocity $U(t)$ in Equation 2.24. Figure 2.37 shows a sample of the water particle velocity $U(t)$ in Equation 2.24 with the spectral density function in Figure 2.36.

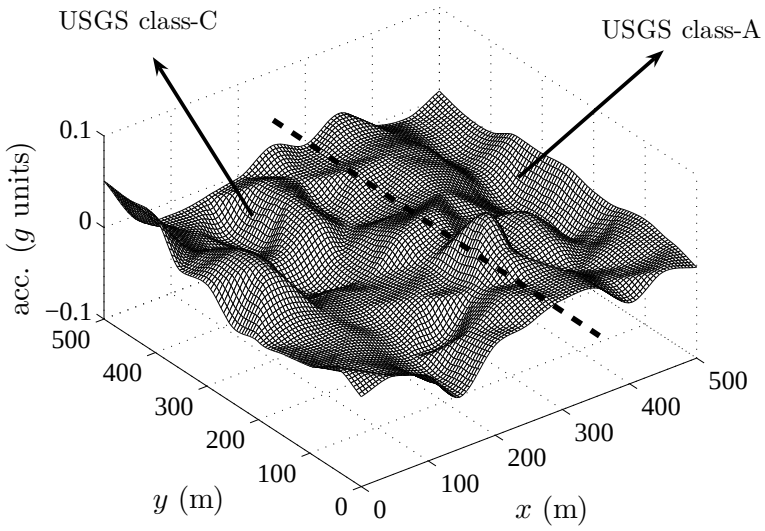

Figure 2.28: Non-Gaussian ground accelerations at $t = 5$ sec on inhomogeneous soil (USGS class-A with γ_4=6.26 and USGS class-C with γ_4=5.58).

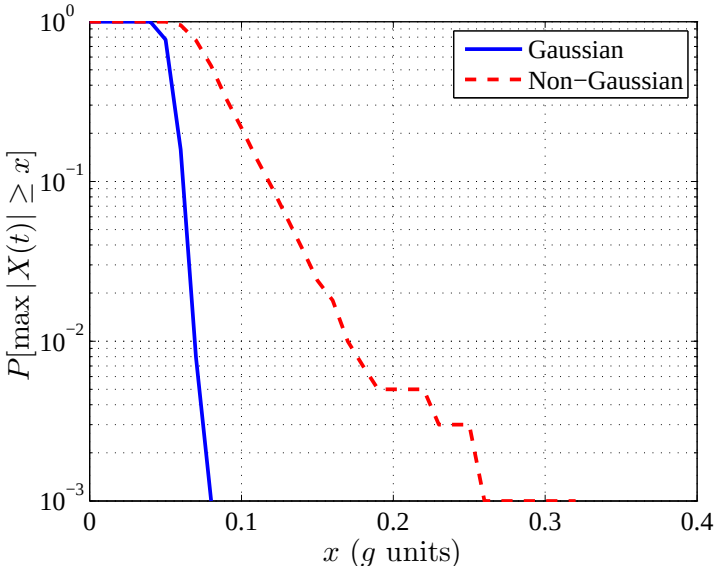

Figure 2.29: Tails of Gaussian and non-Gaussian ground accelerations on USGS class-A soil (γ_4=6.26).

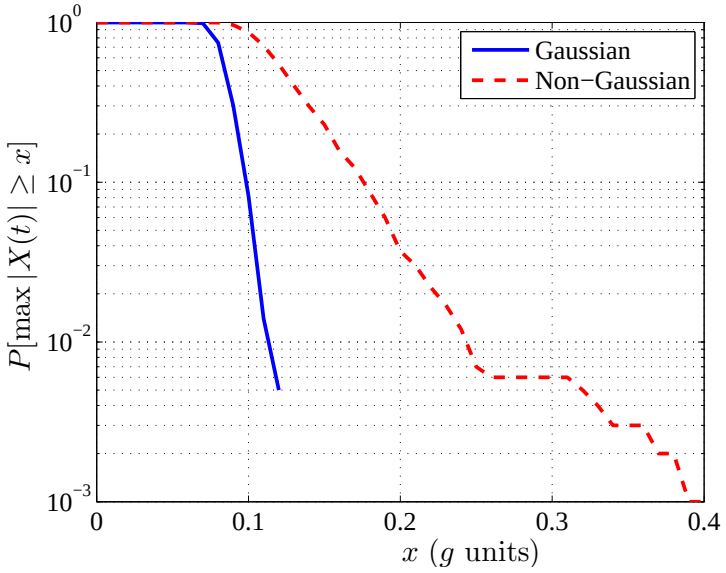

Figure 2.30: Tails of Gaussian and non-Gaussian ground accelerations on USGS class-C soil (γ_4=5.58).

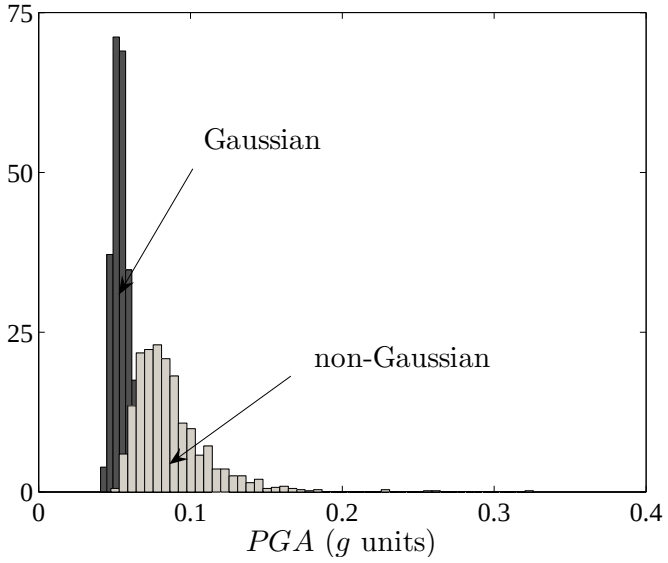

Figure 2.31: Histograms of PGA's for Gaussian and non-Gaussian ground accelerations on USGS class-A soil (γ_4=6.26).

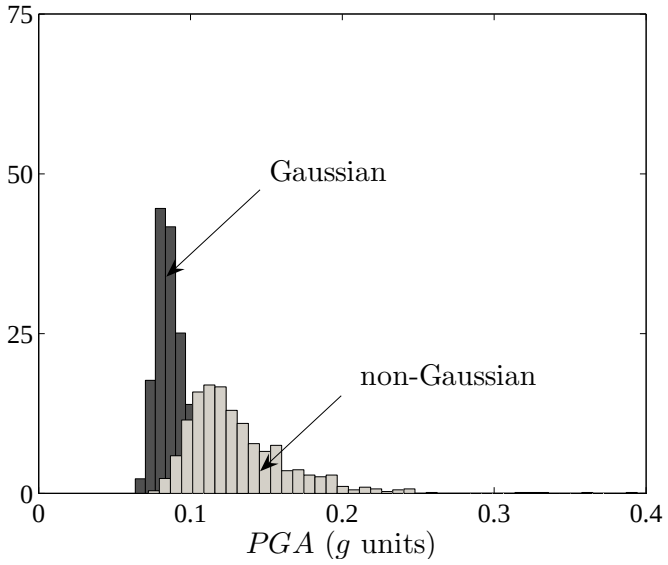

Figure 2.32: Histograms of PGA's for Gaussian and non-Gaussian ground accelerations on USGS class-C soil (γ_4=5.58).

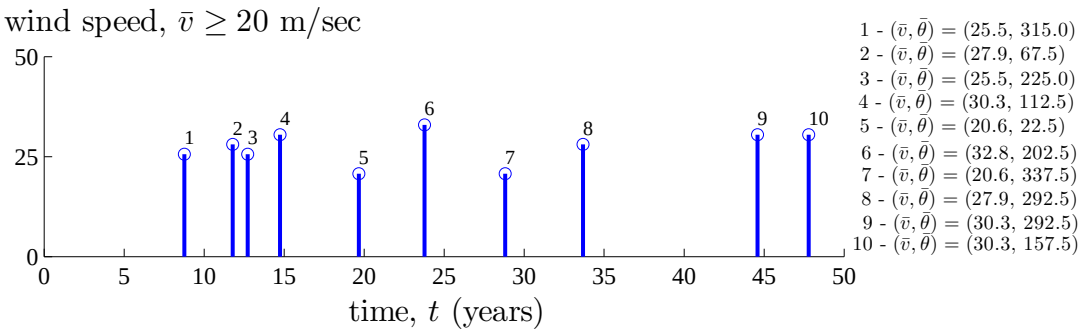

Figure 2.33: A hypothetical sample of the wind hazard for milepost-150.

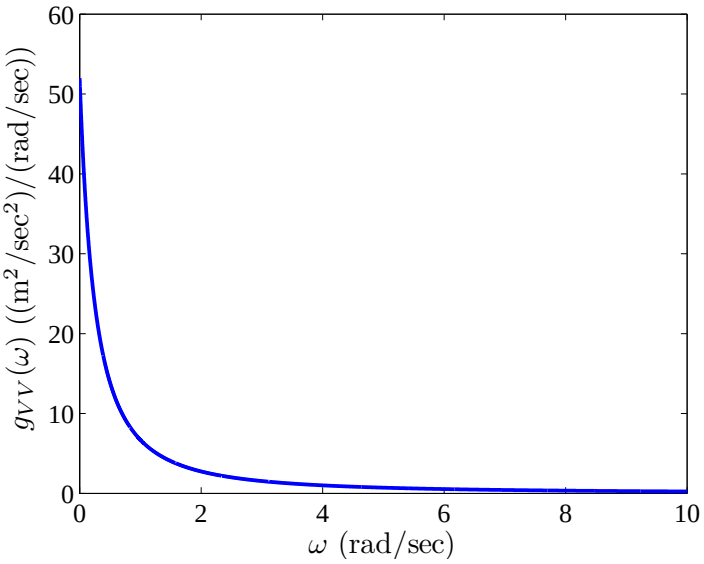

Figure 2.34: Spectral density of wind velocity (for event-6).

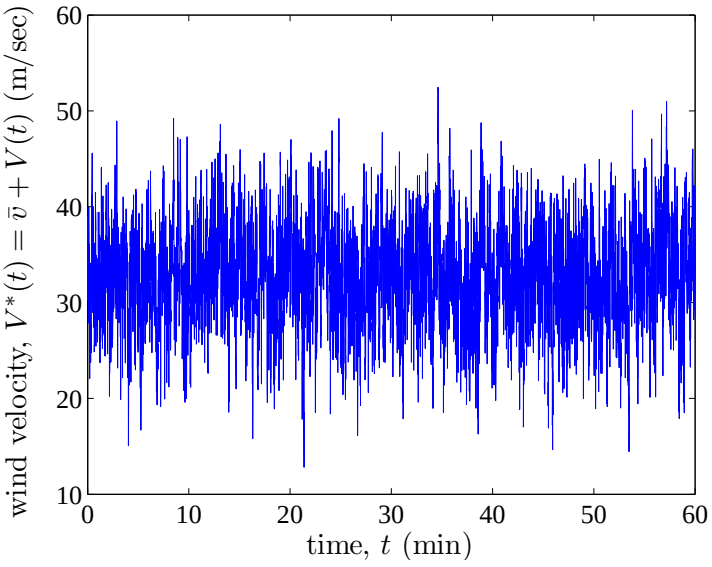

Figure 2.35: A sample of wind velocity (for event-6).

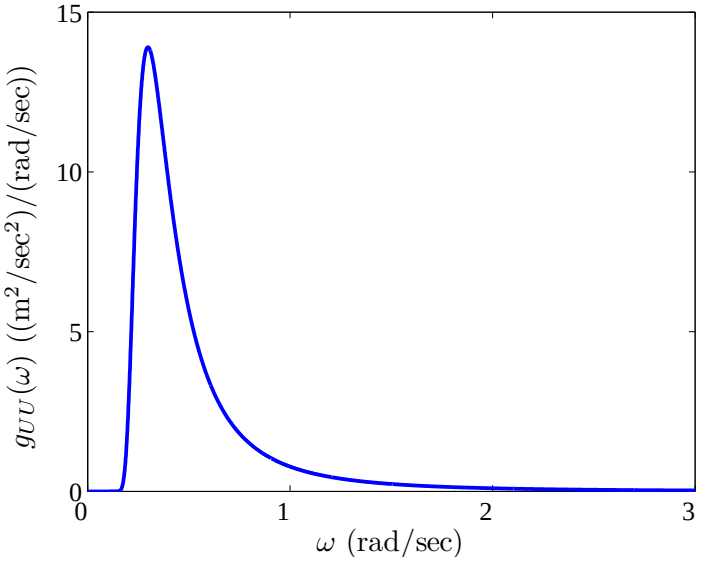

Figure 2.36: Spectral density of wave velocity (for event-6).

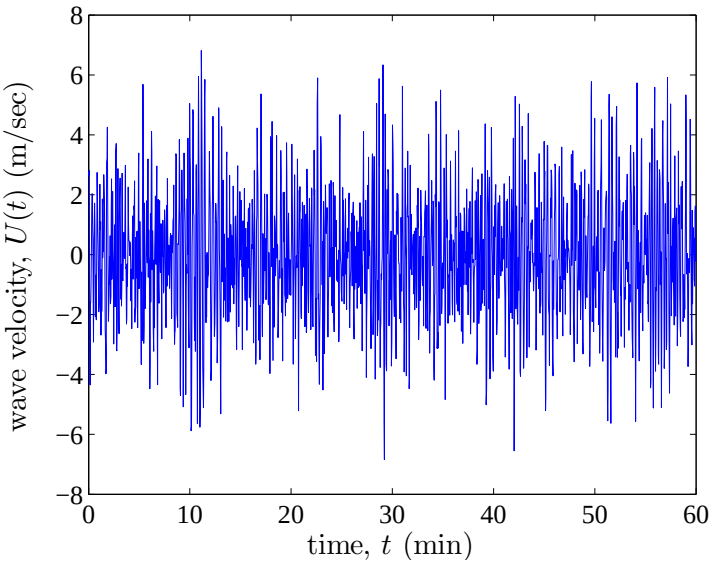

Figure 2.37: A sample of wave velocity (for event-6).

2.6 Multihazard

The overall system risk under a multihazard environment depends on the occurrence of individual hazard events as well as the occurrence of coincidental hazard events. For example, in the case of two independent intermittent hazards, such as seismic and hurricane hazards at a site, there exists three types of events, two individual hazard events and one coincidental hazard event. Figure 2.38 illustrates a sample of two independent hazards occurring at a site in time $(0, \tau)$.

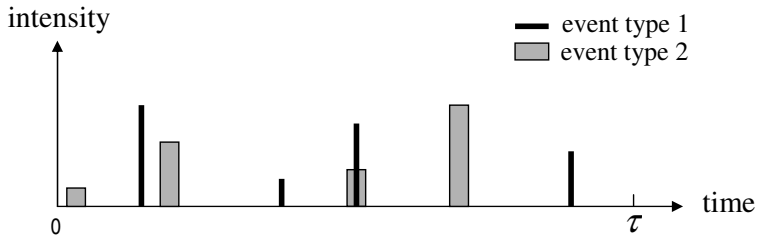

Figure 2.38: A sample of lifetime multihazard.

The multihazard characteristics at a site is evaluated considering a simple case of two independent hazards H_1, H_2 with random durations D_1, D_2, respectively. We assume that the events of hazards $H_1(t)$ and $H_2(t)$ occur in time according to homogeneous Poisson counting processes of intensities ν_1 and ν_2, respectively. It can be shown that the occurrence in time of the coincidental hazard event can be also approximated by a homogeneous Poisson process with intensity [184]

$$\nu_{12} \simeq \nu_1 \nu_2 (\mu_{D_1} + \mu_{D_2}), \tag{2.52}$$

where μ_{D_1} and μ_{D_2} are the expected value of the event durations D_1 and D_2, respectively. The approximation in Equation 2.52 is good when $\nu_1 D_2$ and $\nu_2 D_1$ are small, or $\nu_1 D_1$ (or $\nu_2 D_2$) goes to zero [185]. The mean coincidence duration is given by

$$\mu_{D_{12}} = \mu_{D_1} \mu_{D_2} / (\mu_{D_1} + \mu_{D_2}), \tag{2.53}$$

using Equation 2.52 and the fact that the probability that the coincidence process is *on* at a given time, $\mu_{D_{12}}\nu_{12}$, coincides with the probability that both processes are *on* at that time, which is $\mu_{D_1}\nu_1\mu_{D_2}\nu_2$ because of independence. The probabilities that at any time instant there is no event; a single event of hazard H_i, $i = 1, 2$; and a coincidental event are $p_0 = (1 + \nu_1\mu_{D_1})(1 + \nu_2\mu_{D_2})$; $p_i = \nu_i\mu_{D_i}/p_0$, $i = 1, 2$; and $p_{12} = (\nu_1\mu_{D_1})(\nu_2\mu_{D_2})/p_0$, respectively [150].

Now, consider a simple system located at this site. We can evaluate the performance of this system in $(0, \tau)$ under the hazards H_1 and H_2 from its fragility, that is, the probability of system failure under the hazards H_1 and H_2 in $(0, \tau)$. Failure is defined here as the intensity of a hazard event exceeding a critical value x. An approximation to the system fragility $P_f(x)$ in $(0, \tau)$ under the hazards H_1 and H_2 is [184]

$$P_f(x) = 1 - \exp\left[-\nu_1\tau\left(1 - F_1(x)\right) - \nu_2\tau\left(1 - F_2(x)\right) - \nu_{12}\tau\left(1 - F_{12}(x)\right)\right], \tag{2.54}$$

in which $F_1(x)$, $F_2(x)$ and $F_{12}(x)$ are the probability distributions of intensity of hazard H_1, H_2 and the combined hazard $H_1 + H_2$, respectively, and ν_{12} is given by Equation 2.52. We note that some events are counted twice in Equation 2.54, however, the number of such events is small for hazards with short durations and the approximation to the system fragility in Equation 2.54 is very good in this case [184]. To examine the significance of the second-order term in Equation 2.54, that is, the significance of hazard concurrence, let $\nu_1 = \nu_2 = 2$/year, $\mu_{D_1} = \mu_{D_2} = 0.001$ year, $\tau = 50$ years and $F_1(x) = F_2(x)$ be normal distributions with mean 1 and variance 0.09. Note that is this case $F_{12}(x)$ is a normal distribution with mean 2 and variance 0.18. Figure 2.39 shows the system fragility in Equation 2.54 as a function of hazard intensity x, with and without hazard concurrence (the second-order term). As expected, the second-order term in Equation 2.54 becomes dominant for large values of x, that is, for highly reliable systems.

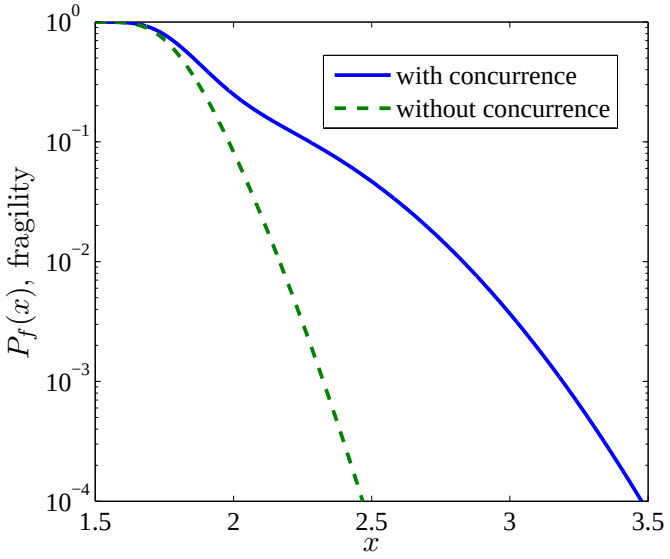

Figure 2.39: System fragility under 2 hazards.

For the case of three independent intermittent hazards H_i, $i = 1, 2, 3$, with mean durations μ_{D_i} and mean occurrence rate ν_i, the simultaneous occurrence of the three hazard events has the mean occurrence rate

$$\nu_{123} \simeq \nu_1\nu_2\nu_3(\mu_{D_1}\mu_{D_3} + \mu_{D_2}\mu_{D_3} + \mu_{D_1}\mu_{D_2}), \tag{2.55}$$

which can be obtained similar to Equation 2.52 noting that the coincidence of events 1 and 2 is a Poisson process with mean rate in Equation 2.52 and mean duration in Equation 2.53. The approximation in Equation 2.55 to the mean occurrence of three simultaneous hazard event is very good under similar conditions given for Equation 2.52. As in the case of two hazards we can obtain the probabilities that at any time instant there is no event, a single event of hazard H_i, $i = 1, 2, 3$, and coincidental event of the three hazards. For example, the probability that at any time instant the structure is subjected to all three hazard events is $p_{123} = (\nu_1\mu_{D_1})(\nu_2\mu_{D_2})(\nu_3\mu_{D_3})/p_0$, in which $p_0 = (1 + \nu_1\mu_{D_1})(1 + \nu_2\mu_{D_2})(1 + \nu_3\mu_{D_3})$ is the probability that at any time instant there is no event.

Chapter 3
System fragility analysis

Consider a dynamic system subjected to a natural hazard event resulting in a m-dimensional forcing function $\boldsymbol{F}(t)$, $t \geq 0$, acting on m system points. Denote by $\boldsymbol{Z}(t)$, $0 \leq t \leq \tau$, a relevant n-dimensional system response process, where τ is a reference time. Figure 3.1 illustrates the relationship between the input $\boldsymbol{F}(t)$ and output $\boldsymbol{Z}(t)$.

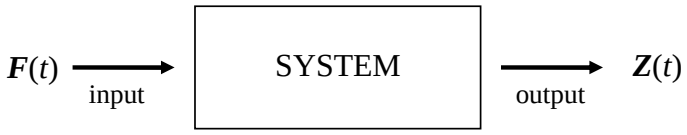

Figure 3.1: Input-output relationship.

Our objective is to find system fragility, that is, the probability that the system response $\boldsymbol{Z}(t)$ leaves a safe set $D \subseteq \mathbb{R}^n$ in $0 \leq t \leq \tau$ if subjected to a natural hazard event of specified intensity. If the safe set D of the system response is associated with a system damage state, fragility becomes a function that describes the probability of exceedance of this damage state, given a hazard intensity [80]. The damage state corresponding to the set D can represent, for example, slight, moderate, extensive damage of the system.

Several methods are available to obtain system fragility information. For example, Monte Carlo simulation [99, 148, 149, 62, 63, 161, 162, 51, 86, 48, 45, 94], reliability analysis [99, 27, 150, 64, 66, 65, 156, 157, 95, 100, 94] or a combination of the two [87, 30, 29] can be used for obtaining structural/nonstructural components and systems fragilities. System fragility can also be based on experimental results [11] or expert opinions [88]. Also, lognormal [80, 148, 149] and extreme type distributions [123, 4] have been used for structural/nonstructural component fragilities.

We plot system fragility against the parameters $\boldsymbol{\phi} = (\phi_1, \ldots, \phi_d)$ characterizing natural hazards (Section 2.3.1), which completely define the probability law of the hazard at the system site so that fragility becomes a d-dimensional surface defined over the set of parameters $\boldsymbol{\phi}$. Accordingly, we denote the probability that the system response $\boldsymbol{Z}(t)$ leaves the safe set D during τ when subjected to an event with parameters $\boldsymbol{\phi}$, that is, the system fragility, by

$$P_f(D; \boldsymbol{\phi}) = 1 - P[\boldsymbol{Z}(t) \in D, 0 \leq t \leq \tau \mid \boldsymbol{\Phi} = \boldsymbol{\phi}]. \tag{3.1}$$

For example, seismic fragility of a system is plotted against the earthquake moment magnitude m and the distance r from the seismic source to the system site and referred to as fragility surfaces [99, 95, 96, 100, 94]. According to our model in Section 2.2.1 (m, r) completely characterizes the ground acceleration process at system site. Similarly, wind and wave fragilities of a system are plotted against the mean wind velocity $\bar{v}$ and principal wind direction $\bar{\theta}$ at system site which completely characterize these hazards at the site (Sections 2.2.2 and 2.2.3). The complement of fragility in Equation 3.1, $1 - P_f(D; \boldsymbol{\phi})$ is a measure of system reliability.

The application of Equation 3.1 to calculate system fragility $P_f(D; \boldsymbol{\phi})$ is generally not practical since the complete probability law of the response process $\boldsymbol{Z}(t)$ is required. We present two methods for approximating the system fragility, (1) crossing theory of stochastic processes and (2) Monte Carlo simulation. The method based on the crossing theory in Section 3.1 can be used for calculating the fragility of linear single and multi degree of freedom systems under stationary/nonstationary Gaussian input. The Monte Carlo method presented in Section 3.2 can be applied to any system and/or input. We use artificial records (i) reduce the uncertainty in the estimated fragility, that can be significant when dealing with actual records because the available sample size is usually small, and (ii) ensure that all records considered in the analysis belong to the same population of known probability law.

3.1 Fragility by crossing theory

The system fragility in Equation 3.1, that is, the probability that the system response $\boldsymbol{Z}(t)$ leaves the safe set D during τ (Figure 3.2) when subjected to an event with

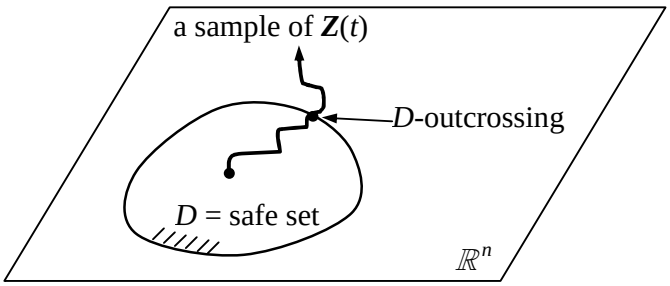

Figure 3.2: D-outcrossing of response process $\boldsymbol{Z}(t)$.

parameters $\boldsymbol{\phi}$, coincides with the probability

$$P_f(D;\boldsymbol{\phi}) = 1 - P[(\boldsymbol{Z}(0) \in D) \cap (N_D(\tau) = 0)] \tag{3.2}$$

that the initial response $\boldsymbol{Z}(0)$ is in the safe sate D and that the number of D-outcrossing of $\boldsymbol{Z}(t)$ in $(0,\tau)$, $N_D(\tau) = 0$, is zero. The fragility in Equation 3.2 can be approximated by

$$\hat{P}_{f,ct}(D;\boldsymbol{\phi}) = 1 - P[(\boldsymbol{Z}(0) \in D)]\, P[(N_D(\tau) = 0)], \tag{3.3}$$

assuming that the events $\{\boldsymbol{Z}(0) \in D\}$ and $\{N_D(\tau) = 0\}$ are independent. In general, it is assumed that the system is at rest so that $P[(\boldsymbol{Z}(0) \in D)] = 1$. If we further assume that the D-outcrossings of $\boldsymbol{Z}(t)$ follow an inhomogeneous Poisson process with intensity $\nu_D(t)$ at time t Equation 3.3 becomes

$$\hat{P}_{f,ct}(D;\boldsymbol{\phi}) = 1 - \exp\left(-\int_0^\tau \nu_D(t)\, dt\right). \tag{3.4}$$

If $\boldsymbol{Z}(t)$ is stationary with mean D-outcrossing rate ν_D, then Equation 3.4 becomes

$$\hat{P}_{f,ct}(D;\boldsymbol{\phi}) = 1 - \exp(-\nu_D \tau). \tag{3.5}$$

The mean D-outcrossings rate of $\boldsymbol{Z}(t)$ at time t in Equation 3.4 is equal to

$$\nu_D(t) = \lim_{\Delta t \to 0} \frac{E[N_D(t+\Delta t)] - E[N_D(t)]}{\Delta t}, \tag{3.6}$$

where $E[N_D(t)]$ is the mean number of D-outcrossings of $\boldsymbol{Z}(t)$ in $(0, t)$. The mean D-outcrossing rate in Equation 3.5, when $\boldsymbol{Z}(t)$ is a stationary process, is time invariant and equal to

$$\nu_D = \frac{E[N_D(\tau)]}{\tau}. \tag{3.7}$$

The crossing theory provides a good approximation to the failure probability when the boundary of D is far enough from $E[\boldsymbol{Z}(t)]$, so that D-outcrossings of $\boldsymbol{Z}(t)$ become nearly independent ([164], Section 7.2).

For a real-valued, nonstationary, zero-mean, mean-square differentiable Gaussian process $Z(t)$ the mean $D = [-z, z]$, $z > 0$, outcrossing rate in Equation 3.6 is given by [164]

$$\nu_D(t) = 2\,\hat{\sigma}(t) \left[\phi\left(\frac{\hat{m}(t)}{\hat{\sigma}(t)}\right) + \frac{\hat{m}(t)}{\hat{\sigma}(t)}\,\Phi\left(\frac{\hat{m}(t)}{\hat{\sigma}(t)}\right)\right] \phi\left(\frac{z}{\sigma(t)}\right)\frac{1}{\sigma(t)}, \quad z > 0, \tag{3.8}$$

where $\sigma^2(t)$ is the variance of $Z(t)$, $\phi(\cdot)$ and $\Phi(\cdot)$ are the density and distribution functions of the standard normal variable, respectively, and the mean and the variance of the conditional Gaussian variable $\dot{Z}(t)|Z(t) = z$, in which $\dot{Z}(t) = dZ(t)/dt$, are

$$\hat{m}(t) = \dot{m}(t) + \left(\left.\frac{\partial \Gamma_{ZZ}(t,s)}{\partial t}\right|_{t=s} \frac{1}{\sigma^2(t)}\right) z, \tag{3.9}$$

$$\hat{\sigma}^2(t) = \left.\frac{\partial^2 \Gamma_{ZZ}(t,s)}{\partial t \partial s}\right|_{t=s} - \left(\left.\frac{\partial \Gamma_{ZZ}(t,s)}{\partial t}\right|_{t=s}\right)^2 \frac{1}{\sigma^2(t)}, \tag{3.10}$$

respectively, with $\dot{m}(t) = E[\dot{Z}(t)] = 0$ and $\Gamma_{ZZ}(t,s) = E[Z(t)Z(s)]$. Since $Z(t)$ is mean-square differentiable we have ([164], Section 4.4.2, Theorem 4.9)

$$\frac{\partial \Gamma_{ZZ}(t,s)}{\partial t} = E[\dot{Z}(t)Z(s)] \Rightarrow \left.\frac{\partial \Gamma_{ZZ}(t,s)}{\partial t}\right|_{t=s} = E[\dot{Z}(t)Z(t)], \tag{3.11}$$

$$\frac{\partial^2 \Gamma_{ZZ}(t,s)}{\partial t \partial s} = E[\dot{Z}(t)\dot{Z}(s)] \Rightarrow \left.\frac{\partial^2 \Gamma_{ZZ}(t,s)}{\partial t \partial s}\right|_{t=s} = E[\dot{Z}^2(t)], \tag{3.12}$$

hence Equations 3.9 and 3.10 become

$$\hat{m}(t) = z\,\frac{E[\dot{Z}(t)Z(t)]}{\sigma^2(t)}, \tag{3.13}$$

$$\hat{\sigma}^2(t) = E[\dot{Z}^2(t)] - \frac{(E[\dot{Z}(t)Z(t)])^2}{\sigma^2(t)}. \tag{3.14}$$

The fragility of a system with nonstationary Gaussian response $Z(t)$ can be approximated using Equation 3.4 with $\nu_D(t)$ in Equation 3.8, with $\hat{m}(t)$ and $\hat{\sigma}^2(t)$ in Equations 3.13 and 3.14, respectively, and $\sigma^2(t) = E[Z^2(t)]$.

For a real-valued, stationary, zero-mean, mean-square differentiable Gaussian process $Z(t)$ with one-sided spectral density function $g_{ZZ}(\omega)$ the mean $D = [-z, z]$, $z > 0$, outcrossing rate in Equation 3.8 becomes [164]

$$\nu_D = \frac{1}{\pi}\frac{\dot{\sigma}}{\sigma}\exp(-\frac{z^2}{2\sigma^2}), \tag{3.15}$$

where

$$\sigma^2 = \int_0^\infty g_{ZZ}(\omega)d\omega, \tag{3.16}$$

$$\dot{\sigma}^2 = \int_0^\infty \omega^2\, g_{ZZ}(\omega)d\omega, \tag{3.17}$$

are the variances of $Z(t)$ and $\dot{Z}(t) = dZ(t)/dt$, respectively. The fragility of a system with stationary Gaussian response $Z(t)$ can be approximated using Equation 3.5 with ν_D in Equation 3.15.

3.2 Fragility by Monte Carlo simulation

The system fragility in Equation 3.1, that is, the probability that the system response $\boldsymbol{Z}(t)$ leaves the safe set D in $(0, \tau)$ when subjected to an event with parameters $\boldsymbol{\phi} = (\phi_1, \ldots, \phi_d)$ can also be approximated using Monte Carlo simulation method. The method involves three steps:

1. Generate n_s independent samples $\{\boldsymbol{f}_i(t)\}$, $i = 1, \ldots, n_s$, of the input process $\boldsymbol{F}(t)$ in Figure 3.1 for each realizable value of $\boldsymbol{\phi}$ delivered by the activity matrix of the natural hazard in Section 2.3.1, using the corresponding probability law in Section 2.2 and the simulation algorithm in Section 2.4.

2. Calculate the system response $\boldsymbol{z}_i(t)$ to each sample $\boldsymbol{f}_i(t)$, $i = 1, \ldots, n_s$, of $\boldsymbol{F}(t)$ in the previous step, using a linear/nonlinear dynamic analysis.

3. Approximate the system fragility in Equation 3.1 for each $\boldsymbol{\phi}$ by

$$\hat{P}_{f,mc}(D; \boldsymbol{\phi}) = \frac{\#\left\{\boldsymbol{z}_i(t) \text{ leaves } D \text{ in } (0, \tau)\right\}}{n_s}\,, \tag{3.18}$$

   where τ is generally taken as the duration of $\boldsymbol{f}_i(t)$.

We note that the above algorithm can be modified by using in step 1 actual rather than synthetic records, and process these records according to steps 2 and 3. As expected, the accuracy of the resulting fragility depends on the number of available records. If this number is small, the collection of actual records can be augmented with synthetic records.

3.3 Seismic fragility

Seismic fragility is the probability that a response of a structural, nonstructural, or geotechnical system exceeds a critical level if subjected to seismic ground motions of specified intensities. We base the intensity of the seismic ground motions on the parameters defining its probability law so that $\boldsymbol{\phi}$ in Equation 3.1 has $d = 2$ components, $\phi_1 =$ the earthquake moment magnitude m, and $\phi_2 =$ the distance r from the seismic source to the site. The seismic activity matrix in Section 2.3.4 provides realizable values of (m, r) at the system site.

The seismic ground acceleration at system site, generated by a seismic event with moment magnitude m and source-to-site distance r, is modeled following Section 2.2.1 as

$$X(t) = e(t)\, Y(t), \quad 0 \leq t \leq \tau, \tag{3.19}$$

where τ is the total duration of the seismic event in Equation 2.1, $e(t)$ is a deterministic modulation function in Equation 2.2 and $Y(t)$ is a zero-mean stationary Gaussian/non-Gaussian process with probability law defined in Sections 2.2.1.1.1 and 2.2.1.1.2, respectively.

Table 3.1 summarizes methods used in this study for calculating fragility information

Table 3.1: Seismic fragility analysis.

	System	
Input $X(t)$	**linear**	**nonlinear**
Gaussian	crossing theory	Monte Carlo
non-Gaussian	Monte Carlo	Monte Carlo

for linear/nonlinear systems under Gaussian/non-Gaussian ground motions. For linear systems subjected to non-Gaussian input we can also use a method based on the sampling theorem [70] for calculating their fragility, this method is discussed in detail in Section 3.4.2.

3.3.1 Linear systems with Gaussian input

Methods based on crossing theory of stochastic processes presented in Section 3.1 are used for calculating fragility surfaces for single and multi degree of freedom linear

systems subjected Gaussian seismic ground accelerations in Section 2.2.1.1.1, and numerical examples are provided.

3.3.1.1 Single degree of freedom systems

Let $Z(t)$ be the relative displacement of a linear single degree of freedom oscillator with natural frequency ω_0 and damping ratio ζ under the ground acceleration $X(t)$ in Equation 3.19, in which the probability law of $Y(t)$ is defined in Section 2.2.1.1.1. The displacement process $Z(t)$ satisfies the equation

$$\ddot{Z}(t) + 2\zeta\omega_0\dot{Z}(t) + \omega_0^2 Z(t) = -X(t) = -e(t)\,Y(t), \tag{3.20}$$

with initial conditions $Z(0) = \dot{Z}(0) = 0$, where $\dot{Z}(t) = dZ(t)/dt$ and $\ddot{Z}(t) = d^2Z(t)/dt^2$. Let

$$Z_\tau = \max_{0\le t\le\tau}(|Z(t)|) \tag{3.21}$$

be the maximum of the absolute value of the relative displacement in $[0, \tau]$, with τ in Equation 3.19. The response and the limit state in our analysis are the maximum relative displacement Z_τ in Equation 3.21 and a critical displacement z, respectively.

Denote by

$$P_f(z; m, r) = P(Z_\tau > z \,|\, m, r), \tag{3.22}$$

the probability that Z_τ exceeds a limit state z if the oscillator is subjected to a seismic ground acceleration $X(t)$ with parameters (m, r).

3.3.1.1.1 Stationary case: Suppose $e(t) = 1,\ t \ge 0$ in Equation 3.20 and consider the steady-state response $Z_{ss}(t)$. The system probability in Equation 3.22 can be approximated by Equation 3.5 with mean D-outcrossing rate in Equation 3.15 and safe set $D = [-z, z]$. Following Equation 3.15 the mean $D = [-z, z]$ outcrossing rate of $Z_{ss}(t)$ is

$$\nu_D = \frac{1}{\pi}\frac{\dot{\sigma}_{Z_{ss}}}{\sigma_{Z_{ss}}}\exp(-\frac{z^2}{2\sigma^2_{Z_{ss}}}), \tag{3.23}$$

where $\sigma^2_{Z_{ss}} = \int_0^\infty g_{Z_{ss}Z_{ss}}(\omega)d\omega$ and $\dot{\sigma}^2_{Z_{ss}} = \int_0^\infty \omega^2\, g_{Z_{ss}Z_{ss}}(\omega)d\omega$ are the variances of $Z_{ss}(t)$ and $\dot{Z}_{ss}(t) = dZ_{ss}(t)/dt$, respectively, and $g_{Z_{ss}Z_{ss}}(\omega)$ is the one-sided spectral density function of $Z_{ss}(t)$,

$$g_{Z_{ss}Z_{ss}}(\omega) = |h_{Z_{ss}}(\omega)|^2\, g_{YY}(\omega; m, r), \tag{3.24}$$

where

$$|h_{Z_{ss}}(\omega)| = \frac{1/\omega_0^2}{\left[\left(1-(\omega/\omega_0)^2\right)^2 + (2\zeta\omega/\omega_0)^2\right]^{1/2}} \tag{3.25}$$

is the transfer function between $X(t)$ and $Z_{ss}(t)$ [164].

The numerical example considers steady-state relative displacement of linear oscillators with duration $\tau = 10$ seconds to strong ground accelerations representing independent samples of stationary Gaussian ground acceleration process $X(t)$ with one-sided spectral density function in Equation 2.3. We note that the specific barrier model delivers the duration of ground motion [74], but we set somewhat arbitrary, $\tau = 10$ seconds irrespective of (m, r). Figures 3.3 and 3.4 show fragility surfaces for two linear

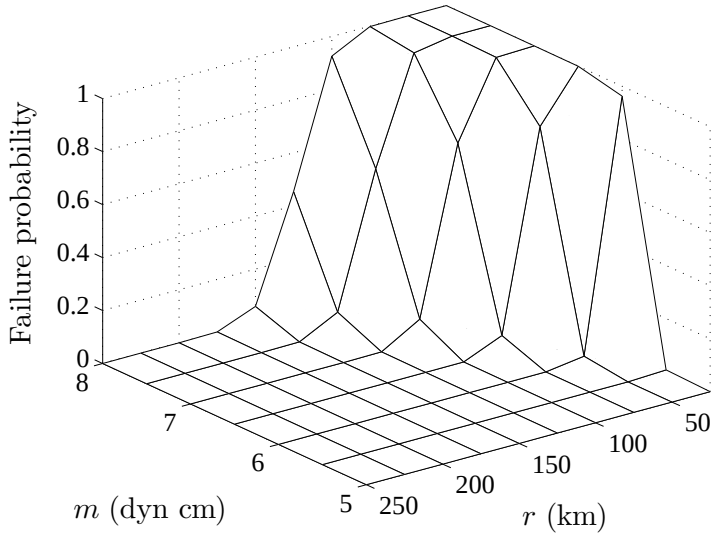

Figure 3.3: Fragility for linear oscillator with low damping ($\zeta = 2\%$).

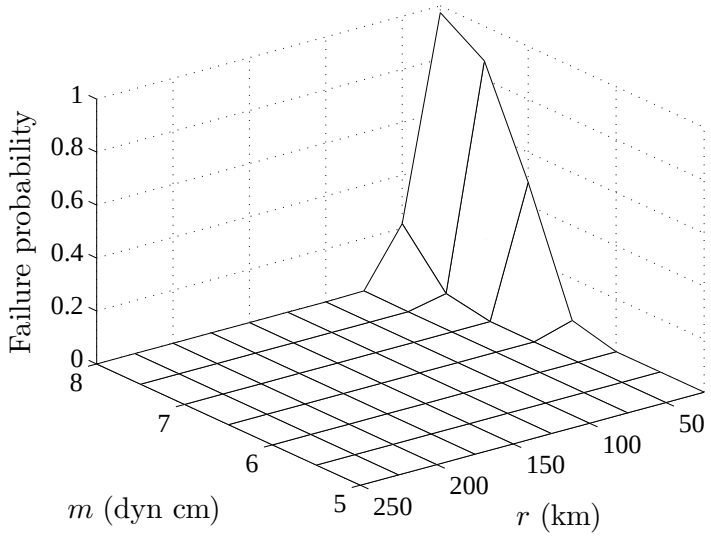

Figure 3.4: Fragility for linear oscillator with high damping ($\zeta = 15\%$).

oscillators located at a site in California on stiff soil (NEHRP site class D, [56]) for the displacement limit state $z = 3$ cm. Both oscillators have $\omega_0 = 5.97$ rad/sec but their damping ratios are $\zeta = 2\%$ and $\zeta = 15\%$. The seismic activity matrix in Figure 2.13 provides realizable values of (m, r) at the system site. As expected the system with higher damping ratio yields lower failure probabilities as its response will be smaller compared to that of the system with lower damping ratio.

3.3.1.1.2 Nonstationary case: The system probability in Equation 3.22 can be approximated by Equation 3.4 with mean D-outcrossing rate in Equation 3.8 and safe set $D = [-z, z]$. The mean D-outcrossing rate in Equation 3.8 is a function of $\hat{m}(t)$ and $\hat{\sigma}^2(t)$ in Equations 3.13 and 3.14, respectively, and $\sigma^2(t) = E[Z^2(t)]$. Accordingly, $E[Z^2(t)]$, $E[\dot{Z}^2(t)]$ and $E[\dot{Z}(t)Z(t)]$ need to be obtained to calculate system fragility in Equation 3.4.

The state space version of Equation 3.20 is

$$\begin{bmatrix} \dot{Z}_1(t) \\ \\ \dot{Z}_2(t) \end{bmatrix} = \begin{bmatrix} 0 & 1 \\ \\ -\omega_0^2 & -2\zeta_0\omega_0 \end{bmatrix} \begin{bmatrix} Z_1(t) \\ \\ Z_2(t) \end{bmatrix} + \begin{bmatrix} 0 \\ \\ -1 \end{bmatrix} X(t), \tag{3.26}$$

in which $Z_1(t) = Z(t)$ and $Z_2(t) = \dot{Z}(t)$ and $X(t)$ is defined in Section 3.3.1.1. Let $\boldsymbol{Z}(t) = [Z_1(t), Z_2(t)]^T$, then the evolution of the system and excitation states can be represented by

$$\dot{\boldsymbol{Z}}(t) = \boldsymbol{a}\,\boldsymbol{Z}(t) + \boldsymbol{g}\,X(t), \tag{3.27}$$

where $\boldsymbol{g} = [0, -1]^T$ and

$$\boldsymbol{a} = \begin{bmatrix} 0 & 1 \\ \\ -\omega_0^2 & -2\zeta_0\omega_0 \end{bmatrix}. \tag{3.28}$$

The solution has the form

$$\boldsymbol{Z}(t) = \int_0^t \boldsymbol{\Phi}(t-\tau)\,\boldsymbol{g}\,X(s)ds, \tag{3.29}$$

where

$$\boldsymbol{\Phi}(t) = e^{-\zeta\omega_0 t} \begin{bmatrix} \cos(\beta t) + \frac{\zeta\omega_0}{\beta}\sin(\beta t) & \frac{1}{\beta}\sin(\beta t) \\ \\ -\frac{{\omega_0}^2}{\beta}\sin(\beta t) & \cos(\beta t) - \frac{\zeta\omega_0}{\beta}\sin(\beta t) \end{bmatrix} \tag{3.30}$$

with $\beta = {\omega_0}^2\sqrt{1-\zeta^2}$. The correlation function of $\boldsymbol{Z}(t)$ can be expressed by ([164],

Section 5.2.1, Example 5.5)

$$\begin{aligned}
\boldsymbol{\Gamma}(t,s) &= E[\boldsymbol{Z}(t)\,\boldsymbol{Z}(s)^T], \quad t \geq s \qquad (3.31)\\
&= E\left[\int_0^t \boldsymbol{\Phi}(t-u)\,\boldsymbol{g}\,X(u)du \int_0^s X(v)\,\boldsymbol{g}^T\,\boldsymbol{\Phi}^T(s-v)dv\right]\\
&= \int_0^t du \int_0^s dv\ \boldsymbol{\Phi}(t-u)\,\boldsymbol{g}\,E[X(u)X(v)]\,\boldsymbol{g}^T\,\boldsymbol{\Phi}^T(s-v)\\
&= \int_0^t du \int_0^s dv\ \boldsymbol{\Phi}(t-u)\,\boldsymbol{g}\boldsymbol{g}^T\,\boldsymbol{\Phi}^T(s-v)\,e(u)e(v)\,E[Y(u)Y(v)]\\
&= \int_0^t du \int_0^s dv \int_0^\infty d\omega\,\left[\boldsymbol{\Phi}(t-u)\,\boldsymbol{g}\boldsymbol{g}^T\,\boldsymbol{\Phi}^T(s-v)e(u)e(v)\right.\\
&\qquad\qquad \left.\times\,\exp(j\omega(v-u))g_{YY}(\omega)\right],
\end{aligned}$$

since $X(t) = e(t)Y(t)$ and $E[Y(u)Y(v)] = \int_0^\infty \exp(j\omega(v-u))g_{YY}(\omega)d\omega$, with $j = \sqrt{-1}$ and $g_{YY}(\omega)$ given by Equation 2.3.

It is difficult to numerically integrate Equation 3.31 to obtain $E[Z^2(t)]$, $E[\dot{Z}^2(t)]$ and $E[\dot{Z}(t)Z(t)]$, which are required to calculate the mean D-crossing rate of $Z(t)$. Instead we adopt the following method.

The seismic ground acceleration process $X(t)$ in Equation 3.19 is approximated by

$$\hat{X}(t) = \sigma_Y e(t)\ddot{Q}(t), \qquad (3.32)$$

where $e(t)$ is the modulation function in Equation 2.2, $\sigma_Y^2 = \int_0^\infty g_{YY}(\omega)d\omega$ is the variance of the zero-mean stationary Gaussian process $Y(t)$ with one-sided spectral density function $g_{YY}(\omega)$ in Equation 2.3, and $\ddot{Q}(t)$ is a zero-mean, unit-variance stationary Gaussian process with one-sided spectral density function of the form [32]

$$g_{\ddot{Q}\ddot{Q}}(\omega) = g_0\,|h_1(\omega)|^2\,|h_2(\omega)|^2, \qquad (3.33)$$

with

$$|h_1(\omega)|^2 = \frac{1+(2\zeta_1\omega/\omega_1)^2}{\left(1-(\omega/\omega_1)^2\right)^2+(2\zeta_1\omega/\omega_1)^2}\,, \qquad (3.34)$$

$$|h_2(\omega)|^2 = \frac{1 + (2\zeta_2\omega/\omega_2)^2}{\left(1 - (\omega/\omega_2)^2\right)^2 + (2\zeta_2\omega/\omega_2)^2}\,. \tag{3.35}$$

It is assumed that the correlation functions of $\ddot{Q}(t)$ and $Y(t)/\sigma_Y$ nearly coincide, so that $g_{\ddot{Q}\ddot{Q}}(\omega) \simeq g_{YY}(\omega)/\sigma_Y^2$, and the variance of $\ddot{Q}(t)$ is 1. The assumption is adequate for some types of correlation functions ([69], Figure 3.1, page 48).

The parameters defining $g_{\ddot{Q}\ddot{Q}}(\omega)$, namely, g_0, ω_1, ζ_1, ω_2 and ζ_2, are obtained by minimizing the objective function

$$\underset{g_0,\omega_1,\zeta_1,\omega_2,\zeta_2}{\text{minimize}} \quad \int_0^\infty \left(g_{\ddot{Q}\ddot{Q}}(\omega) - g_{YY}(\omega)/\sigma_Y^2\right) w(\omega)\, d\omega, \tag{3.36}$$

subject to the constraints g_0, ω_1, $\omega_2 > 0$, and $0 < \zeta_1$, $\zeta_2 < 1$. In Equation 3.36, $w(\omega) = g_{YY}(\omega)/\max_\omega(g_{YY}(\omega))$ is a weighting function. Figure 3.5 shows the

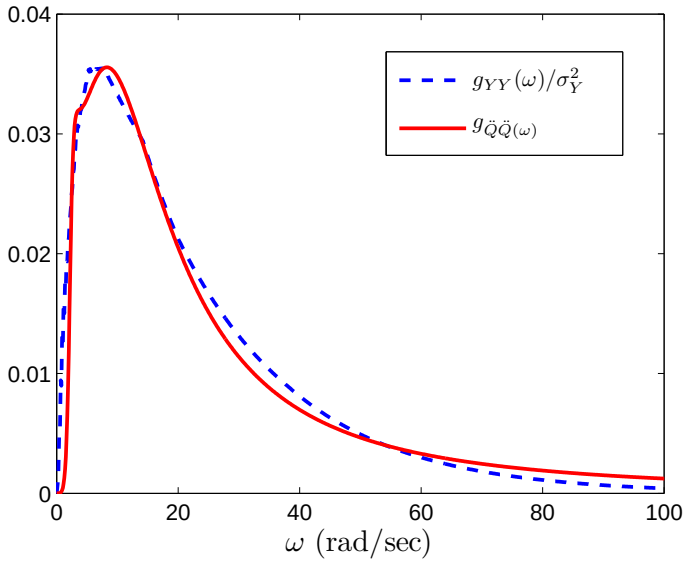

Figure 3.5: Spectral density functions of $\ddot{Q}(t)$ and $Y(t)/\sigma_Y$.

spectral density functions of $\ddot{Q}(t)$ and $Y(t)/\sigma_Y$ for an earthquake with parameters $(m = 8, r = 25$ km$)$. The parameters defining $g_{\ddot{Q}\ddot{Q}}(\omega)$ are $g_0 = 3.4$, $\omega_1 = 2.4$, $\omega_2 = 10$, $\zeta_1 = 0.4$, $\zeta_2 = 0.99$. Note that the parameters g_0, ω_1, ω_2, ζ_1, ζ_2 in $g_{\ddot{Q}\ddot{Q}}(\omega)$, and $e(t)$ are defined by the moment magnitude of the earthquake m and the source-to-site distance r.

Consider a linear single degree of freedom oscillator with natural frequency ω_0 and damping ratio ζ_0 subjected strong seismic ground acceleration process $\hat{X}(t)$ given by Equation 3.32. The equation of motion of the oscillator is

$$\ddot{Z}(t) + 2\zeta\omega_0\dot{Z}(t) + \omega_0^2 Z(t) = -\hat{X}(t) = -\sigma_Y e(t)\ddot{Q}(t), \tag{3.37}$$

with initial conditions $Z(0) = \dot{Z}(0) = 0$. The one-sided spectral density function of $\ddot{Q}(t)$ is given by Equation 3.33. The form of the spectral density is selected so that $\ddot{Q}(t)$ can be obtained by filtering a Gaussian white noise process $W(t)$ with intensity g_0 twice, using two linear single degree of freedom systems with parameters ω_1, ζ_1 and ω_2, ζ_2, respectively. Accordingly,

$$\ddot{P}(t) + 2\zeta_1\omega_1\dot{P}(t) + \omega_1^2 P(t) = W(t), \tag{3.38}$$

$$\ddot{Q}(t) + 2\zeta_2\omega_2\dot{Q}(t) + \omega_2^2 Q(t) = \ddot{P}(t) - W(t). \tag{3.39}$$

Denote by $h_1(\omega)$ the transfer function between $W(t)$ and $\ddot{P}(t) - W(t)$ and by $h_2(\omega)$ the transfer function between $\ddot{P}(t) - W(t)$ and $\ddot{Q}(t)$, so that

$$g_{\ddot{P}-W,\ddot{P}-W}(\omega) = |h_1(\omega)|^2 \, g_{WW}(\omega), \tag{3.40}$$

$$g_{\ddot{Q}\ddot{Q}}(\omega) = |h_2(\omega)|^2, g_{\ddot{P}-W,\ddot{P}-W}(\omega) = g_0 \, |h_1(\omega)|^2 \, |h_2(\omega)|^2, \tag{3.41}$$

since $g_{WW}(\omega) = g_0$. Note that Equations 3.33 and 3.41 are the same.

Let $\boldsymbol{Z}(t) = [Z_1(t), Z_2(t), Z_3(t), Z_4(t), Z_5(t), Z_6(t)]^T$, with $Z_1(t) = Z(t)$, $Z_2(t) = \dot{Z}(t)$, $Z_3(t) = Q(t)$, $Z_4(t) = \dot{Q}(t)$, $Z_5(t) = P(t)$, $Z_6(t) = \dot{P}(t)$, and denote $B(t)$ the standard Weiner process with independent increments $dB(t)$ having zero mean and variance dt. From Equations 3.37-3.39 the augmented state of the oscillator with the excitation satisfies the Itô differential equations

$$d\boldsymbol{Z}(t) = \boldsymbol{a}(t)\boldsymbol{Z}(t)\, dt + \boldsymbol{g}\, dB(t), \tag{3.42}$$

in which $d\boldsymbol{Z}(t)$ is the increment of $\boldsymbol{Z}(t)$ in dt, $\boldsymbol{g} = [0, 0, 0, 0, 0, \sqrt{\pi g_0}]^T$, and

$$\boldsymbol{a}(t) = \begin{bmatrix} 0 & 1 & 0 & 0 & 0 & 0 \\ -\omega_0^2 & -2\zeta_0\omega_0 & \omega_2^2\sigma_Y e(t) & 2\zeta_2\omega_2\sigma_Y e(t) & \omega_1^2\sigma_Y e(t) & 2\zeta_1\omega_1\sigma_Y e(t) \\ 0 & 0 & 0 & 1 & 0 & 0 \\ 0 & 0 & -\omega_2^2 & -2\zeta_2\omega_2 & -\omega_1^2 & -2\zeta_1\omega_1 \\ 0 & 0 & 0 & 0 & 0 & 1 \\ 0 & 0 & 0 & 0 & -\omega_1^2 & -2\zeta_1\omega_1 \end{bmatrix}, \tag{3.43}$$

so that $\boldsymbol{Z}(t)$ is a diffusion process with time dependent linear drift and constant diffusion.

Denote the correlation function of $\boldsymbol{Z}(t)$ by

$$\boldsymbol{\Gamma}(t, s) = E[\boldsymbol{Z}(t)\, \boldsymbol{Z}(s)^T], \quad t \geq s. \tag{3.44}$$

The correlation matrix $\boldsymbol{\Gamma}(t, s),\ t \geq s$ of the linear system defined in Equation 3.43 driven with the white noise can be obtained by solving ([164], Section 5.2.1 Equations 5.58 and 5.59)

$$\frac{\partial}{\partial t}\, \boldsymbol{\Gamma}(t, s) = \boldsymbol{a}(t)\boldsymbol{\Gamma}(t, s), \quad t \geq s, \quad \boldsymbol{\Gamma}(s, s) = \boldsymbol{\Gamma}(s) \tag{3.45}$$

and

$$\frac{d}{dt}\, \boldsymbol{\Gamma}(t) = \boldsymbol{a}(t)\boldsymbol{\Gamma}(t) + \boldsymbol{\Gamma}(t)\boldsymbol{a}(t)^T + \boldsymbol{g}\boldsymbol{g}^T, \quad t \geq 0, \quad \boldsymbol{\Gamma}(0) = \boldsymbol{\Gamma}_0. \tag{3.46}$$

The initial conditions are deterministic and hence $\boldsymbol{\Gamma}_0 = \mathbf{0}$.

We solve Equation 3.46 by numerical integration. Denote the (k, l) component of $d\boldsymbol{\Gamma}(t)/dt$ at time step i by $\dot{\gamma}_{kl,i}$, and assume $\dot{\gamma}_{kl,i} \simeq (\gamma_{kl,i+1} - \gamma_{kl,i})/\Delta t$, so that $\dot{\boldsymbol{\Gamma}}_i \simeq (\boldsymbol{\Gamma}_{i+1} - \boldsymbol{\Gamma}_i)/\Delta t$, where $\boldsymbol{\Gamma}_i = \boldsymbol{\Gamma}(t)$ and $\dot{\boldsymbol{\Gamma}}_i = d\boldsymbol{\Gamma}(t)/dt$ at time step i and Δt is the

length of the time step. Hence Equation 3.46 becomes

$$\boldsymbol{\Gamma}_{i+1} = \boldsymbol{\Gamma}_i + \Delta t\,(\boldsymbol{a}_i\,\boldsymbol{\Gamma}_i + \boldsymbol{\Gamma}_i\,\boldsymbol{a}_i{}^T + \boldsymbol{g}\boldsymbol{g}^T), \quad \boldsymbol{\Gamma}_0 = \mathbf{0}, \quad i = 0, 1, \ldots, \tag{3.47}$$

Figure 3.6 shows the nonstationary correlation functions $E[Z^2(t)]$, $E[\dot{Z}(t)Z(t)]$ and

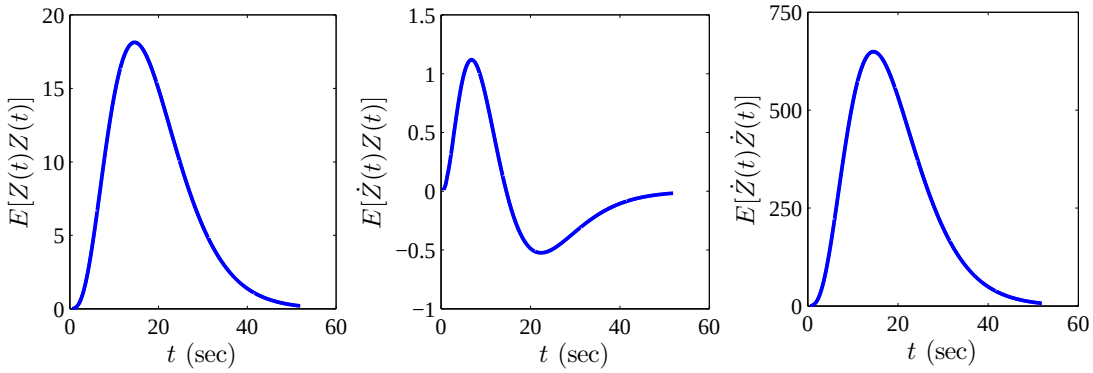

Figure 3.6: Nonstationary correlation functions of the response $Z(t)$.

$E[\dot{Z}^2(t)]$, corresponding to (1,1), (1,2) and (2,2) components of $\boldsymbol{\Gamma}(t)$, respectively, of the response of a linear oscillator with natural frequency $\omega_0 = 5.97$ rad/sec and damping ratio $\zeta = 0.02$, subjected to an earthquake with parameters $(m = 8, r = 25$ km), using a time step $\Delta t = 0.001$ sec.

We recall that mean $[-z, z]$-outcrossing rate of $Z(t)$ in Equation 3.8 is a function of $\hat{m}(t)$ and $\hat{\sigma}^2(t)$ in Equations 3.13 and 3.14, respectively, and $\sigma^2(t)$, which can be calculated based on $E[Z^2(t)]$, $E[\dot{Z}(t)Z(t)]$ and $E[\dot{Z}^2(t)]$, and the system fragility can be approximated using Equation 3.4 with $\nu_D(t)$ in Equation 3.8.

Figure 3.7 shows the mean $[-z, z]$-outcrossing rate in Equation 3.8, for $z = 1.5$ cm, of the relative displacement response $Z(t)$ of a linear oscillator with natural frequency $\omega_0 = 5.97$ rad/sec and damping ratio $\zeta = 0.02$, subjected to an earthquake with parameters $(m = 8, r = 25$ km). The stationary mean $[-z, z]$-outcrossing rate in Equation 3.23 of the steady-state relative displacement response is 1.8072. Note that this value is consistent with the results shown in Figure 3.7.

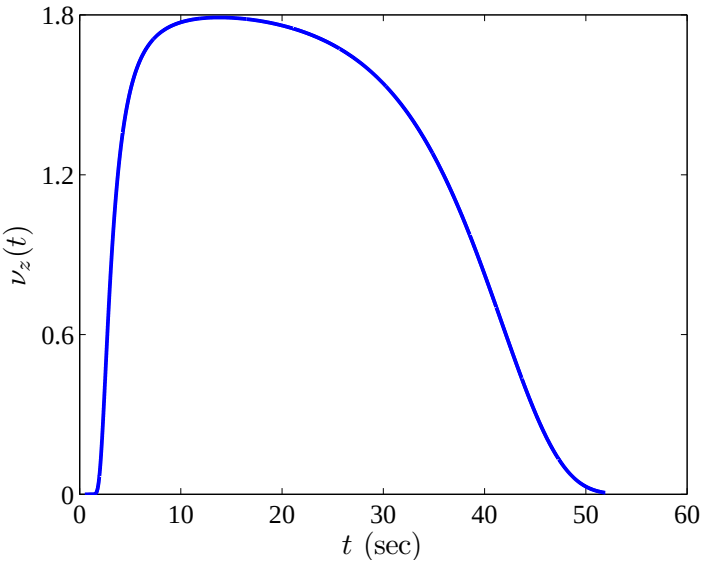

Figure 3.7: Mean crossing rate of $Z(t)$.

Figures 3.8 and 3.9 show fragility surfaces for the two linear oscillators in

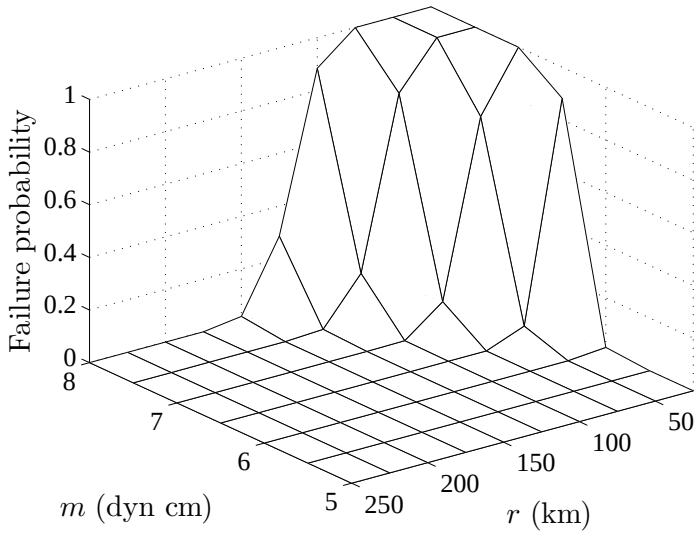

Figure 3.8: Fragility for linear oscillator with low damping ($\zeta = 2\%$).

Figures 3.3 and 3.4 for the same displacement limit state $z = 3$ cm. We note that the fragilities obtained using the stationary mean crossing rate in Equation 3.23 and those

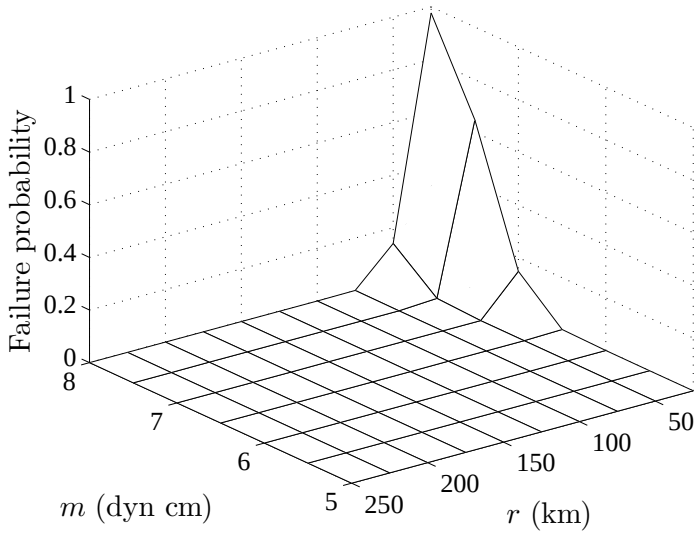

Figure 3.9: Fragility for linear oscillator with high damping ($\zeta = 15\%$).

calculated using the nonstationary mean crossing rate in Equation 3.8 are similar and somewhat different for the linear oscillator with high and low damping, respectively. For the system with high damping the response reaches stationarity at $\tau = 10$ sec since τ exceeds 3 periods, $3(2\pi/\omega_0) = 3.16$ sec ([164], Example 5.5), so that fragilities based on stationary and nonstationary crossing rates, Figures 3.4 and 3.9, respectively, are similar. On the other hand, for the system with low damping the response never reaches stationarity since $\tau = 10$ sec is smaller than 20 periods, $20(2\pi/\omega_0) = 21.05$ sec, accordingly, nonstationary crossing rates are smaller than the stationary ones so that fragilities based on nonstationary crossing rates are smaller (Figures 3.3 and 3.8).

We note that Equation 3.45 can be solved by numerical integration. We can approximate $\partial\mathbf{\Gamma}(t,s)/\partial t$ by $(\mathbf{\Gamma}(t+\Delta t,s) - \mathbf{\Gamma}(t,s))/\Delta t$, hence using Equation 3.45 we have $\mathbf{\Gamma}(t+\Delta t,s) = \mathbf{\Gamma}(t,s) + \Delta t\, \boldsymbol{a}(t)\mathbf{\Gamma}(t,s)$, $t \geq s$. We can then fix a value for s and obtain $\mathbf{\Gamma}(t+\Delta t,s)$ using the initial condition $\mathbf{\Gamma}(s,s) = \mathbf{\Gamma}(s)$ obtained from Equation 3.47. This numerical integration scheme requires very high computer memory for $\Delta t = 0.001$. However, $\mathbf{\Gamma}(t,s)$ is not required for calculating the crossing rate of

$Z(t)$. Crossing rate calculations are based only on $\partial\mathbf{\Gamma}(t,s)/\partial t$ and $\partial^2\mathbf{\Gamma}(t,s)/\partial t\partial s$ at $t = s$.

3.3.1.2 Multi degree of freedom systems

Consider a multi degree of freedom system representing a building structure and single degree of freedom systems attached to it at different points representing nonstructural components. Suppose that the supporting structure and the attached nonstructural components are linear and that the seismic ground acceleration at system site is modeled by a zero-mean, stationary Gaussian process $X(t)$ (Section 2.2.1.1.1), that is, $e(t) = 1,\ t \geq 0$ in Equation 3.20 and consider the steady-state response of the structural and nonstructural systems. In this section we present a method based on crossing theory for calculating fragility surfaces of such nonstructural systems. First, we obtain probability law of the structural system response to ground motions at the points where the nonstructural components are attached. Second, we obtain probability law of the nonstructural system response to floor motions, that is, to structural response at the attachment points. Finally, we calculate nonstructural system fragility by the crossing theory approach.

A simplified mathematical model is developed for a hospital building constructed in 1970's and located in Southern California, referred to as the MCEER Demonstration Hospital Project, WC70. An illustration of the WC70 model with a nonstructural system (NS) consisting of two components C_1 and C_2 attached to it is shown in Figure 3.10. It is assumed that the structure (i) is linear elastic and does not fail, (ii) has a proportional damping, and that (iii) translation in the weak, x, and the strong, y directions are decoupled, (iv) cascade analysis applies, that is, the nonstructural system does not affect the dynamics of the supporting structure, and (v) the direction of seismic ground motion coincides with the weak direction of the structure. The first 12 mode shapes ϕ_i,

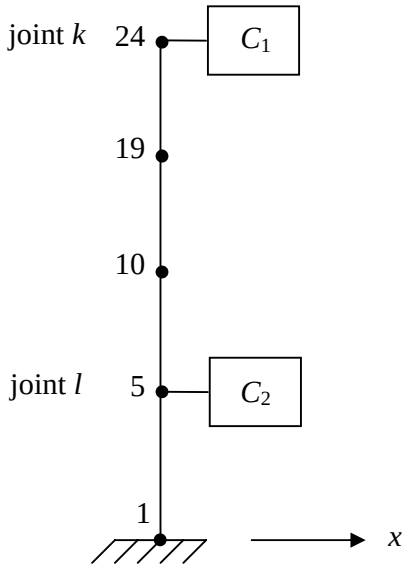

Figure 3.10: Illustration of the system.

modal frequencies $\bar{\omega}_i$, modal participation factors $\Gamma_{x,i}$ and $\Gamma_{y,i}$ in x and y directions, respectively, are calculated using a three dimensional model of the structure. Modal properties of the structure are shown in Table 3.2. It is assumed that all modes have the same damping ratio of $\bar{\zeta}_i = 3\%$, $i = 1, \ldots, 12$. The non-zero modal participation factors in the x and y directions correspond to modes (1, 4, 7, 10) and modes (2, 5, 9, 12), respectively.

The nonstructural system NS consists of two components C_1 and C_2, a water tank and a power generator located at the roof (joint-24) and at the first floor (joint-5), respectively (Figure 3.10). It is assumed that (i) the components are not interacting, (ii) C_1 is drift sensitive and C_2 is velocity sensitive, and (iii) the nonstructural system fails if one or its components fails. The components C_1 and C_2 are modeled as linear single degree of freedom systems with natural frequency $\omega_{0,i}$ and the damping ratio ζ_i, $i = 1, 2$. Properties of the nonstructural components and the limit states d_1 and d_2 defined for their relative displacement response $R_1(t)$ and relative velocity response

Table 3.2: Modal properties of WC70.

Mode	$\bar{\omega}_i$	$\Gamma_{x,i}$	$\Gamma_{y,i}$	ϕ_i
1	7.22	15.83	0.00	translation - x
2	7.68	0.00	15.85	translation - y
3	8.01	0.00	0.00	rotation
4	20.98	-6.00	0.00	translation - x
5	23.03	0.00	5.97	translation - y
6	23.06	0.00	0.00	rotation
7	37.41	3.47	0.00	translation - x
8	39.95	0.00	0.00	rotation
9	41.17	0.00	-3.49	translation - y
10	56.81	2.09	0.00	translation - x
11	58.96	0.00	0.00	rotation
12	62.34	0.00	2.03	translation - x

$\dot{R}_2(t)$ for components C_1 and C_2, respectively, are summarized in Table 3.3.

3.3.1.2.1 Structural response at attachment points: Following the cascade analysis assumption, the equation of motion of a multi degree of freedom structural system subjected to seismic ground acceleration $X(t)$ is given by

$$\mathbf{m}\ddot{\mathbf{Z}}(t) + \mathbf{c}\dot{\mathbf{Z}}(t) + \mathbf{k}\mathbf{Z}(t) = -\mathbf{m}\mathbf{1}X(t), \quad 0 \leq t \leq \tau, \tag{3.48}$$

Table 3.3: Limit states and properties of the components.

Component	Frequency $\omega_{0,i}$ (rad/sec)	Damping ratio ζ_i	Limit state d_i
1	8.0	0.02	15 cm (disp.)
2	20.0	0.03	30 cm/sec (vel.)

with initial conditions $\mathbf{Z}(0) = \dot{\mathbf{Z}}(0) = 0$, where $\mathbf{Z}(t)$ is the relative displacement response in x direction, $\mathbf{1} = [1, \ldots, 1]^T$, τ is the duration of the ground motion in Equation 3.19, and $\mathbf{m}$, $\mathbf{c}$ and $\mathbf{k}$ are the mass, stiffness and the damping matrices of the structural system, respectively. The relative displacement response of the system can be written as

$$\mathbf{Z}(t) = \mathbf{\Phi}\mathbf{Y}(t), \tag{3.49}$$

where $\mathbf{\Phi}$ is a matrix containing the mode shapes as columns and $\mathbf{Y}(t)$ is a vector containing modal responses. Using the orthogonality of the mode shapes we can write the equation of motion in modal coordinates as,

$$\ddot{Y}_i(t) + 2\bar{\zeta}_i\bar{\omega}_i\dot{Y}_i(t) + \bar{\omega}_i^2 Y_i(t) = -\Gamma_i X(t), \quad i = 1, \ldots, n, \tag{3.50}$$

where $n = 12$ is the number of modes, $Y_i(t)$ is the relative displacement response of mode i, and $\bar{\omega}_i$, $\bar{\zeta}_i$ and Γ_i (the subscript x is dropped since the analysis is in the x direction only) are the natural frequency, damping ratio and the modal participation factor of mode i in Table 3.2, respectively. Solution of Equation 3.50 is given by the Duhamel's Integral,

$$Y_i(t) = -\Gamma_i \int_{-\infty}^{\infty} h_i(\tau) X(t-\tau) d\tau, \tag{3.51}$$

where $h_i(\tau) = (1/\bar{\omega}_{d,i}) \exp(-\bar{\zeta}_i\bar{\omega}_i\tau) \sin(\bar{\omega}_{d,i}\tau)$, in which $\bar{\omega}_{d,i} = \bar{\omega}_i\sqrt{1-\bar{\zeta}_i^2}$. Denote the k^{th} coordinate of the j^{th} mode by $\phi_j(k)$. The relative displacement response of joint

k can be written as

$$Z_k(t) = \sum_{j=1}^{n} \phi_j(k) Y_j(t) = -\sum_{j=1}^{n} \phi_j(k) \Gamma_{x,j} \int_{-\infty}^{\infty} h_j(\tau) F(t-\tau) d\tau. \tag{3.52}$$

The steady-state response $\mathbf{Z}(t)$ is a stationary Gaussian vevtor process since it is assumed that the structural system is linear and $X(t)$ is a Gaussian process. The mean response $E[\mathbf{Z}(t)]$ is zero since $E[X(t)] = 0$. The correlation function between the responses at joints k and l is

$$r_{Z_k Z_l}(t,s) = E[Z_k(t) Z_l(s)] = \sum_{i,j=1}^{n} \phi_i(k) \phi_j(l) E[Y_i(t) Y_j(s)] \tag{3.53}$$

$$= \sum_{i,j=1}^{n} \phi_i(k) \phi_j(l) \Gamma_i \Gamma_j \int_{-\infty}^{\infty} \int_{-\infty}^{\infty} h_i(u) h_j(v) E[X(t-u) X(s-v)] du dv,$$

and depends only on $\tau = t - s$ since $r_{XX}(t-u, s-v) = E[X(t-u)X(s-v)]$ is equal to $r_{XX}(t-u, s-v) = r_{XX}(t-u-(s-v)) = r_{XX}(\tau - u + v)$ by the stationarity of $X(t)$. Hence, the correlation between the displacements $Z_k(t)$ and $Z_l(t+\tau)$ at joints k and l becomes

$$r_{Z_k Z_l}(\tau) = \sum_{i,j=1}^{n} \phi_i(k) \phi_j(l) \Gamma_i \Gamma_j \int_{-\infty}^{\infty} \int_{-\infty}^{\infty} h_i(u) h_j(v) r_{XX}(\tau - u + v) du dv. \tag{3.54}$$

Spectral density between displacements at joints k and l is [164]

$$s_{Z_k Z_l}(\omega) = \frac{1}{2\pi} \int_{-\infty}^{\infty} e^{-h\omega\tau} r_{Z_k Z_l}(\tau) d\tau, \quad h = \sqrt{-1}. \tag{3.55}$$

Replacing Equation 3.54 in Equation 3.55 we get

$$s_{Z_k Z_l}(\omega) = s_{XX}(\omega) \sum_{i,j=1}^{n} \phi_i(k) \phi_j(l) \Gamma_i \Gamma_j \int_{-\infty}^{\infty} \int_{-\infty}^{\infty} h_i(u) h_j(v) e^{-h\omega(u-v)} du dv$$

$$= s_{XX}(\omega) \sum_{i,j=1}^{n} \phi_i(k) \phi_j(l) \Gamma_i \Gamma_j H_i(\omega) H_j^*(\omega), \tag{3.56}$$

where $s_{XX}(\omega)$ is the Fourier transform of $r_{XX}(\tau)$,

$$H_i(\omega) = \frac{1}{\bar{\omega}_i^2 - \omega^2 + 2h\bar{\zeta}_i \bar{\omega}_i \omega}, \quad h = \sqrt{-1}, \tag{3.57}$$

is the transfer function between the base acceleration $X(t)$ and the relative displacement response $Y_i(t)$ of mode i, and $H_j^*(\omega)$ is the complex conjugate of $H_j(\omega)$. Spectral densities of the relative velocity and acceleration responses are given by $s_{\dot{Z}_k\dot{Z}_l}(\omega) = \omega^2 s_{Z_kZ_l}(\omega)$ and $s_{\ddot{Z}_k\ddot{Z}_l}(\omega) = \omega^4 s_{Z_kZ_l}(\omega)$, respectively.

The spectral density between the absolute acceleration responses $G_k(t)$ and $G_l(s)$ at joints k and l can be written as

$$s_{G_kG_l}(\omega) = \alpha_k\alpha_l s_{XX}(\omega) - s_{XX}(\omega)\sum_{i=1}^{n}\Gamma_i[\alpha_k\phi_i(l)\tilde{H}_i^*(\omega) + \alpha_l\phi_i(k)\tilde{H}_i(\omega)]$$

$$+\ s_{XX}(\omega)\sum_{i,j=1}^{n}\phi_i(k)\phi_j(l)\Gamma_i\Gamma_j\tilde{H}_i(\omega)\tilde{H}_j^*(\omega)\ , \tag{3.58}$$

where $\alpha_k = 1 - \sum_{j=1}^{n}\phi_j(k)\Gamma_j$,

$$\tilde{H}_i(\omega) = \left(\bar{\zeta}_i^2\bar{\omega}_i^2 - \bar{\omega}_{d,i}^2 + \frac{2\bar{\zeta}_i\bar{\omega}_i\bar{\omega}_{d,i}^2}{\bar{\zeta}_i\bar{\omega}_i + h\,\omega}\right)H_i(\omega) - \frac{2\bar{\zeta}_i\bar{\omega}_i}{\bar{\zeta}_i\bar{\omega}_i + h\,\omega} \tag{3.59}$$

with $H_i(\omega)$ in Equation 3.57 and $h = \sqrt{-1}$.

Means and correlations, namely the second moment properties, define the relative displacement and absolute acceleration response processes completely.

3.3.1.2.2 Fragility of nonstructural systems: Equation of motion for component C_i is

$$\ddot{R}_i(t) + 2\zeta_i\omega_{0,i}\dot{R}_i(t) + \omega_{0,i}^2 R_i(t) = -G_k(t), \tag{3.60}$$

where $R_i(t)$ is the relative displacement response of C_i for $i = 1, 2$, $G_k(t)$ is the absolute acceleration response of the structural system at joint k, and k is 24 and 5 for i equals 1 and 2, representing the roof and the first floor, respectively. Properties of the nonstructural components and the limit states defined for their relative displacement response $R_1(t)$ and relative velocity response $\dot{R}_2(t)$ for components C_1 and C_2, respectively, are summarized in Table 3.3.

Nonstructural system fragility can be estimated using the mean crossing rate of the system response following Section 3.1. Mean crossing rate can be calculated in closed form for stationary Gaussian responses and rectangular safe sets. For a system consisting of linear components an upper bound for the mean crossing rate of the system can be obtained using the mean crossing rates of its components. The fragility of the nonstructural system, that is, the probability that the (stationary) system response process $\mathbf{R}(t) = [R_1(t)\ \dot{R}_2(t)]^T$ leaves the safe set $D = (-d_1, d_1) \times (-d_2, d_2)$ in time interval of length τ (Figure 3.11), is given by,

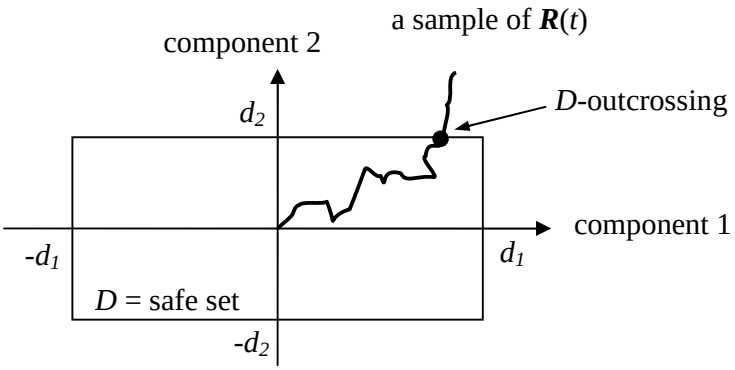

Figure 3.11: D-outcrossing of response process $\boldsymbol{R}(t)$.

$$
\begin{aligned}
P[NS \text{ fails}] &= 1 - P[NS \text{ survives}] = 1 - P[C_1 \text{ survives},\ C_2 \text{ survives}] \\
&= 1 - P[\mathbf{R}(t) \in D,\ t \in [0,\tau]] = 1 - P[\mathbf{R}(0) \in D]\, P[N_D(\tau) = 0] \\
&\simeq 1 - \exp\left(-\nu_D\, \tau\right), \qquad (3.61)
\end{aligned}
$$

assuming that the system is at rest at $t = 0$ so that $P[\mathbf{R}(0) \in D] = 1$, where τ is the duration of ground motion in Equation 3.48, $N_D(\tau)$ is the number of D-outcrossings of $\mathbf{R}(t)$ in τ and ν_D is the mean outcrossing rate of $\mathbf{R}(t)$ with respect to D.

Denote by ν_{D_1} the mean rate at which the stationary Gaussian process $R_1(t)$ passes out of the safe set $D_1 = (-d_1, d_1)$. Following Section 3.1 the mean crossing rate of

$R_1(t)$ is given by

$$\nu_{D_1} = \frac{1}{\pi}\,\frac{\dot{\sigma}_1}{\sigma_1}\,\exp\left(-\frac{d_1^2}{2\sigma_1^2}\right), \tag{3.62}$$

where $\sigma_1^2 = \int_0^\infty g_{R_1R_1}(\omega)d\omega$ and $\dot{\sigma}_1^2 = \int_0^\infty \omega^2\, g_{R_1R_1}(\omega)d\omega$ are the variances of $R_1(t)$ and $\dot{R}_1(t)$, respectively, and $g_{R_1R_1}(\omega)$ is the one-sided spectral density function of $R_1(t)$,

$$g_{R_1R_1}(\omega) = |h_{R_1}(\omega)|^2\, g_{G_kG_k}(\omega), \tag{3.63}$$

in which

$$|h_{R_1}(\omega)| = \frac{1/\omega_{0,1}^2}{\left[\left(1-(\omega/\omega_{0,1})^2\right)^2 + (2\zeta_1\omega/\omega_{0,1})^2\right]^{1/2}} \tag{3.64}$$

is the transfer function between $R_1(t)$ and G_k for $k = 24$. [164]. The mean crossing rate of $\dot{R}_2(t)$ can be obtained in a similar way. Accordingly,

$$\nu_{D_2} = \frac{1}{\pi}\,\frac{\ddot{\sigma}_2}{\dot{\sigma}_2}\,\exp\left(-\frac{d_2^2}{2\dot{\sigma}_2^2}\right), \tag{3.65}$$

where $\dot{\sigma}_2^2 = \int_0^\infty \omega^2\, g_{R_2R_2}(\omega)d\omega$ and $\ddot{\sigma}_2^2 = \int_0^\infty \omega^4\, g_{R_2R_2}(\omega)d\omega$ are the variances of $\dot{R}_2(t)$ and $\ddot{R}_2(t)$, respectively and $g_{R_2R_2}(\omega)$ is the one-sided spectral density function of $R_2(t)$,

$$g_{R_2R_2}(\omega) = |h_{R_2}(\omega)|^2\, g_{G_kG_k}(\omega), \tag{3.66}$$

in which

$$|h_{R_2}(\omega)| = \frac{1/\omega_{0,2}^2}{\left[\left(1-(\omega/\omega_{0,2})^2\right)^2 + (2\zeta_2\omega/\omega_{0,2})^2\right]^{1/2}} \tag{3.67}$$

is the transfer function between $R_2(t)$ and G_k for $k = 5$.

The fragility of C_i can be approximated by (see Section 3.1)

$$P[C_i \text{ fails}] \simeq 1 - \exp\left(-\nu_{D_i}\,\tau\right), \tag{3.68}$$

with τ in Equation 3.48 and ν_{D_i} in Equation 3.65 and 3.65, for C_1 and C_2, respectively.

It can be shown that the mean D-outcrossing rate ν_D of $\boldsymbol{R}(t)$ can be bounded by [181]

$$\hat{\nu}_D = \nu_{D_1} + \nu_{D_2} \geq \nu_D. \tag{3.69}$$

and the fragility of the nonstructural system NS is can be approximated by Equation 3.61 with $\hat{\nu}_D$ in Equation 3.69 and τ in Equation 3.48.

The calculation of fragility surfaces by the crossing theory involves five steps:

- Select earthquake moment magnitude and source-to-cite distance (m, r) and compute spectral density of ground acceleration at the site using Equation 2.3. The seismic activity matrix at the system site delivers the realizable values of (m, r).
- Calculate spectral densities of the absolute acceleration responses at the attachment points (joints 5 and 24) using Equation 3.58.
- Calculate the spectral densities of the linear responses of nonstructural components using the transfer functions in Equations 3.64 and 3.67.
- Calculate the mean crossing rate of the nonstructural components using Equations 3.65 and 3.65, and use the upper bound on the mean crossing rate in Equation 3.69 for the nonstructural system.
- Estimate the fragility of the components and the overall system using Equations 3.68 and 3.61, respectively.

The numerical example considers steady-state responses of the components with duration $\tau = 10$ seconds to strong ground accelerations representing independent samples of stationary Gaussian ground acceleration process $X(t)$ with one-sided spectral density function in Equation 2.3. We note that the specific barrier model delivers the duration of ground motion [74], but we set somewhat arbitrary, $\tau = 10$ seconds irrespective of (m, r). Figures 3.12, 3.13 and 3.14 shows the fragilities of the components C_1 and C_2 and an upper bound for the system fragility for the nonstructural system NS defined previously, respectively. The supporting structure, that is, the WC70 system in Figure 3.10, is located at the site in Figure 3.3, and the seismic activity matrix in Figure 2.13 provides realizable values of (m, r) at this site.

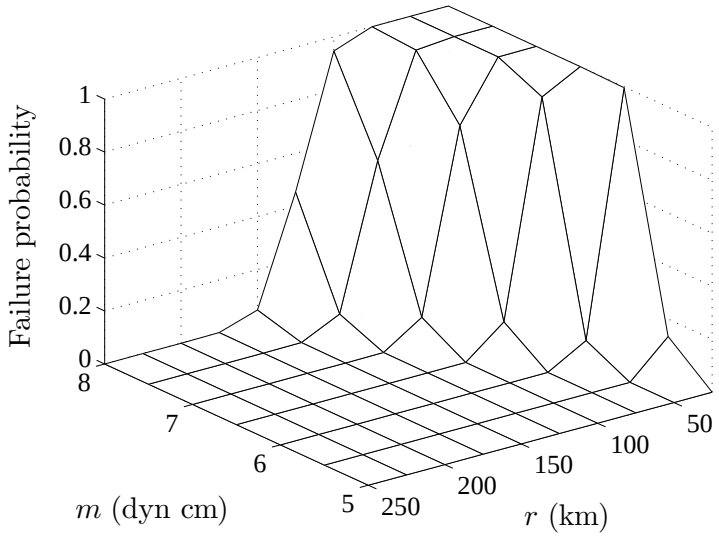

Figure 3.12: Fragility for linear C_1.

3.3.2 General systems and input

Methods based on Monte Carlo simulation presented in Section 3.2 are used for calculating fragility surfaces for single and multi degree of freedom linear/nonlinear systems subjected Gaussian/non-Gaussian seismic ground accelerations in Section 2.2.1, and numerical examples are provided.

3.3.2.1 Single degree of freedom systems.

Let $Z(t)$ be the relative displacement of a nonlinear single degree of freedom oscillator under the Gaussian ground acceleration $X(t)$ in Equation 3.19, in which the probability law of $Y(t)$ is defined in Section 2.2.1.1.1. The displacement process $Z(t)$

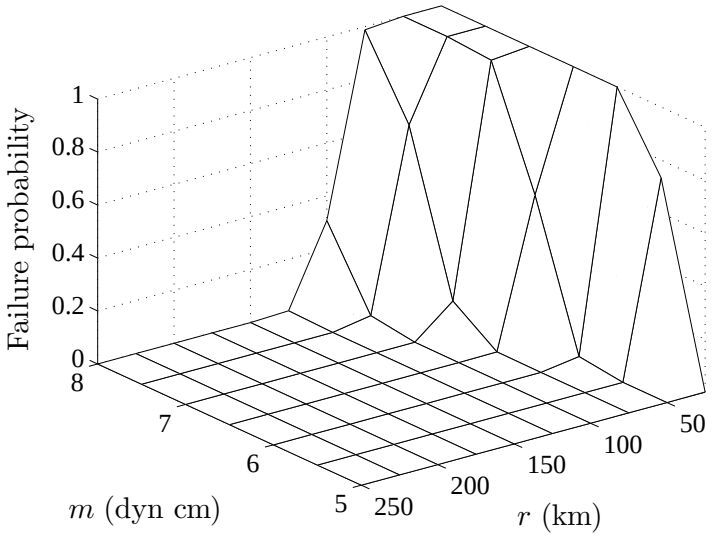

Figure 3.13: Fragility for linear C_2.

satisfies the equations

$$\text{Duffing:} \quad \ddot{Z}(t) + 2\zeta\omega_0\dot{Z}(t) + \omega_0^2\big(Z(t) + \varepsilon Z(t)^3\big) = -X(t), \tag{3.70}$$

$$\text{Bouc-Wen:} \quad \ddot{Z}(t) + 2\zeta\omega_0\dot{Z}(t) + \omega_0^2\big(\rho Z(t) + (1-\rho)W(t)\big) = -X(t) \tag{3.71}$$

$$\dot{W}(t) = \gamma\,\dot{Z}(t) - \alpha\,|\dot{Z}(t)|\,|W(t)|^{n-1}\,W(t) - \beta\,\dot{Z}(t)\,|W(t)|^n,$$

for the Duffing and Bouc-Wen oscillators, where ω_0 and ζ are the natural frequency in rad/sec and the damping ratio of the underlying linear oscillator, that is, Duffing oscillator with $\varepsilon = 0$ and Bouc-Wen oscillator with $\rho = 1$, $W(t)$ is the hysteretic displacement defined by the Bouc-Wen model [183], and ε, ρ, α, β, γ and n are constants. Numerical results are for $\omega_0 = 5.97$ rad/sec, $\zeta = 2\%$, $\varepsilon = -0.0015/\text{cm}^2$, $\rho = 0.1$, $\gamma = 1$, $\alpha = \beta = 0.5/\text{cm}^n$ and $n = 1$ [183, 164]. Suppose that the oscillators are located at the site in Figure 3.3.

Let

$$Z_\tau = \max_{0\le t\le\tau}(|Z(t)|) \tag{3.72}$$

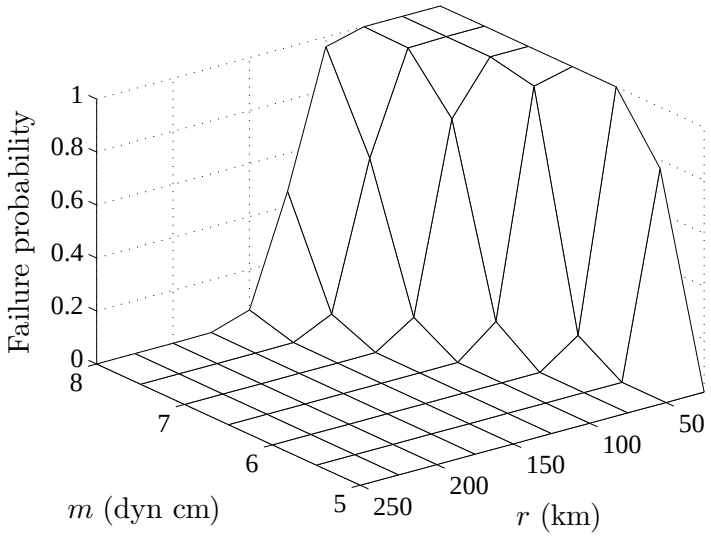

Figure 3.14: Fragility for linear NS.

be the maximum of the absolute value of the relative displacement in $[0, \tau]$, with τ in Equation 3.19.

Calculation of fragility surfaces by Monte Carlo simulation, for the Duffing and Bouc-Wen oscillators involves three steps:

1. Generate n_s independent samples $\{x_i(t)\}$, $i = 1, \ldots, n_s$, of the ground acceleration process $X(t)$ for each realizable value of (m, r) delivered by the seismic activity matrix in Figure 2.13, using the corresponding expressions of $e(t)$ and $g_{YY}(\omega)$ in Equations 2.2 and 2.3, respectively, and the method described in Section 2.4.1.

2. Calculate the system response $z_i(t)$ to each sample $x_i(t)$ of $X(t)$ in the previous step, using a nonlinear dynamic analysis (solving Equations 3.70 or 3.71).

3. Approximate $P_f(z; m, r)$ in Equation 3.22 for each (m, r) by

$$\hat{P}_{f,mc}(z; m, r) = \frac{\#\{z_{\tau,i} > z\}}{n_s}, \tag{3.73}$$

where z is the displacement limit state and $z_{\tau,i} = \max_{0\le t\le\tau}(|z_i(t)|)$, $i = 1,\ldots,n_s$.

Figures 3.15 and 3.16 show results as in Figure 3.3 for nonlinear Duffing and Bouc-

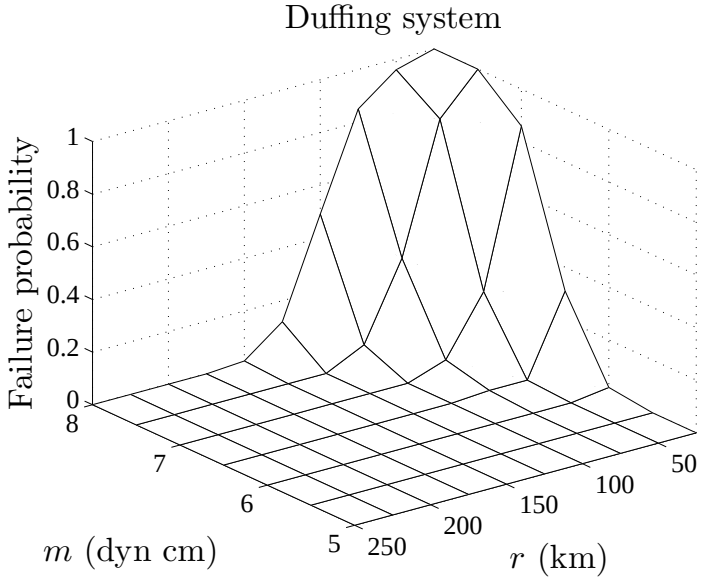

Figure 3.15: Fragility for Duffing oscillator.

Wen oscillators, respectively, with parameters given following Equations 3.70 and 3.71. The results are obtained by Monte Carlo method using $n_s = 100$ samples for each (m, r).

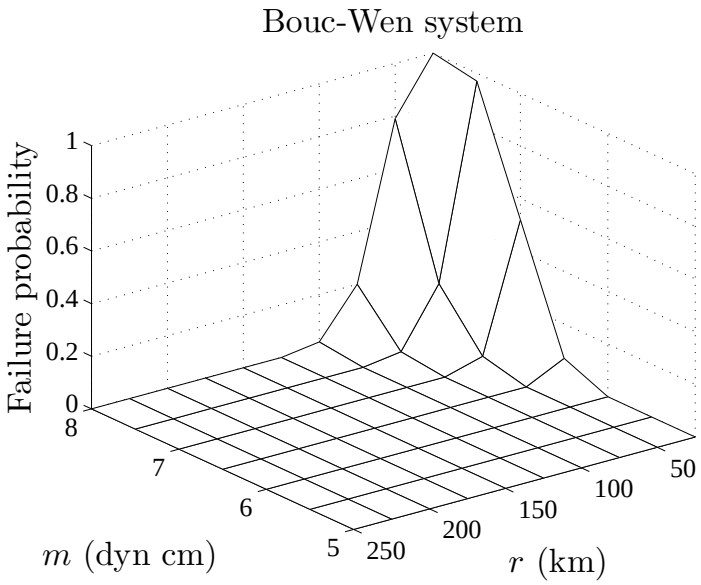

Figure 3.16: Fragility for Bouc-Wen oscillator.

3.3.2.1.1 Effect of analysis method on results: We can compare results obtained by the two methods, that is, based on crossing theory and Monte Carlo simulation, using linear systems. Figures 3.17 and 3.18 show fragility surfaces for the two linear

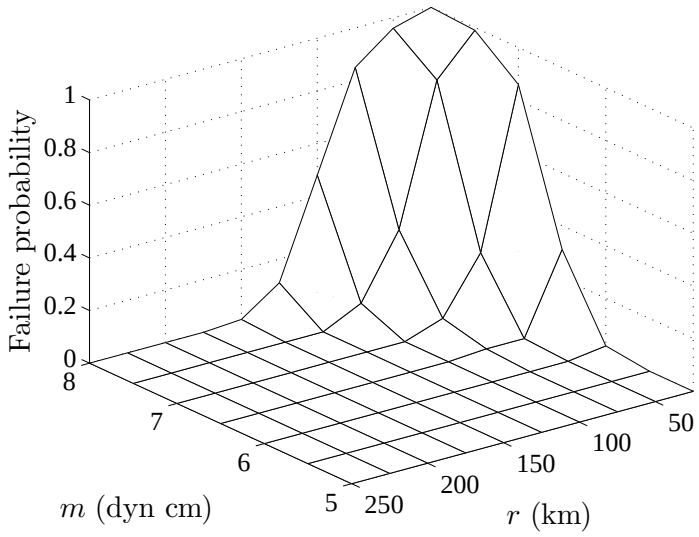

Figure 3.17: Fragility for linear oscillator with low damping ($\zeta = 2\%$).

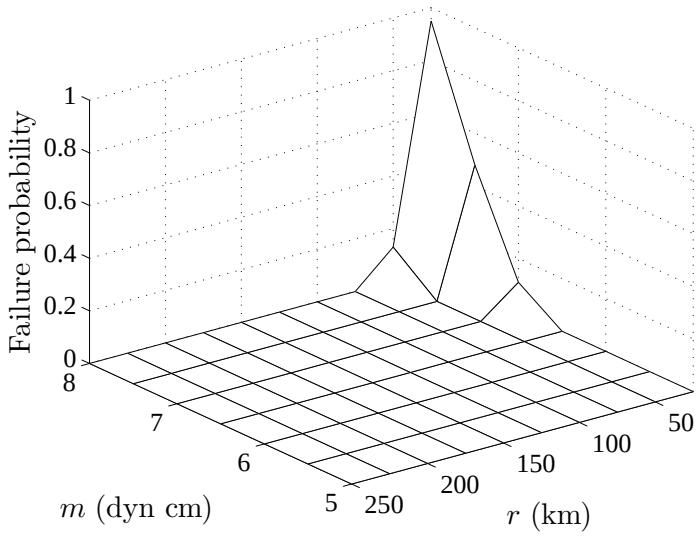

Figure 3.18: Fragility for linear oscillator with high damping ($\zeta = 15\%$).

oscillators in Figures 3.8 and 3.9, obtained by Monte Carlo simulation method for the displacement limit state $z = 3$ cm. As expected, fragilities by Monte Carlo method (Figures 3.17 and 3.18) and crossing theory (Figures 3.8 and 3.9) are similar and somehow different for values of (m, r) corresponding to low and high failure probabilities, respectively. For example, Table 3.4 gives failure probabilities of the linear

Table 3.4: Comparison of fragilities from Monte Carlo method and crossing theory.

	Failure probability		
Earthquake	**Monte Carlo**	**Crossing theory**	**Distance z_σ**
(m=7, r=100 km)	0.0018	0.0019	3.99
(m=6, r=25 km)	0.0120	0.0123	3.18
(m=7, r=25 km)	0.8660	0.9998	1.12

oscillator in Figure 3.8 for $z = 3$ cm and three values of (m, r). Table 3.4 also gives the scaled distances $z_\sigma = (z - E[Z(t)])/\text{std}[Z(t)]$, where $E[Z(t)]$ and $\text{std}[Z(t)]$ are the mean and standard deviation of $Z(t)$ corresponding to the strong motion part of the ground accelerations, for the selected values of z and (m, r). We note that crossing theory provides a conservative approximation of failure probability for values of (m, r) corresponding to low values of z_σ. Accordingly, the mean annual probability of failure based on crossing theory will also be conservative.

3.3.2.1.2 Effect of system characteristics on results: Considering that the nonlinear models in Equations 3.70 and 3.71 represent simple oscillators with dampers, we can assess the performance of these dampers comparing their fragilities in Figures 3.15 and 3.16 by the fragility of the underlying linear model in Figure 3.17. For

instance the Duffing model does not provide any beneficial effects since the fragilities in Figures 3.15 and 3.17 are almost identical. On the other hand, the Bouc-Wen model, system with hysteresis which is relevant in earthquake engineering, provides significant benefits since the fragility of the Bouc-Wen oscillator in Figure 3.16 is considerably lower than that in Figure 3.17.

3.3.2.1.3 Effect of input characteristics on results: We can also compare fragilities obtained by Gaussian and non-Gaussian ground accelerations. Suppose that the linear oscillator in Figure 3.18 is located at a site in California on generic rock (NEHRP site class B, [56]) and subjected to Gaussian and non-Gaussian ground accelerations in Sections 2.2.1.1.1 and 2.2.1.1.2, respectively. Samples of Gaussian/non-Gaussian ground accelerations at system site can be generated following Section 2.4.1. Figure 3.19 gives failure probabilities of this oscillator as a function of the limit state

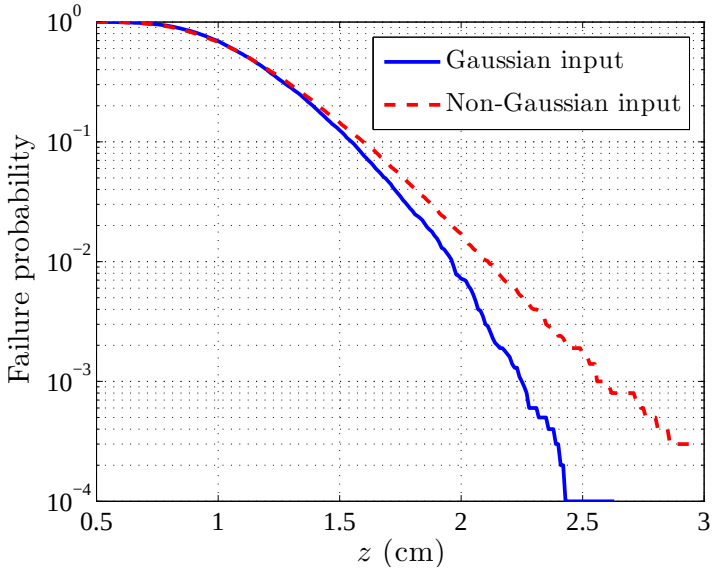

Figure 3.19: Fragility for linear oscillator with high damping ($\zeta = 15\%$) against limit state.

z, subjected to 10,000 independent samples of nonstationary Gaussian/non-Gaussian

ground accelerations with the same second-moment properties corresponding to an earthquake with ($m = 7, r = 25$ km). Since non-Gaussian ground accelerations have higher kurtosis coefficient (Section 2.2.1.1.2), for instance the kurtosis coefficient is 6.26 for the site in this example, the fragilities are higher compared to those obtained using Gaussian ground motions.

We note that fragility surfaces for linear systems subjected to non-Gaussian ground accelerations can be calculated efficiently using a Monte Carlo algorithm based on the sampling theorem [70]. The use of this method for fragility calculations is explained in detail in Section 3.4.2.

3.3.2.2 Multi degree of freedom systems

Consider the structural/nonstructural systems described in Section 3.3.1.2. The seismic ground acceleration at system site is modeled by a zero-mean, stationary Gaussian process $X(t)$ (Section 2.2.1.1.1), that is, $e(t) = 1,\ t \geq 0$ in Equation 3.20 and only the steady-state responses of the structural and nonstructural systems are considered (same as in Section 3.3.1.2).

Nonlinear models for the nonstructural components C_1 and C_2 in Figure 3.10 are obtained by adding a hysteretic element representing a damper attached between the structure and the nonstructural component. Bouc-Wen model [183] is used to represent the hysteretic element. Accordingly, equation of motion for component C_i, $i = 1, 2$, is

$$\ddot{R}_i(t) + 2\zeta_i\omega_{0,i}\dot{R}_i(t) + \omega_{0,i}^2\big(\rho_i R_i(t) + (1-\rho_i)W_i(t)\big) = -G_k(t), \tag{3.74}$$

with

$$\dot{W}_i(t) = \gamma_i\,\dot{R}_i(t) - \alpha_i\,|\dot{R}_i(t)|\,|W_i(t)|^{n_i-1}\,W_i(t) - \beta_i\,\dot{R}_i(t)\,|W_i(t)|_i^n, \tag{3.75}$$

where $R_i(t)$, ζ_i, $\omega_{0,i}$ and $G_k(t)$ are in Equation 3.60 and ρ_i, α_i, β_i, γ_i and n_i are constants. Numerical results are for $\omega_{0,i}$ and ζ_i, $i = 1, 2$, in Table 3.3 and $\rho_i = 0.7$, $\gamma_i = 1$,

$\alpha_i = \beta_i = 0.5/\text{cm}^{n_i}$ and $n_i = 1$, $i = 1, 2$, [183, 164]. The limit states d_1 and d_2 defined for the relative displacement response $R_1(t)$ and relative velocity response $\dot{R}_2(t)$ for components C_1 and C_2, respectively, are summarized in Table 3.3.

Using a Monte Carlo method fragility of the nonstructural system NS, that is, the probability that the (stationary) system response process $\mathbf{R}(t) = [R_1(t)\ \dot{R}_2(t)]^T$ leaves the safe set $D = (-d_1, d_1) \times (-d_2, d_2)$ in time interval of length τ, can be calculated directly, rather than from the fragility of its components as we have seen in Section 3.3.1.2. The Monte Carlo method also allows the use of linear and nonlinear models for components. The dependence between the component responses is also considered.

Let

$$R_{1,\tau} = \max_{0 \le t \le \tau}(|R_1(t)|), \tag{3.76}$$

$$\dot{R}_{2,\tau} = \max_{0 \le t \le \tau}(|\dot{R}_2(t)|), \tag{3.77}$$

be the maximum of the absolute value of the relative displacement response $R_1(t)$ and relative velocity response $\dot{R}_2(t)$ for components C_1 and C_2, respectively, in $[0, \tau]$, with τ in Equation 3.19.

The Monte Carlo method for calculating fragility surfaces involves five steps:

- Select earthquake moment magnitude and source-to-cite distance (m, r) and compute spectral density of ground acceleration at the site using Equation 2.3. The seismic activity matrix at the system site delivers the realizable values of (m, r).
- Calculate spectral densities of the absolute acceleration responses at the attachment points (joints 5 and 24) using Equation 3.58.
- Generate n_s samples of the correlated absolute acceleration processes at the attachment points using the spectral densities in Equation 3.58 and the method

in Section 2.4.2.

- For each sample of the correlated absolute acceleration process generated in the previous step calculate the response of C_i, $i = 1, 2$, using a nonlinear dynamic analysis (solving Equation 3.74) and determine the state of each component.

- Approximate the nonstructural system fragility for (m, r) by

$$\hat{P}_{f,mc}(D; m, r) = \frac{\#\left\{R_{1,\tau} \geq d_1 \text{ or } \dot{R}_{2,\tau} \geq d_2\right\}}{n_s}, \tag{3.78}$$

  with $R_{1,\tau}$ and $\dot{R}_{2,\tau}$ in Equations 3.76 and 3.77, respectively.

Fragility surfaces for the components C_1 and C_2 can be obtained by the same procedure. For example, fragility for C_1 can be estimated by $P_{f,1}(d_1; m, r) \simeq n_{f,1}/n_s$, where $n_{f,1}$ is the number of times the event $\{R_{1,\tau} \geq d_1\}$ is observed.

Similar to Section 3.3.1.2 numerical examples in this section considers steady-state responses of the nonstructural components with duration $\tau = 10$ seconds to strong ground accelerations. We note that the specific barrier model delivers the duration of ground motion [74], but we set somewhat arbitrary, $\tau = 10$ seconds irrespective of (m, r). Figures 3.20, 3.21 and 3.22 show the fragilities of the components C_1 and C_2 and the system fragility for the nonlinear nonstructural system defined previously, respectively. The fragilities for the nonlinear components in Figures 3.20 and 3.21 are lower than those for the linear components in Figures 3.12 and 3.13, showing that dampers located between the nonstructural components and the structure have a beneficial effect. For the nonlinear case the component C_1 is much more fragile than C_2, and, since the components are connected in series, the fragility of the nonstructural system is nearly equal to the fragility of C_1.

Figures 3.23, 3.24 and 3.25 show the fragilities as in Figures 3.12, 3.13 and 3.14, for linear C_1, C_2 and NS defined in Section 3.3.1.2, respectively, based on the Monte Carlo method using 100 ground motions records for each (m, r). The fragilities estimated

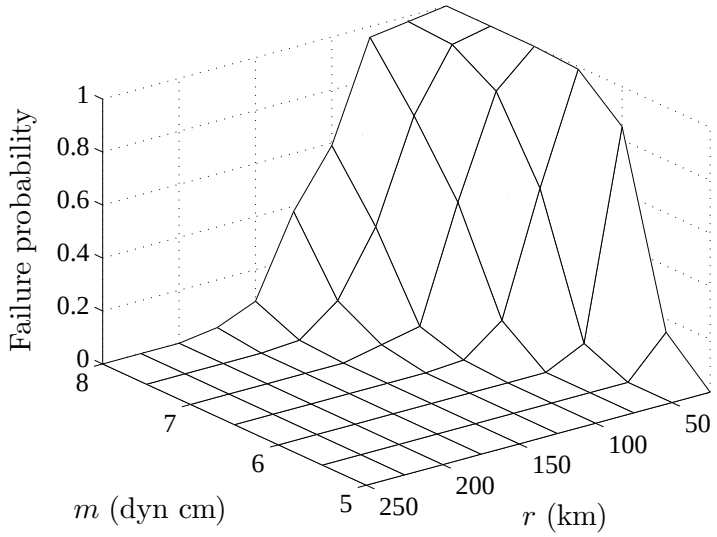

Figure 3.20: Fragility for nonlinear C_1.

by crossing theory in Figures 3.12, 3.13 and 3.14 are higher compared to the fragility surfaces obtained by Monte Carlo simulation. This is an expected result since we have used the upper bound in Equation 3.69 to calculate the system fragility in Equation 3.61. The mean crossing method provides a good approximation for the system fragility in the present example. The computational time needed to estimate the fragility of the system using mean crossing rates is much lower than the time needed for Monte Carlo simulation. It takes about 30 hours to generate fragility surfaces using Monte Carlo simulations on a regular PC and only a few minutes to estimate these surfaces by the crossing theory.

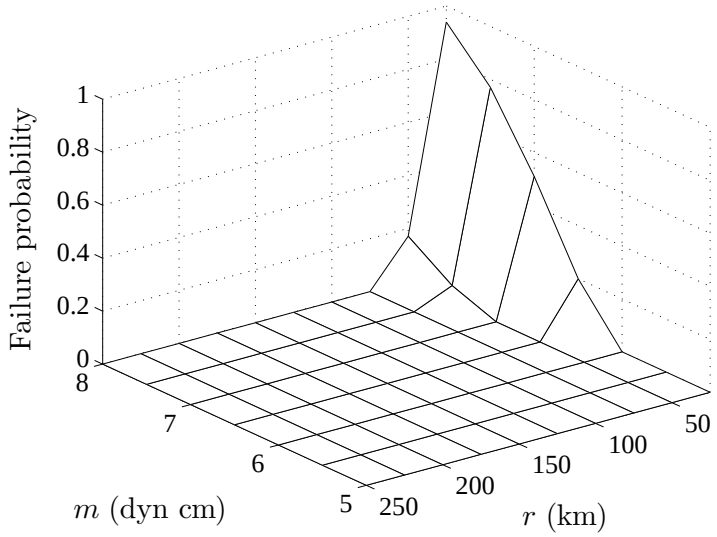

Figure 3.21: Fragility for nonlinear C_2.

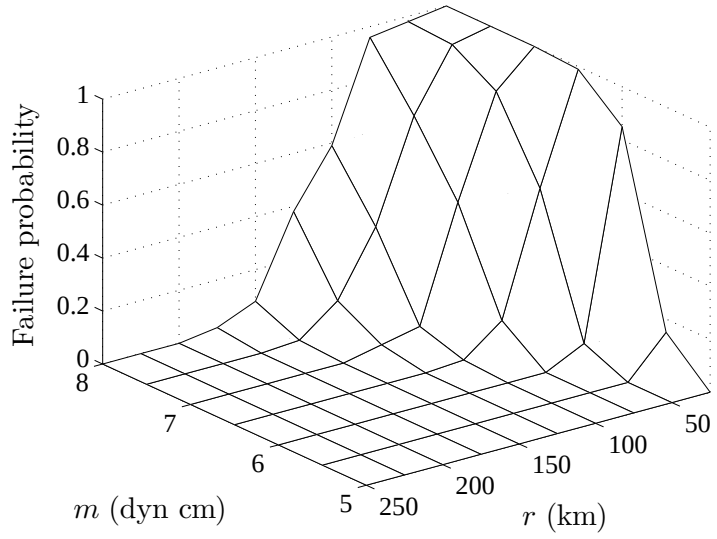

Figure 3.22: Fragility for nonlinear NS.

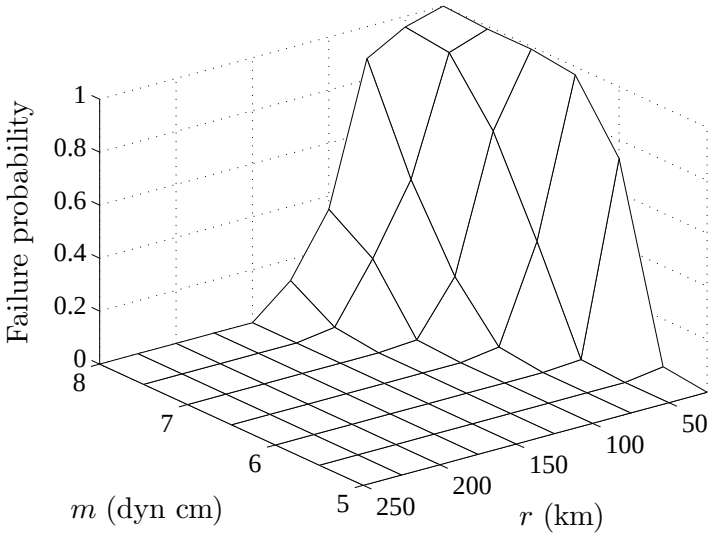

Figure 3.23: Fragility for linear C_1.

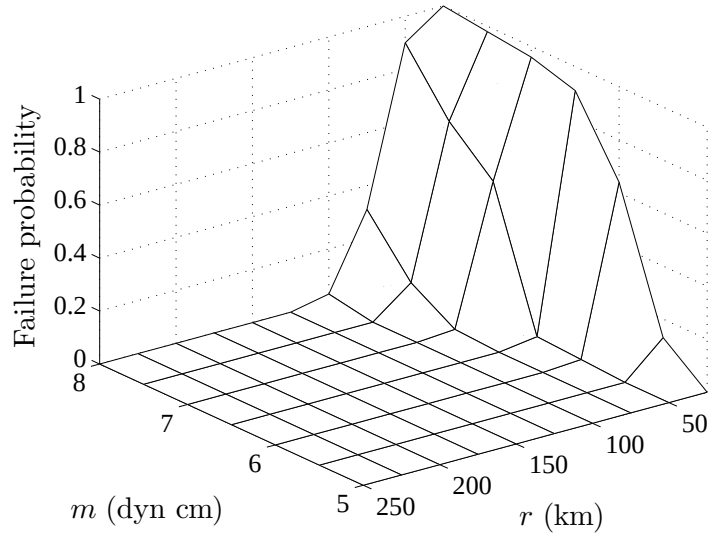

Figure 3.24: Fragility for linear C_2.

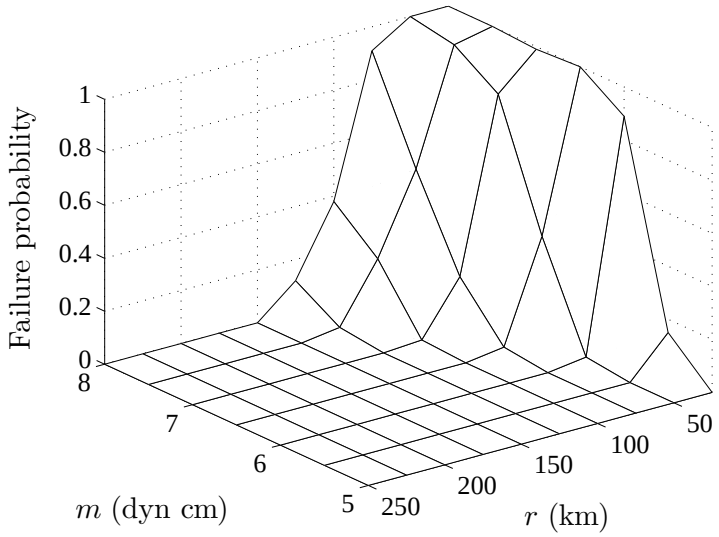

Figure 3.25: Fragility for linear NS.

3.3.3 Traditional fragility analysis

Seismic fragility of a structural, nonstructural, or geotechnical system is generally indexed by a scalar measure of ground motion intensity, hence the relationship between the system failure probability and ground motion intensity is called fragility curve. Several metrics have been considered for ground motion intensity. Traditionally, the peak ground acceleration (PGA) has been used and continued to be used as an intensity measure [86, 87, 88, 4, 30, 63, 149, 14]. Simplicity is the main feature of PGA. Unfortunately, PGA provides an unsatisfactory measure for structural response [76, 46, 50, 95]. Recent methods for assessing the seismic performance of structural systems measure seismic ground motion intensity by pseudo-spectral acceleration $PS_a(\omega_0, \zeta)$, that is, the maximum absolute value of the relative displacement response of a linear oscillator with natural frequency ω_0 and damping ratio ζ multiplied by ω_0^2 [144, 162, 51, 66, 152]. For linear/nonlinear multi degree of freedom systems the oscillator frequency ω_0 coincides with the fundamental frequency of the structural system in its linear range. The correlation between the maximum response of such systems and a vector-valued ground motion intensity measure consisting of $PS_a(\omega_0, \zeta)$ and some additional parameters related to the shape of the response spectrum has been also investigated [13, 12, 117].

A four-step algorithm is commonly used to construct fragility curves defined by, for example, the probability that maximum structural response exceeds a critical level z [86, 63, 144, 162, 160, 124]: (i) select a suite of actual and/or synthetic ground acceleration records $\{x_i(t)\}$ representing the seismicity at the system site, (ii) scale each record by its PGA or $PS_a(\omega_0, \zeta)$ and denote the scaled records by $\{\tilde{x}_i(t)\}$, (iii) calculate maximum system response to $\{\xi\tilde{x}_i(t)\}$ for a collection of constants, $\xi > 0$, and (iv) estimate the system fragility at each ξ by the ratio of the number of times the maximum response exceeds z to the total number of records.

Our objective in this section is to illustrate potential limitations of scalar seismic intensity measures currently used for fragility analysis. The analysis considers linear, Duffing [112], and Bouc-Wen [183] single degree of freedom systems, and artificial ground motion records representing independent samples of a Gaussian process whose probability law is defined by the specific barrier model [130, 131, 127, 75]. We use artificial ground motions to (i) reduce the uncertainty in the estimated fragility, that can be significant when dealing with actual records because the available sample size is usually small, and (ii) ensure that all records considered in the analysis belong to the same population of known probability law.

It is shown that $PS_a(\omega_0, \zeta)$ representation of ground motion intensity provides satisfactory estimates for the maximum relative displacement of Duffing oscillators. On the other hand, estimates of the maximum relative displacement for Bouc-Wen oscillators are inaccurate if based on $PS_a(\omega_0, \zeta)$. Accordingly, fragility curves indexed by $PS_a(\omega_0, \zeta)$ are adequate and inadequate for the Duffing and the Bouc-Wen oscillators, respectively.

3.3.3.1 Seismic intensity measures for response characterization

The seismic ground acceleration at system site, generated by a seismic event with moment magnitude m and source-to-site distance r, is modeled following Section 2.2.1 as $X(t) = e(t)Y(t)$, $0 \leq t \leq \tau$, where τ is the total duration of the seismic event in Equation 2.1, $e(t)$ is a deterministic modulation function in Equation 2.2 and $Y(t)$ is a zero-mean stationary Gaussian process with probability law defined in Sections 2.2.1.1.1. Figure 3.26 (a) and (b) show the spectral density function of $Y(t)$ at a site in California on stiff soil (NEHRP site class D, [56]), for ($m = 5, r = 200$ km) and ($m = 8, r = 25$ km), respectively. The plots in Figure 3.26 show that the frequency content of the seismic ground acceleration depends strongly on the values of m and r.

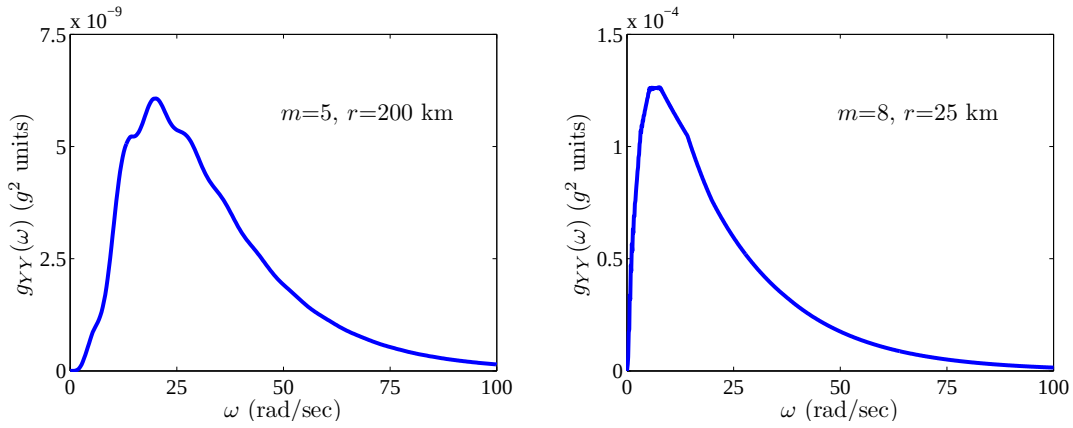

(a) (b)

Figure 3.26: Spectral density function of $Y(t)$.

Samples of ground acceleration $X(t)$ at a site due to an earthquake with moment magnitude m and the source-to-site distance r can be obtained by scaling samples of $Y(t)$ with the modulation function in Equation 2.2. We use the spectral representation method presented in Section 2.4 to generate samples of $Y(t)$. Figure 3.27 shows samples

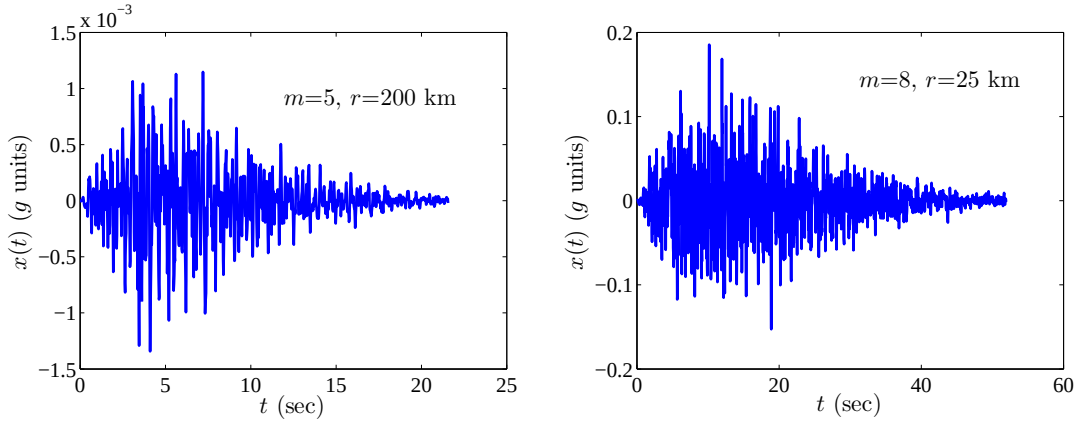

(a) (b)

Figure 3.27: Samples of $X(t)$.

of the ground acceleration process $X(t)$ for the site and earthquakes in Figure 3.26.

The seismic activity matrix defined in Section 2.3.4 provides realizable values of (m, r) at each zip code in the United States, and mean yearly rates, ν_{ij} of earthquakes with moment magnitude m_i and source-to-site distance r_j. Figure 2.13 shows the

seismic activity matrix for Los Angeles, California, normalized by $\nu = \sum_{i,j} \nu_{ij}$. Given that an earthquake occurs at a site, the probability that it has parameters (m_i, r_j) is ν_{ij}/ν.

The analysis in the following sections considers the relative displacement of linear and nonlinear oscillators to ground accelerations representing independent samples of $X(t)$ in Equation 3.19 with the modulation function in Equation 2.2 and the spectral density function in Equation 2.3.

3.3.3.1.1 Scaled ground accelerations: Let $x(t)$ be a sample of the ground acceleration process $X(t)$ defined in Section 3.3.3.1, and $z(t)$ the relative displacement response of a linear single degree of freedom oscillator to $x(t)$. The response $z(t)$ satisfies the differential equation

$$\ddot{z}(t) + 2\zeta\omega_0\dot{z}(t) + \omega_0^2 z(t) = -x(t), \quad t \geq 0, \tag{3.79}$$

where ω_0 is the natural frequency of the oscillator in rad/sec and ζ is the damping ratio. If $x(t)$ is scaled by a constant $c > 0$, that is, if we consider ground acceleration input by $\tilde{x}(t) = x(t)/c$, then $\tilde{z}(t) = z(t)/c$ satisfies

$$\ddot{\tilde{z}}(t) + 2\zeta\omega_0\dot{\tilde{z}}(t) + \omega_0^2\tilde{z}(t) = -\tilde{x}(t), \quad t \geq 0. \tag{3.80}$$

Two scaling constants are commonly used [86, 63, 144, 162, 160, 124]:

$$(i) \quad I = PGA = \max_{0\leq t\leq\tau}(|x(t)|), \tag{3.81}$$

$$(ii) \quad I = PS_a(\omega_0, \zeta) = \omega_0^2 \max_{0\leq t\leq\tau}(|z(t)|), \tag{3.82}$$

where PGA denotes the peak ground acceleration, $PS_a(\omega_0, \zeta)$ is the pseudo-spectral acceleration at the natural frequency ω_0 with damping ζ, and τ is the total duration of the seismic event given by Equation 2.1.

Our objective is to assess the validity of the the hypothesis that $PS_a(\omega_0, \zeta)$ is a ground acceleration measure capable of predicting maximum structural response. If this

hypothesis is valid, the particular values of (m, r) will be irrelevant, that is, a maximum structural response, for example, the maximum relative displacement commonly used in seismic analysis [63, 162, 51, 152], can be approximated accurately from $PS_a(\omega_0, \zeta)$ irrespective of the particular values of (m, r). We consider two values of (m, r) that according to Figure 2.13 are realizable. If the stated hypothesis is valid, maximum structural responses for the two values of (m, r) will be similar. The validation of the above hypothesis considers single degree of freedom linear, Duffing [112] and Bouc-Wen [183] oscillators.

3.3.3.1.2 Response of linear/nonlinear simple oscillators: Let $Z(t)$ be the relative displacement of a single degree of freedom oscillator under ground acceleration $X(t)$ defined in Section 3.3.3.1. The displacement process $Z(t)$ satisfies the Equations 3.20, 3.70 and 3.71 for the linear, Duffing and Bouc-Wen oscillators. Numerical results are for $\omega_0 = 5.97$ rad/sec, two values of damping ratio, $\zeta = 2\%$ and $\zeta = 15\%$, for linear systems, corresponding to low and high damping, respectively, $\zeta = 2\%$ for nonlinear systems, $\varepsilon = -0.0015/\text{cm}^2$, $\rho = 0.1$, $\gamma = 1$, $\alpha = \beta = 0.5/\text{cm}^n$ and $n = 1$ [183, 164].

Let

$$Z_\tau = \max_{0 \le t \le \tau}(|Z(t)|) \tag{3.83}$$

be the maximum of the absolute value of the relative displacement in $[0, \tau]$, with τ in Equation 2.1. The validation procedure involves five steps:

1. Generate 1,000 ground accelerations, that is 1,000 independent samples $\{x_i(t)\}$, $i = 1, \ldots, 1000$, of $X(t)$ for a given (m, r).
2. Scale each record $x_i(t)$ by the pseudo-spectral acceleration $PS_{a,i}(\omega_0, \zeta) = \omega_0^2 \max_{0 \le t \le \tau}(|z_i(t)|)$, where $z_i(t)$ is the relative displacement of the underlying linear oscillator to $x_i(t)$, that is, the solution of Equation 3.20, Equation 3.70 for $\varepsilon = 0$, or Equation 3.71 for $\rho = 1$.

3. Multiply each scaled record by $\xi > 0$ so that all records have the same pseudo-spectral acceleration level ξ.

4. Calculate the response $\tilde{z}_i(t;\xi)$ of the linear, Duffing and Bouc-Wen oscillators to the scaled ground acceleration $\tilde{x}_i(t) = \xi\, x_i(t)/PS_{a,i}(\omega_0,\zeta)$, $\xi > 0$, $i = 1,\ldots,1000$, using Equations 3.20, 3.70 and 3.71, respectively.

5. Calculate the maximum relative displacement for each ground motion and oscillator from

$$\tilde{z}_{\tau,i}(\xi) = \max_{0\le t\le\tau}(|\tilde{z}_i(t;\xi)|), \quad i = 1,\ldots,1000, \tag{3.84}$$

   for the selected values of (m, r) and ξ.

For the linear oscillator in Equation 3.20 with parameters ω_0 and ζ the maximum relative displacement in Equation 3.84 is always equal to ξ/ω_0^2 irrespective of the ground acceleration samples in step 1, since

$$\begin{aligned}\tilde{z}_{\tau,i}(\xi) &= \max_{0\le t\le\tau}(|\tilde{z}_i(t;\xi)|) = \max_{0\le t\le\tau}(|z_i(t)\,\xi/PS_{a,i}(\omega_0,\zeta)|),\\ &= \xi\,\max_{0\le t\le\tau}(|z_i(t)|)/PS_{a,i}(\omega_0,\zeta) = \xi/\omega_0^2,\end{aligned} \tag{3.85}$$

for $i = 1,\ldots,1000$. This shows that the hypothesis that $PS_a(\omega_0,\zeta)$ can predict accurately response maxima irrespective of the particular values of (m, r) holds for the linear oscillator in Equation 3.20.

Table 3.5 gives estimates of the mean and coefficient of variation (c.o.v.) of the maximum relative displacements, $\{\tilde{z}_{\tau,i}(\xi)\}$, $i = 1,\ldots,1000$, for the Duffing and the Bouc-Wen oscillators for scaled ground motions with $(m = 5, r = 200\,\text{km})$, $(m = 8, r = 25\,\text{km})$, and increasing values of ξ. If the hypothesis that $PS_a(\omega_0,\zeta)$ can predict accurately maximum relative displacement irrespective of the particular values of (m, r) holds, then $\tilde{z}_{\tau,i}(\xi)$ should depend only on ξ, and have similar values for $(m = 5, r = 200\,\text{km})$ and $(m = 8, r = 25\,\text{km})$. Estimates of the mean and

Table 3.5: Mean and c.o.v. of maximum relative displacement versus ξ.

	Duffing system				**Bouc-Wen system**			
	(m=5, r=200)		**(m=8, r=25)**		**(m=5, r=200)**		**(m=8, r=25)**	
ξ (g)	**mean** (cm)	**c.o.v.**	**mean** (cm)	**c.o.v.**	**mean** (cm)	**c.o.v.**	**mean** (cm)	**c.o.v.**
0.10	2.7552	0.0090	2.7607	0.0112	1.8001	0.2485	1.9047	0.2840
0.15	4.1424	0.0199	4.1590	0.0248	2.5570	0.2717	2.9809	0.3377
0.20	5.5434	0.0351	5.5847	0.0449	3.3085	0.2864	4.2030	0.3765
0.25	6.9720	0.0542	7.0683	0.0728	4.0654	0.3001	5.5930	0.4067
0.30	8.4500	0.0778	8.6510	0.1133	4.8388	0.3111	7.1234	0.4280
0.35	9.9969	0.1070	10.3602	0.1620	5.6260	0.3206	8.8079	0.4424

c.o.v. of $\tilde{Z}_\tau(\xi)$ obtained from $\{\tilde{z}_{\tau,i}(\xi)\}$ are similar and slightly different, respectively, for the Duffing oscillator for $(m = 5, r = 200\,\text{km})$ and $(m = 8, r = 25\,\text{km})$. The corresponding estimates for the Bouc-Wen oscillator differ. The differences between maximum relative displacement for $(m = 5, r = 200\,\text{km})$ and $(m = 8, r = 25\,\text{km})$ increase with ξ and are nearly 60% and 40% for the mean and c.o.v, respectively, for $\xi = 0.35g$. Figure 3.28 and 3.29 show the normalized histograms of the maximum relative displacements, $\{\tilde{z}_{\tau,i}(\xi)\}$, $i = 1, \ldots, 1000$, of the Duffing and Bouc-Wen oscillators in Table 3.5, respectively, for ($m = 5, r = 200$ km) and ($m = 8, r = 25$ km) at (a) $\xi = 0.10g$ and (b) $\xi = 0.35g$.

We conclude that the maximum relative displacement can be calculated exactly from $PS_a(\omega_0, \zeta)$ for linear single degree of freedom systems. However, $PS_a(\omega_0, \zeta)$ fails to characterize uniquely the maximum relative displacement for a class of

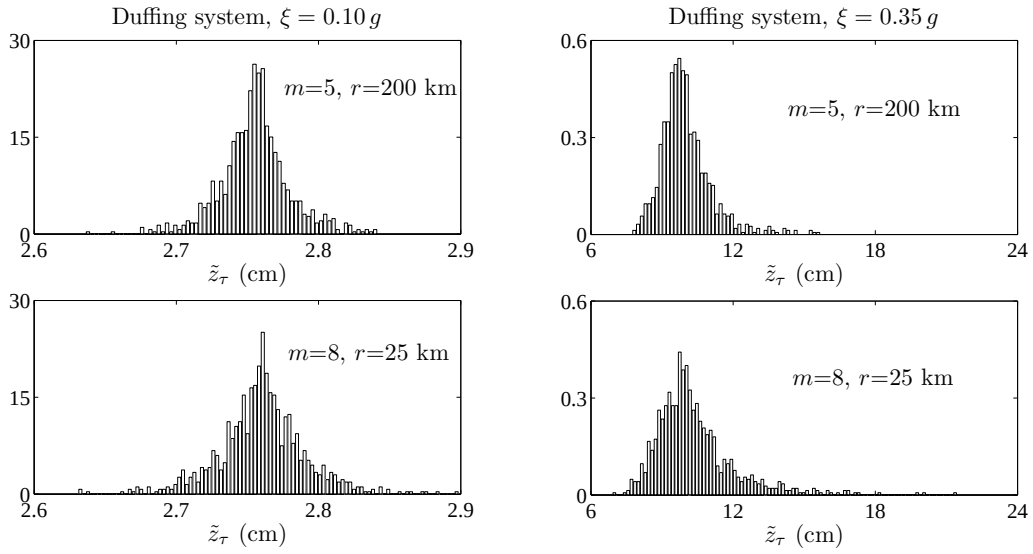

Figure 3.28: Histogram of maximum relative displacement for Duffing system: (a) $\xi = 0.10g$, (b) $\xi = 0.35g$.

nonlinear oscillators. For nonlinear Duffing and Bouc-Wen oscillators, $PS_a(\omega_0, \zeta)$ characterizes satisfactorily and unsatisfactorily the relative displacement response maxima, respectively.

3.3.3.2 Fragility curves

Fragility of a structural system is the probability that a system response exceeds a limit state when subjected to an earthquake of specified intensity. The response and the limit state in our analysis are the maximum relative displacement Z_τ in Equation 3.83 and a critical displacement z, respectively. Fragility curves has been plotted against the PGA [86, 87, 88, 4, 30, 63, 149, 14] or $PS_a(\omega_0, \zeta)$ [144, 162, 51, 66].

Let $Z(t)$ be the relative displacement of a linear/nonlinear oscillator in Equations 3.20, 3.70 or 3.71, and Z_τ its extreme value in Equation 3.83. Denote by

$$P_f(z;\xi) = P(Z_\tau > z \,|\, \xi), \tag{3.86}$$

the probability that Z_τ exceeds a limit state z if the oscillator is subjected to a seismic

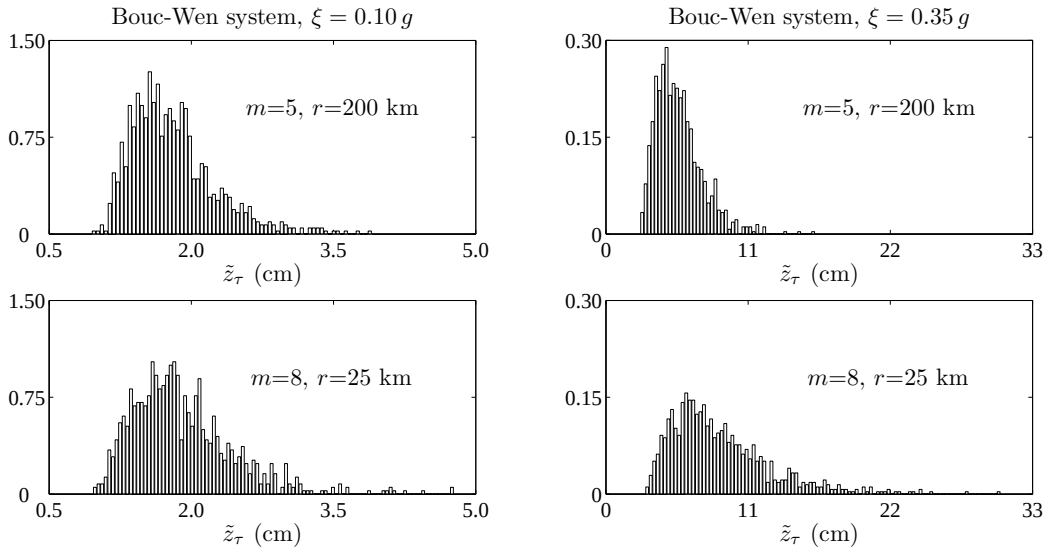

Figure 3.29: Histogram of maximum relative displacement for Bouc-Wen system: (a) $\xi = 0.10g$, (b) $\xi = 0.35g$.

ground acceleration $X(t)$ with intensity ξ. Fragility curves are plots of estimates of $P_f(z;\xi)$ versus ξ, where ξ relates to either PGA or $PS_a(\omega_0,\zeta)$. By abuse of notation, we show these curves as functions of PGA and $PS_a(\omega_0,\zeta)$ for ξ related to PGA and $PS_a(\omega_0,\zeta)$, respectively.

We outline a six-step Monte Carlo algorithm for constructing fragility curves, that follows the traditional approach in earthquake engineering.

1. Generate n_s independent samples $\{x_i(t)\}$, $i = 1,\ldots,n_s$, of $X(t)$ based on the site seismic activity matrix and the specific barrier model. First, generate n_s values of (m,r) from the seismic activity matrix in Figure **??**. Second, generate a sample of $X(t)$ for each generated (m,r) value.

2. Scale the records $\{x_i(t)\}$ such that they have the desired intensity level $I = \xi$, $\xi > 0$. The scaled version of $x_i(t)$ is $\tilde{x}_i(t) = x_i(t)(\xi/I_i)$, where I_i is given by Equations 3.81 and 3.82 with I for $x_i(t)$.

3. Calculate the response $\tilde{z}_i(t)$ of the system to the scaled ground accelerations

$\tilde{x}_i(t) = x_i(t)(\xi/I_i)$, $i = 1, \ldots, n_s$, using a linear/nonlinear dynamic analysis.

4. Calculate the maximum relative displacement for each ground motion and oscillator from

$$\tilde{z}_{\tau,i}(\xi) = \max_{0 \le t \le \tau} (|\tilde{z}_i(t;\xi)|), \quad i = 1, \ldots, n_s. \tag{3.87}$$

5. Approximate $P_f(z;I)$ in Equation 3.86 for $I = \xi$ by

$$\hat{P}_f(z;\xi) = \frac{\#\{\tilde{z}_{\tau,i}(\xi) > z\}}{n_s} \tag{3.88}$$

where z is the displacement limit state.

6. Repeat steps 3-5 by changing the intensity level ξ in step 2 to obtain fragility curve for the system.

The above Monte Carlo algorithm was used to construct fragility curves for linear and nonlinear single degree of freedom oscillators by using $n_s = 1,000$ independent samples of $X(t)$ for three types of ground motions corresponding to (i) the relative frequencies of various (m, r) values in the seismic activity matrix at the system site, (ii) the seismic event with ($m = 5, r = 200$ km), and (ii) the seismic event with ($m = 8, r = 25$ km).

Fragility curves for linear systems plotted against ξ corresponding to the scaling $\tilde{x}_i(t) = x_i(t)(\xi/PS_a(\omega_0,\zeta))$ are independent of the particular value of (m, r), and are equal to $P_f(z;\xi) = 1(\xi \ge z\,\omega_0^2)$. However, these curves depends strongly on (m, r) if ξ corresponds to the scaling $\tilde{x}_i(t) = x_i(t)(\xi/PGA)$, as illustrated in Figures 3.30 and 3.31, for limit state $z = 3$ cm. Hence, PGA is not an adequate intensity measure for fragility analysis.

We have seen that $PS_a(\omega_0,\zeta)$ characterizes Z_τ approximately for nonlinear systems, and the accuracy of the resulting approximation of Z_τ depends on the type of nonlinearity. Figures 3.32 and 3.33 show the fragility curves for the Duffing oscillator

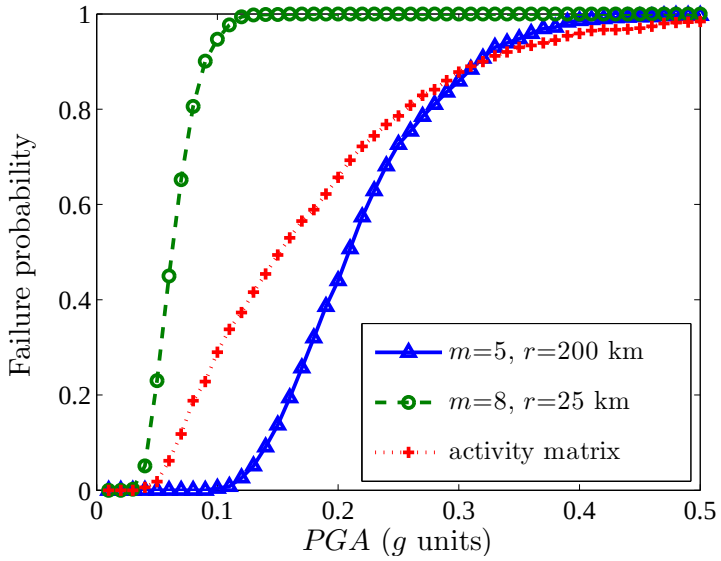

Figure 3.30: Fragility against the PGA for linear system with $\zeta = 2\%$.

plotted against $I = PS_a(\omega_0, \zeta)$, for two limit states, $z = 3$ cm and $z = 8$ cm, respectively, and the three types of ground motions described above, and the fragility curve for the associated linear system ($\varepsilon = 0$). For a yield displacement of 6.67 cm the displacement ductilities for the limit states $z = 3$ and $z = 8$ cm are 0.45 and 1.20, respectively. We can conclude that $PS_a(\omega_0, \zeta)$ is an adequate intensity measure for fragility analysis of the Duffing system.

Figures 3.34 and 3.35 show fragility curves as in Figures 3.32 and 3.33 for the Bouc-Wen oscillator, and the associated linear system ($\rho = 1$). The displacement ductilities for the limit states $z = 3$ and $z = 8$ cm are 2.94 and 7.84, respectively, for a yield displacement of 1.02 cm. The ductility values are in a range that is relevant to earthquake engineering practice [152]. Fragility curves calculated using ground motions from ($m = 5, r = 200$ km), ($m = 8, r = 25$ km) and the seismic activity matrix differ significantly. Hence, $PS_a(\omega_0, \zeta)$ is not an adequate intensity measure for fragility analysis of the Bouc-Wen oscillator. The inadequacy of the $PS_a(\omega_0, \zeta)$ as a ground motion intensity measure for fragility assessment of some nonlinear systems has been

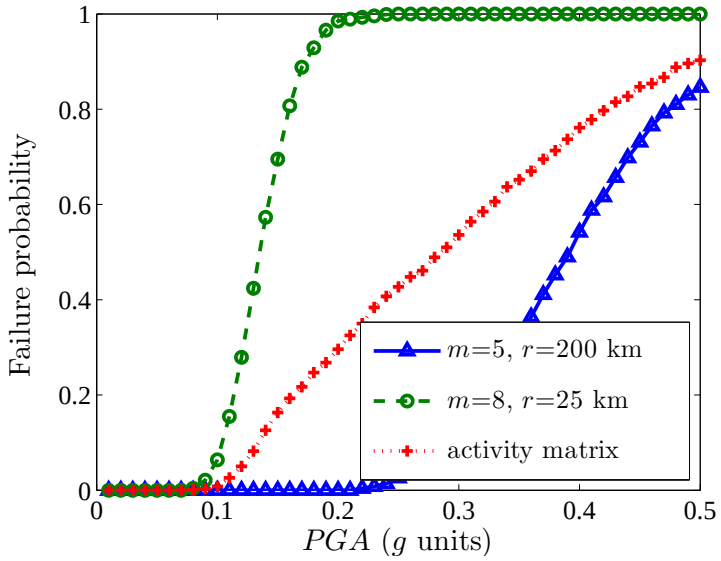

Figure 3.31: Fragility against the PGA for linear system with $\zeta = 15\%$.

also reported elsewhere [148].

3.3.3.3 Conclusions

Seismic fragility of a system is the probability that a system response to seismic ground motions of specified intensities exceeds a critical value. Fragility curve is a relationship between this exceedance probability and a scalar measure of ground motion intensity. Peak ground acceleration and pseudo-spectral acceleration have been widely used as scalar measures of seismic intensity for fragility analysis. Recent studies recommend the use of pseudo-spectral acceleration as a measure for ground motion intensity.

This simulation-based study showed that pseudo-spectral acceleration characterizes completely the maximum relative displacement for linear single degree of freedom systems, but fails to do so for arbitrary nonlinear oscillators. The pseudo-spectral acceleration can be used to approximate the maximum relative displacement of the Duffing oscillator, so that fragility curves as functions of pseudo-spectral acceleration

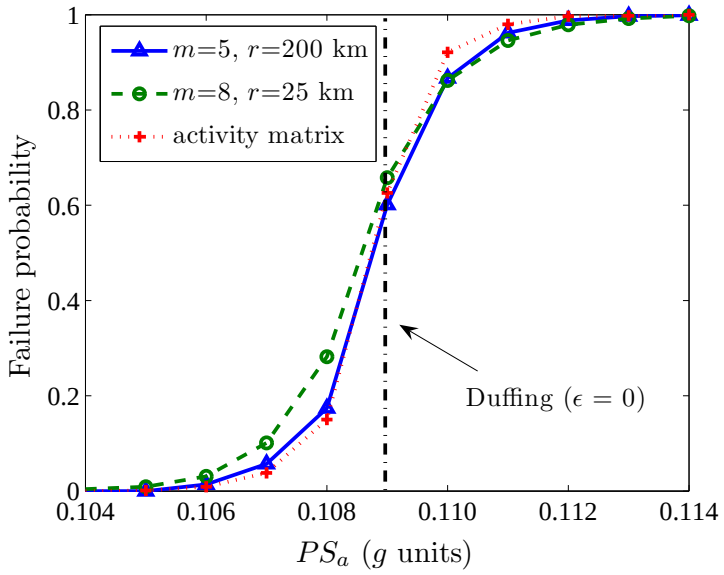

Figure 3.32: Fragility against the $PS_a(\omega_0, \zeta)$ for Duffing system for $z = 3$ cm.

are adequate for this system. On the other hand, the pseudo-spectral acceleration cannot be used to approximate the maximum relative displacement of the Bouc-Wen oscillator. Hence, it is not possible to construct fragility curves depending on pseudo-spectral acceleration for the Bouc-Wen oscillator.

Fragility surfaces, which are probabilities of system failure as a function of earthquake moment magnitude and distance from the seismic source to the system site, are proposed for assessing seismic performance of this oscillator, that is, a nonlinear system with hysteresis which is relevant in earthquake engineering. Fragility surfaces for the linear, Duffing and Bouc-Wen oscillators based on crossing theory and Monte Carlo simulation have been calculated and presented. Crossing theory provides accurate results for highly reliable systems. We note that fragility surfaces can be used in the same way as fragility curves to select an optimal design from a collection of design alternatives, for realistic single and multi degree of freedom structural/nonstructural systems, via life cycle cost-benefit analysis [95, 96].

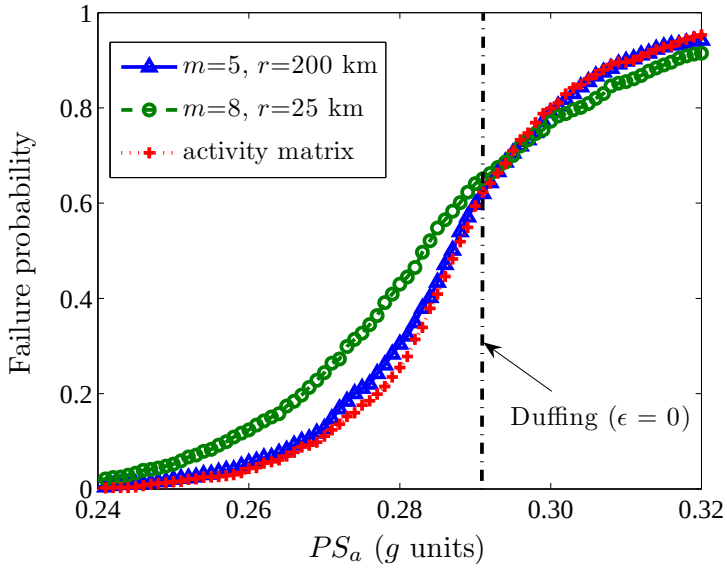

Figure 3.33: Fragility against the $PS_a(\omega_0, \zeta)$ for Duffing system for $z = 8$ cm.

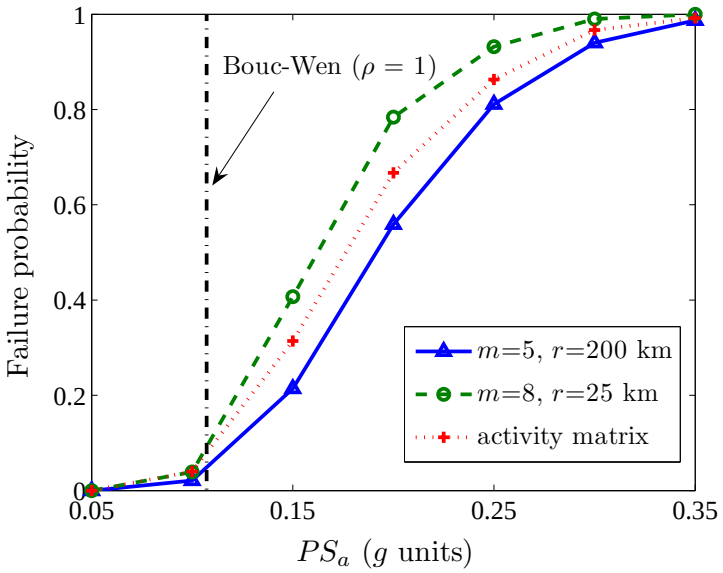

Figure 3.34: Fragility against the $PS_a(\omega_0, \zeta)$ for Bouc-Wen system for $z = 3$ cm.

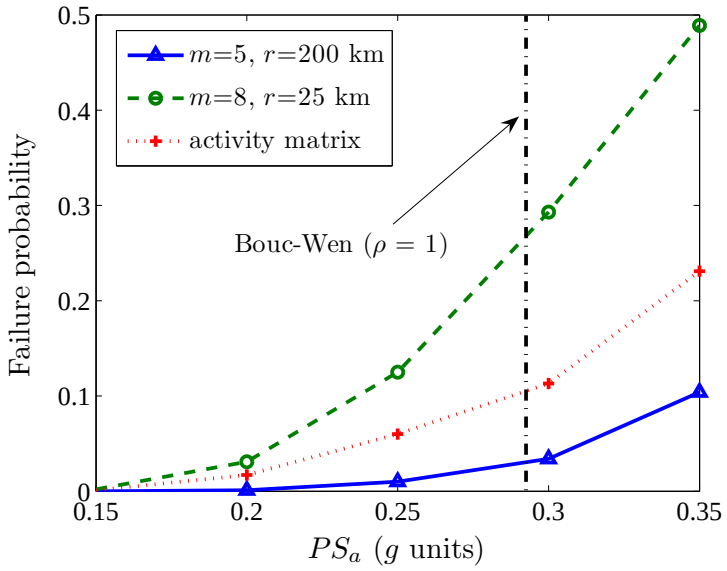

Figure 3.35: Fragility against the $PS_a(\omega_0, \zeta)$ for Bouc-Wen system for $z = 8$ cm.

3.4 Wind fragility

Wind fragility is the probability that a response of a structural, nonstructural, or geotechnical system exceeds a critical level if subjected to wind loads resulting from high winds of specified intensities. We base the intensity of the wind loads on the parameters defining the probability law of the wind velocity so that $\boldsymbol{\phi}$ in Equation 3.1 has $d = 2$ components, $\phi_1 =$ the mean wind velocity at system site $\bar{v}$, and $\phi_2 =$ the principal wind direction $\bar{\theta}$. The wind activity matrix in Section 2.3.5 provides realizable values of $(\bar{v}, \bar{\theta})$ at the system site.

Consider a simple linear structure as shown in Figure 3.36 with mass m, stiffness k

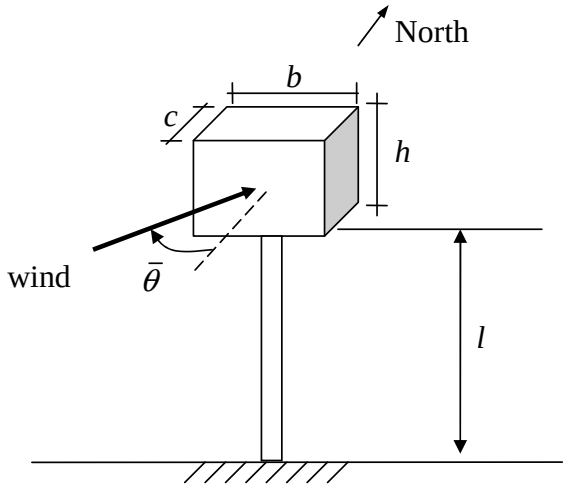

Figure 3.36: Simple system.

and damping c, subjected to high winds caused by a hurricane with mean wind speed $\bar{v}$ blowing in direction $\bar{\theta}$. The wind drag force, that is, the wind force along the principal wind direction $\bar{\theta}$, acting on this structure may be expressed as

$$F(t) = \frac{1}{2}\rho_a c_d a(\bar{\theta}) V^*(t)^2, \quad 0 \le t \le \tau, \tag{3.89}$$

where τ is given in Equation 2.18, ρ_a is the density of air, $a(\bar{\theta})$ is the exposed area perpendicular to the principal wind direction $\bar{\theta}$, $V^*(t)$ is the wind velocity in

Equation 2.18 with probability law defined in Section 2.2.2.1, and c_d is the wind drag coefficient, which depends, in general, on the structural shape, the frequency content of the wind velocity and the principal wind direction ([154], Section 4.7). The wind drag coefficient c_d can be obtained by wind tunnel tests for the selected structure ([154], Section 4.5-4.7), however, in the absence of such data following assumptions are generally made, (1) it is independent of the frequency content of the wind velocity [17], and (2) its variation with wind direction can be related to known cases, for example, using a relationship similar to the one shown in ([154], Section 4.6, Figure 4.6.3).

The wind model in this section uses a constant wind drag coefficient and considers only along-wind response of the system to the loads due to turbulence. The model does not consider other aeroelastic phenomena such as across-wind galloping, vortex-shedding, and flutter (for definitions see [154]). These assumptions are admittedly questionable but are invariably made for purposes of developing a practical approach. Some of these assumptions are relaxed in Chapter 4, in which a more realistic example is considered.

The system in Figure 3.36 is modeled by a linear single degree of freedom system and its along-wind displacement response $Z(t)$ satisfies the differential equation

$$m\ddot{Z}(t) + c\dot{Z}(t) + kZ(t) = F(t), \quad 0 \leq t \leq \tau, \tag{3.90}$$

with initial conditions $Z(0) = \dot{Z}(0) = 0$, where $\dot{Z}(t) = dZ(t)/dt$, $\ddot{Z}(t) = d^2Z(t)/dt^2$ and $F(t)$ is given by Equation 3.89. In general $Z(t)$ is a non-Gaussian random process, since $F(t)$ in Equation 3.89 is a quadratic form of Gaussian process $V^*(t)$, with stationary characteristics during the steady-state part of oscillations.

Denote by

$$P_f(z; \bar{v}, \bar{\theta}) = P(Z_\tau > z \,|\, \bar{v}, \bar{\theta}), \tag{3.91}$$

the probability that the maximum response $Z_\tau = \max_{0 \leq t \leq \tau}(|Z(t)|)$, with τ in Equation 2.18, exceeds a limit state z if the oscillator is subjected to high winds with

parameters $(\bar{v}, \bar{\theta})$. We estimate the system fragility in Equation 3.91 by the method based on the crossing theory of stochastic processes presented in Section 3.1, and compare our results with the “exact" solutions obtained by Monte Carlo simulation method presented in Section 3.1.

In this section we provide (1) an analytical expression for the mean crossing rate of the quasi-static response of the linear oscillator in Figure 3.36 to wind load $F(t)$ in Equation 3.89, which is a quadratic form of the stationary Gaussian process $V(t)$, and (2) an estimation for the mean crossing rate of the dynamic response of the same linear oscillator to wind load $F(t)$ in Equation 3.89 based on the sampling theorem and Monte Carlo algorithm. The method based on the sampling theorem can also be extended to linear multi degree of freedom system [70]. For nonlinear systems subjected to wind loads methods based on the classical Monte Carlo algorithm can be used to calculate the system fragility (see Section 3.2).

3.4.1 Quasi-static response

Consider the simple oscillator in Equation 3.90 with natural frequency $\omega_0 = \sqrt{k/m}$ much larger that the frequencies of the excitation, that is, $\omega_0 \gg \bar{\omega}$, in which $\bar{\omega}$ is the cut-off frequency of the spectral density function in Equation 2.19 of fluctuating wind speed $V(t)$ in Equation 2.18. The response of the oscillator is practically proportional to the excitation and is referred to as quasi-static response. In this section we examine the quasi-static steady-state response of simple linear oscillators to the wind loads modeled as quadratic form of stationary Gaussian processes.

The displacement response of the oscillator to the wind force $F(t)$ in Equation 3.89 is

$$Z(t) = \frac{1}{k}F(t) = \frac{\rho_a c_d a(\bar{\theta})}{2k}(\bar{v} + V(t))^2 = \alpha(\bar{v} + V(t))^2, \tag{3.92}$$

with the notation in Equation 3.89 and $\alpha = \rho_a c_d a(\bar{\theta})/(2k) > 0$.

The mean z-upcrossing rate of $Z(t)$ for $z > 0$, that is, the mean rate at which $Z(t)$ crosses from below a displacement level z, is equal to the mean $(-\sqrt{z/\alpha} - \bar{v}, \sqrt{z/\alpha} - \bar{v})$-outcrossing rate of the zero-mean Gaussian process $V(t)$, and is given by,

$$\nu^+(z) = \nu_V^+(\sqrt{z/\alpha} - \bar{v}) + \nu_V^-(-\sqrt{z/\alpha} - \bar{v}) \,, \tag{3.93}$$

where

$$\nu_V^+(\sqrt{z/\alpha} - \bar{v}) = \frac{1}{2\pi}\frac{\sigma_{\dot{V}}}{\sigma_V}\exp\left(-(\sqrt{z/\alpha} - \bar{v})^2/(2\sigma_V^2)\right) \quad \text{and}$$

$$\nu_V^-(-\sqrt{z/\alpha} - \bar{v}) = \frac{1}{2\pi}\frac{\sigma_{\dot{V}}}{\sigma_V}\exp\left(-(-\sqrt{z/\alpha} - \bar{v})^2/(2\sigma_V^2)\right), \tag{3.94}$$

are, respectively, the mean $(\sqrt{z/\alpha} - \bar{v})$-upcrossing and $(-\sqrt{z/\alpha} - \bar{v})$-downcrossing rates of the zero-mean Gaussian process $V(t)$([164], Section 7.3), in which $\sigma_V = \int_0^{\bar{\omega}} g_{VV}(\omega)d\omega$ and $\sigma_{\dot{V}}^2 = \int_0^{\bar{\omega}} \omega^2 g_{VV}(\omega)d\omega$ are the variances of $V(t)$ and and $\dot{V}(t) = dV(t)/dt$, with the spectral density function $g_{VV}(\omega)$ of $V(t)$ given in Equation 2.19. We note that $\nu^+(z) = 0$ for $z \leq 0$ since the quasi static response $Z(t)$ in Equation 3.92 is always positive. The mean z-upcrossing rate of $Z(t)$ in Equation 3.93 can also be obtained from the joint characteristic function of $\{Z(t), \dot{Z}(t)\}$ or noting that $Z(t)$ is a quadratic form of a Gaussian process. These methods are presented in Appendix D.

Consider the oscillator in Figure 3.36 with $b = c = h = 5$ m, $l = 10$ m, natural frequency $\omega_0 = 15$ rad/sec and mass $m = 5000$ kg, subjected to the wind drag force $F(t)$ in Equation 3.89 with $\rho_a = 1.2$ kg/m^3, a constant drag coefficient $c_d = 2$ ([154], Section 4.5, Table 4.5.1). Figure 2.7 in Section 2.2.2.1 shows the one-sided spectral density function in Equation 2.19 of the fluctuating wind velocity $V(t)$. We note that the natural frequency of the system ω_0 is much larger that the frequencies of the excitation so that the response $Z(t)$ of the oscillator in Equation 3.90 will be quasi-static and equal to $Z(t) = F(t)/k$, where $F(t)$ is in Equation 3.89 and $k = \omega_0^2 m$ is the system stiffness.

The system fragility in Equation 3.91, that is, the probability that the maximum quasi-static response exceeds a limit state $z \geq \mu_Z$, where $\mu_Z = E[Z(t)] = \alpha\sigma_V^2 + \alpha\bar{v}^2$, if

the oscillator is subjected to high winds with specified parameters, can be approximated by Equation 3.5 with mean $D = [-z, z]$-outcrossing rate from Equation 3.93 and τ from Equation 2.18. Note that the mean $D = [-z, z]$-outcrossing rate $\nu_D = \nu^+(z) + \nu(^-{-z})$ in Equation 3.5 is equal to $\nu^+(z)$ in Equation 3.93 since the quasi-static response $Z(t)$ in Equation 3.92 is always non-negative, so that $\nu^-(-z) = 0$ for $z \geq \mu_Z \geq 0$. If the limit state z is less than the mean response μ_Z then $P[(\boldsymbol{Z}(0) \in D)]$ in Equation 3.3 becomes zero so that system fragility in Equation 3.5 becomes 1.

Figure 3.37 shows fragility surface for the linear oscillator in Figure **??** located in

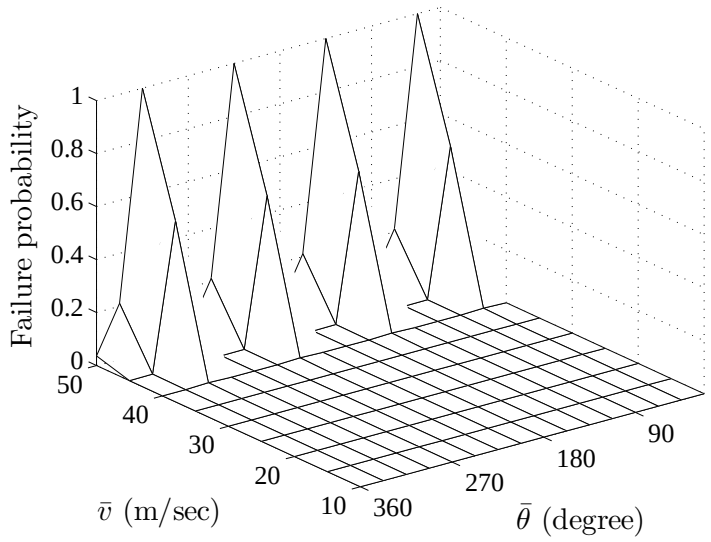

Figure 3.37: Fragility for linear oscillator with $\omega_0 = 15$ rad/sec.

milepost-150 for the displacement limit state $z = 20$ cm. The wind activity matrix in Figure 2.16 provides realizable values of $(\bar{v}, \bar{\theta})$ at the system site. As expected system fragility increases with increasing wind speed. The periodic change in fragility along the $\bar{\theta}$-axis results from the assumed shape of the structure (Figure 3.36). The exposed area $a(\bar{\theta})$ in Equation 3.89 becomes largest at 45, 135, 225 and 315 degrees, resulting in higher loading, hence increased fragility.

3.4.2 Dynamic response

Consider the same oscillator in Section 3.4.1, but this time with a natural frequency ω_0 such that its response to wind load $F(t)$ in Equation 3.89 is dynamic. The equation of motion for the oscillator in Equation 3.90 can alternatively be given by

$$\ddot{Z}(t) + 2\zeta\omega_0\dot{Z}(t) + \omega_0^2 Z(t) = \frac{F(t)}{m}, \quad 0 \leq t \leq \tau, \tag{3.95}$$

where $\omega_0^2 = k/m$, $\zeta = c/(2m\omega_0)$ and τ in Equation 2.18.

Method presented in [70], based on representations of the input process obtained from a Shanon's sampling theorem and Monte Carlo simulation, is used for calculating statistics of the state of the linear system in Equation 3.95 subjected to stationary bandlimited non-Gaussian process $F(t)$ in Equation 3.89. The bandwidth $[0, \bar{\omega}]$ of $F(t)$ is defined by the cut-off frequency of the spectral density function of the fluctuating wind velocity $V(t)$ in Equation 2.19. The system output at a time t is approximated by a finite sum of deterministic functions of t with random coefficients given by equally spaced values of the input process over a window of finite width centered on t. The number of terms in the sum depends on both input and system memory. Results obtained by the sampling theorem are compared with the exact results obtained by classical Monte Carlo simulation.

3.4.2.1 Method based on the classical Monte Carlo simulation:

The simulation method involves three phases:

Step-1. Realization of the stationary Gaussian wind velocity $V(t)$ are generated for a storm of duration τ in Equation 2.18 from its spectral density function in Equation 2.19 following the methods in Section 2.4.1.

Step-2. Deterministic dynamic analyses are performed to determine the response in $(0, \tau)$ to the samples of $F(t)$ in Equation 3.89 obtained from the samples in

step-1. The analyses involve time-domain integrations using Newmark's method ([31], Chapter 5).

Step-3. The calculated response samples are used to calculate means and variances of the response process and mean upcrossing rates.

3.4.2.2 Method based on the sampling theorem:

Consider the following approximation to $F(t)$ in Equation 3.89 obtained by the sampling theorem

$$F_n(t) = \sum_{k=n_t-n}^{n_t+n+1} F(k\,t^*)\,\alpha_k(t;t^*), \quad t \in [n_t\,t^*, (n_t+1)\,t^*], \tag{3.96}$$

in which $t^* = \pi/\bar{\omega}$ with $\bar{\omega}$ in Equation 2.19,

$$\alpha_k(t;t^*) = \frac{\sin(\pi\,(t/t^*-k))}{\pi\,(t/t^*-k)}\,, \tag{3.97}$$

where $n_t = [t/t^*]$ is the largest integer smaller than t/t^* and $n \geq 1$ is an integer defining the size of a window centered on cell $[n_t\,t^*, (n_t+1)\,t^*]$ containing the current time t. The points of the set $\{k\,t^*, k \in \mathbb{Z}\}$ are referred to as nodes, and the spacing t^* between nodes is called Nyquist sampling rate or just sampling rate. The function α_k is one if $t/t^* = k$, is zero if t/t^* is an integer different from k, and decreases to zero as $|t/t^* - k|$ increases. We note that $F_n(t)$ in Equation 3.96 depends linearly on the values of F at $2\,(n+1)$ nodes centered on the cell containing t, and coincides with F at $t = \big(n_t - n\big)\,t^*, \ldots, \big(n_t + n + 1\big)\,t^*$, and is referred to as a local representation.

The displacement response of the oscillator $Z(t)$ is the solution of Equation 3.95 so that

$$Z(t) = Z(0)\,\cos\big(\omega_{0,d}\,t\big) + \frac{\dot{Z}(0) + \zeta\,\omega_0\,Z(0)}{\omega_{0,d}}\,\sin\big(\omega_{0,d}\,t\big) + \int_0^t \phi(t-s)\,F(s)\,ds, \tag{3.98}$$

where $\omega_{0,d} = \omega_0\,\big(1-\zeta^2\big)^{1/2}$, $\phi(u) = \exp\big(-\zeta\,\omega_0\,u\big)\,\sin\big(\omega_{0,d}\,u\big)/\omega_{0,d}$ for $u \geq 0$, and $\phi(u) = 0$ for $u < 0$. The approximate system state $Z_{n,m}(t)$ at time t corresponding to

$F_n(t)$ in Equation 3.96 has the expression

$$Z_{n,m}(t) = \sum_{k=n_t-n_m}^{n_t-1} \sum_{i=k-n}^{k+n+1} \left[\int_{0\vee k\, t^*}^{0\vee(k+1)\, t^*} \phi(t-s)\, \alpha_i(s;t^*)\, ds \right] F(i\, t^*)$$

$$+ \sum_{i=n_t-n}^{n_t+n+1} \left[\int_{n_t\, t^*}^{t} \phi(t-s)\, \alpha_i(s;t^*)\, ds \right] F(i\, t^*) \tag{3.99}$$

for zero initial conditions, where $n_m\, t^*$ is such that the system state at a time t depends weakly on the input prior to time $t - n_m\, t^*$. The time lag $n_m\, t^*$, referred to as system memory, depends only on system properties, and is expressed here in t^*-units for convenience.

The formula in Equation 3.99 shows that the approximate state at time t has the representation

$$Z_{n,m}(t) = \boldsymbol{\beta}(t)\, \boldsymbol{F}_{n,m}, \tag{3.100}$$

where $\boldsymbol{\beta}(t)$ is a deterministic matrix with time-dependent entries assembled from the integrals

$$\int_{0\vee k\, t^*}^{0\vee(k+1)\, t^*} \boldsymbol{\phi}(t,s)\, \alpha_i(s;t^*)\, ds \;\text{ and }\; \int_{n_t\, t^*}^{t} \boldsymbol{\phi}(t,s)\, \alpha_i(s;t^*)\, ds$$

in Equation 3.99 and $\boldsymbol{F}_{n,m} = \big(F((n_t - n_m - n)\, t^*), \ldots, F((n_t + n + 1)\, t^*)\big)$ is a random vector with $2\,(n+1) + n_m$ coordinates consisting of values of X spaced equally at t^*. Since $F(t)$ is assumed to be stationary, the joint distribution of $\boldsymbol{F}_{n,m}$ is invariant to a time shift, that is, the statistics of $\boldsymbol{F}_{n,m}$ do not depend on the particular value of n_t. The definition of the system state in Equation 3.100 suggests the following two-step algorithm for generating output samples. First, samples of the $2\,(n+1) + n_m$-dimensional input vector $\boldsymbol{X}_{n,m}$ need to be generated. Second, system state samples can be obtained by matrix multiplication from $Z_{n,m}(t,\omega) = \boldsymbol{\beta}(t)\, \boldsymbol{F}_{n,m}(\omega)$ according to Equation 3.100. We note that the matrix $\boldsymbol{\beta}(t)$ depends only on system properties and input bandwidth. Once $\boldsymbol{\beta}(t)$ has been calculated for a system and an input bandwidth, it can be used to characterize the system state to input processes with arbitrary probability

law and bandwidth similar to that used to construct $\boldsymbol{\beta}(t)$. If $t < n_m\, t^*$, the matrix $\boldsymbol{\beta}(t)$ needs to be recalculated at each new value of t. On the other hand, if $t \geq n_m\, t^*$, then $\boldsymbol{\beta}(t)$ has the same expression at times t in intervals defined by distinct pairs of consecutive nodes, that is, intervals $[k\, t^*, (k+1)\, t^*]$ and $[l\, t^*, (l+1)\, t^*]$ for $k \neq l$ and $k \wedge l \geq n_m$. This is a particularly useful feature in fatigue studies requiring long stationary state samples.

The mean $(-z, z)$-outcrossing rate of the steady-state response $Z(t)$ can be approximated by an estimate $\hat{\nu}_{n,m}(z)$ of the mean $(-z, z)$-outcrossing rate of $Z_{n,m}(t)$. This estimate is based on n_s independent samples of $Z_{n,m}(t)$ and has the form

$$\hat{\nu}_{n,m}(z) = \hat{\nu}^-_{n,m}(-z) + \hat{\nu}^+_{n,m}(z), \quad \text{with,} \tag{3.101}$$

$$\hat{\nu}^-_{n,m}(-z) = \frac{1}{n_s\, \Delta t} \sum_{i=1}^{n_s} 1\Big(Z_{n,m}(t, \omega_i) \geq -z, Z_{n,m}(t + \Delta t, \omega_i) < -z \Big) \tag{3.102}$$

$$\hat{\nu}^+_{n,m}(z) = \frac{1}{n_s\, \Delta t} \sum_{i=1}^{n_s} 1\Big(Z_{n,m}(t, \omega_i) \leq z, Z_{n,m}(t + \Delta t, \omega_i) > z \Big) \tag{3.103}$$

where $\Delta t > 0$ is a small time interval and $Z_{n,m}(t, \omega_i)$ represents output sample i of $Z_{n,m}(t, \omega_i)$. The selection of $\Delta t > 0$ has to account for the frequency content of $Z_{n,m}(t)$ to obtain reliable results, a common requirement in simulation. We also note that (1) the $Z_{n,m}(t, \omega_i)$ and $Z_{n,m}(t + \Delta t, \omega_i)$ are on the same output sample and (2) the variance, $E[\hat{\nu}_{n,m}(az)]\, \big(1 - E[\hat{\nu}_{n,m}(z)]\big)/n_s$, of $\hat{\nu}_{n,m}(z)$ vanishes as $n_s \to \infty$, where $E\big[\hat{\nu}_{n,m}(z)\big] = P\big(|Z_{n,m}(t)| \leq z, |Z_{n,m}(t + \Delta t)| > z\big)/\Delta t$.

Numerical examples in [70] show that the local representation in Equation 3.96 is accurate for windows of half size $n = 10$ and even smaller. This observation can be used to develop an efficient Monte Carlo algorithm for generating samples of random function with bandlimited spectral densities. Suppose that a sample $F_n(\cdot, \omega)$ of F_n has been generated up to a time $t = (n_t + 1)\, t^*$. The extension of this sample in the next cell

$[(n_t+1)\,t^*, (n_t+2)\,t^*]$ requires to generate a sample of the conditional random variable

$$F((n_t+n+2)\,t^*) \mid [F((n_t+n+1)\,t^*) = F((n_t+n+1)\,t^*, \omega),$$

$$F((n_t+n)\,t^*) = F((n_t+n)\,t^*, \omega), \ldots] \tag{3.104}$$

accounting for the entire past history. The use of this conditional variable is impractical since its properties have to be recalculated at each new node and depend on a vector of increasing length as time progresses. It is proposed to approximate the conditional random variable in Equation 3.104 by the conditional variable

$$\hat{F}((n_t+n+2)\,t^*)$$

$$= F((n_t+n+2)\,t^*) \mid [F((n_t+n+1)\,t^*) = F((n_t+n+1)\,t^*, \omega), \ldots$$

$$\ldots, F((n_t-n+1)\,t^*) = F((n_t-n+1)\,t^*, \omega)] \tag{3.105}$$

considering only the most recent past history. If F is stationary, the probability law of $\hat{F}((n_t+n+2)\,t^*)$ does not change in time so that it has to be calculated once. If F is a Gaussian process, then $\hat{F}((n_t+n+2)\,t^*)$ is a Gaussian variable with known mean and variance.

The generation of state samples by classical Monte Carlo algorithms involves the generation of input samples $F(s,\omega)$, $s \in [0,t]$, and the calculation of corresponding output samples $Z(s,\omega)$, $s \in [0,t]$, by numerical integration. Both the generation of input time histories and the mapping of input into output samples can be time consuming. In contrast to the proposed method delivering state samples at a specified time t, classical Monte Carlo algorithms deliver entire output time histories.

3.4.2.3 Numerical example:

Numerical results have been obtained for the linear oscillator in Figure 3.36 with $\omega_0 = 8$ rad/sec, $\zeta = 0.3$, $b = c = h = 5$ m, $l = 10$ m, and $m = 5000$ kg, subjected to

the wind drag force $F(t)$ in Equation 3.89 with $\rho_a = 1.2$ kg/m^3, $c_d = 2$, caused by high winds with mean wind velocity $\bar{v} = 20$ m/sec and principal direction $\bar{\theta} = 0$. Figure 2.7 in Section 2.2.2.1 shows the one-sided spectral density function in Equation 2.19 of the fluctuating wind velocity $V(t)$ with frequency band $[0, 10]$ rad/sec so that $\bar{\omega} = 10$ rad/sec. A time $t = 15$ seconds is selected for calculations. We note that the response $Z(t)$ is approximately stationary at $t = 15$ since t exceeds 3 periods, $3(2\pi/\omega_0) \simeq 2.5$ seconds, of the oscillator ([164], Example 5.5).

Figure 3.38 shows histograms of (a) $Z_{n,m}(t)$ for a sampling rate $t^* = 0.3142$

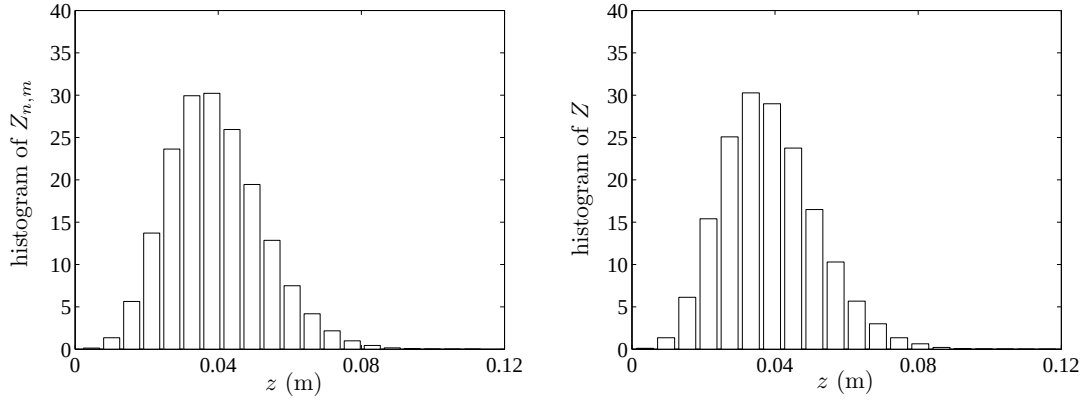

(a) (b)

Figure 3.38: Histogram of $Z(t)$ at $t = 15$: (a) sampling theorem, (b) classical Monte Carlo simulation.

seconds, $n = 10$, and $n_m = [10\,(2\,\pi/\omega_0)/t^*] = 40$ calculated from $n_s = 100,000$ independent samples of this random variable, and (b) $Z(t)$ obtained by classical Monte Carlo simulation based on 100,000 independent samples of the input process $F(t)$ and numerical integration of Equation 3.95 to get samples of $Z(t)$, for $t = 15$ seconds. The estimated mean, variance, skewness, and kurtosis of $Z_{n,m}(t)$ are $\hat{\mu} = 0.0392$, $\hat{\sigma}^2 = 1.73 \times 10^{-4}$, $\hat{\gamma}_3 = 0.4908$, and $\hat{\gamma}_4 = 3.3085$. Figure 3.39 shows time histories of the estimated mean, variance, skewness, and kurtosis of $Z(t)$ obtained by classical Monte Carlo simulation based on 100,000 samples. At $t = 15$ seconds the response

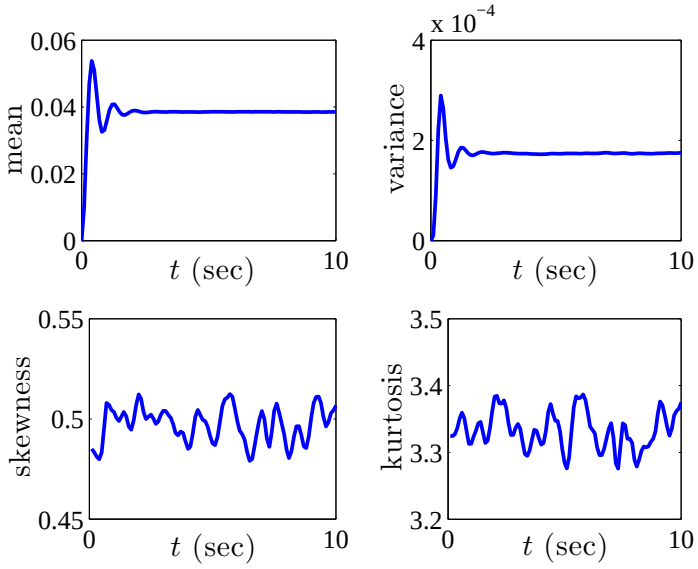

Figure 3.39: Response moments by classical Monte Carlo simulation.

reaches its steady-state as expected, and its estimated mean, variance, skewness, and kurtosis are $\hat{\mu} = 0.0385$, $\hat{\sigma}^2 = 1.75 \times 10^{-4}$, $\hat{\gamma}_3 = 0.5073$, and $\hat{\gamma}_4 = 3.3340$, in agreement with the above results obtained using the sampling theorem. The computation time for generating 100,000 samples of $Z_{n,m}(t)$ and constructing the histogram in Figure 3.38 (a) was 16 seconds on a DELL-GX320 computer with 3GHz CPU and 2GB RAM. On the other hand, the computation time for generating 100,000 samples of $F(t)$ and calculating corresponding samples of $Z(t)$ through numerical integration for constructing the histogram in Figure 3.38 (b) was 7,975 seconds on the same computer, which is, almost 500 times more compared to that from sampling theorem.

Figure 3.40 shows with solid line the estimate $\hat{\nu}^+_{n,m}(z)$ of the mean z-upcrossing rate of $Z_{n,m}(t)$, for $z \geq E[Z(t)]$, obtained by Equation 3.103 using the values of t, t^*, n, n_m and n_s in Figure 3.38 (a). The mean response $E[Z(t)]$ can be approximated by an estimate of the mean $\mu_{n,m}$ of $Z_{n,m}(t)$, $\hat{\mu}_{n,m} = 1/n_s \sum_{i=1}^{n_s} Z_{n,m}(t, \omega_i)$. Figure 3.40 also shows with dotted line estimate of the mean z-upcrossing rates of $Z(t)$ obtained by classical Monte Carlo simulation from the samples in Figure 3.38 (b). The computation

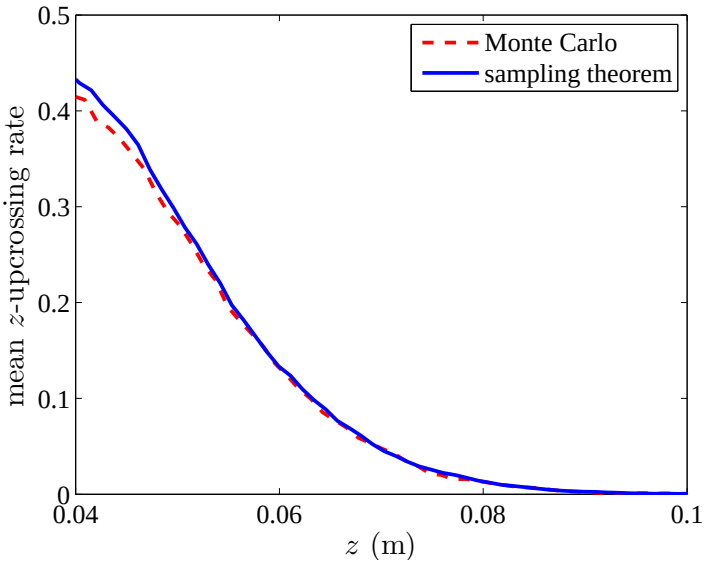

Figure 3.40: Estimates of mean z-upcrossing rates of $Z(t)$ by sampling theorem and classical Monte Carlo simulation.

times for calculating mean crossing rates in Figure 3.40 are 52 and 7,975 seconds using the sampling theorem and classical Monte Carlo simulation, respectively, on a DELL-GX320 computer with 3GHz CPU and 2GB RAM.

The system fragility in Equation 3.91 can be approximated by Equation 3.5 with mean $D = [-z, z]$-outcrossing rate in Equation 3.101 and τ in Equation 2.18. Figure 3.41 shows fragility surface for the linear oscillator in Figure 3.40 located in milepost-150 for the displacement limit state $z = 20$ cm. The wind activity matrix in Figure 2.16 provides realizable values of $(\bar{v}, \bar{\theta})$ at the system site. The change in fragility with respect to the mean wind speed and the principal wind direction is as in Figure 3.37. The failure probabilities of the system with $\omega_0 = 8$ rad/sec in Figure 3.41 are higher than those of the system with $\omega_0 = 15$ rad/sec in Figure 3.37 because the response of the system with $\omega_0 = 15$ rad/sec is quasi-static (see Section 3.4.1) whereas the response of the system with $\omega_0 = 8$ rad/sec is dynamic in nature so that they are larger due to dynamic amplifications.

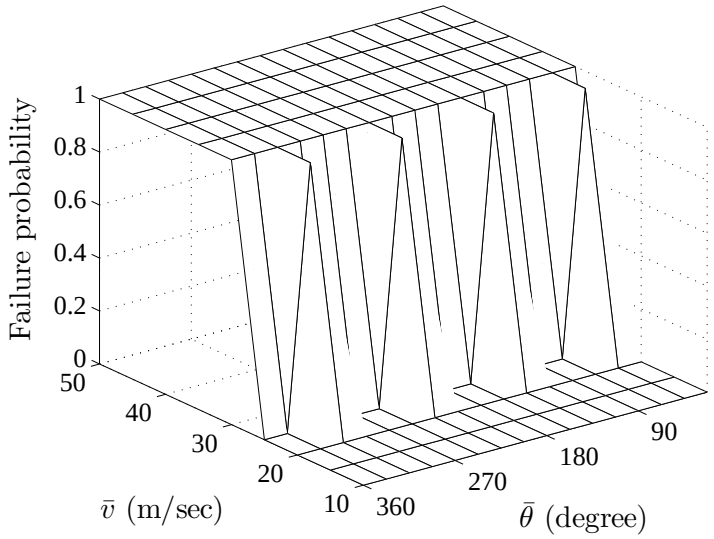

Figure 3.41: Fragility for linear oscillator with $\omega_0 = 8$ rad/sec.

We note that the method presented in this section for characterizing response of linear oscillators to stationary bandlimited processes, based on the sampling theorem and Monte Carlo simulation, can be extended to linear multi degree of freedom system subjected [70].

3.5 Wind and wave fragility

Consider the simple structure in Figure 3.36 and suppose that it is a model of an hypothetical offshore platform in deep waters, for example, a jacket platform, consisting of a deck with dimension b, c and h and a circular column of length l and diameter d_c attaching the deck to the sea-bed so that the submerged length of the column equals the water depth d. Assume that the system is located at a site with possible hurricane activity causing wind loads acting on the deck and wind-induced wave loads acting on the submerged part of the column. In Section 2.2.3 it was shown that the wave hazard at the system site is completely characterized by the mean wind velocity $\bar{v}$, and the

principal wind direction $\bar{\theta}$ at the site. Accordingly, fragility of the system is based on these two parameters completely defining the probability law of all the loads on the system.

The wind activity matrix in Section 2.3.5 provides realizable values of $(\bar{v}, \bar{\theta})$ at a site near the coastline over an open terrain. The respective mean wind speeds over water surface at the system site can be calculated using the similarity model in Section 2.2.2.1 providing a relationship between wind speeds in different surface roughness regimes. Figure 2.8 shows the relationship between hourly mean wind speeds $\bar{v}_1$ over open terrain, and $\bar{v}_2$ over water, at 10 m above the surface. The mean speed is larger over water surface. Hence, the wind activity matrix in Section 2.3.5 can be used for a site over water surface by adjusting the mean wind speeds. In this section $\bar{v}$ denotes the mean hourly speed in meters per second at 10 m above the mean water level.

Wind drag force acting on the deck structure is expressed by Equation 3.89. We represent the total wave force acting on the actual column of the platform by an equivalent force acting on a circular column of unit length with a modified diameter d_c. This assumption is made for purposes of presenting the proposed approach and will be relaxed in Chapter 4. Wave forces acting on the circular column can be modeled by various forms of the Morison equation [121] that disregard or account for flow-structure interaction. Accordingly, the force acting on a section of a pile due to wave motion is made up of a drag force, analogous to the drag force on a body subjected to a steady state of a real fluid associated with wake formation behind the body; and an inertia force, analogous to that on a body subjected to a uniformly accelerated flow of an ideal fluid. The Morison equation carries the implicit assumption that the body size is small relative to the wave length. The noninteractive Morison equation for a cylindrical member of unit length, located near the water surface in deep waters, has the form

$$X(t) = \frac{1}{2} c'_d \rho_w \, d_c \, U^*(t) |U^*(t)| + c_m \rho_w \frac{\pi d_c^2}{4} \dot{U}^*(t) \tag{3.106}$$

in which the first term on the right hand side is the drag force, the second term is the inertia force, ρ_w is the density of water, d_c is the diameter of the cylinder, c'_d and c_m are the drag and inertia coefficients, and $U^*(t) = u_0 + U(t)$ is the total water particle velocity at the water surface obtained from Equation 2.32 using $s = d$ (Figure 2.9), in which u_0 is in Equation 2.31 and $U(t)$ is in Equation 2.24 for $s = d$. $U(t)$ is a stationary Gaussian process with mean zero and one-sided spectral density function in Equation 2.27. The drag and inertia coefficients c'_d and c_m, in Equations 3.106 and 3.107, generally depend on time, Reynolds number, relative displacement of the fluid and some other parameters, and takes on values in the ranges $(0.6, 1.0)$ and $(1.5, 2.0)$, respectively [1]. In this study, although questionable, we use constant values for the drag and inertia coefficients, $c'_d = 1$ and $c_m = 2$, for purposes of illustrating the proposed approach.

The interactive forms of the Morison equation involve time derivatives $\dot{Z}(t)$ and $\ddot{Z}(t)$ of the structural displacement process $Z(t)$. For example, according to the relative velocity model, the wave force for cylindrical members of unit length is

$$X(t) = \frac{1}{2} c'_d \rho_w \, d_c \, [U^*(t) - \dot{Z}(t)] |U^*(t) - \dot{Z}(t)| + c_m \rho_w \frac{\pi d_c^2}{4} \left[\dot{U}^*(t) - (1 - 1/c_m) \ddot{Z}(t) \right]. \tag{3.107}$$

Since the structure's motion is expected to be small compared with the water particle motion for a non-compliant platform, such as the jacket platform model used in this study, the dependence of wave force $X(t)$ on structure motion $Z(t)$ is ignored, and the noninteractive form of the Morison equation in Equation 3.106 is used for analysis. For compliant platforms, which are designed to withstand environmental loads by their ability to deflect from their equilibrium position, the interactive form of the Morison equation in Equation 3.107 should be used for analysis. However, in this case it should be noted that the spectral density of fluctuating wind velocity in Equation 2.19 may result in an overestimation of structural response as it is not suggested for a structure

with a low fundamental frequency of vibration, such as a compliant offshore platform ([154], Section 2.3.3).

The system in Figure 3.36 is modeled by a linear single degree of freedom system whose along-wind displacement response $Z(t)$ to wind and wave loads resulted from a hurricane with mean wind speed $\bar{v}$ blowing in a direction $\bar{\theta}$ satisfies the differential equation

$$m\ddot{Z}(t) + c\dot{Z}(t) + kZ(t) = X(t) + F(t), \quad 0 \leq t \leq \tau, \tag{3.108}$$

with initial conditions $Z(0) = \dot{Z}(0) = 0$, $X(t)$ in Equation 3.106, $F(t)$ in Equation 3.89, and τ in Equation 2.18. In general $Z(t)$ is a non-Gaussian random process with stationary characteristics during the steady-state part of oscillations, since $F(t)$ and $X(t)$ are stationary non-Gaussian processes. We note that for wind flow over water surface the spectral density function of fluctuating wind velocity $V(t)$, in Equation 2.19, is a function of the surface drag coefficient κ in Equation 2.20.

System fragility, that is, the probability that the maximum response $Z_\tau = \max_{0\leq t\leq\tau}(|Z(t)|)$ exceeds a limit state z if the oscillator is subjected to high winds with parameters $(\bar{v}, \bar{\theta})$ is given by Equation 3.91. We estimate the fragility in Equation 3.91 by crossing theory of stochastic processes presented in Section 3.1, and provide (1) an analytical expression for the mean crossing rate of the quasi-static response of the linear oscillator in Figure 3.36 to wave load $X(t)$ in Equation 3.106 and wind load $F(t)$ in Equation 3.89, and (2) an estimation for the mean crossing rate of the dynamic response of the same linear oscillator to the loads $X(t)$ and $F(t)$ based on the sampling theorem and Monte Carlo algorithm, as in Section 3.4.2. For nonlinear systems subjected to wind and wave loads methods based on the classical Monte Carlo algorithm can be used to calculate the system fragility (see Section 3.2).

3.5.1 Quasi-static response

Consider the simple linear oscillator in Equation 3.108 with natural frequency $\omega_0 = \sqrt{k/m}$ much larger that the frequencies of the excitation, that is, $\omega_0 \gg \bar{\omega}$, in which $\bar{\omega} = \max(\bar{\omega}_1, \bar{\omega}_2)$, where $\bar{\omega}_1$ is the cut-off frequency of the spectral density function in Equation 2.19 of fluctuating wind velocity $V(t)$ in Equation 2.18 and $\bar{\omega}_2$ is the cut-off frequency of the spectral density function in Equation 2.27 of fluctuating wave particle velocity $U(t)$ in Equation 2.24. The response of the oscillator is practically proportional to the excitation and is referred to as quasi-static response. In this section we examine the quasi-static response of a simple offshore structure consisting of a cylindrical member of unit submerged depth to the noninteractive form of the Morison equation $X(t)$ in Equation 3.106 and the wind load $F(t)$ in Equation 3.89.

The quasi-static displacement response of the oscillator to $X(t)$ in Equation 3.106 and $F(t)$ in Equation 3.89 is

$$Z(t) = \frac{1}{k}(X(t) + F(t)) = \frac{1}{k}\left[a_1(u_0 + U(t))|u_0 + U(t)| + a_2\dot{U}(t) + a_3(\bar{v} + V(t))^2\right], \tag{3.109}$$

where k is the structural stiffness, $a_1 = (1/2)c'_d\rho_w d_c$, $a_2 = c_m\rho_v(\pi d_c^2)/4$, $a_3 = (1/2)\rho_a c_d a(\bar{\theta})$, u_0 is the current in Equation 2.31, and $V(t)$ and $U(t)$ are stationary Gaussian processes with mean zero and one-sided spectral density functions in Equations 2.19 and 2.27, respectively.

The mean z-upcrossing rate of $Z(t)$, that is, the mean rate at which $Z(t)$ crosses from below a displacement level z, can be obtained from the mean outcrossing rate at which the vector process $\boldsymbol{Y}(t) = \{Y_1(t), Y_2(t), Y_3(t)\}$ leaves the safe domain

$D = \{(y_1, y_2, y_3) : y_1 + y_2 + y_3 < y,\ y_3 \geq 0\}$, in which

$$Y_1(t) = (u_0 + U(t))|u_0 + U(t)|,$$

$$Y_2(t) = a\dot{U}(t),$$

$$Y_3(t) = \beta(\bar{v} + V(t))^2, \tag{3.110}$$

$y = kz/a_1$, $a = a_2/a_1$ and $\beta = a_3/a_1$. The mean D-outcrossing rate of $\boldsymbol{Y}(t)$ is [164]

$$\nu(z)^+ = \int_L d\boldsymbol{y} E[\dot{Y}_n(t)\ +\ |\ \boldsymbol{Y}(t) = \boldsymbol{y}]\, f_{\boldsymbol{Y}}(\boldsymbol{y}), \tag{3.111}$$

in which $\boldsymbol{y} = (y_1, y_2, y_3)$, $f_{\boldsymbol{Y}}(\boldsymbol{y})$ is the first order density of $\boldsymbol{Y}(t)$ and

$$E[\dot{Y}_n(t)\ +\ |\ \boldsymbol{Y}(t) = \boldsymbol{y}] = \int_0^\infty \dot{y}_n f_{\dot{Y}_n\,|\,\boldsymbol{Y}}(\dot{y}_n\,|\,\boldsymbol{y}) d\dot{y}_n \tag{3.112}$$

is the expectation of the positive tail of the projection of $\dot{\boldsymbol{Y}}(t)$ on the exterior normal $\boldsymbol{n} = (1/\sqrt{3}, 1/\sqrt{3}, 1/\sqrt{3})$ to the limit state $L = \{(y_1, y_2, y_3) : y_1 + y_2 + y_3 = y,\ y_3 \geq 0\}$ given that $\boldsymbol{Y}(t) = \boldsymbol{y}$ on L. The conditional density $f_{\dot{Y}_n\,|\,\boldsymbol{Y}}(\dot{y}_n\,|\,\boldsymbol{y})$ in Equation 3.112 can be obtained by differentiating the conditional probability

$$F_{\dot{Y}_n\,|\,\boldsymbol{Y}}(\dot{y}_n\,|\,\boldsymbol{y}) = P[\dot{Y}_n(t) < \dot{y}_n\ |\ Y_1(t) = y_1, Y_2(t) = y_2, Y_3(t) = y_3] \tag{3.113}$$

with respect to $\dot{y}_n$. In Equation 3.113

$$\dot{Y}_n(t) = \frac{1}{\sqrt{3}}[\dot{Y}_1(t) + \dot{Y}_2(t) + \dot{Y}_3(t)], \tag{3.114}$$

in which

$$\dot{Y}_1(t) = 2|u_0 + U(t)|\dot{U}(t),$$

$$\dot{Y}_2(t) = a\ddot{U}(t),$$

$$\dot{Y}_3(t) = 2\beta\dot{V}(t)(\bar{v} + V(t)), \tag{3.115}$$

are the time derivatives of the processes $Y_1(t)$, $Y_2(t)$ and $Y_3(t)$ in Equation 3.110, and $\dot{Y}_n(t)$ is the time derivative of $Y_n(t) = [Y_1(t)+Y_2(t)+Y_2(t)]/\sqrt{3}$. From Equations 3.110, 3.113 and 3.114

$$F_{\dot{Y}_n\,|\,\boldsymbol{Y}}(\dot{y}_n\,|\,\boldsymbol{y}) = P\Bigg[\dot{Y}_1(t) + \dot{Y}_2(t) + \dot{Y}_3(t) < \dot{y}_n\sqrt{3}\,\Bigg|\,(u_0 + U(t))|u_0 + U(t)| = y_1,$$

$$\dot{U}(t) = y_2/a, (\bar{v} + V(t))^2 = y_3/\beta\Bigg]. \tag{3.116}$$

Noting that the first condition implies $|u_0 + U(t)| = \sqrt{|y_1|}$ and using the second condition we have $\dot{Y}_1(t) = 2\sqrt{|y_1|}y_2/a$, also, the third condition implies $\bar{v} + V(t) = \sqrt{y_3/\beta}$ so that $\dot{Y}_3(t) = 2\beta\dot{V}(t)\sqrt{y_3/\beta}$, hence Equation 3.116 becomes

$$F_{\dot{Y}_n\,|\,\boldsymbol{Y}}(\dot{y}_n\,|\,\boldsymbol{y}) = P\Bigg[2\sqrt{|y_1|}y_2/a + a\ddot{U}(t) + 2\beta\dot{V}(t)\sqrt{y_3/\beta} < \dot{y}_n\sqrt{3}\,\Bigg|$$

$$|u_0 + U(t)| = \sqrt{|y_1|}, \dot{U}(t) = y_2/a, \bar{v} + V(t) = \sqrt{y_3/\beta}\Bigg]$$

$$= P\Bigg[\ddot{U}(t) + \frac{2\sqrt{\beta y_3}}{a}\dot{V}(t) < \frac{a\sqrt{3}\dot{y}_n - 2\sqrt{|y_1|}y_2}{a^2}\,\Bigg|$$

$$|u_0 + U(t)| = \sqrt{|y_1|}, \dot{U}(t) = y_2/a, \bar{v} + V(t) = \sqrt{y_3/\beta}\Bigg]$$

$$= P\Bigg[\ddot{U}(t) + \frac{2\sqrt{\beta y_3}}{a}\dot{V}(t) < \frac{a\sqrt{3}\dot{y}_n - 2\sqrt{|y_1|}y_2}{a^2}\,\Bigg|$$

$$|u_0 + U(t)| = \sqrt{|y_1|}\Bigg]. \tag{3.117}$$

The last step follows since U and V are independent processes and a stationary Gaussian process and its time derivative at a given time are independent of each other. Note that

$$|u_0 + U(t)| = \sqrt{|y_1|} \Rightarrow u_0 + U(t) = \frac{y_1}{\sqrt{|y_1|}} \Rightarrow U(t) = \frac{y_1}{\sqrt{|y_1|}} - u_0$$

$$\Rightarrow U(t) = \text{sgn}(y_1)\sqrt{|y_1|} - u_0, \tag{3.118}$$

hence Equation 3.117 becomes

$$F_{\dot{Y}_n\,|\,\boldsymbol{Y}}(\dot{y}_n\,|\,\boldsymbol{y}) = P\Bigg[\ddot{U}(t) + \frac{2\sqrt{\beta y_3}}{a}\dot{V}(t) < \frac{a\sqrt{3}\dot{y}_n - 2\sqrt{|y_1|}y_2}{a^2}\,\Bigg|\, U(t) = \text{sgn}(y_1)\sqrt{|y_1|} - u_0\Bigg]. \tag{3.119}$$

Since $U(t)$ and $V(t)$ are independent of each other we have

$$F_{\dot{Y}_n\,|\,\boldsymbol{Y}}(\dot{y}_n\,|\,\boldsymbol{y}) = \int_{-\infty}^{\infty} P\Bigg[\ddot{U}(t) < \frac{a\sqrt{3}\dot{y}_n - 2\sqrt{|y_1|}y_2}{a^2} - \frac{2\sqrt{\beta y_3}}{a}\,\xi\,\Bigg|\, U(t) = \text{sgn}(y_1)\sqrt{|y_1|} - u_0\Bigg] f_{\dot{V}}(\xi)d\xi, \tag{3.120}$$

where $f_{\dot{V}}(\xi)$ is the first order density of $\dot{V} \sim N(0, \sigma^2_{\dot{V}})$ with $\sigma^2_{\dot{V}} = \int_0^{\bar{\omega}} \omega^2 g_{VV}(\omega)d\omega$ in which $g_{VV}(\omega)$ is given by Equation 2.19, so that $f_{\dot{V}}(\xi) = \phi(\xi/\sigma_{\dot{V}})$ with $\phi(\cdot) =$ density function of standard normal random variable.

Denote by $c(\tau)$ the covariance function of the zero-mean stationary process $U(t)$ so that $c(\tau) = E[U(t)U(t+\tau)]$, $c'(\tau) = E[U(t)\dot{U}(t+\tau)] = E[\dot{U}(t)U(t-\tau)]$ and $c''(\tau) = -E[\dot{U}(t)\dot{U}(t-\tau)]$. Note that $c''(0) = -E[\dot{U}^2(t)] = -\sigma^2_{\dot{U}}$. From $c'(\tau) = E[U(t)\dot{U}(t+\tau)]$ we can also write $c''(\tau) = E[U(t)\ddot{U}(t+\tau)]$ so that $E[U(t)\ddot{U}(t)] = c''(0) = -\sigma^2_{\dot{U}}$. Then,

$$\begin{bmatrix} U(t) \\ \dot{U}(t) \\ \ddot{U}(t) \end{bmatrix} = N\left(\mathbf{0}, \begin{bmatrix} \sigma^2_U & 0 & -\sigma^2_{\dot{U}} \\ 0 & \sigma^2_{\dot{U}} & 0 \\ -\sigma^2_{\dot{U}} & 0 & \sigma^2_{\ddot{U}} \end{bmatrix}\right)$$

$$\Rightarrow \begin{bmatrix} \ddot{U}(t) \\ U(t) \end{bmatrix} = N\left(\mathbf{0}, \begin{bmatrix} \sigma^2_{\ddot{U}} & -\sigma^2_{\dot{U}} \\ -\sigma^2_{\dot{U}} & \sigma^2_U \end{bmatrix}\right), \tag{3.121}$$

hence $\ddot{U}|U = u \sim N\left(-(\sigma^2_{\dot{U}}/\sigma^2_U)u, \sigma^2_{\ddot{U}} - (-\sigma^2_{\dot{U}})^2/\sigma^2_U\right)$, where $\sigma^2_U = \int_0^{\bar{\omega}} g_{UU}(\omega)d\omega$, $\sigma^2_{\dot{U}} = \int_0^{\bar{\omega}} \omega^2 g_{UU}(\omega)d\omega$ and $\sigma^2_{\ddot{U}} = \int_0^{\bar{\omega}} \omega^4 g_{UU}(\omega)d\omega$ are the variances of U, $\dot{U}$ and $\ddot{U}$,

respectively, and $g_{UU}(\omega)$ is given by Equation 2.27. As a result,

$$P\left[\ddot{U}(t) < \frac{a\sqrt{3}\dot{y}_n - 2\sqrt{|y_1|}y_2 - 2a\xi\sqrt{\beta y_3}}{a^2}\,\middle|\, U(t) = \text{sgn}(y_1)\sqrt{|y_1|} - u_0\right],$$

in Equation 3.120, becomes $\Phi\left((a\sqrt{3}\dot{y}_n - b)/c\right)$ for

$$b(\xi) = 2\sqrt{|y_1|}y_2 + 2a\xi\sqrt{\beta y_3} - a^2(\sigma_{\dot{U}}^2/\sigma_U^2)(\text{sgn}(y_1)\sqrt{|y_1|} - u_0),$$

$$c = a^2\left(\sigma_{\ddot{U}}^2 - \sigma_{\dot{U}}^4/\sigma_U^2\right)^{1/2}, \tag{3.122}$$

so that

$$F_{\dot{Y}_n\,|\,\boldsymbol{Y}}(\dot{y}_n\,|\,\boldsymbol{y}) = \int_{-\infty}^{\infty} \Phi\left(\frac{a\sqrt{3}\dot{y}_n - b(\xi)}{c}\right)\phi\left(\frac{\xi}{\sigma_{\dot{Y}}}\right)d\xi, \tag{3.123}$$

with $b(\xi)$ and c in Equation 3.122. Then

$$\begin{aligned} f_{\dot{Y}_n\,|\,\boldsymbol{Y}}(\dot{y}_n\,|\,\boldsymbol{y}) &= \frac{d}{d\dot{y}_n}F_{\dot{Y}_n\,|\,\boldsymbol{Y}}(\dot{y}_n\,|\,\boldsymbol{y}) \\ &= \frac{a\sqrt{3}}{c}\int_{-\infty}^{\infty}\phi\left(\frac{a\sqrt{3}\dot{y}_n - b(\xi)}{c}\right)\phi\left(\frac{\xi}{\sigma_{\dot{Y}}}\right)d\xi, \end{aligned} \tag{3.124}$$

and Equation 3.112 becomes

$$E[\dot{Y}(t)\ +\ |\,\boldsymbol{Y}(t) = \boldsymbol{y}] = \frac{a\sqrt{3}}{c}\int_0^{\infty}\dot{y}_n\int_{-\infty}^{\infty}\phi\left(\frac{a\sqrt{3}\dot{y}_n - b(\xi)}{c}\right)\phi\left(\frac{\xi}{\sigma_{\dot{Y}}}\right)d\xi d\dot{y}_n. \tag{3.125}$$

For $q = a\sqrt{3}\dot{y}_n$ Equation 3.125 becomes

$$E[\dot{Y}(t)\ +\ |\,\boldsymbol{Y}(t) = \boldsymbol{y}] = \frac{1}{a\sqrt{3}}\int_{-\infty}^{\infty}\left(\int_0^{\infty}\frac{q}{c}\phi\left(\frac{q - b(\xi)}{c}\right)dq\right)\phi\left(\frac{\xi}{\sigma_{\dot{Y}}}\right)d\xi, \tag{3.126}$$

in which

$$\int_0^\infty \frac{q}{c}\phi\left(\frac{q-b(\xi)}{c}\right)dq = \int_0^\infty q\frac{1}{\sqrt{2\pi}c}\exp\left(-\frac{(q-b(\xi))^2}{2c^2}\right)dq$$

$$= \left[\int_0^\infty \frac{(q-b(\xi))}{\sqrt{2\pi}c}\exp\left(-\frac{(q-b(\xi))^2}{2c^2}\right)dq + \int_0^\infty \frac{b(\xi)}{\sqrt{2\pi}c}\exp\left(-\frac{(q-b(\xi))^2}{2c^2}\right)dq\right]$$

$$= \left[-c\frac{1}{\sqrt{2\pi}}\exp\left(-\frac{(q-b(\xi))^2}{2c^2}\right)\Big|_0^\infty + b(\xi)\int_0^\infty \phi\left(\frac{q-b(\xi)}{c}\right)dq\right]$$

$$= \left[-c\phi\left(\frac{q-b(\xi)}{c}\right)\Big|_0^\infty + b(\xi)\left(\int_{-\infty}^\infty \phi\left(\frac{q-b(\xi)}{c}\right)dq - \int_{-\infty}^0 \phi\left(\frac{q-b(\xi)}{c}\right)dq\right)\right]$$

$$= \left(-c\left[\phi(\infty) - \phi(-b(\xi)/c)\right] + b(\xi)\left[1-\Phi(-b(\xi)/c)\right]\right)$$

$$= \left[c\phi\left(\frac{b(\xi)}{c}\right) + b(\xi)\Phi\left(\frac{b(\xi)}{c}\right)\right], \tag{3.127}$$

so that Equation 3.127 becomes

$$E[\dot{Y}(t)\ +\ |\ \boldsymbol{Y}(t)=\boldsymbol{y}] = \frac{1}{a\sqrt{3}}\int_{-\infty}^\infty \left[c\phi\left(\frac{b(\xi)}{c}\right) + b(\xi)\Phi\left(\frac{b(\xi)}{c}\right)\right]\phi\left(\frac{\xi}{\sigma_{\dot{Y}}}\right)d\xi, \tag{3.128}$$

with $b(\xi)$ and c in Equation 3.122.

The first order density $f_{\boldsymbol{Y}}(\boldsymbol{y})$ of $\boldsymbol{Y}(t)$, in the mean crossing rate expression given by Equation 3.111, is obtained by differentiating the first order probability

$$F_{\boldsymbol{Y}}(\boldsymbol{y}) = P[\boldsymbol{Y}(t) < \boldsymbol{y}] = P[Y_1(t) < y_1, Y_2(t) < y_2, Y_3(t) < y_3]$$

$$= P[Y_1(t) < y_1]P[Y_2(t) < y_2]P[Y_3(t) < y_3] \tag{3.129}$$

with respect to y_1, y_2 and y_3. The last step in Equation 3.129 follows since the random variables $Y_1(t)$, $Y_2(t)$ and $Y_3(t)$ in Equation 3.110 are independent of each other at time t. Accordingly,

$$f_{\boldsymbol{Y}}(\boldsymbol{y}) = \frac{\partial^3 F_{\boldsymbol{Y}}(\boldsymbol{y})}{\partial y_1 \partial y_2 \partial y_3} = f_{Y_1}(y_1)f_{Y_2}(y_2)f_{Y_3}(y_3), \tag{3.130}$$

where the first order density function of $Y_1(t)$ is

$$
\begin{aligned}
f_{Y_1}(y_1) &= \frac{d}{dy_1} P[Y_1(t) < y_1] = \frac{d}{dy_1} P[U^*(t)|U^*(t)| < y_1] \\
&= \frac{d}{dy_1} P[U^*(t) < \text{sgn}(y_1)\sqrt{|y_1|}] = \frac{d}{dy_1} P[U(t) < \text{sgn}(y_1)\sqrt{|y_1|} - u_0] \\
&= \frac{d}{dy_1} \Phi\left(\frac{\text{sgn}(y_1)\sqrt{|y_1|} - u_0}{\sigma_U}\right) \\
&= \frac{d}{dy_1}\left(\frac{\text{sgn}(y_1)\sqrt{|y_1|}}{\sigma_U}\right) \frac{1}{\sqrt{2\pi}} \exp\left[-\frac{1}{2}\left(\frac{\text{sgn}(y_1)\sqrt{|y_1|} - u_0}{\sigma_U}\right)^2\right] \\
&= \begin{cases} \dfrac{d\sqrt{y_1}}{dy_1} \dfrac{1}{\sigma_U\sqrt{2\pi}} \exp(\ldots) = \dfrac{1}{2\sqrt{y_1}\sigma_U\sqrt{2\pi}} \exp(\ldots); & y_1 > 0, \\ \dfrac{d(-\sqrt{-y_1})}{dy_1} \dfrac{1}{\sigma_U\sqrt{2\pi}} \exp(\ldots) = \dfrac{1}{2\sqrt{-y_1}\sigma_U\sqrt{2\pi}} \exp(\ldots); & y_1 < 0, \end{cases} \\
&= \frac{1}{2\sigma_U\sqrt{2\pi|y_1|}} \exp\left[-\frac{1}{2}\left(\frac{\text{sgn}(y_1)\sqrt{|y_1|} - u_0}{\sigma_U}\right)^2\right], \qquad (3.131)
\end{aligned}
$$

the first order density function of $Y_2(t)$ is

$$
\begin{aligned}
f_{Y_2}(y_2) &= \frac{d}{dy_2} P[Y_2(t) < y_2] = \frac{d}{dy_2} P[a\dot{U}(t) < y_2] = \frac{d}{dy_2} \Phi\left(\frac{y_2/a}{\sigma_{\dot{U}}}\right) \\
&= \frac{1}{a\sigma_{\dot{U}}} \phi\left(\frac{y_2}{a\sigma_{\dot{U}}}\right), \qquad (3.132)
\end{aligned}
$$

and the first order density function of $Y_3(t)$ is (Section 3.4.1)

$$
\begin{aligned}
f_{Y_3}(y_3) &= \frac{d}{dy_3} P[Y_3(t) < y_3] = \frac{d}{dy_3} P[\beta(\bar{v} + V(t))^2 < y_3] \\
&= \frac{1}{\beta\sigma_V^2} f(y_3/(\beta\sigma_V^2), 1, \bar{v}^2/\sigma_V^2) \qquad (3.133)
\end{aligned}
$$

in which $f(\eta, m, \lambda)$ is the noncentral chi-square density with degree of freedom m and non-centrality parameter λ.

The mean z-upcrossing rate of $Z(t)$ in Equation 3.111 can now be written as, using Equation 3.128 and Equation 3.130,

$$\nu(z)^+ = \frac{1}{a\sqrt{3}} \int_L ds f_{Y_1}(y_1) f_{Y_2}(y_2) f_{Y_3}(y_3) \left\{ \int_{-\infty}^{\infty} \left[c\phi\left(\frac{b(\xi)}{c}\right) + b(\xi)\Phi\left(\frac{b(\xi)}{c}\right)\right] \phi\left(\frac{\xi}{\sigma_{\dot{V}}}\right) d\xi \right\}, \quad (3.134)$$

where ds is an area element on the plane defined by $L = \{(y_1, y_2, y_3) : y_1 + y_2 + y_3 = y,\, y_3 \geq 0\}$. Note that for a continuous function $h(y_1, y_2, y_3)$ on the plane L in Equation 3.134, we have

$$\int_L h(y_1, y_2, y_3) ds = \sqrt{3} \int_{-\infty}^{\infty} dy_1 \int_0^{\infty} dy_3\, h(y_1, y - y_1 - y_3, y_3), \quad (3.135)$$

$$= \sqrt{3} \int_{-\infty}^{\infty} dy_2 \int_0^{\infty} dy_3\, h(y - y_2 - y_3, y_2, y_3), \quad (3.136)$$

$$= \sqrt{3} \int_{-\infty}^{\infty} dy_1 \int_{-\infty}^{y-y_1} dy_2\, h(y_1, y_2, y - y_1 - y_2). \quad (3.137)$$

We can integrate the right-hand sides of Equations 3.135-3.137 numerically to obtain $\int_L h(y_1, y_2, y_3) ds$. We use Equation 3.135 for numerical integration as it provides more accurate results with shorter computational times for the function $h(y_1, y_2, y_3)$ and domain L used in this problem. Accordingly, Equation 3.134 becomes

$$\nu(z)^+ = \frac{1}{a} \int_{-\infty}^{\infty} dy_1 f_{Y_1}(y_1) \int_0^{\infty} dy_3 f_{Y_3}(y_3) f_{Y_2}(y - y_1 - y_3) \left\{ \int_{-\infty}^{\infty} \left[c\phi\left(\frac{b(\xi)}{c}\right) + b(\xi)\Phi\left(\frac{b(\xi)}{c}\right)\right] \phi\left(\frac{\xi}{\sigma_{\dot{V}}}\right) d\xi \right\}, \quad (3.138)$$

with b, c in Equation 3.122 for $y_2 = y - y_1 - y_3$, $f_{Y_1}(y_1)$, $f_{Y_2}(y_2)$ and $f_{Y_3}(y_3)$ in Equations 3.131-3.133, and $\sigma_{\dot{V}} = \int_0^{\infty} \omega^2 g_{VV}(\omega) d\omega$, in which $g_{VV}(\omega)$ is given by Equation 2.19. Equation 3.138 is used to calculate the mean z-upcrossing rate of $Z(t)$ in Equation 3.111.

Consider the system in Figure 3.36 consisting of a deck located at 10 m above the water surface with mass $m = 1000$ kg and $b = c = h = 2$ m, and a circular

column of unit length with diameter $d_c = 0.5$ m. The natural frequency of the system is $\omega_0 = 15$ rad/sec. Suppose that high winds with mean wind velocity $\bar{v} = 20$ m/sec and principal direction $\bar{\theta} = 0$ prevail at the system site resulting in wind and wave drag forces $F(t)$ and $X(t)$ in Equations 3.89 and 3.106 with $\rho_a = 1.2$ kg/m^3, $c_d = 2$, $\rho_w = 1000$ kg/m^3, $c_d' = 1$, $c_m = 2$, and current velocity $u_0 = 0.025\bar{v}$. Figure 3.42 shows the one-sided spectral density functions in Equations 2.19 and 2.27

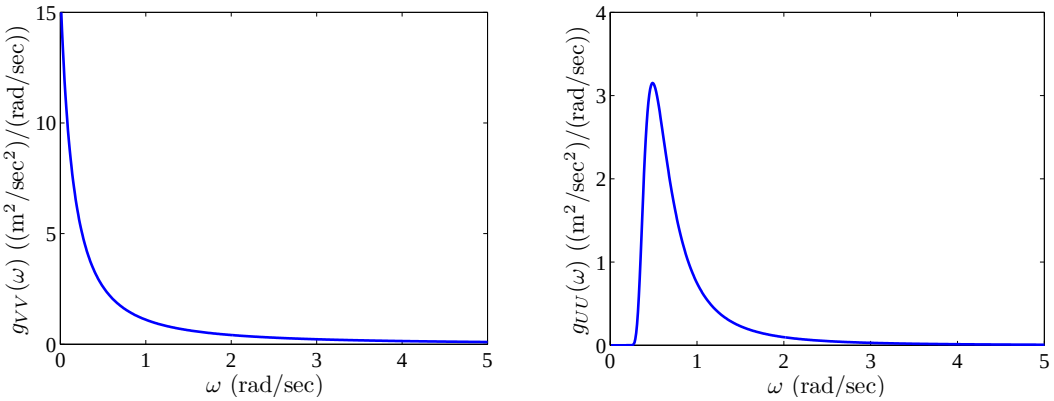

(a) (b)

Figure 3.42: Spectral density functions of (a) $V(t)$, (b) $U(t)$.

of (a) the fluctuating wind velocity $V(t)$ and (b) the water particle velocity $U(t)$. We note that the spectral density of the wind velocity is based on κ in Equation 2.20 for wind flow over water surface. The natural frequency of the system $\omega_0 = 15$ rad/sec is much larger that the frequencies of the excitation so that the response $Z(t)$ of the oscillator in Equation 3.108 will be quasi-static and given by Equation 3.109, where $k = \omega_0^2 m$ is the system stiffness. Figure 3.43 shows the marginal density functions $f_{Y_1}(y_1)$, $f_{Y_2}(y_2)$ and $f_{Y_3}(y_3)$, of Y_1, Y_2 and Y_3 in Equations 3.131-3.133, respectively, and histograms of these random variables calculated from $n_s = 100,000$ independent samples of $V(t)$ and $U(t)$ and Equation 3.110. Samples of $V(t)$ and $U(t)$ are obtained following the method presented in Section 2.4.1 using their spectral density functions in Equations 2.19 and 2.27, respectively. Figure 3.44 shows the mean z-upcrossing

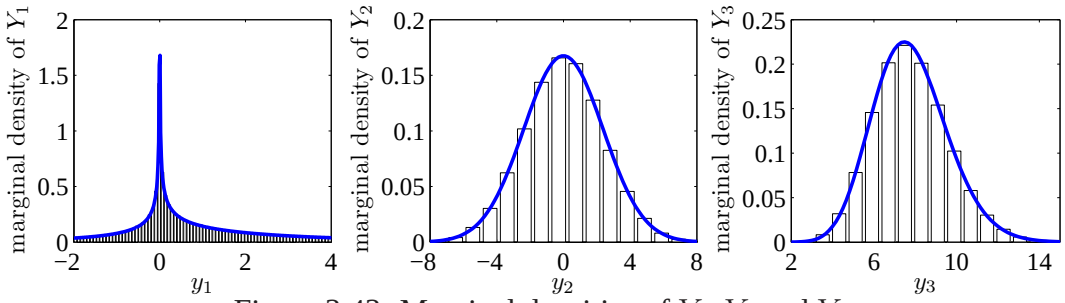

Figure 3.43: Marginal densities of Y_1, Y_2 and Y_3.

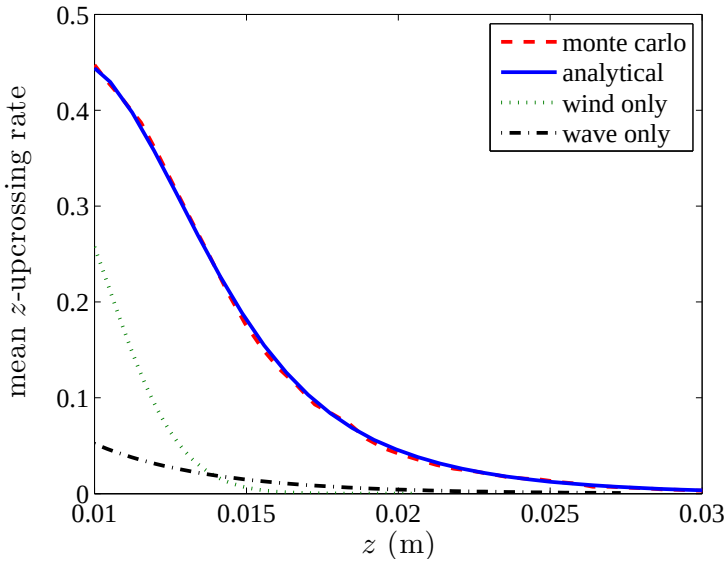

Figure 3.44: Mean upcrossing rate of quasi-static response.

rate of the response $Z(t)$ obtained by Equation 3.138 and estimated by Monte Carlo simulation using Equation 3.109 and $n_s = 100,000$ independent samples of $V(t)$ and $U(t)$ with $dt = 0.1$. Figure 3.44 also shows the mean z-upcrossing rate of the response $Z(t)$ if subjected to wind load $F(t)$ only, and to wave load $X(t)$ only, which can be calculated from Equations 3.93 and following the procedure in Section 3.5.1 for $a_3 = 0$ in Equation 3.109, respectively.

An approximation for the mean crossing rate from the statistical linearization method

The method has been applied extensively to analyze complex dynamic systems, particularly for the estimation of the second-moment descriptors of the response, for example, the mean and variance [145, 163]. Accordingly, the mean z-upcrossing rate Equation 3.138 can be approximated from a linearized representation of the quasi-static displacement response $Z(t)$ in Equation 3.109 of the oscillator, for example,

$$Z_L(t) = \frac{1}{k}\left[a_1 d_u U^*(t) + a_2 \dot{U}^*(t) + a_3 d_v V^*(t)\right], \tag{3.139}$$

in which $U^*(t) = u_0 + U(t)$, $\dot{U}^*(t) = \dot{U}(t)$, $V^*(t) = \bar{v} + V(t)$, and d_u and d_v are linearized wave and wind drag factors, respectively, calculated by means of equivalent linearization techniques [16]. In the case of wave drag the nonlinear term $U^*(t)|U^*(t)|$ in Equation 3.109 is replaced with a linear term $d_u U^*(t)$ such that the linearized drag factor d_u minimizes the mean squared error $E[(d_u U^*(t) - U^*(t)|U^*(t)|)^2]$, which yields,

$$d_u = \frac{E[(U^*(t))^2|U^*(t)|]}{E[(U^*(t))^2]}. \tag{3.140}$$

Since $U^*(t) = u_0 + U(t)$ is a Gaussian process with mean u_0 and variance σ_U^2 we can obtain $E[(U^*(t))^2|U^*(t)|] = (4\sigma_U^3 + 2\sigma_U u_0^2)\phi(u_0/\sigma_U) + (3\sigma_U^2 u_0 + u_0^3)(2\Phi(u_0/\sigma_U) - 1)$. Hence Equation 3.140 becomes

$$d_u = \frac{(4\sigma_U^3 + 2\sigma_U u_0^2)\,\phi\left(\frac{u_0}{\sigma_U}\right) + (3\sigma_U^2 u_0 + u_0^3)\left[2\Phi\left(\frac{u_0}{\sigma_U}\right) - 1\right]}{\sigma_U^2 + u_0^2}. \tag{3.141}$$

Similarly, we can obtain d_v by minimizing the mean squared error $E[(d_v V^*(t) - (V^*(t))^2]$, which yields,

$$d_v = \frac{3\sigma_V^2 \bar{v} + \bar{v}^3}{\sigma_V^2 + \bar{v}^2}. \tag{3.142}$$

Since $U(t)$ and $V(t)$ are stationary Gaussian processes, $Z_L(t)$ is also a stationary Gaussian process with mean z-upcrossing rate

$$\nu^{(L)}(z)^+ = \frac{\sigma_{\dot{Z}_L}}{\sigma_{Z_L}} \frac{1}{\sqrt{2\pi}} \phi\left(\frac{z - \mu_{Z_L}}{\sigma_{Z_L}}\right) = \frac{1}{2\pi}\frac{\sigma_{\dot{Z}_L}}{\sigma_{Z_L}} \exp\left(-\frac{(z - \mu_{Z_L})^2}{2\sigma_{Z_L}^2}\right), \tag{3.143}$$

in which the mean and variance of $Z_L(t)$, and the variance of $\dot{Z}_L(t)$, respectively, are

$$\mu_{Z_L} = E[Z_L(t)] = \frac{1}{k}(a_1 d_u u_0 + a_3 d_v \bar{v}),$$

$$\sigma^2_{Z_L} = Var[Z_L(t)] = \frac{1}{k^2}\Big((a_1 d_u \sigma_U)^2 + (a_2 \sigma_{\dot{U}})^2 + (a_3 d_v \sigma_V)^2\Big),$$

$$\sigma^2_{\dot{Z}_L} = Var[\dot{Z}_L(t)] = \frac{1}{k^2}\Big((a_1 d_u \sigma_{\dot{U}})^2 + (a_2 \sigma_{\ddot{U}})^2 + (a_3 d_v \sigma_{\dot{V}})^2\Big), \qquad (3.144)$$

with d_u and d_v in Equations 3.141 and 3.142, and σ^2_U, $\sigma^2_{\dot{U}}$ and $\sigma^2_{\dot{V}}$ are the variances of U, $\dot{U}$ and V, respectively, and can be calculated from their respective spectral density functions. We note that (1) $E[U(t)V(t)] = E[U(t)]E[V(t)] = 0$ since $U(t)$ and $V(t)$ are zero-mean processes that are independent of each other, and (2) $E[U(t)\dot{U}(t)] = E[U(t)]E[\dot{U}(t)]$ and $E[\dot{U}(t)\ddot{U}(t)] = E[\dot{U}(t)]E[\ddot{U}(t)]$ since a stationary Gaussian process and its time derivative are independent of each other at a given time [164].

The mean z-upcrossing rate in Equation 3.143 of the linearized response $Z_L(t)$ can be used to approximate the mean z-upcrossing rate in Equation 3.138 of $Z(t)$ in Equation 3.109. Figure 3.45 shows the ratio of mean z-upcrossing rate in Equation 3.138 of the response $Z(t)$ in Equation 3.109 to that of the linearized response $Z_L(t)$ given by Equation 3.143. The ratio of the mean crossing rates show that the linear approximation can underestimate significantly the peak response. The standardized threshold $\tilde{z}$ in Figure 3.45 is measured in standard deviation units from the mean and is given by

$$\tilde{z} = \frac{z - \mu_Z}{\sigma_Z}\,, \qquad (3.145)$$

where z is the specified crossing level for the displacement response $Z(t)$ in Equation 3.109, and mean and variance of $Z(t)$ are

$$\mu_Z = E[Z(t)] = E\left[\frac{a_1}{k}(Y_1(t) + Y_2(t) + Y_3(t))\right] = \frac{a_1}{k}(\mu_{Y_1} + \mu_{Y_3})$$

$$\sigma^2_Z = Var[Z(t)] = \left(\frac{a_1}{k}\right)^2 \left(\sigma^2_{Y_1} + \sigma^2_{Y_2} + \sigma^2_{Y_3}\right), \qquad (3.146)$$

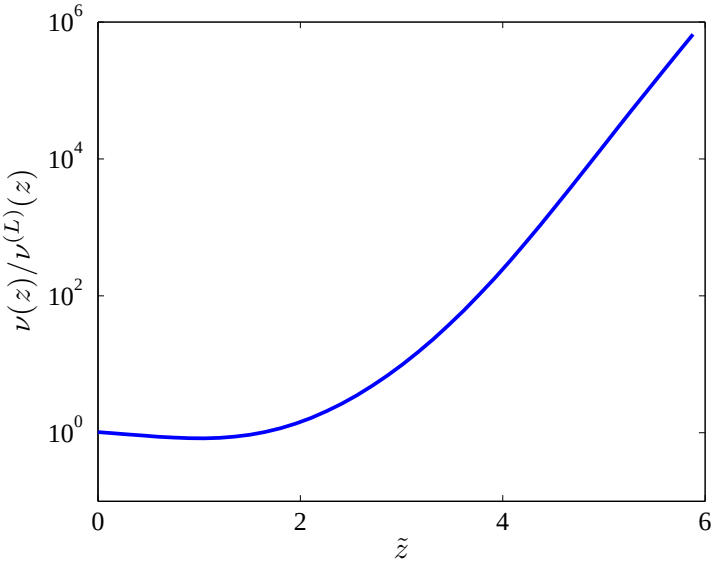

Figure 3.45: Ratio of the exact to approximate mean crossing rates.

respectively. In Equation 3.146 μ_{Y_i} and $\sigma^2_{Y_i}$ are the mean and variance of $Y_i(t)$, $i = 1, 2, 3$, respectively, and can be calculated in closed form using the corresponding marginal density function $f_{Y_i}(y_i)$ in Equations 3.131, 3.132, 3.132, for $i = 1, 2, 3$. Accordingly, $\mu_{Y_1} = (\sigma_U^2 + u_0^2)\,[2\Phi\,(u_0/\sigma_U) - 1] + 2\sigma_U u_0 \phi\,(u_0/\sigma_U)$, $\sigma^2_{Y_1} = (3\sigma_U^4 + 6\sigma_U^2 u_0^2 + u_0^4) - \mu^2_{Y_1}$, $\mu_{Y_2} = 0$, $\sigma^2_{Y_2} = a^2\sigma^2_{\dot{U}}$, $\mu_{Y_3} = \beta\sigma_V^2(1 + \bar{v}^2/\sigma_V^2)$ and $\sigma^2_{Y_3} = 2(\beta\sigma_V^2)^2(1+2\bar{v}^2/\sigma_V^2)$. Figure 3.45 shows that the difference between the mean crossing rates $\nu(z)^+$ and $\nu_L(z)^+$ increases with the threshold and can be significant for large values of the threshold. Thus statistical linearization method should not be applied to estimate the peak response. The large errors in statistical linearization are primarily caused by the implicit assumption in this method that the response is a Gaussian process. A possible use of the method could be in fatigue studies involving exceedings of relatively low thresholds.

The system fragility in Equation 3.91, that is, the probability that the maximum quasi-static response exceeds a limit state $z \geq \mu_Z$ if the oscillator is subjected to high winds and wind-induced waves with specified parameters, can be approximated

by Equation 3.5 with τ from Equation 2.18 and mean $D = [-z, z]$-outcrossing rate $\nu_D = \nu(z)^+ + \nu(-z)^-$, in which $\nu(z)^+$ is given by Equation 3.93 and $\nu(-z)^-$ can be simply obtained by replacing y with $-y$ in Equation 3.93 and changing $b(\xi)$ accordingly. If the limit state z is less than the mean response μ_Z then $P[(\boldsymbol{Z}(0) \in D)]$ in Equation 3.3 becomes zero so that system fragility in Equation 3.5 becomes 1.

Figure 3.46 shows fragility surface for the linear oscillator in Figure 3.44 located

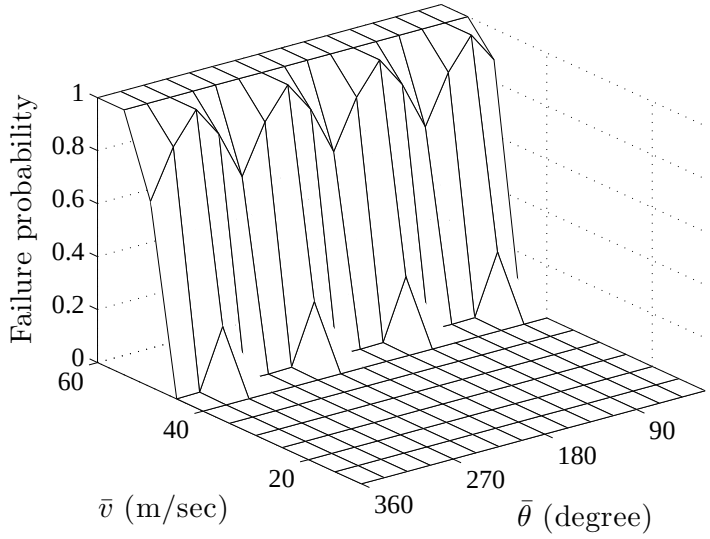

Figure 3.46: Fragility for linear oscillator with $\omega_0 = 15$ rad/sec.

near milepost-150 for the displacement limit state $z = 20$ cm. The wind activity matrix in Figure 2.16 provides realizable values of $(\bar{v}, \bar{\theta})$ at the milepost. We calculate corresponding values of $\bar{v}$ over the sea surface using Figure 2.8. As expected system fragility increases with increasing wind speed. The periodic change in fragility along the $\bar{\theta}$-axis results from the assumed shape of the structure (Figure 3.36). The exposed area $a(\bar{\theta})$ in Equation 3.89 becomes largest at 45, 135, 225 and 315 degrees, resulting in higher wind loading, hence increased fragility. The wind direction has no effect on the wave loads acting on this structure since the column attaching the deck to sea-bed has a circular cross-section.

3.5.2 Dynamic response

Consider the same oscillator in Section 3.5.1, but this time with a natural frequency ω_0 such that its response to $X(t) + F(t)$, with $X(t)$ in Equation 3.106 and $F(t)$ in Equation 3.89, is dynamic. The equation of motion for the oscillator in Equation 3.108 can alternatively be given by

$$\ddot{Z}(t) + 2\zeta\omega_0\dot{Z}(t) + \omega_0^2 Z(t) = \frac{1}{m}\left(F(t) + X(t)\right), \quad 0 \leq t \leq \tau, \tag{3.147}$$

where $\omega_0^2 = k/m$, $\zeta = c/(2m\omega_0)$ and τ in Equation 2.18.

This section develops probabilistic characteristics of the steady-state response $Z(t)$ calculated by the sampling theorem and Monte Carlo simulation presented in Section 3.4.2. Results obtained by the sampling theorem are compared with (1) the exact results obtained by classical Monte Carlo simulation, and (2) approximate results based on the statistical linearization of the load processes.

3.5.2.1 Method based on the classical Monte Carlo simulation:

The classical Monte Carlo simulation method presented in Section 3.4.2.1 is used here for characterizing the response process. We note that the first step in Section 3.4.2.1 should also involve generation of realization of $U(t)$ and $\dot{U}(t)$ from

$$U(t) = \sum_{i=1}^{n} \sigma_i \left[A_i \cos(\omega_i t) + B_i \sin(\omega_i t)\right] \tag{3.148}$$

$$\dot{U}(t) = \sum_{i=1}^{n} \omega_i \sigma_i \left[-A_i \sin(\omega_i t) + B_i \cos(\omega_i t)\right], \tag{3.149}$$

respectively, where A_i and B_i are independent zero-mean, unit variance Gaussian variables and σ_i^2 is the variance associated with the frequency ω_i, $i = 1, \ldots, n$, obtained from the spectral density function of $U(t)$ given by Equation 2.27 (Section 2.4.1). In the second step, we perform deterministic dynamic analyses to determine the response in $(0, \tau)$ to the samples of $F(t)$ in Equation 3.89 and $X(t)$ in Equation 3.106 obtained

from the samples in step-1. The last step involves the estimation of mean, variance and mean upcrossing rates of the response process from the calculated response samples.

3.5.2.2 Method based on the sampling theorem:

The sampling theorem method [70] presented in Section 3.4.2.2 is used here for calculating statistics of the state of the linear system in Equation 3.147 subjected to stationary bandlimited non-Gaussian process $F(t)+X(t)$, with $X(t)$ in Equation 3.106 and $F(t)$ in Equation 3.89. The bandwidth $[0,\bar{\omega}]$ of $F(t)+X(t)$ is defined by $\bar{\omega}=\max(\bar{\omega}_1,\bar{\omega}_2)$, where $\bar{\omega}_1$ is the cut-off frequency of the spectral density function in Equation 2.19 of fluctuating wind velocity $V(t)$ in Equation 2.18 and $\bar{\omega}_2$ is the cut-off frequency of the spectral density function in Equation 2.27 of fluctuating wave particle velocity $U(t)$ in Equation 2.24. The system output at a time t is approximated by a finite sum of deterministic functions of t with random coefficients given by equally spaced values of the input process over a window of finite width centered on t. The number of terms in the sum depends on both input and system memory.

Consider the following approximation to $F(t)+X(t)$ in Equation 3.147 obtained by the sampling theorem [70]

$$(F(t)+X(t))_n=\sum_{k=n_t-n}^{n_t+n+1}(F(k\,t^*)+X(k\,t^*))\,\alpha_k(t;t^*),\quad t\in[n_t\,t^*,(n_t+1)\,t^*],\tag{3.150}$$

with the notation in Equation 3.96. The approximate system state $Z_{n,m}(t)$ at time t corresponding to $(F(t)+X(t))_n$ in Equation 3.150 has the expression

$$\begin{aligned}Z_{n,m}(t)=&\sum_{k=n_t-n_m}^{n_t-1}\sum_{i=k-n}^{k+n+1}\left[\int_{0\vee k\,t^*}^{0\vee(k+1)\,t^*}\phi(t-s)\,\alpha_i(s;t^*)\,ds\right](F(i\,t^*)+X(i\,t^*))\\&+\sum_{i=n_t-n}^{n_t+n+1}\left[\int_{n_t\,t^*}^{t}\phi(t-s)\,\alpha_i(s;t^*)\,ds\right](F(i\,t^*)+X(i\,t^*))\end{aligned}\tag{3.151}$$

with the notation in Equation 3.99. The mean $(-z,z)$-outcrossing rate of the steady-state response $Z(t)$ in Equation 3.147 can be approximated by an estimate $\hat{\nu}_{n,m}(z)$ of

the mean $(-z, z)$-outcrossing rate of $Z_{n,m}(t)$ in Equation 3.99, which has the form in Equation 3.101.

3.5.2.3 Method based on the statistical linearization:

The statistical linearization method presented in Section 3.5.1 can be used to obtain a linearized representation of the dynamic response $Z(t)$ in Equation 3.109 of the oscillator, for example,

$$\ddot{Z}_L(t) + 2\zeta\omega_0\dot{Z}_L(t) + \omega_0^2 Z_L(t) = \frac{1}{m}\left[a_1 d_u U^*(t) + a_2\dot{U}^*(t) + a_3 d_v V^*(t)\right], \quad (3.152)$$

in which $U^*(t) = u_0 + U(t)$, $V^*(t) = \bar{v} + V(t)$, and d_u and d_v are linearized wave and wind drag factors given by Equations 3.141 and 3.142, respectively. Since $Z_L(t)$ is a linear function of the stationary Gaussian processes $U(t)$ and $V(t)$, the approximate steady-state response is also a stationary Gaussian process with mean $\mu_{Z_L} = (a_1 d_u u_0 + a_3 d_v \bar{v})/m$ and spectral density function

$$g_{Z_L Z_L}(\omega) = |h(\omega)|^2 \frac{1}{m^2}\left[(a_1 d_u)^2 g_{UU}(\omega) + a_2^2 g_{\dot{U}\dot{U}}(\omega) + (a_3 d_v)^2 g_{VV}(\omega)\right], \quad (3.153)$$

where $g_{UU}(\omega)$ and $g_{VV}(\omega)$ are the one-sided spectral density functions in Equations 2.27 and 2.19 of the fluctuating wave and wind velocities $U(t)$ and $V(t)$, respectively, $g_{\dot{U}\dot{U}}(\omega) = \omega^2 g_{UU}(\omega)$ is the spectral density function of $\dot{U}(t)$, and $h(\omega)$ is the transfer function between the linearized input and the displacement response such that $|h(\omega)|^2 = 1/[(\omega^2 - \omega_0^2)^2 + (2\zeta\omega\omega_0)^2]$. We note the following property of weakly stationary processes which is required for obtaining Equation 3.153. For a weakly stationary process $U(t)$, the spectral density function of $U(t) + \dot{U}(t)$ is the sum of the spectral density functions of $U(t)$ and $\dot{U}(t)$, since the cross correlation functions between $U(t)$ and $\dot{U}(t)$ have the property $r_{U\dot{U}}(\tau) = -r_{\dot{U}U}(\tau)$.

The mean z-upcrossing rate of the steady-state linearized response $Z_L(t)$ can be calculated using Equation 3.143 for $\mu_{Z_L} = (a_1 d_u u_0 + a_3 d_v \bar{v})/m$, $\sigma_{Z_L}^2 =$

$\int_0^\infty g_{Z_L Z_L}(\omega)d\omega$ and $\sigma^2_{\dot{Z}_L \dot{Z}_L} = \int_0^\infty \omega^2 g_{Z_L Z_L}(\omega)d\omega$ with $g_{Z_L Z_L}(\omega)$ in Equation 3.153, and can be used to approximate the mean z-upcrossing rate of $Z(t)$ in Equation 3.147.

3.5.2.4 Numerical example:

Numerical results have been obtained for the system in Figure 3.36 consisting of a deck located at 10 m above the water surface with mass $m = 1000$ kg and $b = c = h = 2$ m, and a circular column of unit length with diameter $d_c = 0.5$ m. The natural frequency and the damping ratio of the system are $\omega_0 = 8$ rad/sec and $\zeta = 0.10$, respectively. Suppose that high winds with mean wind velocity $\bar{v} = 15$ m/sec and principal direction $\bar{\theta} = 0$ prevail at the system site resulting in wind and wave drag forces $F(t)$ and $X(t)$ in Equations 3.89 and 3.106 with $\rho_a = 1.2$ kg/m^3, $c_d = 2$, $\rho_w = 1000$ kg/m^3, $c'_d = 1$, $c_m = 2$, and current velocity $u_0 = 0.025\bar{v}$. Figure 3.42 shows the one-sided spectral density functions in Equations 2.19 and 2.27 of (a) the fluctuating wind velocity $V(t)$ and (b) the water particle velocity $U(t)$, with frequency band $[0, 10]$ rad/sec so that $\bar{\omega} = 10$ rad/sec. We note that the spectral density of the wind velocity is based on κ in Equation 2.20 for wind flow over water surface. A time $t = 15$ seconds is selected for calculations. We note that the response $Z(t)$ is approximately stationary at $t = 15$ since t exceeds 3 periods, $3(2\pi/\omega_0) \simeq 2.5$ seconds, of the oscillator ([164], Example 5.5).

Figure 3.47 shows histograms of (a) $Z_{n,m}(t)$ for a sampling rate $t^*/2 = 0.1571$ seconds, $n = 20$, and $n_m = [15\,(2\,\pi/\omega_0)/(t^*/2)] = 120$ calculated from $n_s = 100,000$ independent samples of this random variable, and (b) $Z(t)$ obtained by classical Monte Carlo simulation based on 100,000 independent samples of the input process $F(t) + X(t)$ and numerical integration of Equation 3.147 to get samples of $Z(t)$, for $t = 15$ seconds. The estimated mean, variance, skewness, and kurtosis of $Z_{n,m}(t)$ are $\hat{\mu} = 0.0352$, $\hat{\sigma}^2 = 5.23 \times 10^{-4}$, $\hat{\gamma}_3 = 0.2242$, and $\hat{\gamma}_4 = 3.5550$. Figure 3.48 shows time histories of the estimated mean, variance, skewness, and kurtosis of $Z(t)$

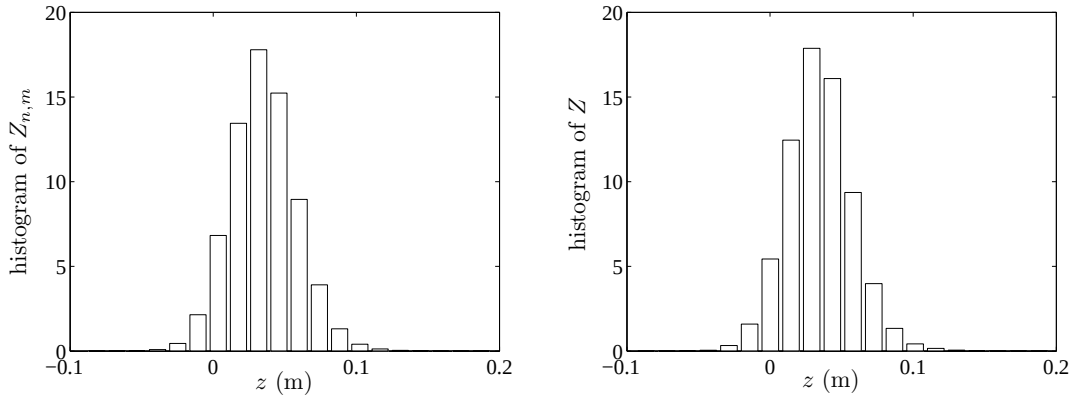

Figure 3.47: Histogram of $Z(t)$ at $t = 15$: (a) sampling theorem, (b) classical Monte Carlo simulation.

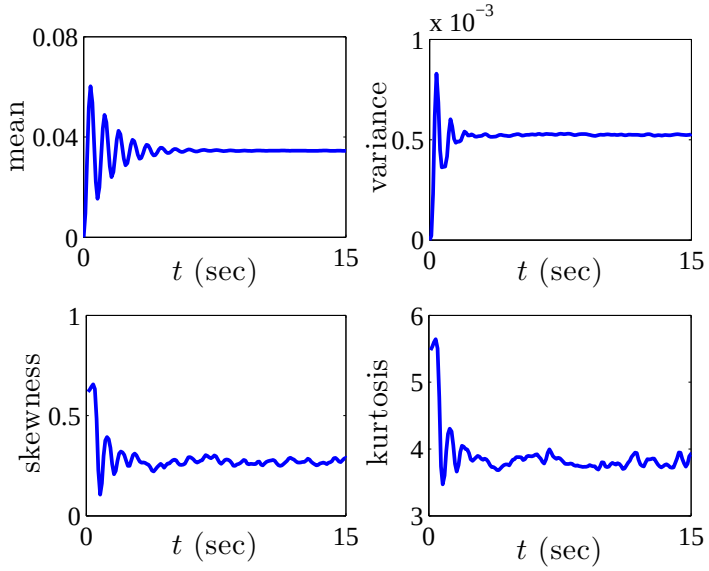

Figure 3.48: Response moments by classical Monte Carlo simulation.

obtained by classical Monte Carlo simulation based on 100,000 samples. We note that at $t = 15$ seconds the response reaches its steady-state as expected, and its estimated mean, variance, skewness, and kurtosis are $\hat{\mu} = 0.0345$, $\hat{\sigma}^2 = 5.19 \times 10^{-4}$, $\hat{\gamma}_3 = 0.2478$, and $\hat{\gamma}_4 = 3.7503$, in agreement with the above results obtained using the sampling theorem. The computation time for generating 100,000 samples of $Z_{n,m}(t)$ and constructing the

histogram in Figure 3.38 (a) was 52 seconds on a DELL-GX320 computer with 3GHz CPU and 2GB RAM. On the other hand, the computation time for generating 100,000 samples of $F(t)$ and calculating corresponding samples of $Z(t)$ through numerical integration for constructing the histogram in Figure 3.38 (b) was 29,233 seconds on the same computer, which is, more than 550 times more compared to that from sampling theorem.

Figure 3.49 shows with solid line the estimate $\hat{\nu}^{+}_{n,m}(z)$ of the mean z-upcrossing

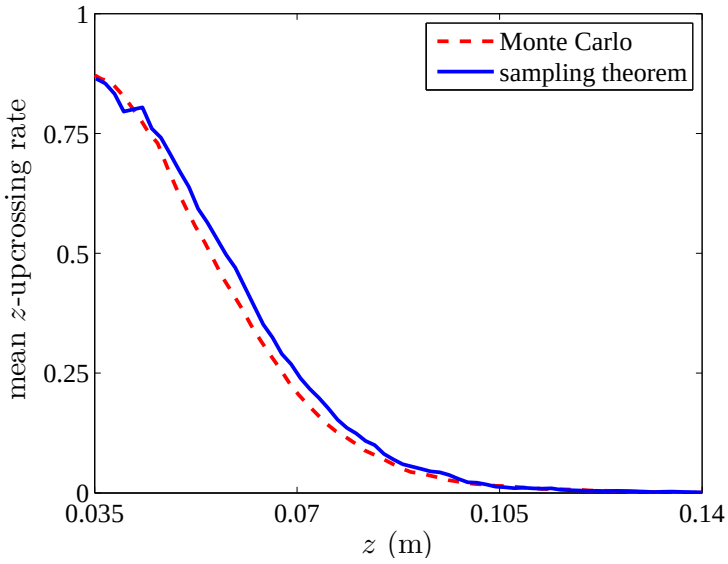

Figure 3.49: Estimates of mean z-upcrossing rates of $Z(t)$ by sampling theorem and classical Monte Carlo simulation.

rate of $Z_{n,m}(t)$, for $z \geq E[Z(t)]$, obtained by Equation 3.103 using the values of t, t^*, n, n_m and n_s in Figure 3.47 (a). The mean response $E[Z(t)]$ can be approximated by an estimate of the mean $\mu_{n,m}$ of $Z_{n,m}(t)$, $\hat{\mu}_{n,m} = 1/n_s \sum_{i=1}^{n_s} Z_{n,m}(t, \omega_i)$. Figure 3.49 also shows with dotted line estimate of the mean z-upcrossing rates of $Z(t)$ obtained by classical Monte Carlo simulation from the samples in Figure 3.47 (b). The computation times for calculating mean crossing rates in Figure 3.40 using the sampling theorem and classical Monte Carlo simulation are, respectively, 104 and 29,233 seconds, on a

DELL-GX320 computer with 3GHz CPU and 2GB RAM.

The system fragility in Equation 3.91 can be approximated by Equation 3.5 with mean $D = [-z, z]$-outcrossing rate in Equation 3.101 and τ in Equation 2.18. Figure 3.50 shows fragility surface for the linear oscillator in Figure 3.49 located in

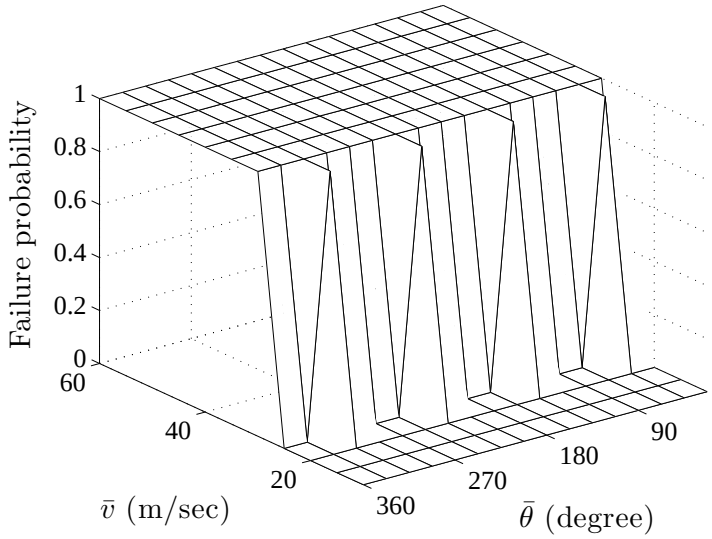

Figure 3.50: Fragility for linear oscillator with $\omega_0 = 8$ rad/sec.

milepost-150 for the displacement limit state $z = 20$ cm. The wind activity matrix in Figure 2.16 provides realizable values of $(\bar{v}, \bar{\theta})$ at the milepost. We calculate corresponding values of $\bar{v}$ over the sea surface using Figure 2.8. The change in fragility with respect to the mean wind speed and the principal wind direction is as in Figure 3.37. The failure probabilities of the system with $\omega_0 = 8$ rad/sec in Figure 3.50 are higher than those of the system with $\omega_0 = 15$ rad/sec in Figure 3.46 because the response of the system with $\omega_0 = 15$ rad/sec is quasi-static (see Section 3.4.1) whereas the response of the system with $\omega_0 = 8$ rad/sec is dynamic in nature so that they are larger due to dynamic amplifications.

Chapter 4
Life-cycle analysis

Life-cycle risk analysis of infrastructural systems is concerned with the performance of these systems subjected to natural and/or man-made hazards during their lifetime. The results from a life-cycle risk analysis can be used to (1) identify an optimal retrofitting technique for structural/nonstructural systems from a collection of design alternatives [96, 60, 24, 25], or (2) determine the relative importance of different hazards [17].

In Section 4.1 a methodology is presented for calculating the seismic performance of structural/nonstructural systems and developing rational strategies for increasing the seismic resilience of these systems. The seismic performance is measured by fragility surfaces, that is, the probability of system failure as a function of moment magnitude and site-to-source distance, consequences of system damage and failure, and system recovery time following seismic events. The input to the analysis consists of seismic hazard, geotechnical and structural/nonstructural systems properties, performance criteria, rehabilitation strategies, and a reference time. Estimates of losses and recovery times, referred to as life-cycle losses and recovery times, can be derived using fragility information and financial models. MCEER West Coast Demonstration Hospital is used to demonstrate the methodology. Fragilities are obtained for structural/nonstructural components and systems for several limit states. Also, statistics are obtained for lifetime losses and recovery times corresponding to different rehabilitation alternatives. The proposed loss estimation methodology is based on (i) seismic hazard analysis, (ii) fragility analysis and (iii) capacity and cost estimation. Figure 4.1 shows a schematic chart summarizing the loss estimation methodology. Although in the current example the decision support methodology considers only seismic hazards, the extension to systems under multiple hazards is simple, as discussed briefly at the end of this section.

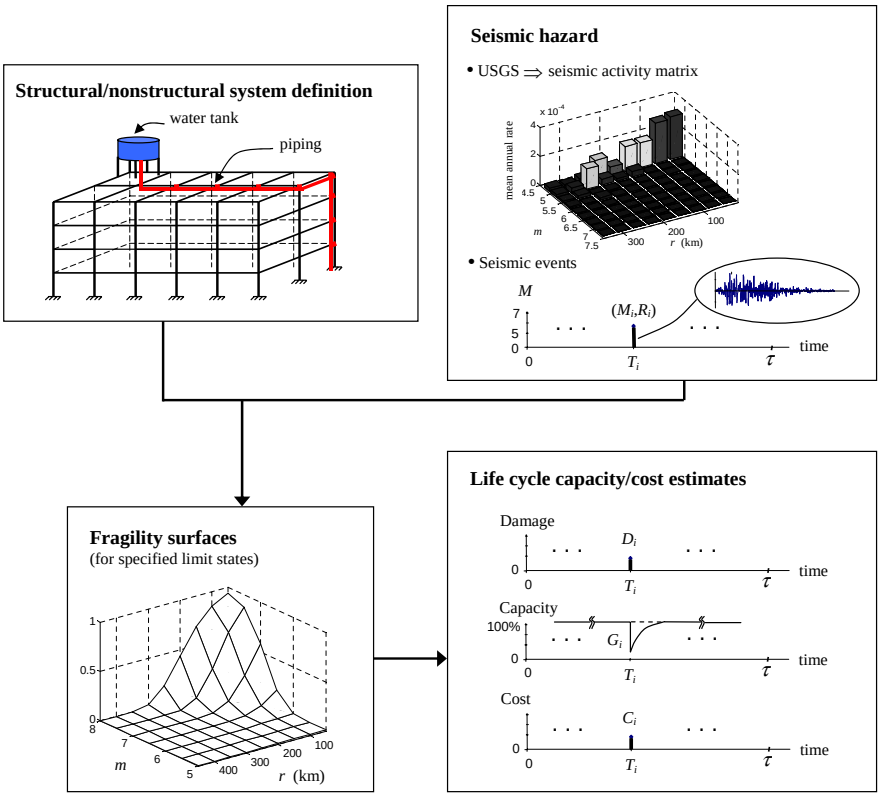

Figure 4.1: Loss estimation methodology.

In Section 4.1 a methodology is presented for assessing performance of a system under multihazard environment. The methodology is illustrated by examining a simple model of an offshore structure subjected to seismic and hurricane hazards. The lifetime system performance is assessed based on (i) seismic and hurricane hazard analyses, (ii) fragility analysis and (iii) lifetime probabilities of failure.

In Section 4.3 a probabilistic model is presented for selecting an optimal maintenance strategy for deteriorating systems using reliability constraints. Consider a structural system designed for a lifetime $\tau > 0$. The overall objective is the development of an optimal maintenance policy such that the probability that the total life-cycle cost exceeds a critical value is minimized under the constraint that the system functions at the required performance level in $[0, \tau]$. The total life-cycle cost includes repair/replacement

costs due to system damage following a seismic event, and maintenance related costs. The maintenance policy is defined by the number of inspections, inspection times, and inspection quality. Probabilistic models are used for the seismic activities and seismic ground accelerations at the site where the system is located. Fragility surfaces for several damage levels, that is the probabilities that the system enters various damage levels as a function of moment magnitude and site-to-source distance, are used to assess system's seismic performance. It is assumed that the system fragility increases in time due to deterioration, and the system is brought back to its original state after each earthquake/maintenance related repair. The input to the analysis consists of (1) site seismic activity matrix delivering the mean annual rates of earthquakes for different magnitudes and source-to-site distances, (2) system fragility surfaces for each damage level, (3) probability laws of system deterioration rates, (4) required performance level, (5) costs of maintenance, repair and replacement, and (6) a lifetime τ. We note that items 1 and 6 are required for the seismic hazard analysis, 2-4 are related to the fragility analysis and 5 is a part of the life-cycle cost analysis illustrated in Figure 4.1. The probability law of the total life-cycle cost is obtained using Monte Carlo simulation. First, random samples of the seismic hazard at the system's site during a given lifetime τ are generated using site's seismic activity matrix. Second, the system damage level is simulated for each event in a seismic hazard sample using the fragility surfaces at the time of the events. Third, the total life-cycle cost for a sample is obtained by discounting and summing the maintenance costs and costs of repair and replacement due to the seismic events in that sample. Finally, optimal number of inspections and inspection times are obtained by minimizing the probability that the total life-cycle cost exceeds a critical value. A numerical example is presented to demonstrate the methodology.

4.1 Rehabilitation decision analysis:

MCEER Demonstration Hospital

Capital allocation decisions for a health care facility include, for example, opening a new unit, extending or closing some existing units, buying new equipment, and relocating the hospital building. These decisions are based on life cycle capacity, viewed as the level of performance defined for a service, and cost estimates. Existing geotechnical, structural/nonstructural systems can be left as they are or can be retrofitted using one of the available rehabilitation alternatives. Leaving a system as it is seems to be reasonable for short-term decisions but retrofitting the system, despite its initial costs, might be beneficial in the long run. A probabilistic methodology is required to make a rehabilitation decision since seismic hazard and system performance are uncertain. Figure 4.2 shows a chart illustrating the principal elements of a fragility-based capital

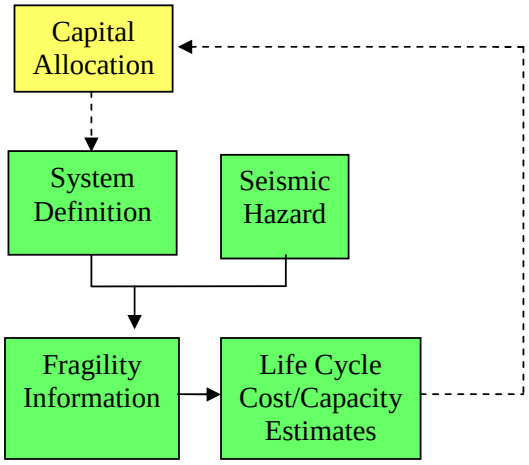

Figure 4.2: Capital allocation decision support methodology.

allocation decision support system.

The main objective of this section is the development of a methodology for evaluating the seismic performance and development of optimal rehabilitation strategies

of individual health care facilities during a specified time interval. The seismic performance is measured by fragility surfaces, that is, the probability of system failure as a function of moment magnitude and site-to-source distance, consequences of system damage and failure, and system recovery time following seismic events. The input to the analysis consists of seismic hazard, geotechnical and structural/nonstructural systems properties, performance criteria, rehabilitation strategies, and a reference time. Estimates of losses and recovery times, referred to as life-cycle losses and recovery times, can be derived using fragility information and financial models. Life-cycle costs consist of (1) initial cost related to the rehabilitation of the system, (2) repair/replacement costs for bringing the damaged systems back to their original states, (3) cost of life, and (4) indirect costs related to the loss of capacity of the hospital. MCEER West Coast Demonstration Hospital, from this point forward referred to as MCEER Hospital, is used to demonstrate the method. Statistics are obtained for lifetime losses and recovery times corresponding to different rehabilitation strategies and an optimal rehabilitation strategy is selected using these statistics.

The MCEER Hospital is an inpatient facility in the Northridge Hospital Medical Center. The facility was constructed in the early 1970's to meet the seismic requirements of of the 1970 Uniform Building Code. The seismic risk of the MCEER Hospital is assessed based on the performance of its structural system and three nonstructural systems attached to the structural systems at different locations, namely, the Heat-Ventilation-Air Conditioning (HVAC) system consisting of two water chillers, piping system and partition walls. Figure 4.3 illustrates a two-dimensional model of the 4-storey structural system and the three nonstructural systems. The architectural drawings of the MCEER Hospital show that there are 93 beds in the building. Table 4.1 shows the number of beds in each floor. The net revenue per bed per day (per patient day) is $1,500 [98].

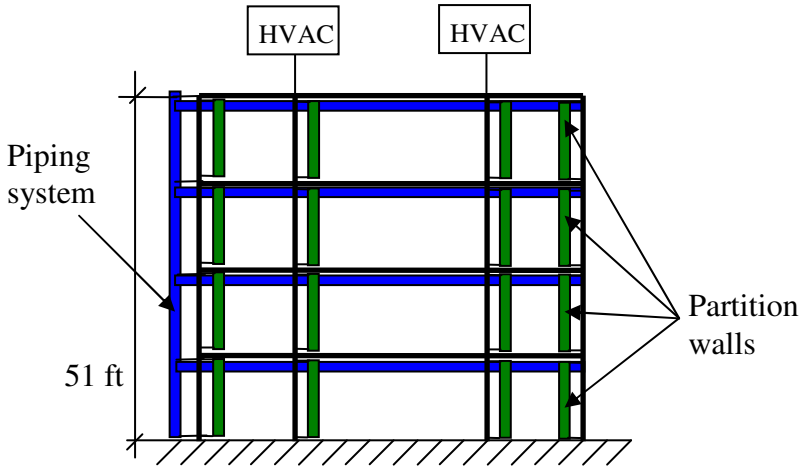

Figure 4.3: Illustration of structural/nonstructural systems.

Table 4.1: Number of beds in the MCEER Hospital.

Floor	Number of beds
1	No patient rooms
2	43 beds
3	50 beds
4	No patient rooms

4.1.1 Loss estimation method

Some of the current loss estimation methods are briefly examined and a method based on seismic hazard analysis, fragility analysis and life-cycle capacity/cost estimation, is proposed.

4.1.1.1 Current loss estimation methods

Most of the existing earthquake loss estimation methodologies usually calculate life-cycle losses based on the maximum credible earthquake during the projected lifetime of the system. The ATC-13 [8] methodology provides damage and loss estimates, based on expert-opinion, for industrial, commercial, residential, utility and transportation

facilities. Although the ATC-13 methodology is most applicable for a large number of structures and should not be applied to individual facilities [8], in current practice it is used to estimate the probable maximum loss of individual structures for insurance and investment decisions. HAZUS [79] estimates potential losses on a regional basis and these estimates are essential to decision-making at all levels of government, providing a basis for developing mitigation policy, emergency preparedness, and response and recovery planning. Both methods were developed to estimate losses for a large number of structures in a specified region using the maximum credible earthquake and should not be applied to an individual facility.

Losses estimated by using the maximum credible earthquake may not be accurate. Here is an example. Let $N(\tau)$ be the number of earthquake events occurring during the lifetime τ of a system and assume that $N(t)$, $t > 0$, is a Poisson process of intensity $\lambda > 0$. Denote by T_k and $X_k, k = 1, \ldots, N(\tau)$, the arrival time and the intensity of event k, respectively. Assume that $X_k, k = 1, \ldots, N(\tau)$ are independent identically distributed random variables with distribution function F of support $[0, \infty)$. Let $g : [0, \infty) \to [0, \infty)$ be an increasing function representing the cost due to a seismic event, *i.e.*, $g(X_1)$ is the cost caused by a seismic event of intensity X_1. Denote by $C(\tau)$ the total cost in time $[0, \tau]$, that is, the life-cycle cost. First model, referred as model-A, uses the maximum credible earthquake in $[0, t]$ to calculate the losses. Accordingly,

$$C(\tau) = g(X_{\max}) \,, \tag{4.1}$$

where $X_{\max} = \max_{1 \le k \le N(\tau)}\{X_k\}$. The mean and the variance of the total cost can be calculated as $E[C(\tau)] = E[g(X_{\max})]$ and $Var[C(\tau)] = E[g(X_{\max})^2] - (E[g(X_{\max})])^2$, respectively. In the second model, referred as model-B, the total cost is calculated by

$$C(\tau) = \sum_{k=1}^{N(\tau)} g(X_k) \,. \tag{4.2}$$

The mean and the variance of $C(\tau)$ are $E[C(\tau)] = \nu\, E[g(X_1)]$ and $Var[C(\tau)] =$

$\nu\, E[g(X_1)^2]$, respectively, where $\nu = \lambda\,\tau$ is the average number of seismic events in τ years.

Two cases are considered. In the first case X_1 has a uniform distribution in $[a, b]$, $0 < a < b$, in the second case X_1 has an exponential distribution with parameter ρ shifted to $c > 0$. In both cases the cost function has the form $g(x) = x^2$. Figure 4.4 shows the (a) mean and (b) variance of $C(t)$ per year, that is, $\tilde{C}(\tau) = C(\tau)/\tau$, given by,

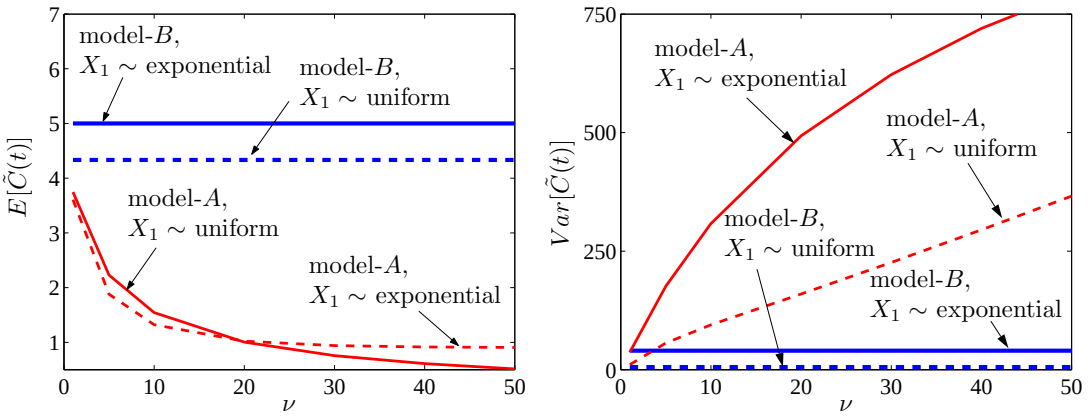

(a) (b)

Figure 4.4: Mean and variance of $\tilde{C}(t)$.

$E[\tilde{C}(\tau)] = E[C(\tau)]/\tau$ and $Var[\tilde{C}(\tau)] = Var[C(\tau)]/\tau^2$, respectively, calculated using models A and B for $\tau = 1$, $a = 1$, $b = 3$, $\rho = 1$, $c = 1$, and $\nu = 1, 5, 10, 20, 30, 40, 50$. The differences between the means and variances of the total cost under models A and B are relatively small and very large, respectively. Decisions based on the two models may differ significantly.

4.1.1.2 Loss estimation method

The proposed method is based on (i) seismic hazard analysis, (ii) fragility analysis and (iii) lifetime capacity/cost estimation [96]. The method (i) considers a realistic seismic hazard model rather than using the maximum credible earthquake, (ii) includes all components of costs, that is, the costs related to the structural failure and downtime,

retrofitting, repair, loss of capacity in services, and loss of life, and (iii) is designed for individual facilities rather than a large population of them. The method is based on Monte Carlo simulation, probabilistic seismic hazard, fragility and capacity/cost analyses. Figure 4.5 shows a chart summarizing the loss estimation method for a

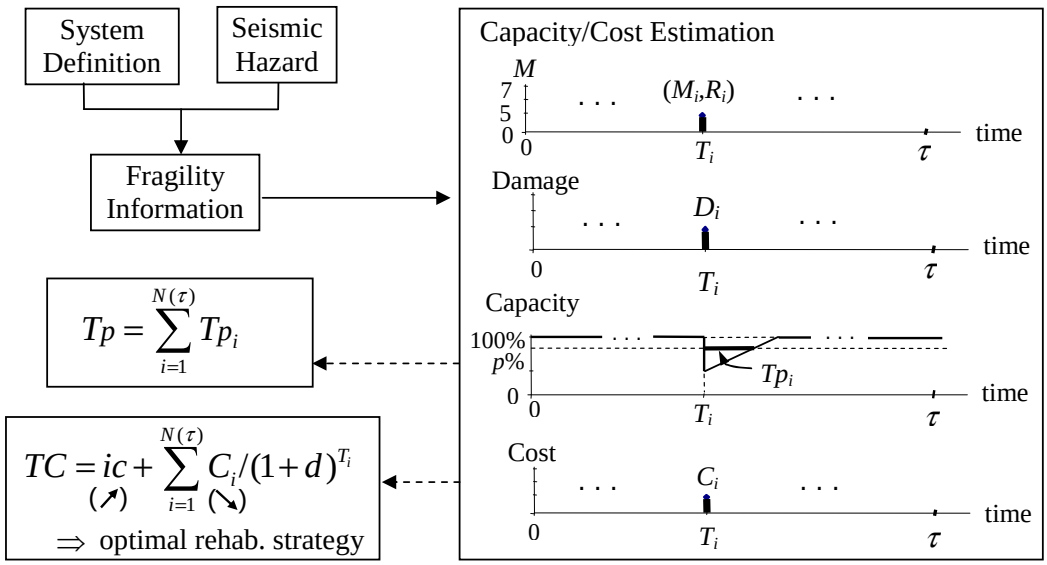

Figure 4.5: Loss estimation method.

system with projected life τ. The probabilistic seismic hazard models presented in Sections 2.3.4 and 2.2.1.1 are used to characterize (1) the moment magnitude M_i, source-to-site distance R_i and the arrival time T_i of the seismic event i, (2) the ground accelerations at the system site resulting from seismic event i characterized by (M_i, R_i), and (3) the total number of seismic events $N(\tau)$ in τ. The seismic fragility analysis presented in Section 3.3.1.1 is used to characterize the damage in the structural/nonstructural systems. For example, let D_i be a discrete random variable characterizing the damage state of a nonstructural system after seismic event i with moment magnitude m_i and source-to-site distance r_i, $i = 1, \ldots, N(\tau)$. Assume that a nonstructural system enters damage state d_k, with probability $p_{k,i}$ for $k = 1, \ldots, n$, where n is the number of damage states. The probabilities $p_{k,i}$ can be obtained from

the fragility information of the nonstructural system and are functions of the limit state defining the damage state d_k and (m_i, r_i). Similarly, we can define random variables characterizing the damage in the structural system and components of the selected nonstructural systems.

In Figure 4.5

$$Tp = \sum_{i=1}^{N(\tau)} Tp_i \tag{4.3}$$

is the total time the system operates below $p\%$ capacity in τ, in which Tp_i is the time the system operates below $p\%$ capacity after event i and

$$TC = ic + \sum_{i=1}^{N(\tau)} \frac{C_i}{(1+d)^{T_i}} \tag{4.4}$$

is the total cost in τ in present value, in which ic is the initial cost related to the rehabilitation, d is the discount rate, and C_i is the cost related to event i including costs of repair/replacement, capacity losses and life losses due to the damage in structural and nonstructural systems. It is expected that with an increasing initial cost ic in Equation 4.4, the cost C_i due to event i will decrease and for some rehabilitation alternative we will have the optimum solution. The numerical results in the following sections are for $p = 90$ and $d = 0.05$.

The resilience metrics, that is, the decision variables used for selecting the optimal rehabilitation alternative are the total time Tp the system operates below $p\%$ capacity, and the total cost TC in τ, given by Equations 4.3 and 4.4, respectively. Estimates of the distributions of Tp and TC can be obtained using Monte Carlo simulation. First, a seismic hazard sample at the site during lifetime τ is generated using the Monte Carlo algorithms developed in Section 2.4. The seismic hazard sample is defined by the number of earthquakes during the time τ, and magnitude and source-to-site distance and arrival time of each of them. For each event in the seismic hazard sample damages states of structural/nonstructural systems are simulated from their fragility information,

and corresponding capacity losses and costs are calculated. The total time the system operates below $p\%$ capacity and the total cost in $[0, \tau]$ corresponding to the seismic hazard sample are simply obtained by adding contributions from each event in the seismic hazard sample, that is, using Equations 4.3 and 4.4, respectively. Repeating the above analysis for n_s independent samples, we obtain n_s samples of Tp and TC. Hence histograms and other cost statistics of Tp and TC depending on user's objectives can be calculated from the seismic hazard samples.

4.1.2 Seismic hazard information and dynamic analysis

The MCEER West Coast Demonstration Hospital is in Northridge, California with coordinates (118.518^o West, 34.237^o North) [182]. The life time is $\tau = 50$ years. Figure 2.13 shows the seismic activity matrix at the system site, providing the mean annual arrival rate of earthquakes with different moment magnitude m, and source-to-site distance r. The hospital is located on stiff soil (NEHRP site class D, [56]).

The cascade approach is used for the dynamic analysis of the structural and nonstructural systems. The stationary response with duration 10 seconds to strong ground motion is used in seismic performance analysis. We note that the specific barrier model delivers the duration of ground motion (Section 2.2.1.1), but we set somewhat arbitrary, 10 seconds irrespective of (m, r). Methods based on crossing theory of stochastic processes presented in Section 3.1 are used for calculating fragility surfaces for structural/nonstuctural linear systems subjected Gaussian seismic ground accelerations in Section 2.2.1.1.1. It is assumed that all the systems are brought the their original states after each seismic event.

4.1.3 Structural system information

Several mathematical models of the MCEER West Coast Demonstration Hospital are available in [187]. The model used in this study corresponds to WC70 model in [187]. A two-dimensional inelastic model of WC70 was considered in [59]. One-dimensional equivalent linear versions of the two-dimensional inelastic models are used in this study for seismic risk analysis [98].

4.1.3.1 Models

- *Existing system:* A simplified version of the model described in [59], and referred to as the WC70 model, is used. Following assumptions are made for seismic analysis.
  - Damping matrix remains constant.
  - First storey of WC70 behaves linearly between limit states (Figure 4.6), all other storeys remain linear. In Figure 4.6, $K = 351$ kN/mm, $\varepsilon = 0.03$ [98].

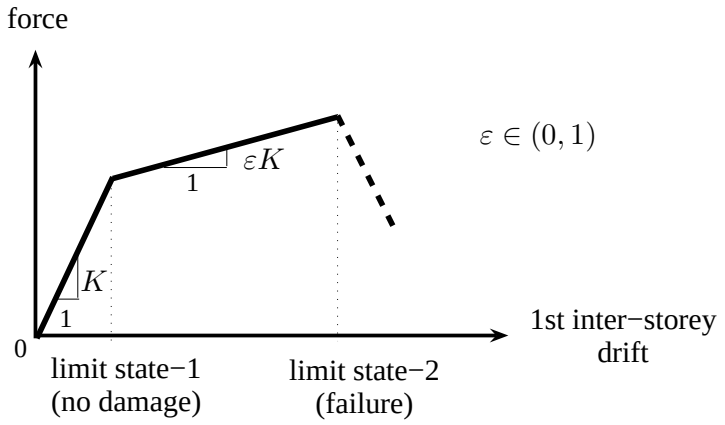

Figure 4.6: Force-displacement model for the 1st storey.

  - For small earthquakes initial stiffness K of the first storey is used for calculating the system stiffness matrix. For large earthquakes the bilinear

force-displacement curve in Figure 4.6 is replaced by an equivalent linear curve with slope 0.0726K [98] and system stiffness matrix is calculated accordingly. Table 4.2 (a) and (b) show the dynamic characteristics of the initial linear and equivalent linear models, respectively.

Table 4.2: Modal parameters of the (a) initial linear and (b) equivalent linear models.

(a)

Linear model			
Mode	ω_i **(rad/sec)**	ζ_i **(%)**	Γ_i
1	8.83	2.00	1.38
2	26.56	1.62	-0.43
3	40.49	2.00	-0.20
4	49.75	2.31	0.04

(b)

Equivalent Linear model			
Mode	ω_i **(rad/sec)**	ζ_i **(%)**	Γ_i
1	8.19	8.77	1.40
2	25.07	2.97	-0.38
3	39.48	2.00	-0.14
4	49.68	1.68	0.02

- *Rehabilitated systems:* Three alternative designs, with (1) the same stiffness as the existing system and (2) linear viscous dampers with damping constants shown in Table 4.3, and inserted in the central bay in each storey of the exterior moment-

Table 4.3: Damping coefficient for a viscous damper.

	Damping coefficients (kN-sec/mm)		
Storey	**Rehab. alt. 1 20% damping**	**Rehab. alt. 2 25% damping**	**Rehab. alt. 3 30% damping**
1	18.3	22.8	27.4
2	17.8	22.3	26.8
3	15.9	19.9	23.8
4	12.0	15.0	18.0

resisting frame of the WC70 model (see Figure 4.7), are considered. There are 8 dampers in total. Table 4.4 shows the modal damping ratios for the three rehabilitation alternatives.

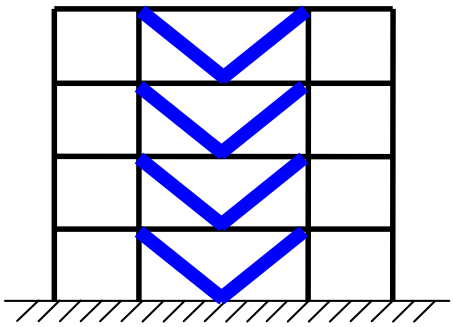

Figure 4.7: Damper locations (in exterior frames only).

Table 4.4: Modal damping ratios.

	Damping ratios (%)		
Mode	**Rehab. alt. 1**	**Rehab. alt. 2**	**Rehab. alt. 3**
1	20.00	25.00	30.00
2	5.20	6.19	7.19
3	2.00	2.00	2.00
4	0.60	0.12	0.00

4.1.3.2 Damage states and fragilities

Maximum inter-storey drift is used to assess the structural performance. Table 4.5, from [58], defines structural damage and limit states based on maximum inter-storey drift ratios. Fragilities are calculated from (i) model, (ii) response (using Equation 3.56) and (iii) damage states. Figure 4.8 shows the probability that the maximum inter-storey displacement ratio exceeds 2.5% for (a) the base system and (b-d) the three rehabilitation alternatives in Table 4.4. As expected, system fragility gets smaller from (a) to (d) as more damping is added to the system as a result of different levels of rehabilitation.

4.1.3.3 Cost estimates

- *Repair and replacement:* Table 4.6 gives repair/replacement costs corresponding to the damage states described in Table 4.5. The repair and replacement costs do

Table 4.5: Structural system damage states and corresponding max inter-storey drift ratios.

Damage state	**Description**	**Limit state (drift, %)**
Immediate occupancy	Minor local yielding at few places. No fractures. Minor buckling. Minor observable permanent distortion.	< 0.7
Life safety	Hinges form. Local buckling in some beams. Severe joint distortion. Isolated moment connection fractures. Few elements with partial fracture. Shear connections remain intact.	$[0.7, 2.5)$
Collapse prevention	Extensive distortion in beams and columns. Many fractures at moment connections Shear connections remain intact.	$[2.5, 5.0)$
Collapse		≥ 5.0

not include disruption losses.

Table 4.6: Structural system repair/replacement costs.

Damage state	**Repair/replacement cost ($)**
Immediate occupancy	280,000
Life safety	1,512,000
Collapse prevention	67,500,000
Collapse	67,500,000

- *Rehabilitation:* The costs for the rehabilitation alternatives defined in Table 4.3 are given in Table 4.7. The costs include all the dampers used in the rehabilitation of the whole structure. Since the dampers are proposed to be placed only in the external moment resisting frames, there will be no disruption of hospital function, hence no business interruption losses.

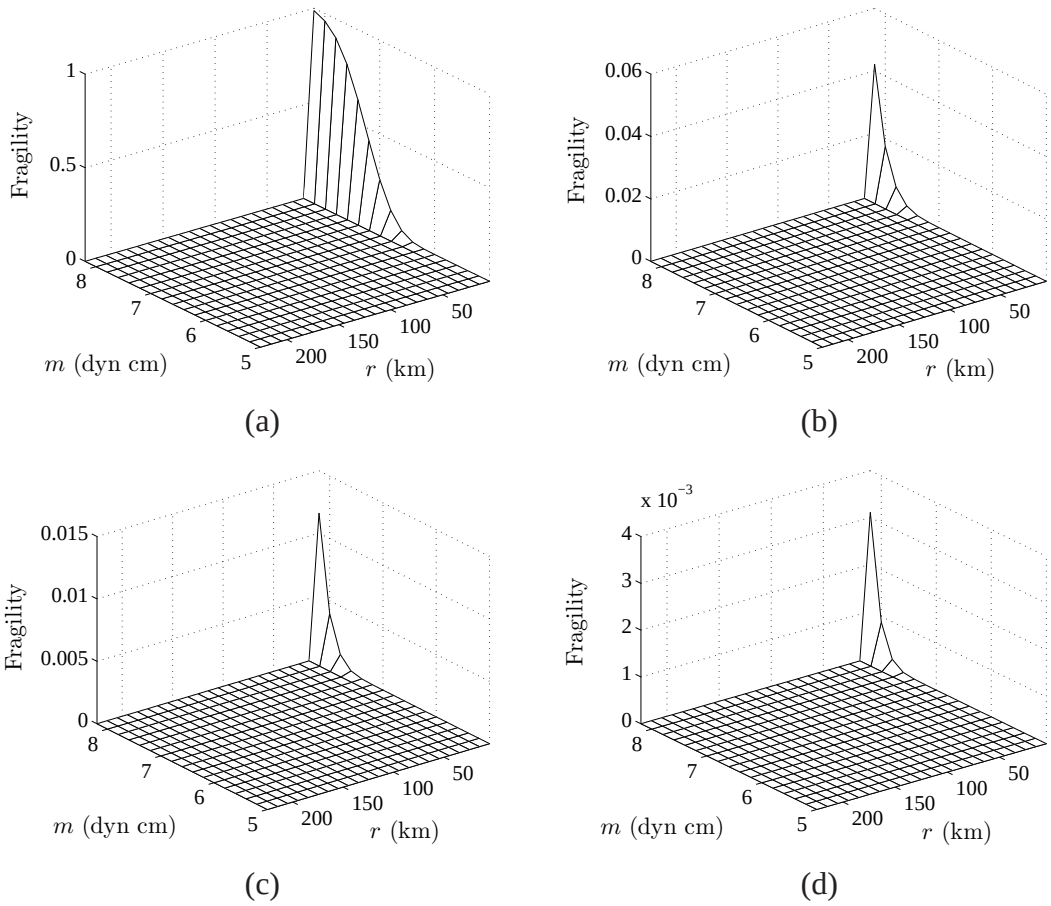

Figure 4.8: Structural system fragility: (a) base system, (b) rehab. alt. 1, (c) rehab. alt. 2, (d) rehab. alt. 3.

Table 4.7: Structural system rehabilitation costs.

Rehab. alt.	**Rehabilitation cost ($)**
1	109,000
2	133,000
3	180,000

- *Capacity loss:* Table 4.8 shows the consequences of the damages states defined in Table 4.5.
- *Life loss:* Life loss is considered only for the collapse damage state. It is assumed that there are 150 people in the building at the time of earthquake and

Table 4.8: Structural system damage states and corresponding consequences.

Damage state	**Consequences/disruption**	**Cost ($)**
Immediate occupancy	Minor structural repair may be needed. Hospital is 100% operational.	0
Life safety	Structural strengthening required. 2 years for repair (5% capacity loss).	4,380,000
Collapse prevention	Complete loss. 4 years for reconstruction.	203,670,000
Collapse	Complete loss. 4 years for reconstruction.	203,670,000

the probability of death is 0.1. The value of life is $2,200,000 [49].

More explanations on building cost estimates are provided in Appendix E.

4.1.4 Nonstructural systems information

The seismic performances of three nonstructural systems illustrated in Figure 4.3, namely, HVAC system, partition walls and piping system, are examined. It is assumed that the nonstructural systems are not interacting, that is, the responses of these systems are independent of each other.

4.1.4.1 HVAC system

It is assumed that the HVAC system consists of two identical water chillers attached to the roof of the building.

4.1.4.1.1 Models:

- *Existing system:* A three dimensional nonlinear model of the HVAC equipment is used [54], which delivers relative acceleration response of the center of mass of the HVAC equipment in the longitudinal, transverse and vertical directions.

The response in only the transverse (short) direction of HVAC is used for seismic performance analysis.

- *Rehabilitated systems:* None

4.1.4.1.2 Damage states and fragilities: HVAC equipment is an acceleration sensitive nonstructural system. Table 4.9, from [7], defines the damage and limit states. Fragilities are calculated from (i) model, (ii) response (excitation at attachment points,

Table 4.9: HVAC equipment damage states and corresponding accelerations.

Damage state	**Description**	**Limit state (acceleration, g units)**
None		< 2.0
Moderate	Control panel relays jump. System shuts down.	$[2.0, 4.0)$
Extensive	Chiller has permanent damage. System has to be replaced.	≥ 4.0

using Equation 3.58) and (iii) damage states. Figure 4.9 (a) and (b) show the probability

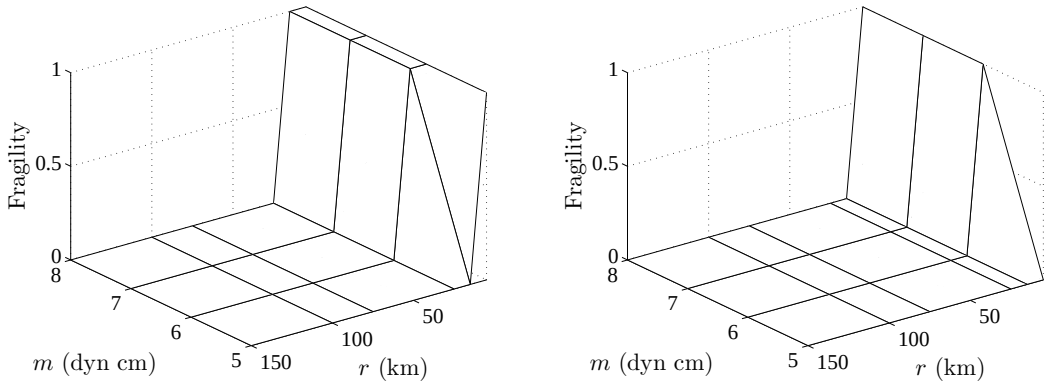

(a) (b)

Figure 4.9: HVAC equipment fragility: (a) acc $\geq 2.0g$, (b) acc $\geq 4.0g$.

that the maximum acceleration response of a HVAC equipment exceeds 2.0 g and 4.0

g, respectively, assuming that the equipment is attached to the existing structural system (no rehabilitation). As expected, fragility is lower for the larger limit state.

4.1.4.1.3 Cost estimates:

- *Repair and replacement:* The repair/replacement costs are given in Table 4.10 for the damage states described in Table 4.9. The repair and replacement costs do not include disruption losses.

Table 4.10: HVAC equipment repair/replacement costs.

Damage state	Repair/replacemet cost per HVAC ($)
None	0
Moderate	90,000
Extensive	500,000

- *Capacity loss:* Table 4.11 shows the consequences of the damages states defined in Table 4.9.

Table 4.11: HVAC equipment damage states and corresponding consequences.

Damage state	Consequences/disruption per HVAC	Cost/HVAC ($)
None		0
Moderate	50% of the beds are lost for 2 days	139,500
Extensive	50% of the beds are lost for 20 days	1,395,000

More explanations on cost estimates are provided in Appendix E.

4.1.4.2 Partition walls

Table 4.12 shows the number of partition walls in each floor of the MCEER Hospital (estimated using its architectural drawings).

Table 4.12: Number of partition walls and their effects on bed capacity.

Floor	Partition walls	Effects on bed capacity
1	80	No patient rooms
2	80	43 beds on the 2nd floor - 14 walls effecting 1 bed - 18 walls effecting 2 beds - 7 walls effecting 3 beds - 6 walls effecting 4 beds - 1 wall effecting 5 beds - 1 wall effecting 6 beds
3	60	50 beds on the 3rd floor - 2 walls effecting 1 bed - 28 walls effecting 2 beds - 2 walls effecting 3 beds - 8 walls effecting 4 beds
4	80	No patient rooms

4.1.4.2.1 Models: Seismic performance of gypsum drywalls is reported in [120]. It is assumed that the partition walls in MCEER Hospital are of the types reported in [120]. Partition wall damage was given as a function of the inter-storey drift in [120]. Hence no wall model is required for fragility analysis and loss estimation.

- *Existing system:* A typical setup (tests 1, 2, 5 and 6 in [120], page 50) is considered to represent the existing partition wall type.
- *Rehabilitated systems:* None.

4.1.4.2.2 Damage states and fragilities: Partition walls are drift sensitive nonstructural components. Fragility curves for minor, moderate, extensive damage states and complete failure are shown in Figure 4.10. Fragility surfaces are calculated from (i) model, (ii) response (using Equation 3.56) and (iii) damage states. Figure 4.11 shows the probability that a partition wall, located on the (a) 1st, (b) 2nd, (c) 3rd or (d)

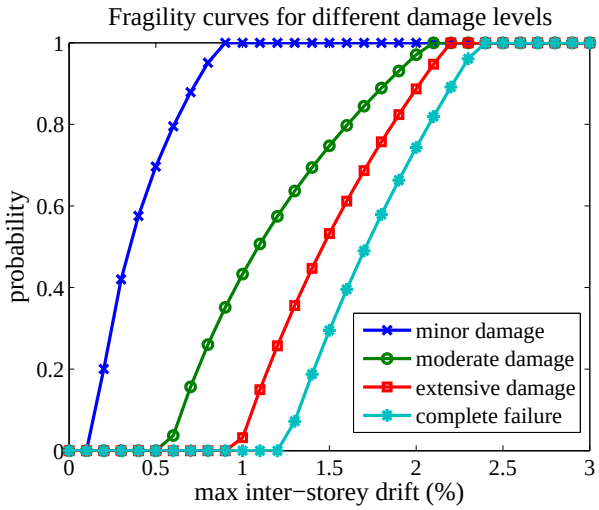

Figure 4.10: Fragility curves for partition walls (after [120]).

4th floor, has extensive damage or completely failed, assuming that the wall is attached to the existing structural system (no rehabilitation).

4.1.4.2.3 Cost estimates:

- *Repair and replacement:* The repair/replacement costs are given in Table 4.13 for the damage states in Figure 4.10 ([120], Figures 128, 129 and 130). The repair and replacements costs do not include disruption losses.

Table 4.13: Partition wall repair/replacement costs.

Damage state	**Repair/replacement cost per wall ($)**
None	0
Minor	230
Moderate	460
Extensive	690
Complete failure	920

- *Capacity loss:* Table 4.14 shows the consequences of the damages states in Figure 4.10.

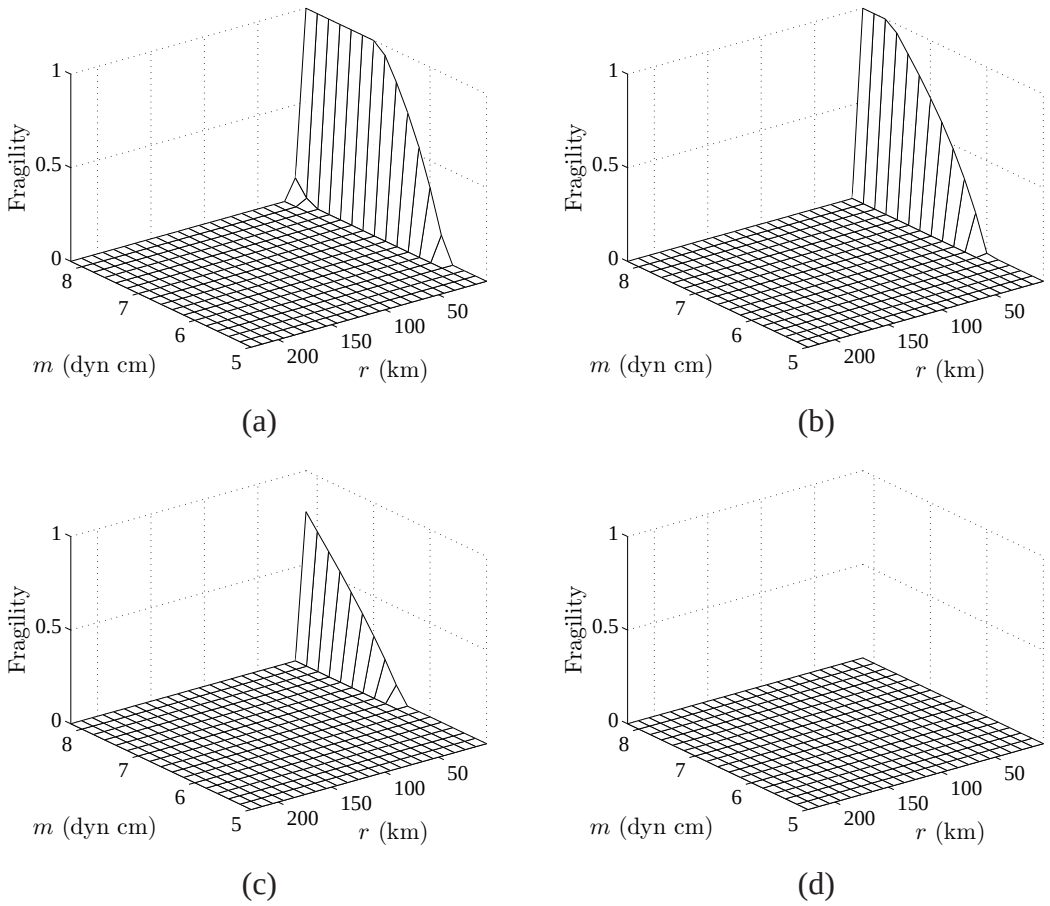

Figure 4.11: Partition wall fragility: (a) 1st floor, (b) 2nd floor, (c) 3rd floor, (d) 4th floor.

More explanations on cost estimates are provided in Appendix E.

4.1.4.3 Piping system

It is assumed that the piping system tested at University of Nevada at Reno [68] [REF Robert Corbin's MS thesis] can be used to describe limit/damage states of the existing piping system at the demonstration hospital. The experimental results were acquired for a steel/threaded piping system with unbraced and braced alternatives. The number of different elements in the sanitary piping system at each floor of the MCEER Hospital are estimated using its architectural drawings, and considering only the pipes with diameter

Table 4.14: Partition wall damage states and corresponding consequences.

Damage state	**Consequences/disruption per wall**
None	
Minor	effected beds are unavailable for 1 day
Moderate	effected beds are unavailable for 2 days
Extensive	effected beds are unavailable for 3 days
Complete failure	effected beds are unavailable for 3 days

greater than or equal to 1 inch (see Table 4.15). The number of hangers are estimated assuming a spacing of 10 feet.

Table 4.15: Number of elements of the piping system.

Floor	**Length (ft)**	**Elbow-connect.**	**T-connect.**	**Valves**	**Hangers**
1	330	30	15	15	33
2	510	65	50	40	51
3	510	65	50	40	51
4	270	30	30	25	27

4.1.4.3.1 Models: Piping system damage is assumed to be a function of the inter-storey drift. Hence, no pipe model is required for fragility analysis and loss estimation.

- *Existing system:* The unbraced system is considered as the existing system.
- *Rehabilitated system:* The braced system is used as the rehabilitated alternative. It is assumed that the pipes are braced at every second hanger location with a clevis support and bracing cables (J. Lewis).

4.1.4.3.2 Damage states and fragilities: Piping systems are considered to be drift sensitive nonstructural components. Table 4.16 defines the damage and limit states. Fragility surfaces are calculated from (i) model, (ii) response (using Equation 3.56) and

Table 4.16: Damage state descriptions for steel/threaded system.

Damage state	**Description**	**Limit state (drift, %)**	
		Existing sys.	**Rehab. sys.**
Slight		< 1.1	< 2.2
Moderate	The piping joints contained manageable leaks.	$[1.1, 2.2)$	$[2.2, 5.0)$
Extensive	The piping connections contained permanent damage.	≥ 2.2	≥ 5.0

(iii) damage states. Figure 4.12 shows the probability that existing (unbraced) piping system attached to the structural system with no rehabilitation, located on the (a) 1st, (b) 2nd, (c) 3rd or (d) 4th floor, has extensive damage.

4.1.4.3.3 Cost estimates:

- *Repair and replacement:* The repair/replacement costs are given in Table 4.17 for each floor, for the damage states described in Table 4.16.

Table 4.17: Piping system repair/replacement costs per floor.

	Repair/replacement cost per floor ($)			
Damage state	**1**	**2**	**3**	**4**
Slight	1,100	1,690	1,690	900
Moderate	1,720	4,380	4,380	2,290
Extensive	1,860	4,950	4,950	2,290

- *Rehabilitation:* The rehabilitation cost for the piping system is $120,000. The rehabilitation costs do not include business interruption losses.
- *Capacity loss:* Table 4.18 shows proposed consequences and disruption for the damage states given in Table 4.16.

More explanations on cost estimates are provided in Appendix E.

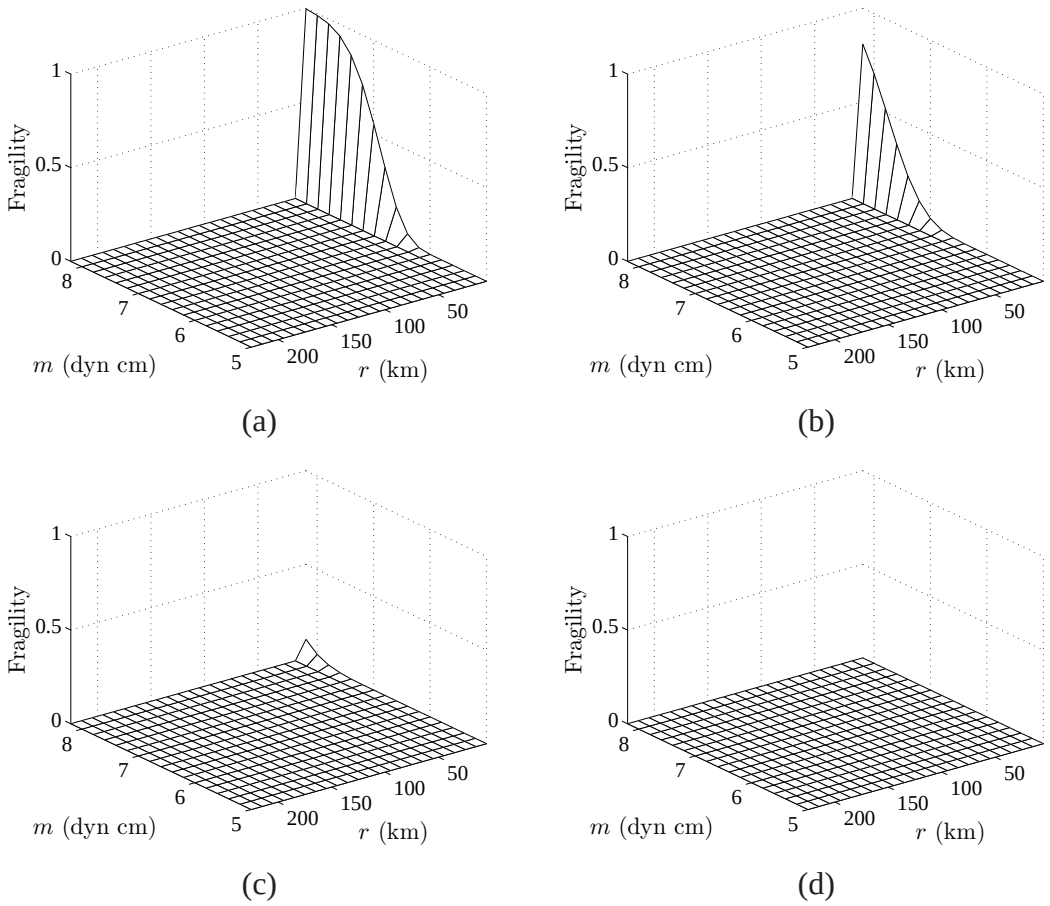

Figure 4.12: Piping system fragility: (a) 1st floor, (b) 2nd floor, (c) 3rd floor, (d) 4th floor.

4.1.5 Loss estimation algorithm and the RDAT

The Monte Carlo based algorithm for calculating the decision variables (1) the total time Tp the system operates below $p\%$ capacity, and (2) the total cost TC, in τ, which are used for selecting the optimal rehabilitation alternative is outlined in Figure 4.13. First, for a given event in a lifetime seismic hazard sample damage state probabilities for the structural/nonstructural systems are obtained from their corresponding fragility surfaces (Section 4.1.1.2). We then generate samples of damage states for the structural/nonstructural systems. Next, recovery time and total event cost (consisting of repair, replacement, capacity loss and life losses due to structural/nonstrutural damage)

Table 4.18: Piping system damage states and corresponding consequences per floor.

Damage state	Consequences/disruption	Cost per floor ($) 1	2	3	4
None	No capacity loss.	0	0	0	0
Moderate	System shut down, short period of time. 10% of the beds are lost for one week.	0	45,150	52,500	0
Extensive	System shut down, indefinitely. 25% of the beds are lost for one month.	0	483,750	562,500	0

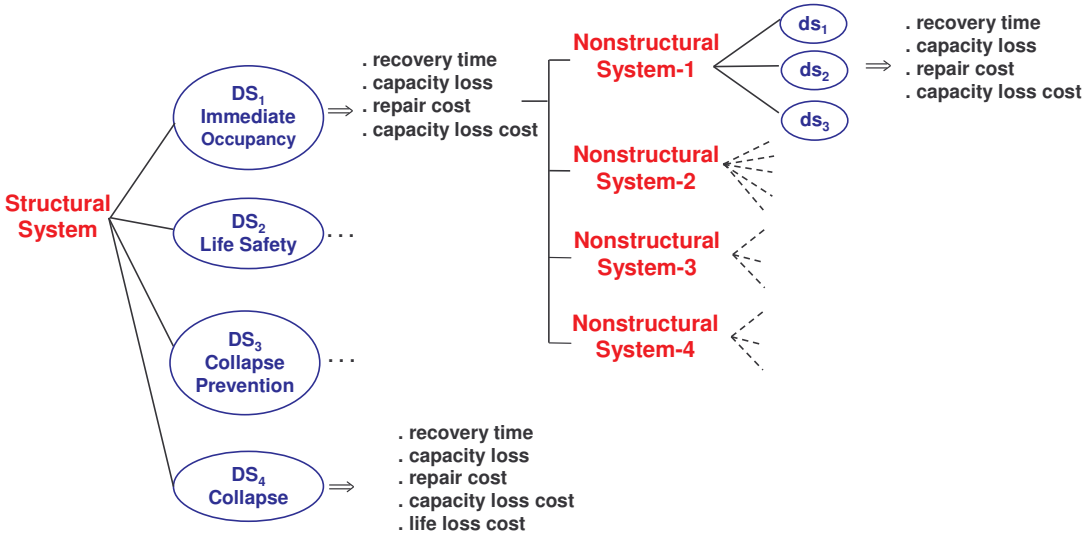

Figure 4.13: Monte Carlo algorithm for loss estimation.

for this event, are obtained from the available consequence/financial information (Sections 4.1.3 and 4.1.3). Recovery times and total event costs from all events in a hazard sample are added to obtain a sample of Tp and TC. The probability laws of Tp and TC are estimated by generating many samples of lifetime seismic hazards and obtaining corresponding values for Tp and TC.

The algorithm in Figure 4.13 is implemented in Rehabilitation Decision Analysis Toolbox (RDAT), a MATLAB based program for calculating the seismic resilience

of structural/nonstructural systems in a health care facility [97]. Using the RDAT it is possible to (i) compare the effectiveness of different rehabilitation alternatives for structural and nonstructural systems using the estimates of life cycle losses, and (ii) develop rational rehabilitation alternatives for increasing the seismic resilience of these systems. RDAT version 1 is limited to linear single degree of freedom structural/nonstructural systems and is available on the MCEER Users Networks [119]. RDAT version 2 extends to linear multi degree of freedom systems and is presented in detail in [97]. The final version of the RDAT with an application to the MCEER West Coast Demonstration hospital will be made available to the MCEER Users Networks by Fall 2007. Appendix E provides some excerpts from the final version RDAT software.

4.1.6 Results

Figure 4.14 (a) and (b) show the marginal probability density functions of the (a)

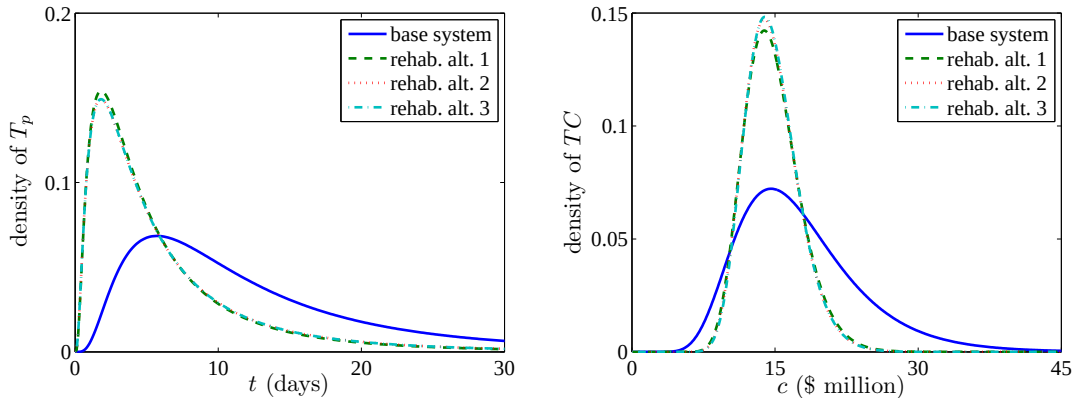

(a) (b)

Figure 4.14: Probability density functions: (a) Tp, (b) TC.

total time Tp the system operates below $p = 90\%$ capacity in $\tau = 50$ years, and (b) total cost TC in $\tau = 50$ years, for the base system and the three rehabilitation alternatives, calculated by Monte Carlo simulation using 1000 samples. Figure 4.15 shows estimates of the joint probability density function of (Tp, TC) in $\tau = 50$ years for the (a) base

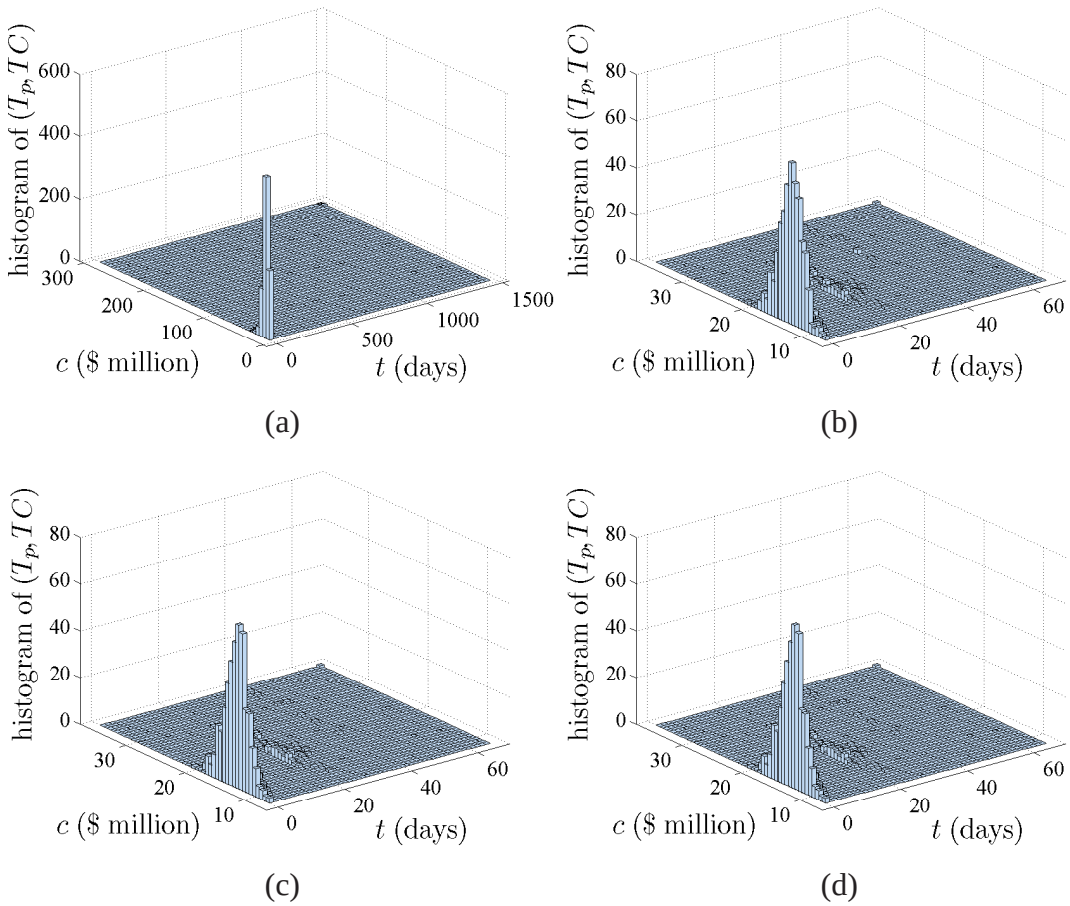

Figure 4.15: Probability density function of (Tp, TC): (a) base system, (b) rehab. alt. 1, (c) rehab. alt. 2, (d) rehab. alt. 3.

system, (b) rehab. alt. 1, (c) rehab. alt. 2, and (d) rehab. alt. 3 calculated by Monte Carlo simulation using 1000 samples.

Figure 4.16 (a) and (b) show $P(Tp > t)$ and $P(TC > c)$. A possible measure for comparing the effectiveness of different rehabilitation alternatives can be the probability that the total time Tp the system operates below 90% capacity exceeds a level t_{cr} (or similarly, the probability that the total cost TC exceeds a level c_{cr}). Accordingly, the optimal solution is the one with the lowest $P(Tp > t_{cr})$ (or $P(TC > c_{cr})$) and depends on the selected value of t_{cr} (or c_{cr}). For example, Figure 4.16 (a) shows that the optimal solutions are rehabilitation alternatives 1, 2 and 3 for $t_{cr} = 30$ days, or Figure 4.16

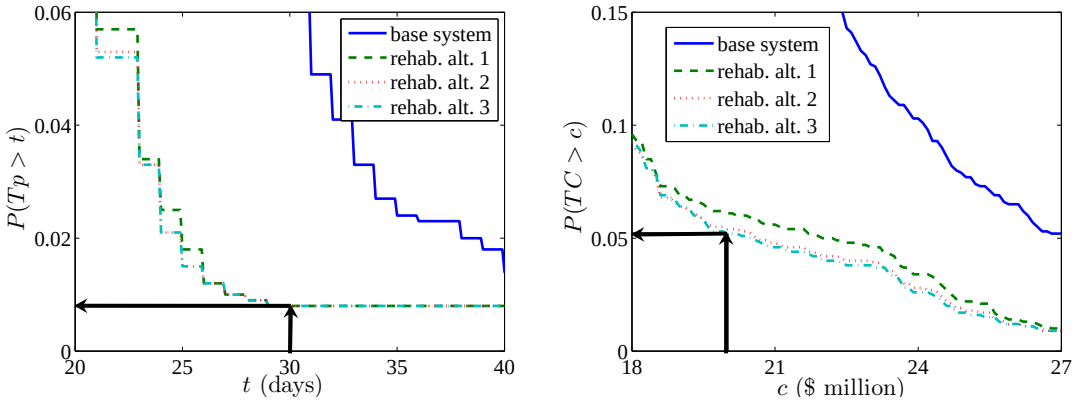

(a) (b)

Figure 4.16: Decision based on (a) Tp or (b) TC.

(b) shows that the optimal solution is the rehabilitation alternative 3 for $c_{cr} = \$20$ million. If both Tp and TC are considered for selecting an optimal solution, then the alternative resulting in the highest $P(Tp \leq t_{cr}, TC \leq c_{cr})$ is the optimal solution. Figure 4.17 shows that for $t_{cr} = 30$ days and $c_{cr} = \$20$ million, the optimal solution is the rehabilitation alternative 3.

The extension of the presented loss estimation method to systems under multiple hazards is immediate. For example, in the case of two independent intermittent hazards, such as seismic and hurricane hazards at a site, the lifetime hazard sample may include three types of events, two individual hazard events and one coincidental hazard event (Section 2.6). For the individual hazard events presented loss estimation method can be directly applied provided that the fragility information of the system for these hazards are readily available (Sections 3.3-3.5). For the coincidental hazard event system fragility under the combined hazards is required. Following section presents an example in which fragility of a simple offshore structure is obtained under coincidental earthquake and sea-storm events. Once the system fragility is calculated lifetime loss estimation can be performed following the presented algorithm.

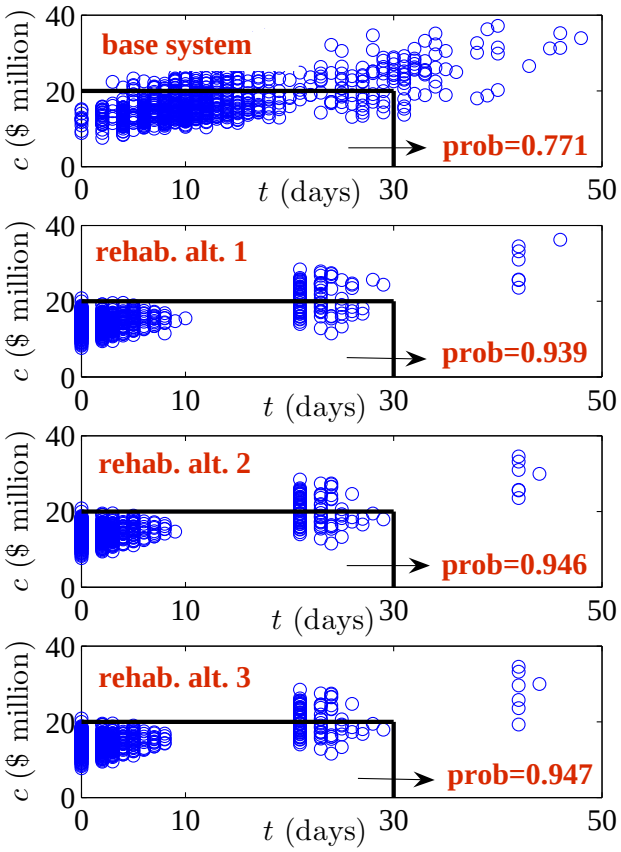

Figure 4.17: Decision based on (Tp, TC).

4.2 Multihazard risk analysis:

Simple offshore structure

Multihazard risk analysis of a system deals with the assessment of the system performance under multiple random loads caused by natural and/or man-made hazards, some of which may occur simultaneously. The main objectives of this section are (1) the development of a methodology for evaluating the performance of a system subjected to several types of natural hazards during a specified time interval and (2) to determine the relative importance of loads caused by these hazards in the system performance. The

system performance is measured by fragility surfaces, that is, the probability of system failure as a function of the parameters which completely define the probability law of the hazards at the system site. Failure occurs when a system response reaches a limit state. The input to the analysis consists of system properties, hazard information, performance criteria and a reference time.

The methodology is presented using a simple offshore platform exposed to seismic and hurricane hazards. System failure probability during its lifetime, namely, life-cycle probability of failure, is calculated for two limit states based on the relative displacement and the total acceleration responses of the deck of the platform. The relative displacement response can be used for assessing the performance of the oil platform, on the other hand, the total acceleration response can be used for the safety analysis of acceleration sensitive secondary systems attached to the deck of the platform.

4.2.1 System information

Figure 4.18 illustrates a simple offshore platform consisting of a deck and three legs. The deck has a rectangular shape with height $h = 5$ m, width $b = 50$ m and length $c = 50$ m. The legs have circular cross sections with diameter $d_c = 3.7$ m and length $l = 60$ m, and are rigidly attached to the sea-bed. The distance from the sea-bed to the mean water surface level is $d = 50$ m.

The platform is modeled as a linear single degree of freedom system with only horizontal motion along the principal (predominant) wind direction $\bar{\theta}$. The rotational motion and vertical drop of the deck are neglected. The modal mass is $m_p = 5.44 \times 10^6$ kg, natural frequency is $\omega_0 = 5$ rad/sec, and damping ratio is $\zeta = 0.04$.

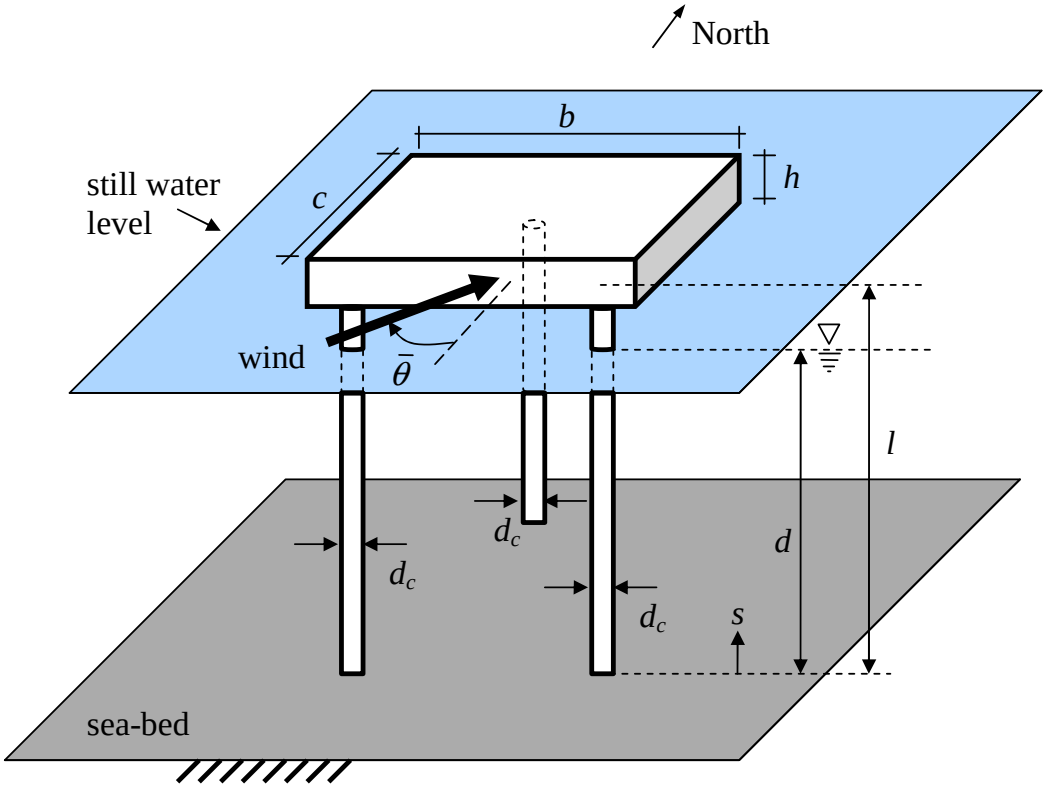

Figure 4.18: Offshore system.

4.2.2 Lifetime environmental loads

It is assumed that the offshore platform is located near the shores of Charleston, South Carolina and that the projected lifetime of the system is $\tau = 50$ years. Loads from earthquakes, winds and wind-induced waves due to hurricanes are considered in this study. Lifetime seismic and hurricane hazards, specifying the random arrival times of individual events at the system site during the projected lifetime τ and the random properties of the events under considerations, are characterized by the probabilistic models in Section 2.3. The random loads resulting from each seismic or hurricane event are defined by the probabilistic event models developed in Section 2.2.

4.2.2.1 Earthquake load

The earthquake load applied to the system due to a seismic event of moment magnitude m and source-to-site distance r is

$$F_1(t; m, r) = -m_p X(t; m, r), \quad 0 \leq t \leq \tau_e, \tag{4.5}$$

where m_p is the modal mass of the offshore platform, $X(t; m, r)$ is the seismic ground acceleration process due to the earthquake with (m, r) given by Equation 2.1 with $e(t) = 1$, $t \geq 0$, and one sided spectral density function $g_{YY}(\omega)$ in Equation 2.3, and τ_e is set to 20 sec arbitrarily. We note that the response of the system to $F_1(t; m, r)$ is approximately stationary at $\tau_e = 20$ seconds since τ_e exceeds 7 periods $2\,\pi/\omega_0 = 2.8431$ seconds of the oscillator ([164], Example 5.5). Accordingly, $F_1(t; m, r)$ is a zero-mean stationary Gaussian process with one-sided spectral density function

$$g_{F_1F_1}(\omega; m, r) = m_p^2\, g_{YY}(\omega; m, r). \tag{4.6}$$

The seismic hazard at the system site during the projected lifetime τ of the system is characterized by the probabilistic lifetime model presented in Section 2.3.4. The model delivers probability laws of the (1) number of seismic events in $[0, \tau]$, (2) temporal distributions of seismic events in $[0, \tau]$, and (3) magnitude M and source-to-site distance R of each of them. The input to the seismic hazard model consists of seismic activity matrix for the site, the projected life τ of the system, and soil properties at the site. The seismic activity matrix for the site gives the mean annual rate of earthquakes for different (M, R). An estimate of the joint probability density function $f_{M,R}(m, r)$ of (M, R) can be obtained from the normalized seismic activity matrix (Section 2.3.4, Equation 2.37). Figure 4.19 shows the seismic activity matrix for Charleston, South Carolina, normalized by $\nu = \sum_{i,j} \nu_{ij} = 0.137$, that is, the joint probability density function of $(\Phi_1 = M, \Phi_2 = R)$ in Equation 2.37. Given that an earthquake occurs at a site, the probability that it has parameters (m_i, r_j) is ν_{ij}/ν.

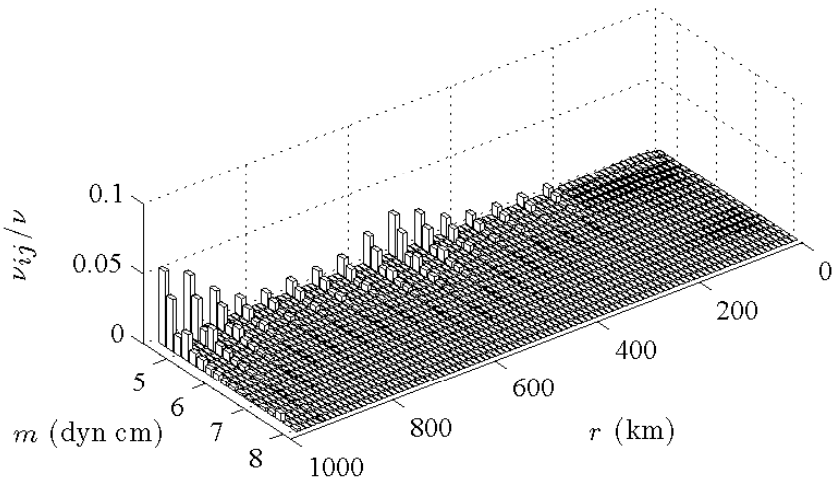

Figure 4.19: Normalized seismic activity matrix for Charleston.

4.2.2.2 Wind load

The wind drag force, that is, the wind force along the principal wind direction $\bar{\theta}$, acting on the deck of the platform due to a hurricane is

$$F_2(t;\bar{v},\bar{\theta}) = \frac{1}{2}\rho_a c_d(\bar{\theta}) a_d(\bar{\theta})(\bar{v} + V(t;\bar{v}))^2, \quad 0 \le t \le \tau_2, \tag{4.7}$$

where $\bar{v}$ is the hurricane mean wind speed in Equation 2.18, $\tau_2 = 1$ hour (see Equation 2.18), $\rho_a = 1.2$ kg/m^3 is the density of air, $c_d(\bar{\theta})$ is the wind drag coefficient given in Figure 4.21, $a_d(\bar{\theta})$ is the exposed area perpendicular to the principal wind direction $\bar{\theta}$ as illustrated in Figure 4.20, and $V(t;\bar{v})$ is the fluctuating wind velocity in Equation 2.18 with one sided spectral density function $g_{VV}(\omega;\bar{v})$ in Equation 2.19. Although the mean wind speed in Equation 4.8 is the wind speed at 10 m above the water surface, it is applied throughout the height range of the deck ([154], Section 2.3.3).

A linearized version of the wind drag force is used in multihazard risk analysis to demonstrate the methodology, although in Section 3.5.1 it was shown that the linear approximation can underestimate significantly the peak response. The linearized wind

drag force is

$$\hat{F}_2(t;\bar{v},\bar{\theta}) = \alpha(\bar{\theta})d_v(\bar{v})[\bar{v} + V(t;\bar{v})]. \tag{4.8}$$

where $\alpha(\bar{\theta}) = [1/2\rho_a c_d(\bar{\theta})a_d(\bar{\theta})]$ and $d_v(\bar{v})$ is the linearized wind drag factor in Equation 3.142 obtained by statistical linearization method, $d_v(\bar{v}) = (3\sigma^2_{V(\bar{v})}\bar{v} + \bar{v}^3)/(\sigma^2_{V(\bar{v})} + \bar{v}^2)$, in which $\sigma^2_{V(\bar{v})} = \int_0^\infty g_{VV}(\omega;\bar{v})d\omega$. Accordingly, $\hat{F}_2(t;\bar{v},\bar{\theta})$ is a stationary Gaussian process with mean

$$\mu_{\hat{F}_2}(\bar{v},\bar{\theta}) = E[F_{2,d}(t;\bar{v},\bar{\theta})] = \alpha(\bar{\theta})d_v(\bar{v})\bar{v}, \tag{4.9}$$

and one-sided spectral density function

$$g_{\hat{F}_2\hat{F}_2}(\omega;\bar{v},\bar{\theta}) = \alpha^2(\bar{\theta})d_v^2(\bar{v})g_{VV}(\omega;\bar{v}). \tag{4.10}$$

In general, the wind acting on the deck of the platform results in two types of forces, the drag force in Equation 4.7 acting along the wind direction, and a lift force acting perpendicular to the wind direction, neglecting the rotational and upward forces, other aeroelastic phenomena such as across-wind galloping, vortex-shedding, and flutter. The lift force has a similar form to the drag force in Equation 4.7 with $c_d(\bar{\theta})$ and $a_d(\bar{\theta})$ replaced by the wind lift coefficient $c_l(\bar{\theta})$ and the exposed area $a_l(\bar{\theta})$ perpendicular to the direction of the lift force, respectively. Figure 4.20 illustrates the direction of wind drag

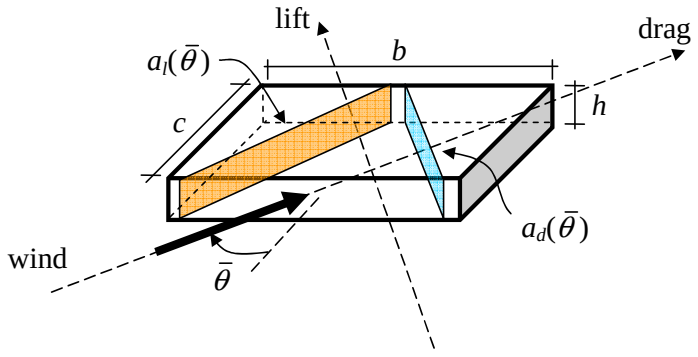

Figure 4.20: Wind drag and lift.

and lift forces and the corresponding exposed areas. The wind drag and lift coefficients, $c_d(\bar{\theta})$ and $c_l(\bar{\theta})$, depend, in general, on the structural shape, the frequency content of the wind velocity and the principal wind direction [154] and can be obtained by wind tunnel tests for the selected structure. For example, Figure 4.21 shows the drag and

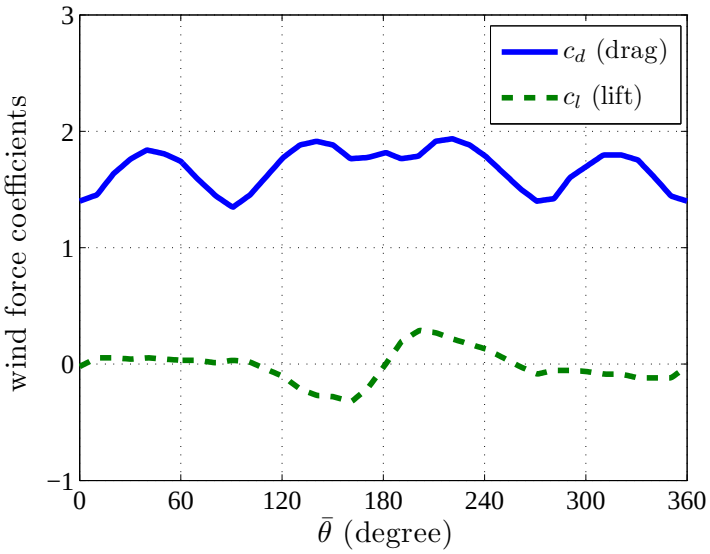

Figure 4.21: Wind drag and lift coefficients (after [154]).

lift coefficients c_d and c_l as functions of the principal wind direction $\bar{\theta}$ for the offshore platform in ([154], Section 14.1.2), which has a similar geometry to the platform under consideration in Figure 4.18. It is observed that the drag coefficient c_d is much larger than the lift coefficient c_l for all directions. It is also noted that $a_d(\bar{\theta}) = a_l(\bar{\theta})$ for all $\bar{\theta}$ since $b = c$ in Figure 4.20. Based on these observations the wind lift force is neglected in the following analysis. The wind drag coefficient c_d in Equation 4.8 is given by Figure 4.21.

The hurricane hazard at the system site during the projected life τ of the system is characterized by the probabilistic lifetime model presented in Section 2.3.5. The model delivers probability laws of the (1) number of events in $[0, \tau]$, (2) temporal distributions of events in $[0, \tau]$, and (3) mean wind speed $\bar{V}$ and principal direction $\bar{\Theta}$ of each of them.

The input to the hurricane hazard model consists of the hurricane activity matrix for the site and the projected life τ of the system. The hurricane activity matrix for the site gives the mean annual rate of hurricanes for different $(\bar{V}, \bar{\Theta})$. The joint probability density function $f_{\bar{V},\bar{\Theta}}(\bar{v}, \bar{\theta})$ of $(\bar{V}, \bar{\Theta})$ can be obtained directly from the normalized hurricane activity matrix (Section 2.16, Equation 2.37). Figure 4.22 shows the wind

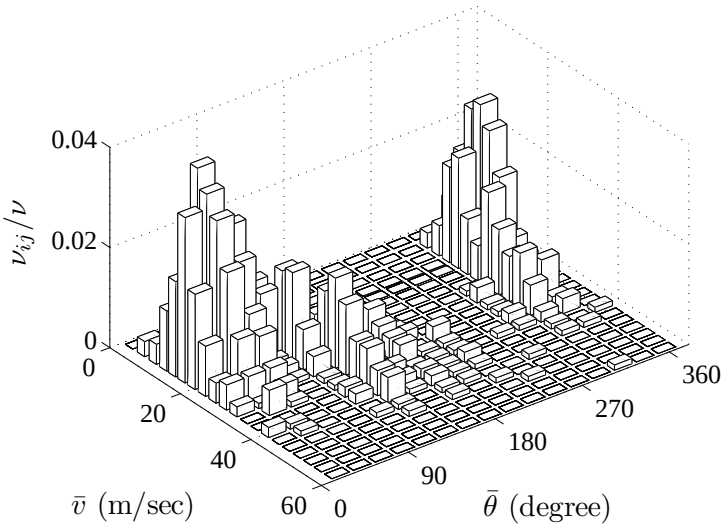

Figure 4.22: Normalized wind activity matrix for Charleston.

activity matrix for Charleston, South Carolina, normalized by $\nu = \sum_{i,j} \nu_{ij} = 0.580$, that is, the joint probability density function of $(\Phi_1 = \bar{V}, \Phi_2 = \bar{\Theta})$ in Equation 2.37. Given that a hurricane occurs at a site, the probability that it has parameters $(\bar{v}_i, \bar{\theta}_j)$ is ν_{ij}/ν.

4.2.2.3 Wave load

The wind-induced wave force acting on a unit section of a leg at an elevation s from the sea-bed is given by the noninteractive Morison equation

$$F_u(t;\bar{v}) = \frac{1}{2}c'_d\rho_w d_c[u_0(s;\bar{v}) + U(t,s;\bar{v})]|u_0(s;\bar{v}) + U(t,s;\bar{v})|$$

$$+ c_m\rho_w\frac{\pi d_c^2}{4}\dot{U}(t,s;\bar{v}), \quad 0 \le t \le \tau_2,$$

where $\bar{v}$ and τ_2 are given in Equation 4.7, $\rho_w = 1000$ kg/m^3 is the density of water, $c'_d = 1$, $c_m = 2$ are drag and inertia coefficients, d_c is the diameter of the leg, and $u_0(s;\bar{v})$ and $U(t,s;\bar{v})$ are the current and the fluctuating wave particle velocities at an elevation s from the sea-bed, given by Equations 2.31 and 2.24, respectively.

As in the wind load model, a linearized version of the wave force in Equation 4.11 is used in multihazard risk analysis to demonstrate the methodology, although in Section 3.5.1 it was shown that the linear approximation can underestimate significantly the peak response. The linearized wave force acting on a unit section of a leg is

$$\hat{F}_u(t;\bar{v}) = a_1 d_u(s)[u_0(s;\bar{v}) + U(t,s;\bar{v})] + a_2\dot{U}(t,s;\bar{v}), \tag{4.11}$$

where $a_1 = (1/2)c'_d\rho_w d_c$, $a_2 = c_m\rho_v(\pi d_c^2)/4$ and $d_u(s;\bar{v})$ is the linearized wave drag factor in Equation 3.140 obtained by statistical linearization method. We note that since U is a zero-mean, stationary, mean-square differentiable process the cross correlation function of between U and $\dot{U}$ have the property $r_{U\dot{U}}(\tau) = -r_{\dot{U}U}(\tau)$ so that the spectral density function of $\hat{F}_u$ can be calculated from

$$g_{\hat{F}_u\hat{F}_u}(\omega,s;\bar{v}) = (a_1 d_u(s))^2 g_{UU}(\omega,s;\bar{v}) + a_2^2 g_{\dot{U}\dot{U}}(\omega,s;\bar{v}), \tag{4.12}$$

in which the spectral density function of the fluctuating wave particle velocity $g_{UU}(\omega,s;\bar{v})$ is obtained from that of the free surface elevation $g_{\eta\eta}(\omega;\bar{v})$ using

$$g_{UU}(\omega,s;\bar{v}) = \omega^2\frac{\cosh^2(ks)}{\sinh^2(kd)}g_{\eta\eta}(\omega;\bar{v}) \tag{4.13}$$

based on the linear wave theory in Equations 2.24 and 2.25, and $g_{\dot{U}\dot{U}}(\omega, s; \bar{v}) = \omega^2 g_{UU}(\omega, s; \bar{v})$. The mean of $\hat{F}_u$ is given by

$$\mu_{F_u}(\bar{v}) = E[F_u(t; \bar{v})] = a_1 d_u(s; \bar{v}) u_0(s; \bar{v}) \tag{4.14}$$

The total linearized wind-induced wave force acting on the three legs is obtained by integrating Equation 4.11 along the submerged length

$$\hat{F}_3(t; \bar{v}) = 3\left[a_1 \int_0^d d_u(s)[u_0(s; \bar{v}) + U(t, s; \bar{v})]ds + a_2 \int_0^d \dot{U}(t, s; \bar{v})ds\right]. \tag{4.15}$$

The mean of $F_3(t; \bar{v})$ is

$$\mu_{\hat{F}_3}(\bar{v}) = E[F_3(t; \bar{v})] = 3a_1 \int_0^d d_u(s; \bar{v}) u_0(s; \bar{v})ds = 3a_1 \frac{c\bar{v}}{d} \int_0^d s d_u(s; \bar{v})ds,$$

in which c is defined in Equation 2.31 and assumed to be 0.03, and its correlation function is

$$\begin{aligned} r_{\hat{F}_3\hat{F}_3}(\tau; \bar{v}) &= E[\hat{F}_3(t; \bar{v})\hat{F}_3(t + \tau; \bar{v})] \\ &= 9E\left[\int_0^d a_1 d_u(s)[u_0(s; \bar{v}) + U(t, s; \bar{v})] + a_2 \dot{U}(t, s; \bar{v})ds \right. \\ &\quad \left. \times \int_0^d a_1 d_u(r)[u_0(r; \bar{v}) + U(t + \tau, r; \bar{v})] + a_2 \dot{U}(t + \tau, r; \bar{v})dr\right], \end{aligned} \tag{4.16}$$

in which k is the wave number given by the linear wave theory in Equation 2.25. The one-sided spectral density function of $\hat{F}_3(t; \bar{v})$ can be obtained by taking the Fourier transform of its correlation function in Equation 4.16. However, although $U(t, s; \bar{v})$ and $\dot{U}(t, s; \bar{v})$ are independent of each other at a given time (as U is a stationary Gaussian process), $U(t, s; \bar{v})$ and $\dot{U}(t + \tau, s; \bar{v})$, as well as $\dot{U}(t, s; \bar{v})$ and $U(t + \tau, s; \bar{v})$, are correlated. Accordingly, calculation of the one-sided spectral density function of $\hat{F}_3(t; \bar{v})$ from its correlation function in Equation 4.16 becomes very difficult. An approximation of the one-sided spectral density function of $\hat{F}_3(t; \bar{v})$ can be obtained from Equations 4.12 and 4.13 assuming that the linearized wave forces in Equation 4.11

acting on different unit sections on a leg are independent of each other, and is given by ([143], Section 7.6)

$$g_{\hat{F}_3\hat{F}_3}(\omega,\bar{v}) = 9g_{\eta\eta}(\omega;\bar{v})\left\{\frac{\omega^2 a_1^2}{\sinh^2(kd)}\left[\int_0^d d_u(s;\bar{v})\cosh(ks)ds\right]^2 + \frac{\omega^4 a_2^2}{k^2}\right\}.$$

Since U is a Gaussian process (Section 2.2.3.1), so is $\hat{F}_3(t;\bar{v})$ and its second moment properties completely define its probability law.

The wave loads are induced by hurricane winds so that the lifetime model for wave hazard is completely defined by the hurricane hazard at the system site given in the previous section.

4.2.3 Fragility analysis

The system fragility under seismic and/or sea-storm activities is calculated for two limit states based on the relative displacement and the total acceleration responses of the deck of the platform. The structural resistances, and accordingly the system limit states, are assumed to be deterministic in this study.

The relative displacement response $Z(t)$ of the simple linear oscillator in Section 4.2.1 representing the platform to earthquake and/or wind and wave loads in Section 4.2.2.1, 4.2.2.2 and 4.2.2.3, respectively, satisfies the differential equation

$$\ddot{Z}(t) + 2\zeta\omega_0\dot{Z}(t) + \omega_0^2 Z(t) = \frac{1}{m_p}Y(t), \quad 0 \le t \le \tau, \tag{4.17}$$

with initial conditions $Z(0) = \dot{Z}(0) = 0$ and m_p, ω_0 and ζ given in Section 4.2.1. For three loading cases, namely, (i) earthquake only, (ii) sea-storm only (wind and wave), and (iii) earthquake and sea-storm, $Y(t)$ and τ in Equation 4.17 are, respectively, (i) $Y(t) = F_1(t;m,r)$ and $\tau = \tau_e$ with $F_1(t;m,r)$ and τ_e in Equation 4.5, (ii) $Y(t) = \hat{F}_2(t;\bar{v},\bar{\theta}) + \hat{F}_3(t;\bar{v})$ and $\tau = \tau_2$ with $\hat{F}_2(t;\bar{v},\bar{\theta})$ and τ_2 in Equation 4.8 and $\hat{F}_3(t;\bar{v})$ in Equation 4.15, and (iii) $Y(t) = F_1(t;m,r) + \hat{F}_2(t;\bar{v},\bar{\theta}) + \hat{F}_3(t;\bar{v})$ and

$\tau = \tau_2$. We note that the third load case assumes that earthquake loads are in the same direction as the wind/wave loads, which yields in conservative results.

The fragility of the linear system in Section 4.2.1 under the earthquake load in Section 4.2.2.1 or combined wind and wave loads in Sections 4.2.2.2 and 4.2.2.3 resulting from a sea-storm is calculated following the methods described in Section 3.1 based on the crossing-theory. Figures 4.23 shows system fragility for displacement limit

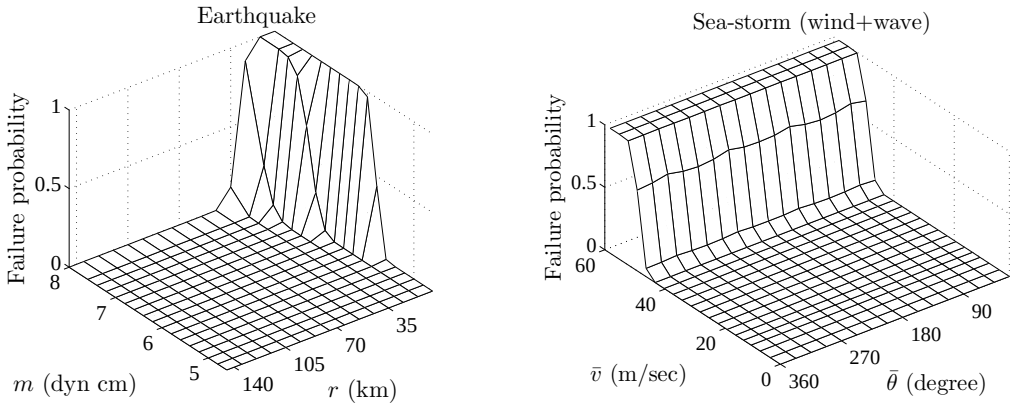

(a) (b)

Figure 4.23: Fragility surfaces for displacement limit state $d = 0.25$ m: (a) Earthquake only, (b) Sea-storm only.

state $d = 0.25$ m under (a) earthquake and (b) sea-storm loads. Similarly, Figure 4.24 shows system fragility for acceleration limit state $a = 1.25$ m/sec^2.

The system fragility under the coincidental load (earthquake and sea-storm) is calculated based on the following observations and assumptions: (1) earthquake and sea-storm events are independent of each other, (2) the probability law of the coincidental event is completely characterized by four parameters, earthquake moment magnitude M, the distance R from the seismic source to the site, sea-storm mean wind speed $\bar{V}$ and direction $\bar{\Theta}$ and (3) the duration of the coincidental event is equal to the duration of the earthquake event. Accordingly, the system fragility can be calculated following the methods described in Section 3.1 based on the crossing-theory and becomes a 4

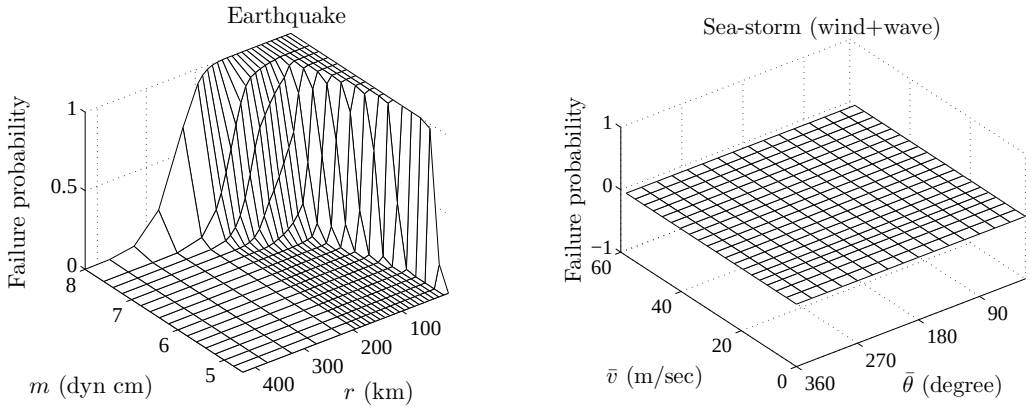

(a) (b)

Figure 4.24: Fragility surfaces for acceleration limit state $a = 1.25$ m/sec^2: (a) Earthquake only, (b) Sea-storm only.

dimensional surface.

The conditional probability that the system response leaves a safe set D, for example, $D = [-d, d]$ for displacement response and $D = [-a, a]$ for acceleration response, given that a hazard event occurs is calculated by convolving the system fragility with the probability law of the parameters defining the event so that

$$P_{f,event} = \int_{\boldsymbol{\phi}} P_f(D; \boldsymbol{\phi}) f_{\boldsymbol{\Phi}}(\boldsymbol{\phi}) d\boldsymbol{\phi}, \tag{4.18}$$

where $\boldsymbol{\Phi}$ is a vector containing the random parameters defining the probability law of the hazard event, $f_{\boldsymbol{\Phi}}(\boldsymbol{\phi})$ is the joint probability density function of $\boldsymbol{\Phi}$, and $P_f(D; \boldsymbol{\phi})$ is the system fragility, that is, the probability that the system response leaves the safe set D when subjected to an event with parameters $\boldsymbol{\phi}$. For a seismic event the joint probability density function of $\boldsymbol{\Phi} = (M, R)$ is approximated by the normalized seismic activity matrix in Figure 4.19. Similarly, the normalized wind activity matrix in Figure 4.22 can be used to approximate the joint probability density function of $\boldsymbol{\Phi} = (\bar{V}, \bar{\Theta})$. Accordingly, for earthquake only and sea-storm only events the conditional probability in Equation 4.18 is obtained by convolving fragility surfaces, for example, in Figure 4.23 (a) and (b) with corresponding normalized activity matrices in Figures 4.19 and 4.22,

respectively.

For a coincidental event the joint probability density function of $\mathbf{\Phi} = (M, R, \bar{V}, \bar{\Theta})$ is obtained by multiplying those of $\mathbf{\Phi} = (M, R)$ and $\mathbf{\Phi} = (\bar{V}, \bar{\Theta})$ since earthquake and sea-storm events are assumed to be independent of each other. The conditional probability in Equation 4.18 for a coincidental load is obtained by convolving the 4 dimensional fragility surface described previously with the joint probability density function of $\mathbf{\Phi} = (M, R, \bar{V}, \bar{\Theta})$. However, it is important to note that the duration of a sea-storm is considerably longer than that of an earthquake, 1 hour versus 20 seconds in our example. Consequently, in case of a coincidental event, in addition to the coincidental load we should also consider the period in which the sea-storm load continues to act alone [17]. Accordingly, for a coincidental event, the conditional probability that the system response leaves the safe set D given that an event occurs becomes

$$P_{f,coevent} = 1 - \left(1 - \int_{m,r,\bar{v},\bar{\theta}} P_f(D; m, r, \bar{v}, \bar{\theta}) f_{M,R,\bar{V},\bar{\Theta}}(m, r, \bar{v}, \bar{\theta}) dm dr d\bar{v} d\bar{\theta}\right) \times \left(1 - \int_{\bar{v},\bar{\theta}} P_f(D; \bar{v}, \bar{\theta}) f_{\bar{V},\bar{\Theta}}(\bar{v}, \bar{\theta}) d\bar{v} d\bar{\theta}\right), \quad (4.19)$$

where $P_f(D; m, r, \bar{v}, \bar{\theta})$ and $P_f(D; \bar{v}, \bar{\theta})$ are the fragilities under the coincidental loads and sea-storm loads only, respectively, and $f_{M,R,\bar{V},\bar{\Theta}}(m, r, \bar{v}, \bar{\theta})$ and $f_{\bar{V},\bar{\Theta}}(\bar{v}, \bar{\theta})$ are the joint probability density function of $(M, R, \bar{V}, \bar{\Theta})$ and $(\bar{V}, \bar{\Theta})$, respectively.

Figures 4.25 and 4.26 show the conditional probability of failure given that an event occurs (earthquake only, sea-storm only, earthquake and sea-strom) against the displacement and acceleration limit states d and a, respectively. Figure 4.25 indicates that when the displacement response is considered different actions can be significant at different reliability levels. If $P_{f,event} > 10^{-3}$ then the sea-storm loads are dominant, if $P_{f,event} < 10^{-4}$ then the earthquake loads are dominant, in between the coincidental loads are relevant. On the other hand, when the acceleration response is considered,

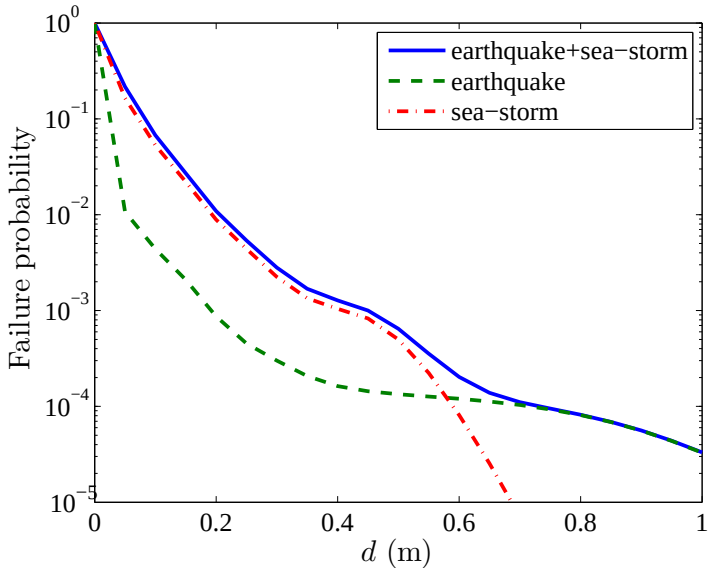

Figure 4.25: Conditional probability of failure per event for displacement limit state.

Figure 4.26 shows that the combined load effect is dominant for all relevant reliability levels.

4.2.4 Lifetime risk analysis

The lifetime failure probability, that is, the probability that a system response R does not exceed a critical level r during its projected lifetime $\tau \geq 0$ due to a single intermittent load event occurring in time according to a homogeneous Poisson counting process $N(\tau)$ of intensity ν is given by

$$P_{f,\tau} = 1 - P_{s,\tau}, \tag{4.20}$$

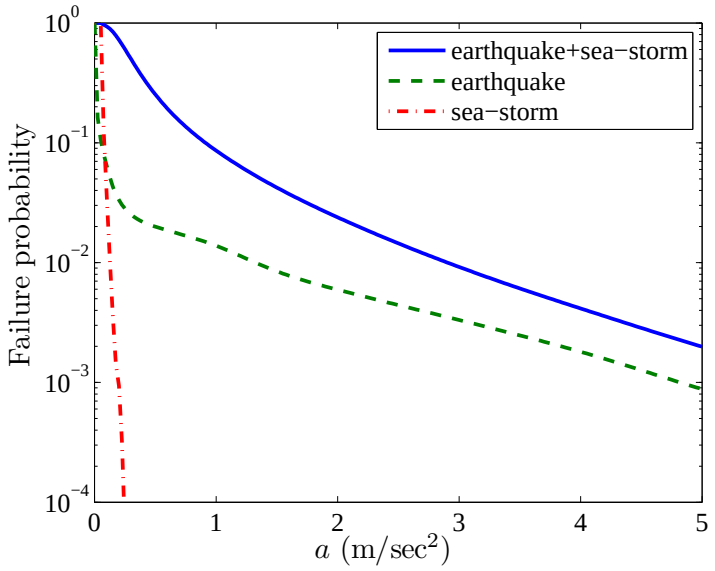

Figure 4.26: Conditional probability of failure per event for acceleration limit state.

where $P_{s,\tau}$ is the probability that the system does not fail in $(0,\tau)$ and equals

$$
\begin{aligned}
P_{s,\tau} &= P\left(\max_{i=1,\ldots,N(\tau)}\{R_i\} \le r\right) \\
&= \sum_{n=0}^{\infty} P\left(\max_{i=1,\ldots,n}\{R_i\} \le r | N(\tau)=n\right) P(N(\tau)=n) \\
&= \sum_{n=0}^{\infty} P\left(\bigcap_{i=1}^{n}(R_i \le r)\right) \frac{(\nu\tau)^n}{n!}\, e^{-\nu\tau} = e^{-\nu\tau}\sum_{n=0}^{\infty} P\left(R_1 \le r\right)^n \frac{(\nu\tau)^n}{n!} \\
&= e^{-\nu\tau}\sum_{n=0}^{\infty} \frac{(\nu\tau P(R_1 \le r))^n}{n!} = e^{-\nu\tau} e^{\nu\tau P(R_1 \le r)} \\
&= e^{-\nu\tau[1-P(R_1 \le r)]}, \qquad (4.21)
\end{aligned}
$$

since the events $\{\max_{i=1,\ldots,n}\{R_i\} \le r\}$ and $\{N(\tau)=n\}$ are independent of each other, and R_i, $i=1,\ldots,n$, are independent and identically distributed. Hence, the lifetime failure probability in Equation 4.20 becomes

$$P_{f,\tau} = 1 - e^{-\nu\tau P_{f,event}}, \qquad (4.22)$$

in which $P_{f,event} = P(R_1 > r)$ is the conditional probability that the system response R_1 exceeds r given that an event occurs and is given by Equation 4.18.

The lifetime failure probability in Equation 4.20 for two independent intermittent loads, occurring in time according to homogeneous Poisson counting processes of intensities ν_1 and ν_2, can be approximated by (Section 2.6)

$$P_{f,\tau} = 1 - \exp\Big[-(\nu_1 P_{f,event-1} + \nu_2 P_{f,event-2} + \nu_{12} P_{f,coevent})\tau\Big], \tag{4.23}$$

in which ν_{12} is given by Equation 2.52, $P_{f,event-i}$ is given by Equation 4.18 for event i, and $P_{f,coevent}$ is given by Equation 4.19.

Figure 4.27 shows lifetime failure probabilities based on displacement limit state for

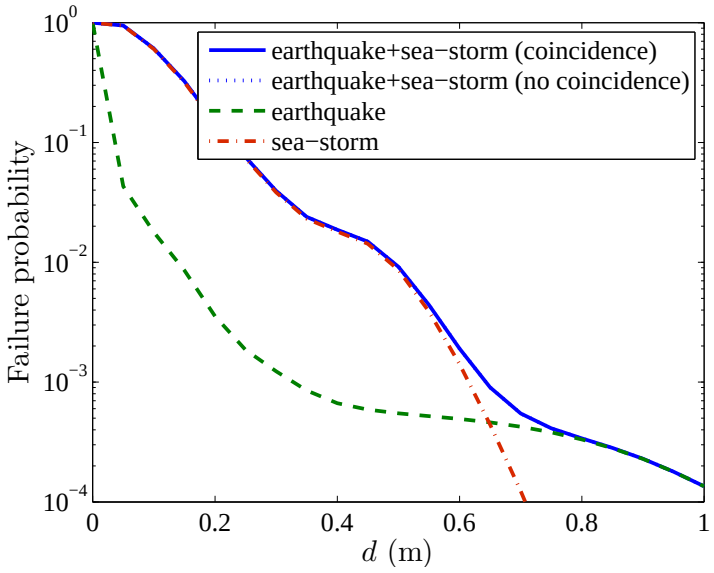

Figure 4.27: Lifetime probability of failure for displacement limit state.

four different load cases, namely, earthquake only, sea-storm only, and earthquake and sea-storm loads with and without coincidence, for $\tau = 30$ years. We observe that (1) the sea-storm load governs the design at low reliability levels and the earthquake load governs at high reliability levels, and (2) the effect of coincidental load on the overall risk is negligible. Figure 4.28 shows similar results for acceleration limit state. In this

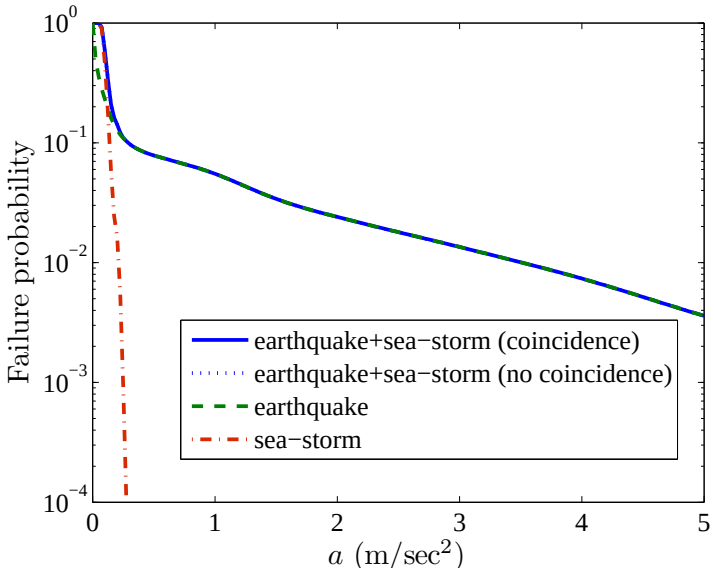

Figure 4.28: Lifetime probability of failure for acceleration limit state.

case only the earthquake load is relevant at all reliability levels.

4.3 Selecting the optimal maintenance strategy for deteriorating systems

An optimal maintenance policy is developed for a deteriorating system under seismic hazard designed for a given lifetime such that (1) the probability that total life-cycle cost exceeds a critical value is minimal, and (2) the system functions at the required performance level during its lifetime. The total life-cycle cost includes costs of replacement and repair due to damage in the system following a seismic event and maintenance related inspection and repair costs. The maintenance policy is defined by the number of inspections, inspection times and inspection quality.

The optimal maintenance policy is obtained by minimizing the total life-cycle cost such that system reliability at any given time t in $(0, \tau)$ is greater than a specified level.

A two-step analysis is performed to establish an optimal maintenance policy. The input to the analysis consists of (1) seismic activity matrix for the site giving the mean annual rate of earthquakes for different magnitudes and source-to-site distances, (2) system fragility surfaces, that is the probabilities that the system enters various damage levels as a function of moment magnitude and site-to-source distance, (3) probability laws of system deterioration rates, (4) required performance level, (5) costs of maintenance, repair and replacement, and (6) a lifetime $\tau > 0$. The first step of the Monte Carlo simulation is used to estimate the total life-cycle cost distribution and system failure probability for a specified number of inspections and inspection times. The second step delivers optimal inspection times under a reliability constraint for a specified number of inspections. The optimal maintenance policy, that is, the optimal number of inspections and inspection times, results by running the second step for several values of the number of inspections.

4.3.1 Seismic hazard

The input to the seismic hazard model consists of site seismic activity matrix, the projected life τ of the system, and soil properties at the site. The site seismic activity matrix delivers the mean annual rate of earthquakes for different magnitudes and source-to-site distances, and it can be constructed directly from the data available from the USGS (see Section 2.3.4 for details). The ground acceleration at the system site for an earthquake with moment magnitude m and source-to-site distance r is modeled by a stationary Gaussian process whose spectral density function is given by the specific barrier model (Section 2.2.1.1, Equation 2.1 with $e(t) = 1,\ t \geq 0$). Monte Carlo algorithms developed in Section 2.4 are used for generating (i) random samples of the seismic hazard at the site during lifetime τ using the using the probabilistic models discussed in Section 2.3, and (ii) seismic ground acceleration samples for these seismic

hazard samples using the probabilistic models discussed in Section 2.2.1.1. Each seismic hazard sample is defined by the number of earthquakes $N(\tau)$ during the lifetime τ, and arrival time T, magnitude M and source-to-site R distance of each earthquake event. Figure 4.29 shows the seismic activity matrix for New York City. Figure 4.30

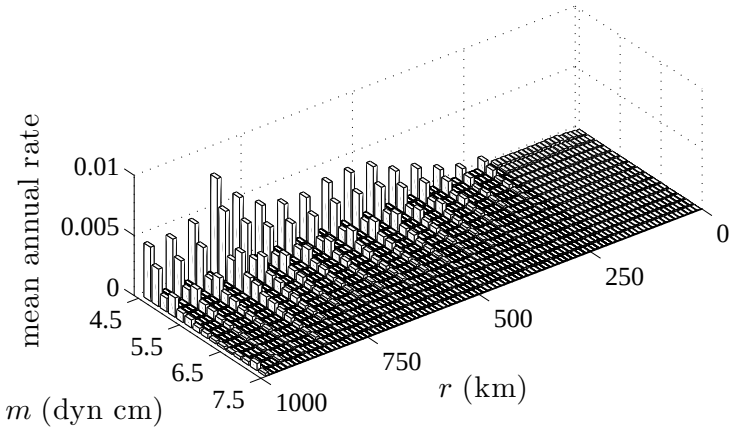

Figure 4.29: Seismic activity matrix for New York City.

shows a sample of seismic hazard scenario in New York City for $\tau = 50$ years.

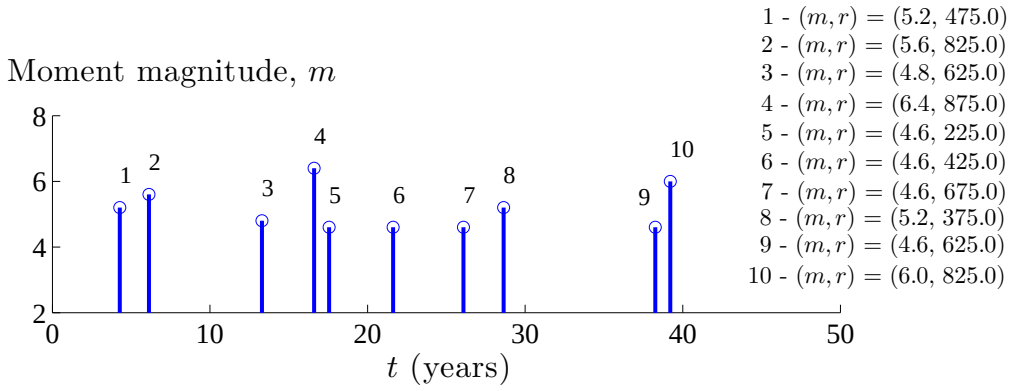

Figure 4.30: A hypothetical sample of the seismic hazard for New York City.

4.3.2 Seismic fragility

Fragility information is used to characterize the damage in the system. Seismic fragility of a system is defined in Section 3.3, where the probability that a system response enters a damage state viewed as a function of the seismic moment magnitude M and the distance from the seismic source to system site R is called system fragility surface. Calculation of fragility surfaces using Monte Carlo simulation and crossing theory of stochastic processes are also presented in Section 3.3. It is assumed that the system fragility increases in time due to deterioration.

Suppose that the seismic performance of the system is measured by its peak displacement response X in time t. The probability that the peak displacement exceeds a critical value given a seismic event characterized by (M, R) is increasing in time due to system deterioration. We assume that system fragility at a time $t > 0$, for limit state x_i, can obtained using

$$P^{(i)}(t) = P(X > x_i | M = m, R = r; t) = \min\{P_0^{(i)} L(t), 1\}, \tag{4.24}$$

where $P_0^{(i)}$ is the seismic fragility at time $t = 0$ for limit state x_i, $L(t)$ is a deterioration function defined below, and x_i, $i = 1, \ldots, m$, are the limit states for the peak response X. It is assumed that a damaged system is brought to its original state after each seismic event so that system fragility for limit state x_i right after an event is given by $P_0^{(i)}$.

In this study we consider a very simple deterioration model to demonstrate our methodology, although complex damage/deterioration models exists in the literature [169, 39]. The deterioration is related to a crack growth. The crack length at a time $t > 0$ is

$$A(t) = A_0 \exp(\Lambda t), \quad t > 0, \tag{4.25}$$

where A_0 denotes the initial crack length and Λ is the rate at which the crack length increases in time. The parameters A_0 and Λ are assumed to be random variables

independent of each other and uniformly distributed in some intervals $(a_{0,1}, a_{0,2})$ and (λ_1, λ_2), respectively, where $0 < a_{0,1} < a_{0,2}$ and $0 < \lambda_1 < \lambda_2$. These properties of A_0 and Λ are denoted by $A_0 \sim U(a_{0,1}, a_{0,2})$ and $\Lambda \sim U(\lambda_1, \lambda_2)$. It is assumed that the deterioration function $L(t)$ in Equation 4.24 has the form

$$L(t) = A(t)/A_0 = \exp(\Lambda t), \quad t > 0. \tag{4.26}$$

Figure 4.31 shows fragility surfaces of a linear single degree of freedom system with

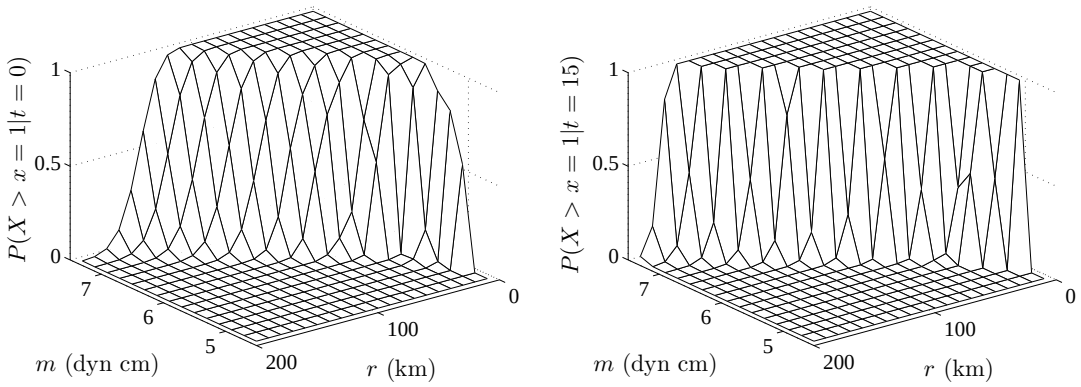

(a) (b)

Figure 4.31: Seismic fragility surfaces at (a) $t = 0$ and (b) $t = 15$ years.

a natural frequency of 5 rad/sec and a damping ratio of 5% at times (a) $t = 0$ and (b) $t = 15$ years, for $\Lambda \sim U(0.1, 0.3)$ and $x = 1$ cm. The fragility surface for $t = 0$ are estimated using the mean crossing rate of the system response (see Section 3.3.1.1 for details). The fragility surface for $t = 15$ years is obtained using Equation 4.24. Let D_k be a discrete random variable characterizing the damage state of the system after seismic event k arriving at time $t = T_k$ and characterized by (M_k, R_k), $k = 1, \ldots, N(\tau)$, where $N(\tau)$ is the number of seismic events in $[0, \tau]$. The damage state of the system following

event k is

$$D_k = \begin{cases} d_1, & \text{with probability} \quad 1 - P^{(1)}(T_k) \\ d_2, & \text{with probability} \quad P^{(1)}(T_k) - P^{(2)}(T_k) \\ \ldots, & \ldots \\ d_m, & \text{with probability} \quad P^{(m-1)}(T_k) - P^{(m)}(T_k) \\ d_{m+1}, & \text{with probability} \quad P^{(m)}(T_k) \end{cases}, \tag{4.27}$$

in which $P^{(i)}(T_k)$, $i = 1, \ldots, m$, is calculated using Equation 4.24.

4.3.3 Probability model for the total life-cycle cost

The following assumptions/constraints define system performance and maintenance policy.

- Cracks of length larger and smaller than $a_1 > 0$ are and are not detected, respectively, that is, we use a unit step probability of detection. Detected cracks are repaired and brought to their initial random length.
- Cracks of length exceeding a critical value $a_2 > 0$ are deemed unsafe, and the system is said to fail with probability $P(A(t) > a_2)$. System with cracks exceeding a_2 is replaced with a nominally identical one, so that its initial state is given by a crack of a random length with the same distribution as A_0 in Equation 4.25 but independent of A_0.
- Peak seismic responses smaller and larger than $x_1 > 0$ cause no damage and moderate damage, respectively. Damaged system is repaired and brought back to its original state after the seismic event.
- If the peak seismic response exceeds a critical value $x_2 > 0$, the system has extensive damage. An extensively damaged system is replaced with a nominally

identical one.

- System probability of failure $P(A(t) > a_2)$ remains below a critical value $p_{cr} \in (0, 1)$ at all times during the design life $[0, \tau]$.
- Connection between the peak system response X and the crack length $A(t)$ is not explicitly defined in this model, rather, it is implicit through Equation 4.24, where the probability law of X is given as a function of the deterioration function $L(t)$, which is in turn a function of the crack length $A(t)$.

Some of these assumptions can be relaxed. For example, complex damage or deterioration models can be used in place of Equations 4.25 and 4.26 [169, 39], the binary detection function considered here can be replaced with some probability of detection curves, and system response can be explicitly related to the crack length.

Figure 4.32 illustrates the proposed algorithm for total life-cycle cost calculation for

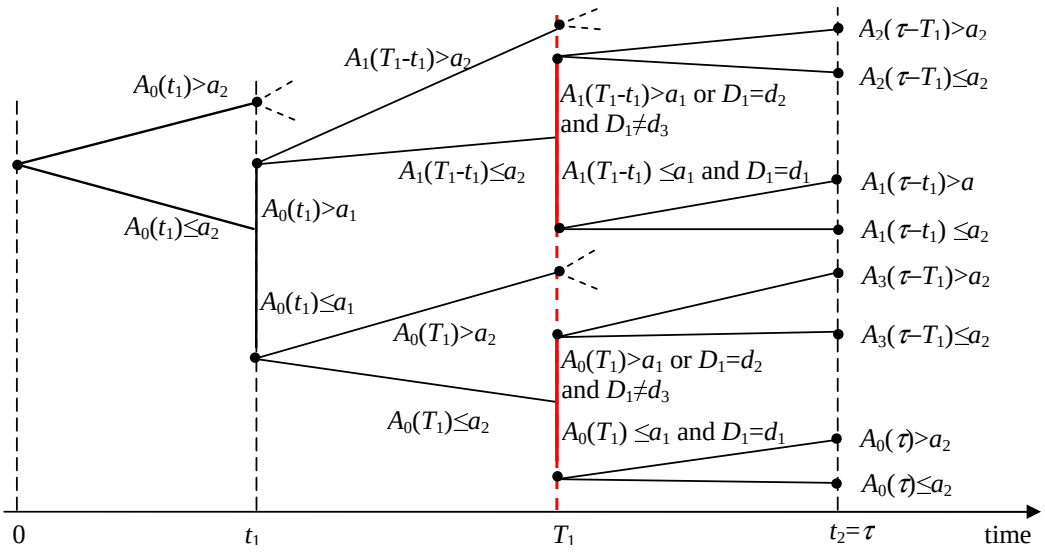

Figure 4.32: Inspection and maintenance policy.

$n = 2$ inspection times t_1 and t_2 such that $0 < t_1 < t_2 = \tau$, and a seismic hazard sample with a single event with magnitude M_1, source-to-site distance R_1 and arrival

time T_1, such that $t_1 < T1 < \tau$. The second inspection at $t = t_2 = \tau$ is required to ensure that the reliability constraint is not violated at τ, that is, the system probability of failure $P(A(\tau) > a_2)$ at τ remains below the critical value p_{cr}. Accordingly, no repair/replacement is required after the last inspection.

- **At time $t = t_1$:** The crack length at the first inspection time $t = t_1$ is the random variable $A(t_1) = A_0 \exp(\Lambda t_1)$. The system fails and survives at time $t = t_1$ with probabilities $P(A(t_1) > a_2)$ and $1 - P(A(t_1) > a_2)$, respectively. If the system fails, that is, the event $A(t_1) > a_2$ is observed, it is replaced with a new system characterized by an initial crack of random length with the same distribution as A_0 in Equation 4.25 but independent of A_0. Accordingly, the original cycle beginning at time $t = 0$ is restarted at time $t = t_1$, and this fact is illustrated in Figure 4.32 by the dotted lines. Similarly, the dotted lines $t = T_1$ indicate initiation of a damage cycle resembling the original cycle but starting at time $t = T_1$. If the system survives, that is, under the event $A(t_1) \leq a_2$, the crack may or may not be detected depending on its length. If $A(t_1) \leq a_1$, the crack is not detected so that it will continue to grow reaching the length $A(T_1) = A_0 \exp(\Lambda T_1)$ at the occurrence of the seismic event at $t = T_1$. If the crack is detected, it is repaired and brought to its initial random state, so that its length is A_0' following repair and $A_0' \exp(\Lambda'(T_1 - t_1))$ at T_1, where A_0' and Λ' are independent copies of A_0 and Λ , respectively. Irrespective of the system damage state there is a cost c_i associated with the inspection performed at time $t = t_1$. The inspection cost may or may not be augmented depending on the crack length and an associated repair/replacement cost. If $A(t_1) > a_2$, the system needs to be replaced by a nominally identical system so that total cost at time $t = t_1$ is $c_i + c_f$. If $A(t_1) \leq a_2$, the system survives. Under the surviving event, there are two possibilities. If $A(t_1) > a_1$, damage is detected and repaired, so that the total cost at time $t = t_1$ is $c_i + c_{r,m}$.

If $A(t1) \leq a_1$, damage is not detected, so that no action is taken and the total cost at time $t = t_1$ is c_i.

- **At time $t = T_1$:** An unscheduled inspection is done following the seismic event occurring at time $t = T_1$. The failure or survival of the system depends of the crack length at time $t = T_1^-$, that is, prior to the seismic event, as well as the damage caused by the seismic event occurring at $t = T_1$. The crack length at time $t = T_1^-$ is the random variable $A(T_1^-) = A_0 \exp(\Lambda T_1^-)$ or $A_0' \exp(\Lambda'(T_1^- - t_1))$ with probabilities $P(A(T_1^-) \leq a_1)$ and $P(A(T_1^-) > a_1)$, respectively. The damage state of the system at time $t = T_1^+$, that is, right after the seismic event, is the discrete random variable D_1 taking values d_1, d_2, and d_3 with probabilities $1 - P^{(1)}(T_1^+)$, $P^{(1)}(T_1^+) - P^{(2)}(T_1^+)$, and $P^{(2)}(T_1^+)$, respectively, (Equations 4.24 and 4.27). The damage states d_1, d_2, and d_3 corresponds to no damage, moderate damage and extensive damage, respectively. Again, the inspection cost may or may not be augmented depending on the crack length and the damage state of the system. If $A(T_1^-) > a_2$ or $D_1 = d_3$, the system needs to be replaced by a nominally identical system so that total cost at time $t = T_1$ is $c_i + c_f$. If $A(T_1^-) \leq a_2$ and $D_1 \neq d_3$, the system survives. Under the surviving event, there are four possibilities. If $A(T_1^-) > a_1$ and $D_1 = d_1$, only damage due to deterioration is detected and repaired, so that the total cost at time $t = T_1$ is $c_i + c_{r,m}$. If $A(T_1^-) \leq a_1$ and $D_1 = d_2$, only damage due to the earthquake is detected and repaired, so that the total cost at time $t = T_1$ is $c_i + c_{r,e}$. If $A(T_1^-) > a_1$ and $D_1 = d_2$, both damages are detected and repaired, so that the total cost at time $t = T_1$ is $c_i + c_{r,m} + c_{r,e}$. If $A(T_1^-) \leq a_1$ and $D_1 = d_1$ damage is not detected, so that no action is taken and the total cost at time $t = T_1$ is the inspection cost c_i. This approach assumes that the crack length is not affected by a seismic event, but system damage due to a seismic event depends on the crack

length at the time of the event. This assumption is admittedly questionable but is invariably made for purposes of developing a practical approach.

- **At time $t = t_2 = \tau$:** No repair/replacement is required at the last inspection time. The only cost considered at time $t = \tau$ is the inspection cost c_i.

Similar considerations can be used to complete the cost analysis for any number of inspection times and seismic events. The model presented here can be used to calculate the distribution of life-cycle cost and the evolution of failure probability in time.

Estimates of the total cost distribution at time τ and of the time evolution of system failure probability can be obtained using Monte Carlo simulation. The algorithm is based on the following considerations. Let $A_0(\omega)$ and $\Lambda(\omega)$ be samples of the initial crack length A_0 and crack growth rate Λ. Depending on the values of $A_0(\omega)$, $\Lambda(\omega)$, the number n of inspections and the inspection times $(t_1, \ldots, t_n)$, and the number of seismic events, the system will evolve along one of the possible distinct damage paths. Figure 4.32 shows these paths for $n = 2$ inspections and $N(\tau) = 1$ seismic event. Let $TC(\omega)$ denote the discounted total life-cycle cost collected over the sample ω. Repeating the above analysis for n_s independent samples, we obtain n_s cost samples $TC(\omega)$, $\omega = 1, \ldots, n_s$. Hence cost histograms and other cost statistics depending on user's objectives can be calculated from the cost samples. Also, estimates for the evolution of system failure probability $P(A(t) > a_2)$ in the time interval $[0, \tau]$ can be calculated. Since $P(A(t) > a_2)$ is an increasing function of time between consecutive inspection times, we only need the values of these probabilities at inspection times, that is, the probabilities $P(A(t_k) > a_2)$, $k = 1, \ldots, n$, for the optimization algorithm in the following section.

Consider a system located in New York City designed for a lifetime $\tau = 50$ years. The system is a linear oscillator with a natural frequency = 5 rad/sec and a damping ratio = 5%. The limit states on the maximum displacement response are $x_1 = 1$, $x_2 = 4$

cm. Suppose that the maintenance policy consists of 4 inspections taking place at the times $(t_1 = 5, t_2 = 20, t_3 = 35, t_4 = 50)$ years. Detectable and critical crack lengths are $a_1 = 2$ and $a_2 = 6$, respectively, and the damage model in Equation 4.25 has the parameters $(a_{0,1} = 0, a_{0,2} = 1)$ and $(\lambda_1 = 0.1, \lambda_2 = 0.3)$. The inspection, maintenance and earthquake related repair and replacement costs are $c_i = 2$, $c_{r,m} = 10$, $c_{r,e} = 30$, and $c_f = 100$, respectively. The discount rate is 5%. Figure 4.33 shows the histogram of the

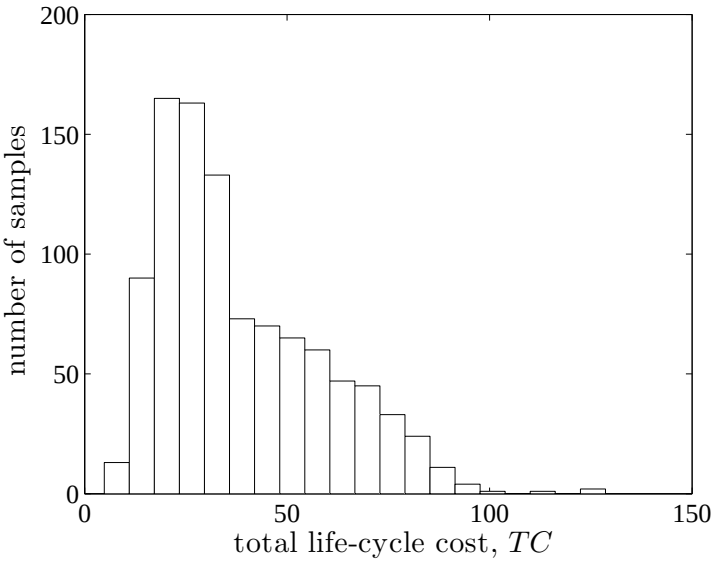

Figure 4.33: Histogram of the total life-cycle cost TC.

total life-cycle cost TC obtained using $n_s = 1000$ samples. System failure probability in $[0, t_1]$, that is, the probability that the crack length exceeds a_2 in this time interval, can be estimated by

$$\hat{P}_f(t) = \frac{\sum_{\omega=1}^{n_s} 1\left(A(t,\omega) > a_2\right)}{n_s}, \quad t \in [0, t_1], \tag{4.28}$$

where $1(B) = 1$ or $1(B) = 0$ if the event B or the complement of B occurs, respectively. Similar calculations can be used to estimate the system failure probability $P_f(t)$ at any time in $[0, \tau]$. Figure 4.34 shows the time evolution of an estimate $\hat{P}_f(t)$ of the failure probability $P_f(t) = P(A(t) > a_2)$ calculated for the same parameters

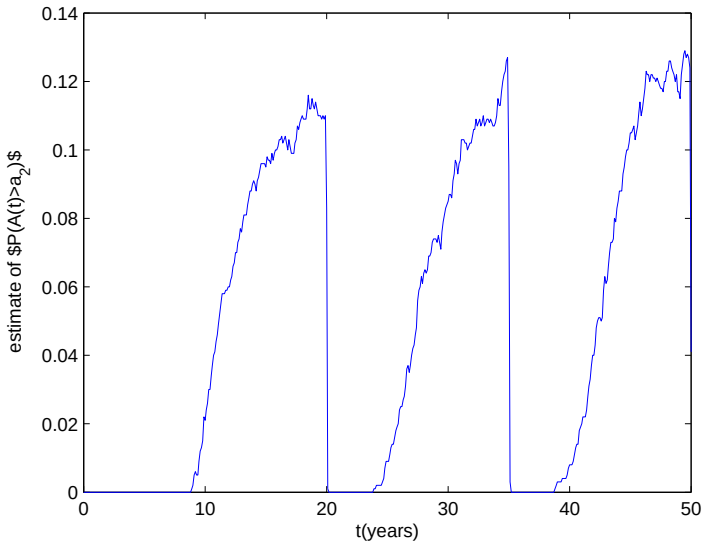

Figure 4.34: Evolution of probability of failure in time.

as in Figure 4.33. The probabilities $\hat{P}_f(t)$ have negative jumps at inspection times and are increasing functions between consecutive inspection times. Estimates of the system failure probability, that is the probability that the crack length exceeds a_2, at the inspection times t_1, t_2, t_3, and t_4 are $P(A(t_1) > a_2) = 0$, $P(A(t_2) > a_2) = 0.105$, $P(A(t_3) > a_2) = 0.128$ and $P(A(t_4) > a_2) = 0.123$, respectively.

4.3.4 Optimization problem

Suppose that the time interval $[0, \tau]$ and the number of inspections n in this interval are fixed. Let $c^* > 0$ and $p_{cr} \in (0, 1)$ denote a critical cost and a target failure probability, respectively. The probability $q_n(c; t_1, \ldots, t_n)$ that the total life-cycle cost in τ exceeds a value $c > 0$ under inspection times $(t_1, \ldots, t_n = \tau)$ can be obtained from the cost histograms developed in the previous section, for example, Figure 4.33.

Our main objective is the selection of optimal inspection times, that is, inspection times that minimize cost in some sense under the condition that system reliability

does not fall below an acceptable level, for given number of inspections n. This objective can be achieved by solving a constraint optimization problem requiring to minimize the objective function $q_n(c; t_1, \ldots, t_n)$ under the constraint that the system failure probability remains smaller than p_{cr} during the time interval $[0, \tau]$, that is, the problem

$$\underset{t_1,\ldots,t_n}{\text{minimize}} \{q_n(c^*; t_1, \ldots, t_n)\}, \quad \text{with} \tag{4.29}$$

$$t_0 = 0 < t_1 < t_2 < \ldots < t_n = \tau, \quad \text{and}$$

$$P(A(t_k) > a_2) < p_{cr}, \quad k = 0, 1, \ldots, n.$$

As previously stated, it is sufficient to impose the condition that the system failure probability is smaller than p_{cr} only at inspection times since this probability increases with time between consecutive inspection times, see Figure 4.34.

The objective function $q_n(c^*; t_1, \ldots, t_n)$ in Equation 4.29 can be replaced with other functions. For example, we may minimize cost expectation, variance, or some higher order moments of cost. The assumption that the number of inspections n is specified simplifies calculations significantly, but is restrictive. To circumvent this restriction, the above algorithm needs to be applied for increasing values of n to identify the optimal number of inspections n_{opt} and the corresponding optimal inspection times $(t_1^{opt}, \ldots, t_n^{opt})$. The resulting optimal number of inspections and corresponding optimal inspection times minimize $q_n(c^*; t_1, \ldots, t_n)$ under the constraint $P(A(t_k^{opt}) > a_2) < p_{cr}$, $k = 0, 1, \ldots, n$, for $n = n_{opt}$.

Figure 4.35 (a) shows the feasible region in the (t_1, t_2) space for the case in which two inspections are scheduled in $(0, \tau)$ and one inspection is scheduled for $t = \tau$. The feasible region is defined by the constraints on the system failure probability $P(A(t) > a_2)$ in Equation 4.29. The figure also shows the optimal inspection times (t_1^{opt}, t_2^{opt}). Results are for no seismic activity, $n = 3$, $c^* = 75$, $p_{cr} = 0.10$, $\tau = 50$, $a_1 = 5$,

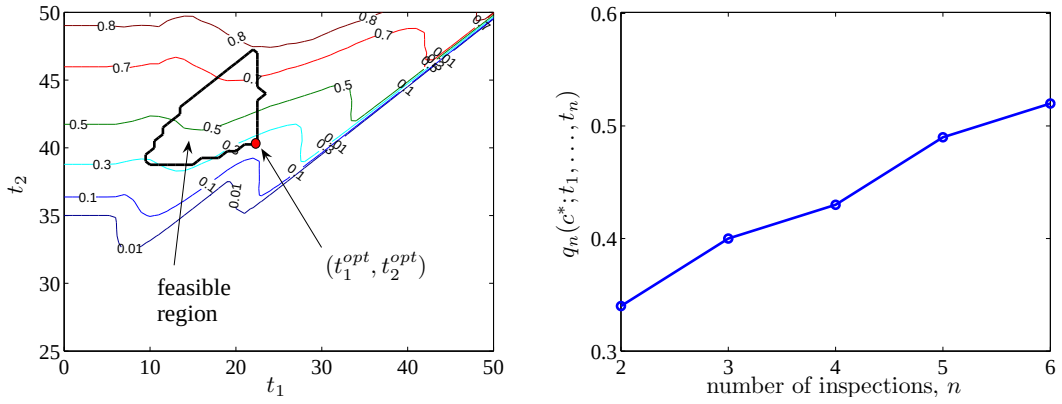

(a) (b)

Figure 4.35: Optimal inspection number and inspection times.

$a_2 = 300$, $(a_{0,1} = 0, a_{0,2} = 1)$, $(\lambda_1 = 0.1, \lambda_2 = 0.3)$, $c_i = 5$, $c_{r,m} = 40$, $c_f = 500$, and are based on $n_s = 10,000$ samples. Figure 4.35 (b) shows the dependence of the optimal values of $q_n(c^*; t_1, \ldots, t_n)$ on the number of inspections for the parameters in Figure 4.35 (a), except for the value of n. There is no solution for $n = 1$ since the constraints $P(A(t_1) > a_2) < p_{cr}$ cannot be satisfied. The optimal inspection strategy for this example is two inspections performed at $(t_1^{opt} = 13.55, t_2^{opt} = 27.54)$ and last inspection performed at $t = \tau = 50$.

Chapter 5
Conclusions and future work

5.1 Conclusions

The main objectives of this study were (1) developing a methodology for assessing performance of structural/nonstructural systems subjected to multiple hazards during their lifetimes and (2) identifying a rational strategy from a collection of design alternatives for increasing the resilience of these systems. System performance was measured by (i) lifetime total losses, that is, rehabilitation and repair/replacement costs and capacity and life losses, caused by hazard events, and (ii) system fragility, that is, the probability that a system response exceeds a critical value subjected to a hazard event of known intensity. The methodology was based on site hazard analysis, system fragility analysis and capacity/cost estimation. Estimates of losses, referred to as life cycle losses, were derived from hazard characteristics of the system site, system fragility information and financial models.

Probabilistic lifetime hazard models were used to specify (i) the random arrival times of individual hazard events, such as earthquakes and hurricanes, at the system site during its lifetime, and (ii) the random properties, for example, magnitude and source-to-site distance for an earthquake, or, mean wind velocity and predominant wind direction for an hurricane, of the individual hazard events under considerations. Probabilistic event models were used for characterizing the probability law of the load processes acting on the system due to an individual or combined hazard event. Accordingly, a natural hazard event at a site, such as seismic ground acceleration or wind velocity, was characterized by a random process with a probability law derived from measurements and/or analytical

models. Also, Monte Carlo algorithms were developed for generating samples of these natural hazards. For a system in a multihazard environment the occurrence of both individual and coincidental hazard events were considered.

We have presented two methods for estimating system fragility, crossing theory of stochastic processes and Monte Carlo simulation. We have shown that fragility information of a simple linear system under stationary band-limited loads can be efficiently calculated by the sampling theorem. Also, we have shown that the current approach of plotting system fragility against a single hazard intensity parameter can be inadequate for some systems.

The proposed models were implemented in computer programs and the life-cycle risk analysis methodology was illustrated through numerical examples. In the first example MCEER West Coast Demonstration Hospital was analyzed to identify an optimal rehabilitation strategy with respect to total life-cycle losses using the concepts of seismic activity matrix and fragility surfaces. It was shown that proposed retrofitting alternatives do not change the mean value of the life-cycle costs significantly, however, the probability of exceeding large costs was lower for the retrofitted systems. The life-cycle loss estimation methodology for a hospital system under seismic hazard was implemented in Rehabilitation Decision Analysis Toolbox (RDAT), a MATLAB based program for calculating the seismic resilience of structural/nonstructural systems in a health care facility. Using the RDAT it is possible to (i) compare the effectiveness of different rehabilitation alternatives for structural and nonstructural systems using the estimates of life cycle losses, and (ii) develop rational rehabilitation alternatives for increasing the seismic resilience of these systems. The second example discussed the case of a typical offshore platform under earthquake and hurricane hazards. This example demonstrated how different hazards can be dominant at different reliability levels and . The last example presented a method for selecting an optimal maintenance

policy for a deteriorating system by minimizing the total life-cycle cost such that system reliability at any given time is greater than a specified level.

5.2 Suggested future work

Following is a brief list of the suggested future studies:

1. The sampling theorem method presented in this study for estimating statistics of the state of a simple linear system can be extended to nonlinear systems. It has been shown here that the sampling theorem provides a much more efficient method for fragility analysis compared to methods based on the classical Monte Carlo algorithm.
2. The proposed life-cycle risk analysis methodology has been demonstrated using a simple system under the seismic and hurricane hazards. The methodology can be extended to more realistic systems under other types of natural and man-made hazards, such as, floods, wild fires and terrorist attacks, with little modifications.
3. The financial model used in life-cycle loss estimation methodology can incorporate insurance policy conditions so that the results can be directly used for insurance pricing.

Appendix A
Specific barrier model

The seismic source model is the essential ingredient for the ground acceleration models in this study. The model quantifies the radiated seismic energy from a source, that is, the acceleration source spectrum $s(f)$, giving the seismic energy as a function of the frequency f. Current seismic source models include:

1. Single corner frequency model [22, 23]:

$$s(f) = (2\pi f)^2 \frac{m_0}{1 + \left(\frac{f}{f_c}\right)^2} \tag{A.1}$$

   where m_0 is the seismic moment and f_c is the corner frequency given by

$$f_c = 4.9\, 10^6\, \beta \left(\frac{\Delta\sigma}{m_0}\right)^{1/3} \tag{A.2}$$

   with $\Delta\sigma$ being the stress drop of the seismic event.

2. Two corner frequency model [10]:

$$s(f) = (2\pi f)^2 m_0 \left[\frac{1-\varepsilon}{1+(f/f_a)^2} + \frac{\varepsilon}{1+(f/f_b)^2}\right] \tag{A.3}$$

   where, for $m_0 \geq 4$:

$$\log \varepsilon = 2.52 - 0.637\, m_0$$

$$\log f_a = 2.41 - 0.533\, m_0$$

$$\log f_b = 1.43 - 0.188\, m_0$$

and when $m_0 < 4$:

$$\varepsilon = 1$$

$$\log f_a = 2.678 - 0.5\, m_0$$

$$\log f_b = 2.678 - 0.5\, m_0$$

3. Another Two corner frequency model [71]:

$$s(f) = (2\pi f)^2 m_0 \left[\frac{1}{(1 + (f/f_a)^8)^{1/8}} + \frac{1}{(1 + (f/f_b)^8)^{1/8}} \right] \qquad \text{(A.4)}$$

where

$$\log f_a = 2.3 - 0.5\, m_0$$

$$\log f_b = 3.4 - 0.5\, m_0$$

4. Specific barrier model [130, 131, 127]: According to the specific barrier model (SBM), a rectangular fault, with dimensions w and l, is assumed to consist of uniformly distributed, equal-size circular regions separated by unbroken barriers that can rupture and release energy. Strong ground motions result when a relatively large collection of circular areas rupture consecutively in a small time interval. Subevents are represented by circular cracks, the ruptures of which start randomly and independently at the center and spread out radially with a constant rupture velocity. The healing phase is initiated after the rupture front arrives at the barrier of the circular region. A wave front (healing front) starts propagating inwards, towards the center. Rupture at a given point in the cracking region stops when the healing front reaches to that point. According to SBM acceleration source spectrum is,

$$s(f) = (2\pi)^2 \sqrt{N \left[1 + (N-1) \left(\frac{\sin(\pi f T)}{\pi f T} \right)^2 \right]} f^2 \tilde{m}_{o_i}(f), \qquad \text{(A.5)}$$

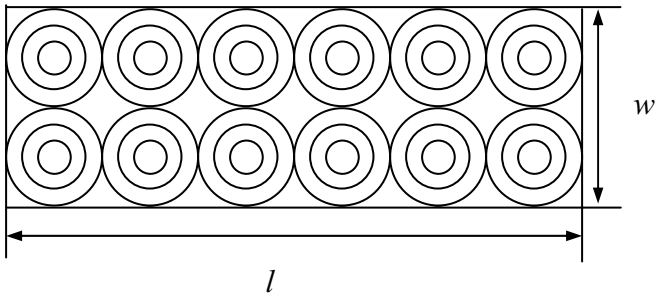

Figure A.1: Illustration of the fault plane according to SBM.

where T is the source duration, N is the number of circular subevents comprising the main event, and $f^2\tilde{m}_{o_i}(f)$ is the source spectrum of the acceleration for an individual subevent, which is defined as

$$f^2\tilde{m}_{o_i}(f) = \frac{m_{o_i} f_2^2}{1 + \left(\frac{f_2}{f}\right)^2}, \tag{A.6}$$

where m_{o_i} is the seismic moment and f_2 is the corner frequency of the subevent.

A single site located very far from a fault is illustrated in Figure A.2. The Fourier amplitude spectrum of the strong ground motion at the site is given by

$$|a(f,r)| = c\, s(f) d(f,r) p(f) z(f) l(f), \tag{A.7}$$

where f is the frequency in Hertz, r is the source-to-site distance, c is a scaling factor, $s(f)$ is the acceleration source spectrum, $d(f,r)$ is the attenuation function, $p(f)$ is the high frequency cut-off filter, $z(f)$ is a function which defines local soil effects at the site and $l(f)$ is a function used to get the desired output (acceleration, velocity or displacement site spectrum). Detailed definitions for c, $s(f)$, $d(f,r)$, $p(f)$, $z(f)$ and $l(f)$ are provided in [74].

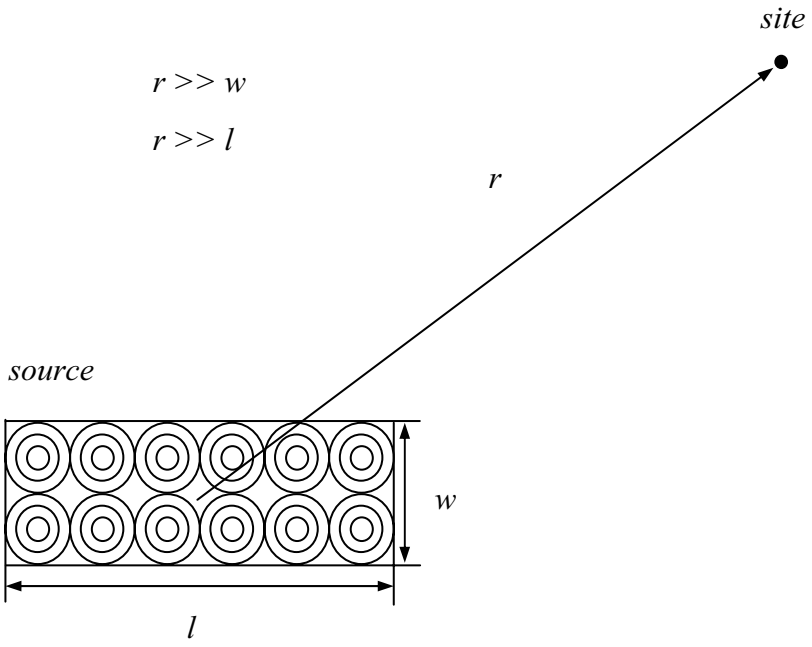

Figure A.2: Illustration of a single site.

The one-sided spectral density function of the strong ground motion process at the site is given by [186]

$$g(\omega, r) = \frac{1}{2\pi t_w} \left| a(\omega, r) \right|^2, \tag{A.8}$$

in which t_w is the duration of motion given by SBM and $|a(\omega, r)|$ is given by Equation A.7 for $\omega = 2\pi f$.

Appendix B
Ground motion statistics

First four moments are calculated for the strong motion part of the free field ground acceleration time histories from Western United States on Pacific Earthquake Engineering Research Center (PEER) Strong Ground Motion Database [133]. It is assumed that the strong ground acceleration records are samples from stationary ergodic series with finite moments. Let $X_1, \ldots, X_n$ denote the strong motion part of a ground acceleration record. The estimates of the mean, variance, skewness and kurtosis are

$$\hat{\mu} = \frac{1}{n}\sum_{i=1}^{n} X_i, \tag{B.1}$$

$$\hat{\sigma}^2 = \frac{1}{n}\sum_{i=1}^{n} (X_i - \hat{\mu})^2, \tag{B.2}$$

$$\hat{\gamma}_3 = \left[\frac{1}{n}\sum_{i=1}^{n} (X_i - \hat{\mu})^3\right] / \hat{\sigma}^3, \tag{B.3}$$

$$\hat{\gamma_4} = \left[\frac{1}{n}\sum_{i=1}^{n} (X_i - \hat{\mu})^4\right] / \hat{\sigma}^4. \tag{B.4}$$

If the sequence $X_1, \ldots, X_n$ is Gaussian, then $\gamma_3 = 0$ and $\gamma_4 = 3$. Notable differences from these values would indicate that $X_1, \ldots, X_n$ is a non-Gaussian series.

The strong motion part of the ground acceleration records is obtained by Husid's plot [85] using the Arias intensity

$$e(t) = \frac{\pi}{2g}\int_0^{t_f} a^2(t)dt, \;\; 0 \leq t \leq t_f, \tag{B.5}$$

where $a(t)$ is the ground acceleration time history, t_f is the total duration of the accelerogram and g is the acceleration due to gravity. The time interval of the strong

part of the seismic ground acceleration, (t_1, t_2), is defined by the conditions

$$e(t_1) = 0.05\, e(t_f) \tag{B.6}$$

$$e(t_2) = 0.95\, e(t_f),$$

following [173, 47].

Soil conditions are essential establishing site amplification functions. Current classifications of soil conditions are discussed in this section. The PEER Strong Ground Motion Database uses Unites States Geological Survey (USGS) soil classes to characterize the site [133]. A more recent and widely used classification is given by National Earthquake Hazard Reduction Program (NEHRP) [55, 118]. The NEHRP and USGS site classifications are based on the average shear wave speed v in the upper 30 meters of a soil profile beneath the site. These two site classifications were developed using strong ground acceleration data recorded in California. Tables B.1 and B.2 show

Table B.1: USGS classification.

Class	$v \quad (m/s)$
A	$v > 750$
B	$360 < v < 750$
C	$180 < v < 360$
D	$v < 180$

the USGS and NEHRP site classifications, respectively. Frankel *et al.* [61] and Boore and Joyner [20] have calculated site amplification functions based on the average of shear wave speed over depth. Halldorsson *et al.* [74] defined alternative soil classes based on the developments in [61] and [20]. Table B.3 shows the site classification

Table B.2: NEHRP classification.

Class	$v \quad (m/s)$	**Soil type**
A	$v > 1500$	hard rock
B	$760 < v < 1500$	rock
C	$360 < v < 760$	very dense soil
D	$180 < v < 360$	stiff soil
E	$v < 180$	soft soil
F	-	special soil requiring site specific evaluation

defined by Halldorsson *et al.* [74] and used in the specific barrier model (SBM). This classification is used in this study to calculate the frequency dependent site amplification functions. Table B.4 presents the relationship between the three classifications.

Strong ground acceleration records from PEER database [133] are divided into four groups according to USGS site classification (Table B.1). Ten records were used in each class, with the exception of class-D for which only four free field acceleration records were available in the database. Tables B.5, B.6, B.7, and B.8 give estimates of mean, skewness and kurtosis coefficients defined in Eq. B.1 for USGS class-A, B, C and D soils, respectively. The means and skewness coefficients are nearly zero suggesting that the marginal density of the ground acceleration process is an even function. Figure B.1 shows the dependence of γ_4 on soil conditions. The average kurtosis coefficients for classes A, B, C and D are 6.26, 5.67, 5.58 and 4.06, respectively. Hence, the ground acceleration records cannot be modeled by Gaussian processes for which γ_4 is 3.

Table B.3: SBM classification.

Class	$v\ (m/s)$	**Soil type**
1	620	generic rock
2	520	very dense soil
3	310	generic soil
4	255	stiff soil
5	2900	generic very hard rock
6	760	rock/hard rock

Table B.4: Site classifications.

SBM	**NEHRP**	**USGS**
1	C	B
2	C	B
3	D	C
4	D	C
5	A	A
6	B-C boundary	A-B boundary

Table B.5: Statistics for records on USGS class-A soil.

Earthquake	**Date**	$\hat{\mu}$	$\hat{\gamma}_3$	$\hat{\gamma}_4$
Anza (Horse Cany)	1980/02/25	-3.2E-04	-0.01	5.08
Anza (Horse Cany)	1980/02/25	-1.5E-04	-0.04	4.32
Cape Mendocino	1992/04/25	1.0E-03	2.53	17.23
Coyote Lake	1979/08/06	-1.0E-04	0.25	5.02
Morgan Hill	1984/04/24	1.1E-04	-0.27	3.61
Hollister	1974/11/28	-1.2E-04	0.49	4.86
Landers	1992/06/28	-9.5E-05	0.14	3.65
Loma Prieta	1989/10/18	1.1E-04	-0.54	6.78
Loma Prieta	1989/10/18	1.7E-04	0.64	6.06
Loma Prieta	1989/10/18	5.0E-06	-0.69	6.01

Table B.6: Statistics for records on USGS class-B soil.

Earthquake	**Date**	$\hat{\mu}$	$\hat{\gamma}_3$	$\hat{\gamma}_4$
Anza (Horse Cany)	1980/02/25	6.4E-05	0.61	6.18
Cape Mendocino	1992/04/25	-1.6E-04	-0.75	6.59
Cape Mendocino	1992/04/25	8.5E-05	0.12	5.14
Cape Mendocino	1992/04/25	-2.2E-05	0.15	6.69
Coyote Lake	1979/08/06	1.0E-04	-0.49	6.02
Loma Prieta	1989/10/18	-5.3E-04	0.10	4.90
Loma Prieta	1989/10/18	6.3E-04	0.07	5.10
Hollister	1986/01/26	1.7E-04	-0.12	5.11
Landers	1992/06/28	2.3E-05	-0.13	4.34
Landers	1992/06/28	1.1E-04	0.31	6.62

Table B.7: Statistics for records on USGS class-C soil.

Earthquake	**Date**	$\hat{\mu}$	$\hat{\gamma}_3$	$\hat{\gamma}_4$
Borrego Mtn	1968/04/09	-5.0E-06	0.24	3.97
Cape Mendocino	1992/04/25	1.5E-03	0.10	7.96
Coalinga	1983/05/02	-3.6E-05	-0.25	5.09
Coalinga	1983/05/02	-5.0E-04	-0.24	3.69
Coyote Lake	1979/08/06	1.8E-04	-0.03	5.75
Coyote Lake	1979/08/06	-2.7E-05	-0.77	7.68
Coyote Lake	1979/08/06	9.0E-06	0.06	7.94
Imperial Valley	1979/10/15	4.3E-05	0.03	2.96
Imperial Valley	1979/10/15	8.6E-04	0.04	4.48
Imperial Valley	1979/10/15	5.2E-04	0.56	6.23

Table B.8: Statistics for records on USGS class-D soil.

Earthquake	**Date**	$\hat{\mu}$	$\hat{\gamma}_3$	$\hat{\gamma}_4$
Loma Prieta	1989/10/18	-1.3E-03	0.29	3.82
Loma Prieta	1989/10/18	-7.8E-05	0.03	3.56
Morgan Hill	1984/04/24	6.8E-04	-0.29	5.09
Morgan Hill	1984/04/24	-5.0E-06	-0.19	3.78

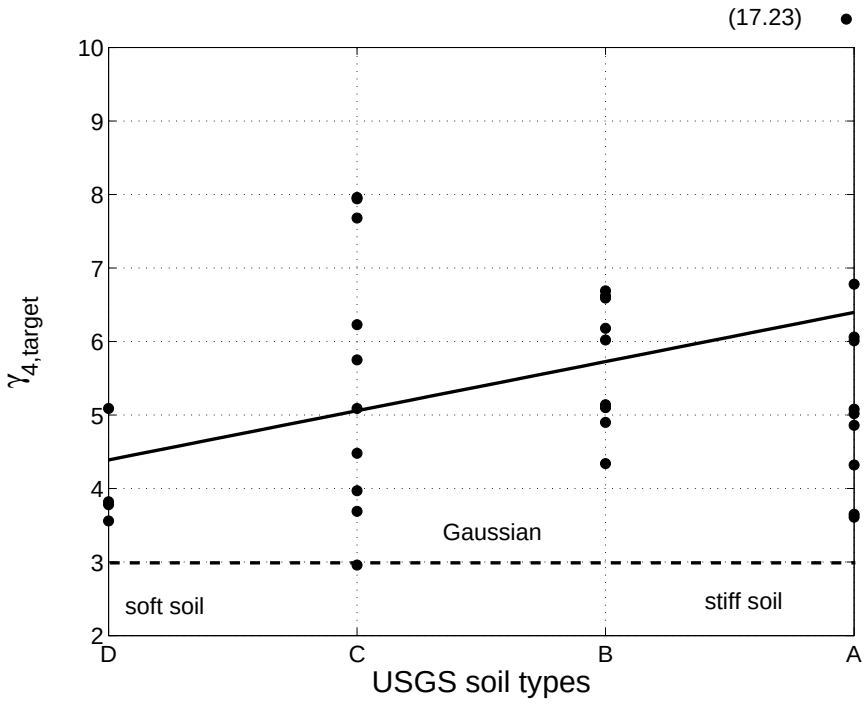

Figure B.1: Change in the kurtosis coefficient with USGS site class.

Appendix C
Spatial variability of seismic motions

There are four different causes of spatial variability of earthquake induced ground motions. The first one is the loss of coherency, a frequency domain measure of spatial variation, due to scattering in the heterogeneous medium as well as the due to the differential superpositioning of seismic waves coming from an extended source, this is referred as the incoherence effect. The second one is called wave passage effect, which is due to the difference in arrival times of seismic waves at separate stations. Third effect is due to the geometric spreading of waves and the energy dissipation in the ground medium, which is called the attenuation effect. Attenuation effect has a little influence on the spatial variability [44]. The last one is the effect of spatially varying soil profile. These effects are characterized by the coherency function, which is a complex valued function defined by

$$\gamma_{jk}(\omega) = \frac{g_{jk}(\omega)}{\sqrt{g_{jj}(\omega) g_{kk}(\omega)}} \tag{C.1}$$

where $g_{jj}(\omega)$ and $g_{kk}(\omega)$ are the power spectral densities of the sites j and k respectively, and $g_{jk}(\omega)$ is the cross power spectral density between the sites. The coherency, $\gamma_{jk}(\omega)$, is commonly written as

$$\gamma_{jk}(\omega) = |\gamma_{jk}(\omega)|\, exp\,[\, i\, \theta_{jk}(\omega)] \tag{C.2}$$

with

$$\theta_{jk}(\omega) = tan^{-1}\left(\frac{I[g_{jk}(\omega)]}{R[g_{jk}(\omega)]}\right) \tag{C.3}$$

where $|\gamma_{jk}(\omega)|$ is referred as the lagged coherency, which removes the directional dependance representing the wave passage effect and $\theta_{jk}(\omega)$ is the phase spectrum in which $I[g_{jk}(\omega)]$ and $R[g_{jk}(\omega)]$ are the imaginary and the real parts of the cross spectral

density function $g_{jk}(\omega)$. Recent empirical studies using data from SMART-I array in Taiwan have shown the effects of incoherence and wave passage on the coherency. Most of the models assume that the random field is isotropic, in addition being homogeneous. As a consequence, the lagged coherency becomes a function of separation distance ξ and frequency ω only and not the direction. Table C.1 shows several lagged coherency models. Table C.2 shows models that take into account the directional dependence (anisotropy) of the spatial variation of the seismic ground accelerations.

Harichandran and Vanmarcke's model [78] is used to define spatial coherency function in this study. The decay of coherency along a particular direction (the incoherence effect) is modeled by $\rho(\vec{\xi_{ij}}, \omega)$ part. Note that $\rho(\vec{\xi_{ij}}, \omega) = \rho(\vec{\xi_{ij}}, -\omega)$ and $\rho(\vec{\xi_{ij}}, \omega) = \rho(\vec{\xi_{ji}}, \omega)$. Dependence of $\rho(\vec{\xi_{ij}}, \omega)$ on the separation distance only, and not on the actual location, implies the homogeneity of the random field. In order to model the observed, unaligned, motions (the apparent propagation, or the wave passage, effect) the phase component, $e^{-i\omega d}$, is added. According to this model alignment changes only the phases, and not the absolute values of coherency, for any pair of accelerogram. This coherency function describes a homogeneous, non-isotropic, space-time random field.

Table C.1: Isotropic coherency models.

Reference	**Coherency function**
Loh [114]	$$\mid \gamma(\xi,\omega) \mid = \exp\left(-a(\omega) \mid \xi \mid\right) \quad \text{(C.4)}$$ where $a(\omega)$ is a function determined from data of Event 5.
Loh and Yeh [116]	$$\mid \gamma(\xi,\omega) \mid = \exp\left(-a\,\frac{\omega \mid \xi \mid}{2\,\pi c}\right) \quad \text{(C.5)}$$ where parameter a is estimated using data of Events 39 and 40.
Loh and Lin [115]	$$\mid \gamma(\xi,\omega) \mid = \exp\left(-a\,\xi^2\right) \quad \text{(C.6)}$$ $$\mid \gamma(\xi,\omega) \mid = \exp\left((-a - b\,\omega^2) \mid \xi \mid\right) \quad \text{(C.7)}$$ $$\mid \gamma(\xi,\omega) \mid = \exp\left(-a - b\,\omega\right) \mid \xi \mid^c) \quad \text{(C.8)}$$ in which parameters a, b and c estimated using SMART-I array data.
Hao *et al.* [77] and Oliveira *et al* [125]	$$\mid \gamma(\xi_l,\xi_t,\omega) \mid = \exp\left(-\beta_1 \mid \xi_l \mid - \beta_2 \mid \xi_t \mid\right)$$ $$\times \exp\left[-(\alpha_1(\omega)\sqrt{\mid \xi_l \mid} + \alpha_2(\omega)\sqrt{\mid \xi_t \mid})\left(\frac{\omega}{2\pi}\right)^2\right] \quad \text{(C.9)}$$ in which ξ_l and ξ_t are the projected separation distances along and normal to the direction of propagation of the motions respectively, $\alpha_i(\omega) = 2\pi a_i/\omega + b_i\omega/(2\pi) + c_i,$ for $i = 1, 2$, and parameters $\beta_i,\ a_i$ and b_i are estimated using SMART-I array data.

Table C.2: Anisotropic coherency models.

Reference	**Coherency function**
Loh and Lin [115]	$\mid \gamma(\xi,\omega) \mid = \exp\left[(-a_1 - b_1\omega^2)\mid \xi\cos\theta \mid\right]$ $\times \exp\left[(-a_2 - b_2\omega^2)\mid \xi\sin\theta \mid\right]$ (C.10) θ is the angle between the direction of the propagation of the waves and the station separation, parameters a_i and b_i for $i = 1, 2$ are estimated using SMART-I array data.
Abrahamson *et al.* [2]	$\tanh^{-1}[\mid \gamma(\xi,\omega) \mid] = (2.54 - 0.012\,\xi)$ $\left[\exp\left(-0.115 - 0.00084\xi\right)\omega + \frac{\omega^{-0.878}}{3}\right] + 0.35$ (C.11) parameters estimated using data from LSST array and are valid for separation distances less than 100 m.
Harichandran and Vanmarcke [78]	$\gamma\left(\vec{\xi_{ij}},\omega\right) = \rho\left(\vec{\xi_{ij}},\omega\right) e^{-i\omega d}$, where (C.12) $d = \frac{\vec{V}.\,\vec{\xi_{ij}}}{\mid \vec{V} \mid^2}$, (C.13) $\rho(\vec{\xi_{ij}},\omega) = A\exp\left(\frac{B}{a\theta(\omega)}\right) + (1-A)\exp\left(\frac{B}{\theta(\omega)}\right)$, (C.14) $B = -2\vert\vec{\xi_{ij}}\vert(1 - A + aA),\ \theta(\omega) = k\left(1 + \left(\frac{\mid\omega\mid}{2\pi f_0}\right)^b\right)^{-1/2}$ (C.15) $\vec{\xi_{ij}}$ is the separation vector between sites i and j, $\vec{V}$ is the apparent velocity vector whose direction coincides with the direction of the site from the source, and parameters A, a, k, f_0, b are estimated using Event 20 of SMART-I array.

Appendix D
Crossing rate of a quadratic form of Gaussian process

The mean z-upcrossing rate of the displacement response

$$Z(t) = \alpha(\bar{v} + V(t))^2, \tag{D.1}$$

of the oscillator in Section 3.4.1 with the notation in Equation 3.92 can be obtained from ([69], Appendix E, Equation E.25)

$$\nu(z)^+ = -\frac{1}{(2\pi)^2}\int_{-\infty}^{\infty} du \exp(-iuz)\int_{-\infty}^{\infty} dv \frac{1}{v}\frac{\partial\varphi(u,v)}{\partial v}, \quad z > 0, \tag{D.2}$$

where $\varphi(u,v) = E[\exp\{i(uZ(t) + v\dot{Z}(t))\}]$ is the joint characteristic function of $\{Z(t), \dot{Z}(t)\}$ given by

$$\begin{aligned}
\varphi(u,v) &= E\left[E\left[\exp\{i(uZ(t) + v\dot{Z}(t))\}|V(t)\right]\right] \\
&= E\left[\exp\{i(uZ(t)\}E\left[\exp\{iv\dot{Z}(t)\}|V(t)\right]\right] \\
&= E\left[\exp\{V^2(t)(iu\alpha - 2v^2\sigma_{\dot{V}}^2\alpha^2) + Y(t)(iu - 2v^2\sigma_{\dot{V}}^2\alpha)2\alpha\bar{v} + iu\alpha\bar{v}^2\right. \\
&\qquad \left. -0.5v^2\sigma_{\dot{V}}^2(2\alpha\bar{v})^2\}\right] \\
&= \int_{-\infty}^{\infty} \exp\left[\xi^2(iu\alpha - 2v^2\sigma_{\dot{V}}^2\alpha^2) + \xi(iu - 2v^2\sigma_{\dot{V}}^2\alpha)2\alpha\bar{v} + iu\alpha\bar{v}^2\right. \\
&\qquad \left. -0.5v^2\sigma_{\dot{V}}^2(2\alpha\bar{v})^2\right] f_V(\xi)d\xi,
\end{aligned} \tag{D.3}$$

in which $f_V(\xi) = 1/(\sqrt{2\pi}\sigma_V)\ \exp(-\xi^2/(2\sigma_V^2))$ is the density of the Gaussian random variable $V(t)$, and $\sigma_V = \int_0^{\bar{\omega}} g_{VV}(\omega)d\omega$ and $\sigma_{\dot{V}}^2 = \int_0^{\bar{\omega}} \omega^2 g_{VV}(\omega)d\omega$ are the variances of $V(t)$ and and $\dot{V}(t) = dV(t)/dt$, with the spectral density function $g_{VV}(\omega)$ of $V(t)$ given

in Equation 2.19. From Equations D.2 and D.3 the mean z-upcrossing rate of $Z(t)$ in Equation D.2 becomes

$$\nu(z)^+ = -\frac{\alpha}{2\pi^2}\frac{\sigma_{\dot{V}}}{\sigma_V}\int_{-\infty}^{\infty} du \exp(-iuz)\int_{-\infty}^{\infty}(\xi+\bar{v})\exp(iu\alpha(\xi+\bar{v})^2)\exp(-\xi^2/(2\sigma_V^2))d\xi. \tag{D.4}$$

The double integral in Equation D.4 needs to be evaluated numerically to obtain $\nu(z)^+$.

A simpler approach can be followed to obtain the mean z-upcrossing rate of $Z(t)$ noting that:

1. the second moment properties of $Z(t)$ are

$$\mu_Z = E[Z(t)] = \alpha\sigma_V^2 + \alpha\bar{v}^2$$

$$\sigma_Z^2 = E[(Z(t)-\mu_Z)^2] = 2\alpha^2\sigma_V^4 + 4\alpha^2\sigma_V^2\bar{v}^2$$

$$\begin{aligned} c_{ZZ}(\tau) &= E[(Z(t)-\mu_Z)(Z(t+\tau)-\mu_Z)] \\ &= 2\alpha^2 r_{VV}(\tau)^2 + 4\alpha^2\bar{v}^2 r_{VV}(\tau), \end{aligned} \tag{D.5}$$

   where $r_{VV}(\tau) = E[V(t)V(t+\tau)] = \int_0^\infty g_{VV}(\omega)\cos(\omega\tau)d\omega$ is the correlation function of $V(t)$,

2. $\dot{Z}(t) = 2\alpha\dot{V}(t)(\bar{v}+V(t))$, so that $\dot{Z}(t)|V(t)=v$ is a zero-mean Gaussian variable with variance $E[\dot{Z}^2(t)|V(t)=v] = 4\alpha^2\sigma_{\dot{V}}^2(\bar{v}+v)^2$, and $\dot{Z}(t)|Z(t)=z$ is a zero-mean Gaussian variable with variance $E[\dot{Z}^2(t)|Z(t)=z] = 4\alpha\sigma_{\dot{V}}^2 z$,

3. the joint density of $\{Z(t), \dot{Z}(t)\}$ is

$$f(z,\xi) = \frac{1}{\alpha\sigma_V^2} f_Z(z/(\alpha\sigma_V^2), 1, \bar{v}^2/\sigma_V^2)\frac{1}{2\sqrt{\alpha z}\sigma_{\dot{V}}}\,\phi\left(\frac{\xi}{2\sqrt{\alpha z}\sigma_{\dot{V}}}\right) \tag{D.6}$$

   where

$$f_Z(\eta, m, \lambda) = \frac{1}{2}\exp\left[-(\eta+\lambda)/2\right]\left(\frac{\eta}{\lambda}\right)^{(m-2)/4}\boldsymbol{I}_{m/2-1}\left(\sqrt{\lambda\eta}\right) \tag{D.7}$$

is the noncentral chi-square density with degree of freedom $m > 0$ and non-centrality parameter $\lambda > 0$, in which $\boldsymbol{I}_\mu$ is the modified Bessel function of the first kind of order μ.

The mean z-upcrossing rate of $Z(t)$ can be obtained using the Rice formula

$$\nu(z)^+ = \int_0^\infty \xi f(z,\xi) d\xi, \tag{D.8}$$

in which $f(z,\xi)$ is given by Equation D.6, and becomes

$$\nu(z)^+ = \sigma_{\dot{Z}} \sqrt{\frac{z/(\alpha\sigma_V^2)}{2\pi\,(1+\bar{v}^2/\sigma_V^2)}}\, f_Z(z/(\alpha\sigma_V^2), 1, \bar{v}^2/\sigma_V^2), \tag{D.9}$$

where $\sigma_{\dot{Z}}^2 = E[(\dot{Z}(t) - E[\dot{Z}(t)])^2] = E[4\alpha\dot{V}^2(t)Z(t)] = 4\alpha^2\sigma_{\dot{V}}^2(\sigma_V^2 + \bar{v}^2)$ and $f_Z(\eta, m, \lambda)$ is given by Equation D.7. We note that $\nu(z)^+ = 0$ for $z \leq 0$ since the quasi static response $Z(t)$ in Equation 3.92 is always positive.

Appendix E
MCEER demonstration hospital

This section provides some details on the seismic risk analysis of the MCEER Demonstration Hospital presented in Section 4.1. Figure E.1 shows the organizations

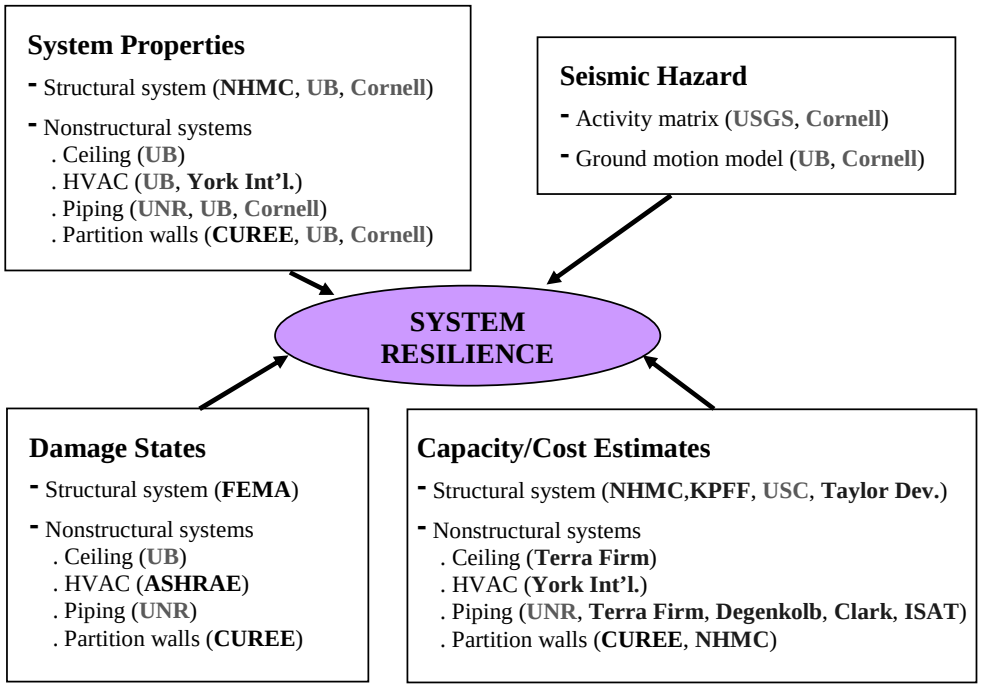

Figure E.1: Benchmark problem collaboration.

and institutions involved in this study. We would like to acknowledge A. Bansal (Degenkolb), F. Case (Clark), Dr. A. Filiatrault (University at Buffalo), J. Lewis (Terra Firm), R.J. Love (Degenkolb), Dr. M. Maragakis (University of Nevada, Reno), P. Marks (York International), J. Massey (ISAT), J. Mitchell (York International), R. Omens (NHMC, CWU), R. Rozanski (NHMC, CWU), A. Taylor (KPFF), D.P. Taylor (Taylor Devices) and Dr. D. von Winterfeldt (University of Southern California) for

their invaluable contributions and critical reviews.

Building repair/replacement costs

The repair costs in Table 4.6 are obtained using the following information. The number of plastic hinges in an interior and an exterior moment resisting frame in the IFL facility are obtained by a nonlinear push-over analysis, for a given drift level [59]. For drift equals 0.7% Figure E.2 shows the number and location of plastic hinges. There

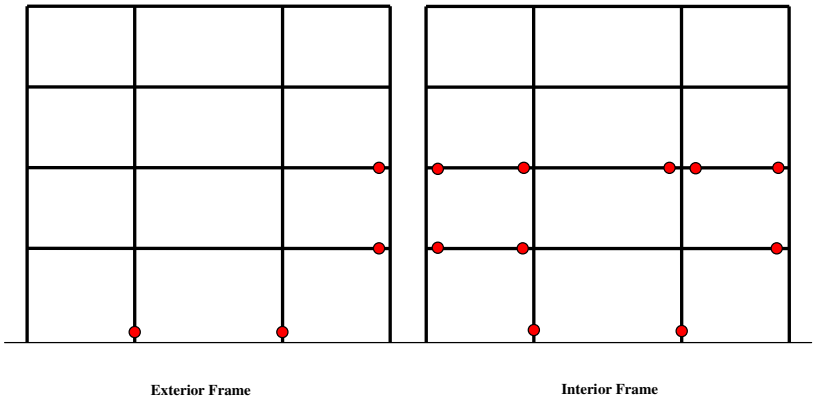

Figure E.2: Plastic hinge locations for 0.7% drift.

are 2 column and 2 beam hinges in the exterior moment resisting frame and 2 column and 8 beam hinges in the interior moment resisting frame. The IFL facility has two interior and two exterior moment resisting frames resulting in 28 hinges in total. For interstory drift equals 2.5% Figure E.3 shows the number and location of plastic hinges. There are 6 column and 15 beam hinges in the exterior moment resisting frame and 4 column and 17 beam hinges in the interior moment resisting frame, resulting in 84 hinges in total.

Considering material, labor and unforseen conditions and unexpected delays the total cost per beam/column joint is assumed to be $10,000 and $18,000 for immediate

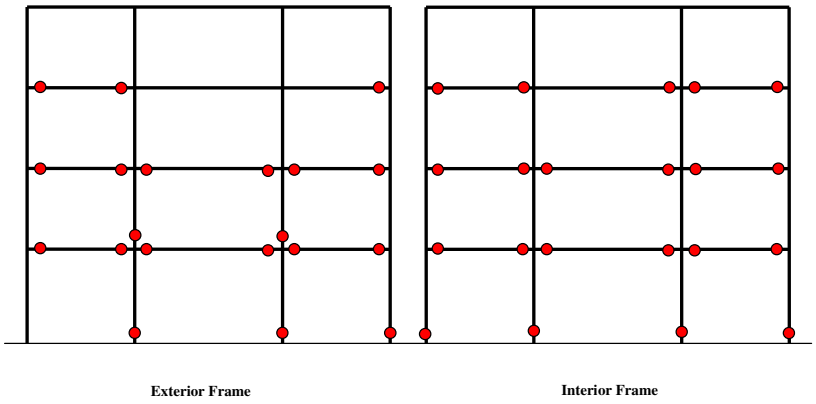

Figure E.3: Plastic hinge locations for 2.5% drift.

occupancy and life safety levels, respectively. Accordingly, the building repair costs are $280,000 and $1,512,000 for immediate occupancy and life safety levels, respectively.

The building replacement cost consists of structural system replacement ($53 million) and nonstructural system replacement ($14 million) resulting in $67 million in total.

Building rehabilitation

The damping coefficients provided in Table 4.3 are for a single fluid viscous damper. The dampers are inserted in the central bay (there are three bays) in each story (there are four stories) of the exterior moment resisting frames (there are four moment resisting frames). Accordingly the total number of dampers = (1 bay)x(4 storeys)x(2 frames) = 8.

For the benchmark building the design earthquake forces per the 1976 UBC code are 483, 436, 296 and 158 kips, and the floor weights are 2110, 2530, 2530 and 2610, for floors 4, 3, 2 and 1, respectively [187]. Hence the floor accelerations are 483/2110=0.229g, 436/2530=0.172g, 296/2530=0.117g, and 158/2610=0.060g floors

4, 3, 2 and 1, respectively. The fundamental frequency is 7.222 rad/sec [187]. The maximum expected velocities for the floors are given in Table E.1. Four damper sizes

Table E.1: Spectral velocities.

Floor	Spectral velocity (in/sec)
1	0.060*g/7.222 = 3.209
2	0.117*g/7.222 = 6.257
3	0.172*g/7.222 = 9.198
4	0.229*g/7.222 =12.247

are used for all rehabilitation alternatives, 980 KN, 1335 KN, 1960 KN, and 2500 KN. The sizes picked for an individual case are dependent on the damping coefficients given in Table 4.3 and spectral velocities given in Table E.1. All costs include the dampers and the estimated brace extender and attachment clevises and attachment pins required for the installation. All the contractor must do is weld/bolt the attachments to the building and hoist the damper in place so the clevis pins can be inserted. Installation costs have been estimated on this basis. Diagonal brace mounting is also assumed. Costing is as follows:

- 20% case: 2pc 980 KN, 4pc 1335 KN, 2pc 1960 KN dampers, braces, attachments are $89,000. Install estimated at $10,000.
- 25% case: 2pc 1335 KN, 6pc 1960 KN dampers, braces, and attachments are $105,000. Install estimated at $14,000.
- 30% case: 4pc 1960 KN, 4pc 2500 KN dampers, braces, and attachments are $144,000. Install estimated at $18,000.

To include the usual contractor management and supervisor charges, install costs are doubled.

The costs given in Table 4.7 include the cost of dampers, braces, attachments, installation and usual contractor management and supervisor charges. They do not

include business interruption losses. However, in general, during the retrofit the hospital remains in service during the installation, working on one/two rooms at a time if a damper was located there.

HVAC system

Following items are noted for the HVAC system:

- Excitation is applied in the transverse direction of the HVAC system, this direction is assumed to be weaker.
- It is assumed that the chiller is filled with water, which is assumed to cause larger responses.
- Replacement cost of an existing water cooled centrifugal chiller is about $400,000. The cost may be $100,000 to $200,000 more depending on the complexity involved in the replacement. Repair cost of an existing chiller is difficult to estimate without the diagnosis of the condition of the chiller. An upper bound for repair cost of a moderately damaged equipment could be $90,000. The repair for moderate damage could be around one day to diagnose and another day to repair (assuming the required parts are in stock). For extensive damage repair could take 2 weeks or more.

Partition walls

Gypsum drywall is widely accepted in residential, commercial, industrial and institutional constructions [120]. The walls researched in [120] were standard construction according to the 1997 Uniform Building Code [89] and were all 8 ft. by 16 ft. In ([120], page 33) it is noted that the damage observed in cyclic tests was less severe

than that seen for compatible drifts in shake table experiments of a full scale house, which results in conservative estimates for seismic performance of drywalls.

Piping system

Following items are noted for the piping system:

- An estimate is used for the material cost based on the assumed number of (additional) braces used for rehabilitation. Disruption during rehabilitation is not included (no information available).
- The limit states in Table 4.16 can have large uncertainties.
- The limit states can be misleading since there are no constraints in the lab experiment and pipes are free to swing. In reality there are other piping systems or obstructions in very close distances, which may cause reaching a damage states before the inter-storey drift reaches the value obtained in the lab. However, it was noted that no damage related to the proximity of the pipes to the walls or other obstacles in previous earthquakes were experienced in previous earthquakes.

The piping system tested at University of Nevada at Reno (UNR) [68] [REF Robert Corbin's MS thesis] is used to estimate repair/replacement and rehabilitation costs for the existing piping system in the IFL facility. Table E.2 summarizes the ranges of both the repair and replacement costs in relationship to its accessibility for the UNR system. Whether it is easily accessible or not, the cost to repair slight damages refers to the repairing of a single brace while the cost of repairing moderate damages involves the repair of a single joint and the amount to fix any extensive damage that might have occurred involves the repairing of a single connection. Table E.3 shows the installation costs of different retrofitting equipment used in the rehabilitation of the UNR system.

Table E.2: Piping system repair and replacement costs.

Damage state	Repair/replacement cost ($)			
	Easily accessible	Downtime (hrs.)	Not easily accessible	Downtime (hrs.)
Slight damage	$134.75	None	$226.65	None
Moderate damage	$120.00	3	$257.86	6
Extensive damage	$146.20	3	$284.06	6

Table E.3: Piping retrofitting equipment costs.

Material type	Rehabilitation cost ($)	
	Easily accessible	Not easily accessible
Longitudinal brace	$133.47	$219.42
Transverse brace	$134.10	$220.05
Clevis support	$136.67	$222.62

Downtime for both the piping system and hospital are not included since the piping systems can remain fully operational during the installation of the braces.

Repair costs in Table 4.17 for the existing piping system are calculated by (1) averaging the values in Table E.2, (2) using a 90% increase in the cost (for selective demolition and patching by other trades to gain access to the piping), and (3) considering the total number of braces, joints and connections in the UNR systems and IFL facility. There are 11 hangers, 10 joints and 7 connections in the UNR system. Corresponding values for the existing system can be obtained from Table 4.15.

Rehabilitation cost for the existing piping system in the IFL facility is calculated as follows. It is assumed that either a longitudinal of a transverse brace, and a clevis support is used. From Table E.3 an average value for a brace is $((133.47+219.42)/2+(134.10+220.05)/2)/2 \simeq \$177$ and for a clevis support is $(136.67 + 222.62)/2 \simeq \$180$. Hence rehabilitation of a hanger rod costs $357. There are 33+51+51+27=162 hanger roads in total, hence the total cost is 162*357=$57834. Use a 15% increase in the cost following

F. Case's first comment and another 75% increase following his second comment. Hence the total rehabilitation cost becomes $57834 * 1.15 * 1.75 = 116,390 \simeq \$120,000$.

RDAT software

Figures E.4-E.9 show excerpts from the RDAT software.

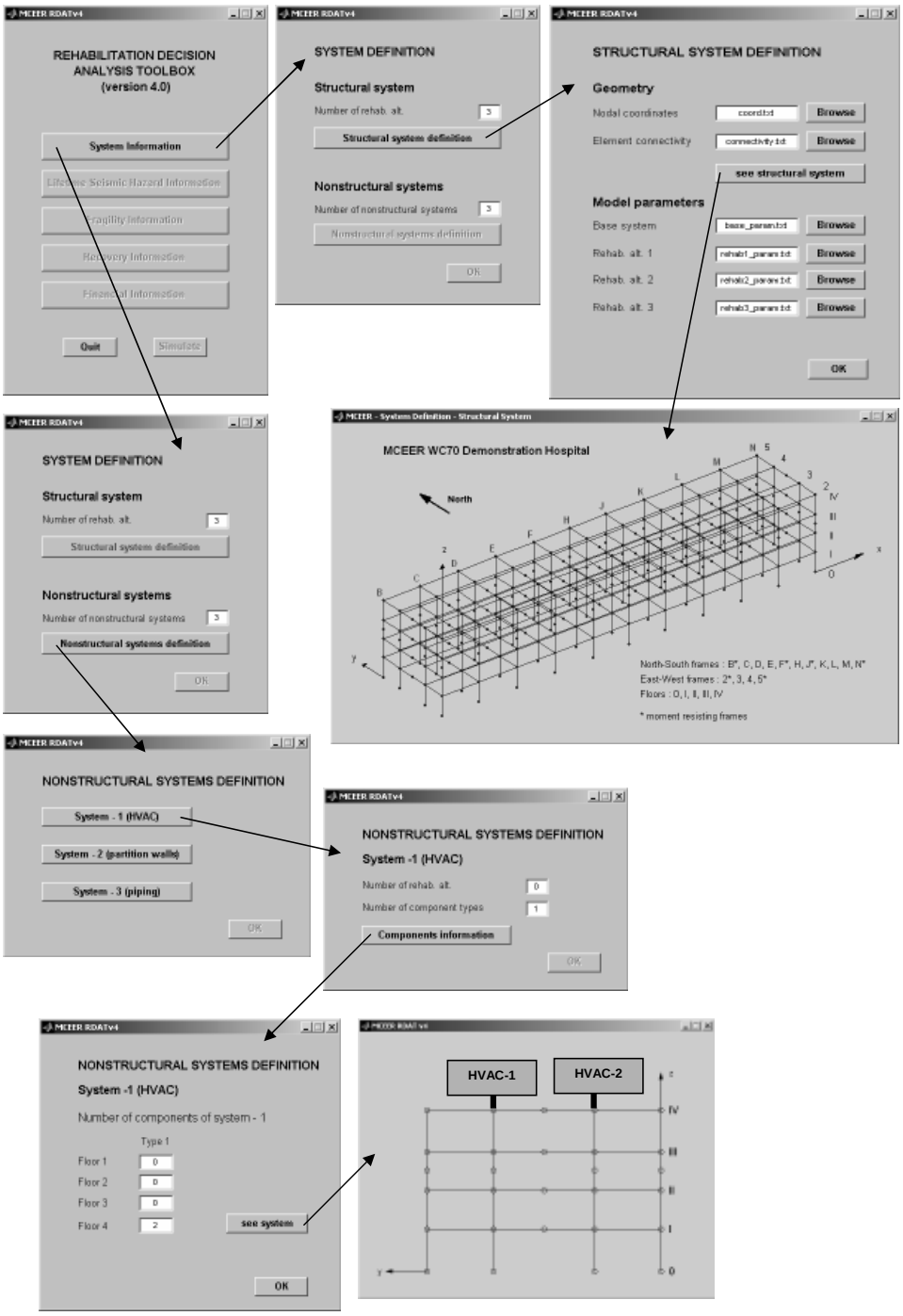

Figure E.4: RDAT: System information.

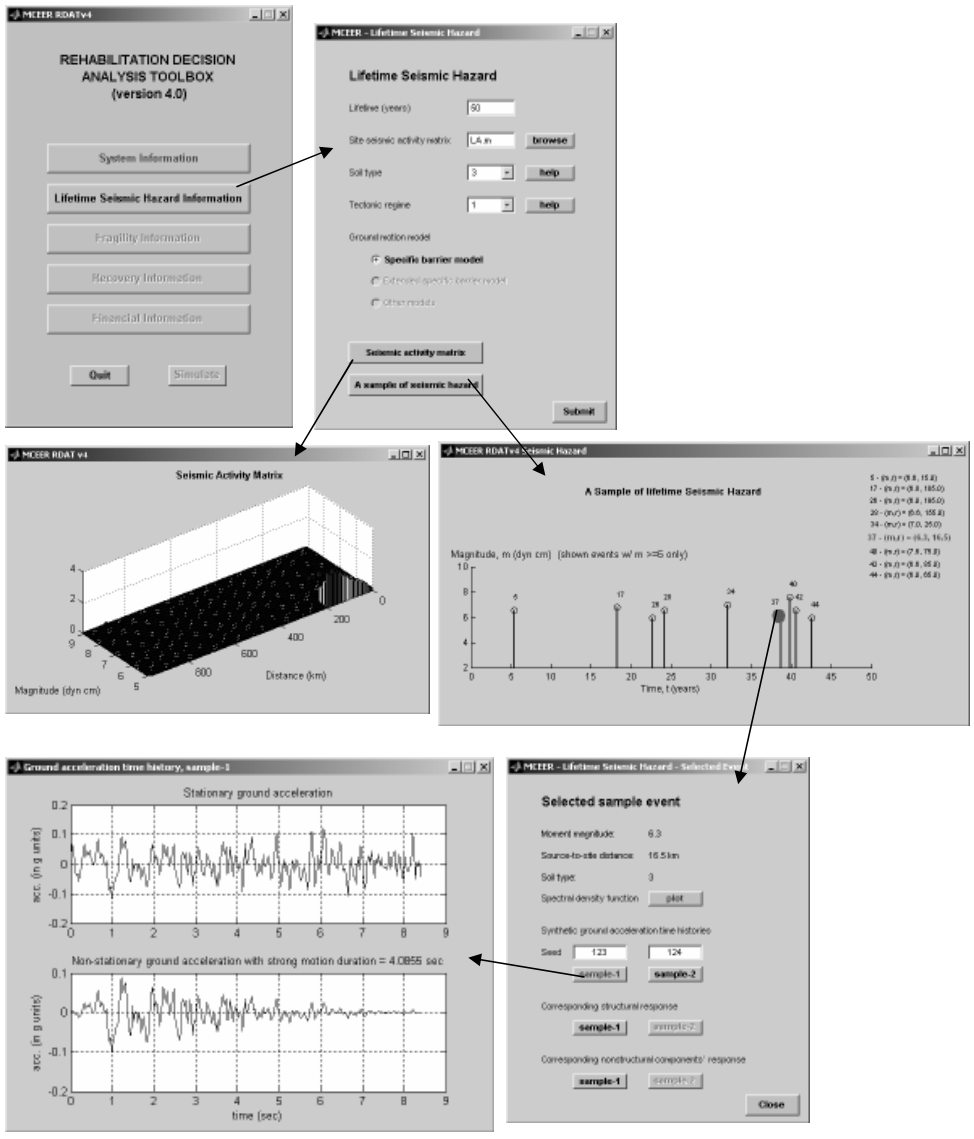

Figure E.5: RDAT: Seismic hazard information.

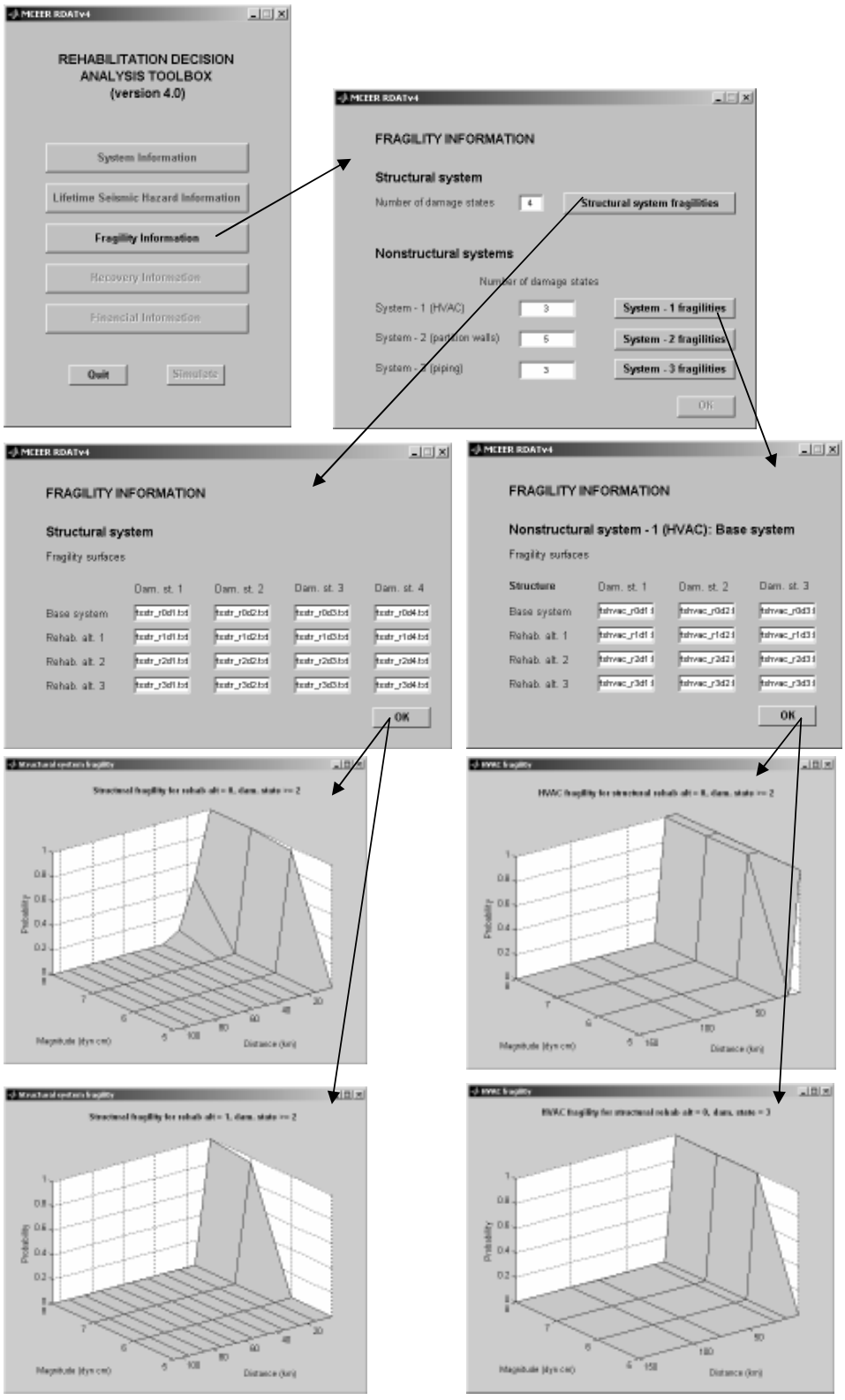

Figure E.6: RDAT: Fragility information.

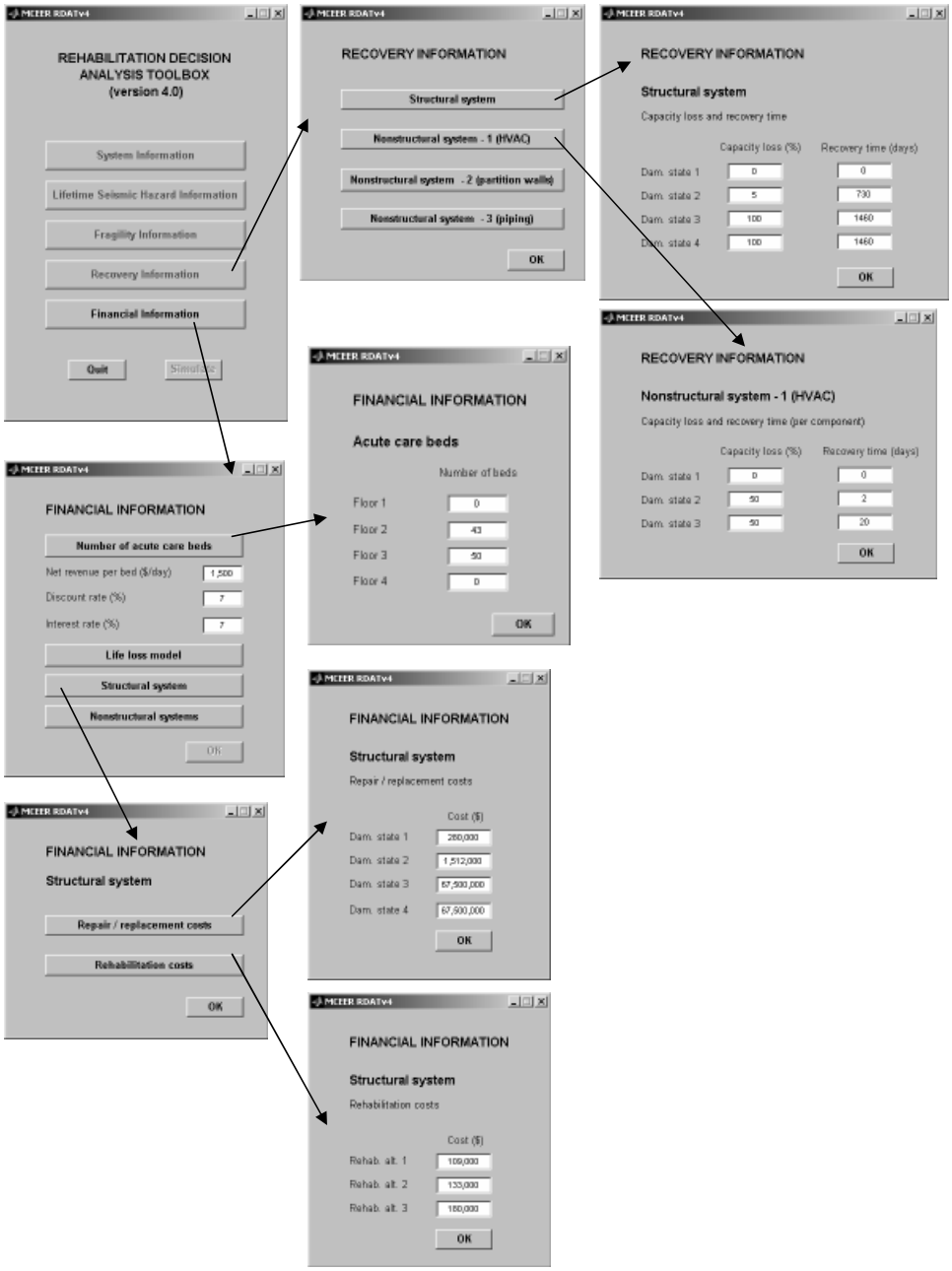

Figure E.7: RDAT: Recovery and financial information.

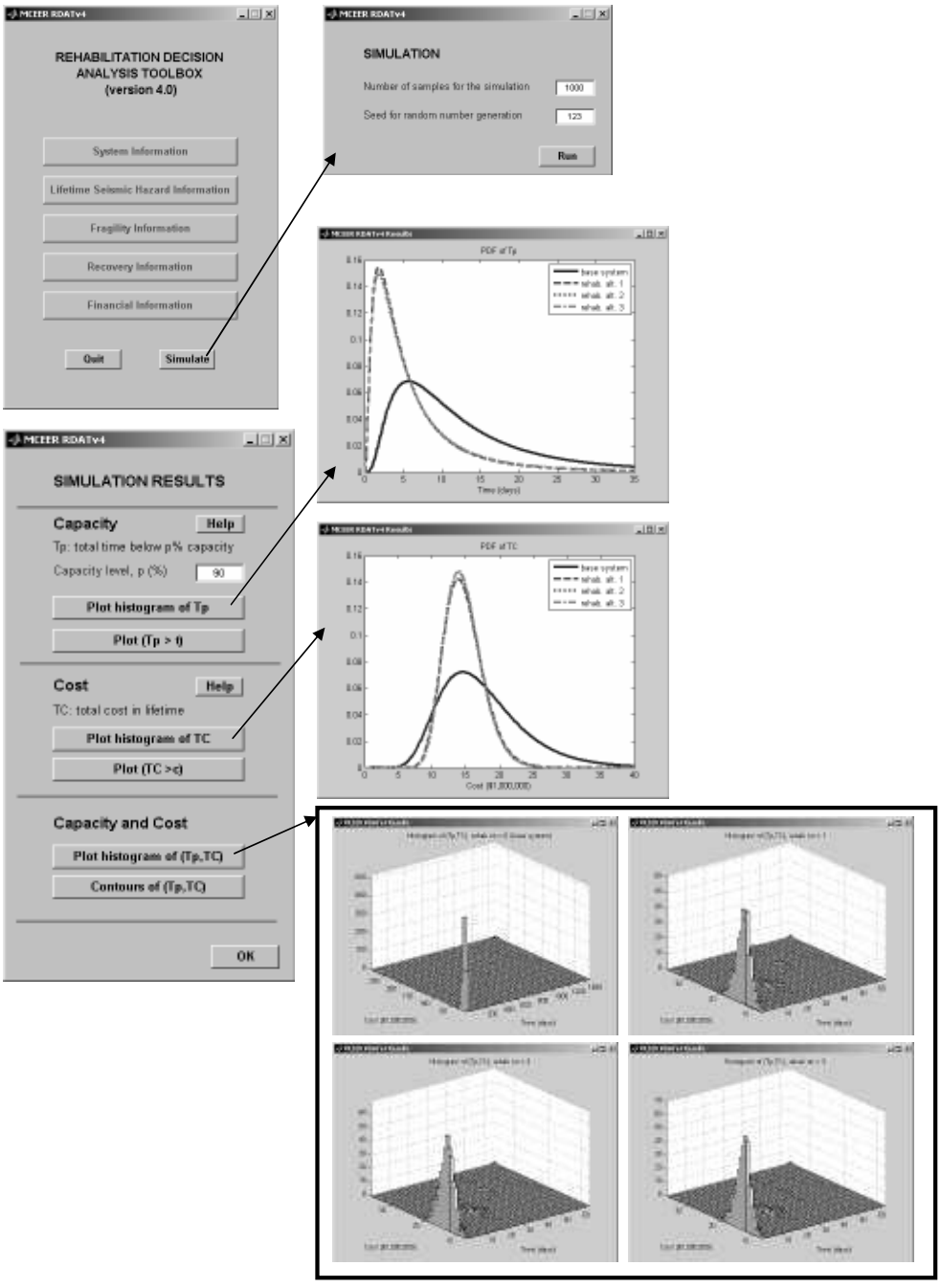

Figure E.8: RDAT: Simulation results.

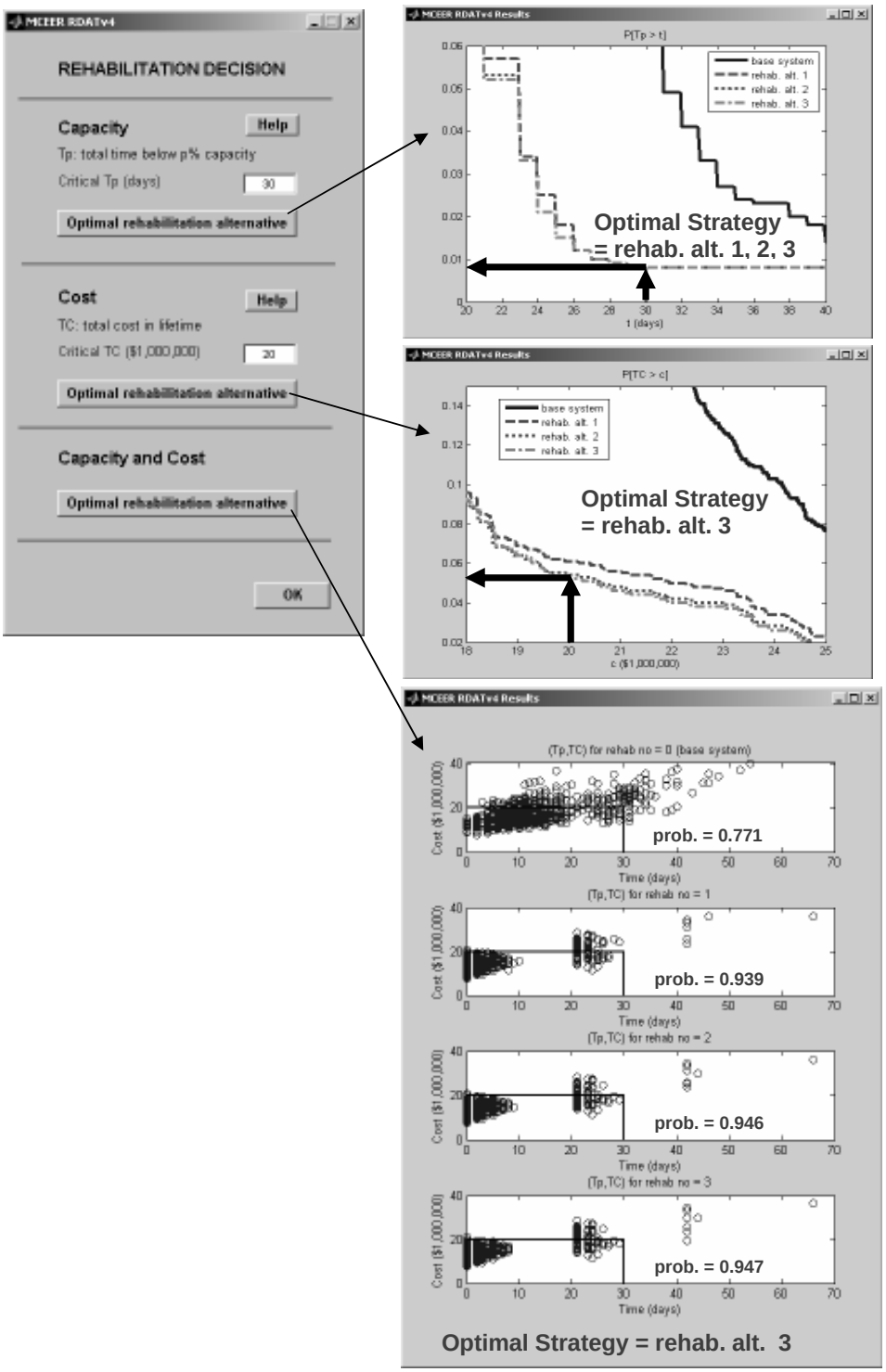

Figure E.9: RDAT: Rehabilitation decision.

REFERENCES

[1] *American Petroleum Institute Recommended Practice for Planning, Designing and Construction of Fixed Offshore Platforms*, volume API RP 2A. American Petroleum Institute, Washington, DC, 9 edition, 1977.

[2] N. A. Abrahamson, J. F. Schneider, and J. C. Stepp. Spatial variation of strong ground motion for use in soil-structure interaction analyses. In *Proceedings of 4th US National Conference on Earthquake Engineering*, pages 317–326, Palm Springs, CA, 1990.

[3] K. Aki and P. Richards. *Quantitative Seismology: Theory and Methods, Volume I, II*. W. H. Freeman and Company, San Francisco, CA, 1980.

[4] A. H.-S. Ang, J. A. Pires, and R. Villaverde. A model for the seismic reliability assessment of electric power transmission systems. *Reliability Engineering and System Safety*, 51(4):7–22, 1996.

[5] ANSI. Building code requirements for minimum design loads. Technical Report A58.1-1982, American National Standards Institute, New York, NY, 1982.

[6] ASCE 7-98. Minimum design loads for buildings and other structures. ASCE Standard 7, American Society of Civil Engineers, New York, NY, 1998.

[7] ASHRAE. *ASHRAE Handbook - HVAC Applications*. American Society of Heating, Refrigerating and Air-Conditioning Engineers, Atlanta, GA, 2003. Chapter 34, Thermal Storage.

[8] ATC 13. Earthquake damage evaluation data for California. ATC Report 13, Applied Technology Council, Redwood City, CA, 1985.

[9] ATC 25. Seismic vulnerability and impact of disruption of lifelines in the conterminous U.S. ATC Report 25, Applied Technology Council, Redwood City, CA, 1991.

[10] G. M. Atkinson and D. M. Boore. Ground motion relations for Eastern North America. *Bulletin of the Seismological Society of America*, 85:17–30, 1995.

[11] H. Badillo-Almaraz. Seismic fragility testing of suspended ceiling systems. Master's thesis, State University of New York at Buffalo, 2003.

[12] J. W. Baker and C. A. Cornell. Choice of a vector of ground motion intensity measures for seismic demand hazard analysis. In *Proceedings of the Thirteenth*

World Conference on Earthquake Engineering (13 WCEE), Vancouver, Canada, 2004.

[13] J. W. Baker and C. A. Cornell. A vector-valued ground motion intensity measure consisting of spectral acceleration and epsilon. *Earthquake Engineering and Structural Dynamics*, 34:1193–1217, 2005.

[14] N. I. Basöz, A. S. Kiremidjian, S. A. King, and K. H. Law. Statistical analysis of bridge damage date from the 1994 Northridge, CA, earthquake. *Earthquake Spectra*, 15(1):25–54, 1999.

[15] M. E. Batts, L. R. Russell, and E. Simiu. Hurricane wind speeds in the United States. *ASCE Journal of the Structural Division*, 100:2001–2015, 1980.

[16] J. R. Benjamin and C. A. Cornell. *Probability, Statistics, and Decision for Civil Engineers*. McGraw–Hill, New York, NY, 1970.

[17] B. K. Bhartia and E. H. Vanmarcke. Multi–hazard risk analysis: Case of a simple offshore structure. Technical Report NCEER-88-0023, National Center for Earthquake Engineering Research, Buffalo, NY, 1988.

[18] D. M. Boore. Stochastic simulation of high-frequency ground motions based on seismological models of the radiated spectra. *Bulletin of the Seismological Society of America*, 73:1865–1894, 1983.

[19] D. M. Boore. Simulation of ground motion using the stochastic method. *Pure and Applied Geophysics*, 160:635–676, 2003.

[20] D. M. Boore and W. B. Joyner. Site amplifications for generic rock sites. *Bulletin of the Seismological Society of America*, 87:327–341, 1997.

[21] M. Bouchon. A simple method to calculate green's functions for elastic layered media. *Bulletin of the Seismological Society of America*, 71(4):959–971, 1981.

[22] J. N. Brune. Tectonic stress and the spectra of seismic shear waves from earthquakes. *Journal of Geophysical Research*, 75:4997–5009, 1970.

[23] J. N. Brune. Correction. *Journal of Geophysical Research*, 76:5002, 1971.

[24] M. Bruneau, S. E. Chang, D. T. Eguchi, G. C. Lee, T. D. O'Rourke, A. M. Reinhorn, M. Shinozuka, K. Tierney, W. A. Wallace, and D. von Winterfeldt.

A framework to quantitatively assess and enhance the seismic resilience of communities. *Earthquake Spectra*, 19(4):733–752, 2003.

[25] M. Bruneau and A. M. Reinhorn. Exploring the concept of seismic resilience for acute care facilities. *Earthquake Spectra*, 23(1):41–62, 2007.

[26] CAO. City of Los Angeles Northridge Earthquake after-action report, 1994. City Administrative Officer report presented to the Emergency Operations Board, City of Los Angeles, CA.

[27] A. Chaudhuri and S. Chakraborty. Sensitivity evaluation in seismic reliability analysis of structures. *Computational Methods in Applied Mechanics and Engineering*, 193:59–68, 2004.

[28] G.L.F Chiu. Extreme winds as a component of catastrophic risk. In *Proceedings of Seventh ASCE Specialty Conference on Probabilistic Mechanics and Structural Reliability*, pages 498–501, Rochester, NY, 1996.

[29] E. Choi. Fragility of as-built and retrofitted highway bridges in Central and Southeastern United States. Technical report, Korea Railroad Research Institute, Kyounggi-Do, Korea, 2003.

[30] E. Choi, R. DesRoches, and B. Nielson. Seismic fragility of typical bridges in moderate seismic zones. *Engineering Structures*, 26:187–199, 2004.

[31] A. Chopra. *Dynamics of Structures: Theory and Applications to Earthquake Engineering*. Prentice Hall, Boston, 2 edition, 2000.

[32] R. W. Clough and J. Penzien. *Dynamics of Structures*. McGraw-Hill, New York, 1975.

[33] J. P. Conte, K. S. Pister, and S. A. Mahin. Nonstationary ARMA modeling of seismic motions. *Soil Dynamics and Earthquake Engineering*, 11:411–426, 1992.

[34] A. Cornell. Stochastic process models in structural engineering. Technical Report Technical Report 34, Department of Civil Engineering, Stanford University, Stanford, CA, 1964.

[35] A. M. Cruz. Engineering contributions to the field of emergency management. In D. A. McEntire, editor, *Disciplines, Disasters and Emergency Management: The Convergence of Concepts Issues and Trends From the Research Literature*. 2005.

[36] A. M. Cruz, L. J. Steinberg, and R. Luna. Identifying hurricane-induced hazardous materials release scenarios in a petroleum refinery. *Natural Hazards Review*, 2(4):203–210, 2001.

[37] K. Dan, T. T. Watanabe, and R. Sato. Stability of earthquake ground motion synthesized by using different small-event records as empirical green's functions. *Bulletin of the Seismological Society of America*, 80(6):1433–1455, 1990.

[38] G. R. Dargahi-Noubary. Models for seismic records, why uniformly modulated ARMA. *Soil Dynamics and Earthquake Engineering*, 11:381–385, 1992.

[39] P. C. Das, editor. *Safety of Bridges*, London, UK, 1997. Thomas Telford.

[40] A. G. Davenport. The dependence of wind load upon meteorological parameters. In *Proceedings of the International Research Seminar on Wind Effects on Buildings and Structures*, pages 19–82, Toronto, Canada, 1968.

[41] W. Dawkins. Corporate Japan shakes in after-shock of quake - some companies' losses rom the Kobe tragedy may prove competitors' gains, 1995. Financial Times, International Company News, February 24, page 30.

[42] M. R. Degg and D. K. Chester. Seismic and volcanic hazards in Peru: Changing attitudes to disaster mitigation. *The Geographical Journal*, 171(2):125–145, 2005.

[43] G. Deodatis. Nonstationary stochastic vector processes: Seismic ground motion applications. *Probabilistic Engineering Mechanics*, 11:149–168, 1996.

[44] A. Der Kiureghian. A coherency model for spatially varying ground motions. *Earthquake Engineering and Structural Dynamics*, 25:99–111, 1996.

[45] S. L. Dimova and A. Elenas. Seismic intensity parameters for fragility analysis of structures with energy dissipating devices. *Structural Safety*, 24:1–28, 2002.

[46] E. DiPasquale and A. S. Cakmak. Detection and assessment of seismic structural damage. Technical Report NCEER-87-0015, National Center for Earthquake Engineering Research, Buffalo, NY, 1987.

[47] R. Dobry, I. M. Idris, and E. Ng. Duration characteristics of horizontal components of strong-motion earthquake records. *Bulletin of the Seismological Society of America*, 68:1487–1520, 1978.

[48] E. Dumova-Jovanoska. Fragility curves for reinforced concrete structures in Skopje (Macedonia) region. *Soil Dynamics and Earthquake Engineering*, 19:455–466, 2000.

[49] J. Eidinger and K. Goettel. The benefits and costs of seismic retrofits of nonstructural components for hospitals, essential facilities and schools. In *Proceedings of Seminar on Seismic Design, Retrofit, and Performance of Nonstructural Components (ATC-29-1)*, pages 491–504, San Francisco, CA, 1998.

[50] A. Elenas. Correlation between seismic acceleration parameters and overall structural damage indices of buildings. *Soil Dynamics and Earthquake Engineering*, 20:93–100, 2000.

[51] B. R. Ellingwood. Earthquake risk assessment of building structures. *Reliability Engineering and System Safety*, 74(4):251–262, 2001.

[52] B. R. Ellingwood, R. Smilowitz, D. O. Dusenberry, D. Duthinh, H. S. Lew, and N. J. Carino. Best practices for reducing the potential for progressive collapse in buildings. Technical Report NISTIR 7396, National Institute of Standards and Technology, New York, NY, 2007.

[53] G. W. Ellis and A. S. Cakmak. Modeling earthquake ground motions in seismically active regions using parametric time series methods. Technical Report NCEER-87-0014, National Center for Earthquake Engineering Research, Buffalo, NY, 1987.

[54] S. Fathali and A. Filiatrault. *Restraint and Isolation of Nonstructural Components (RINC) Version 1.01*. Multidisciplinary Center for Earthquake Engineering Research, Buffalo, NY, 2007. In Preparation.

[55] FEMA 222A/223A. Recommended provisions for seismic regulations for new buildings. FEMA Report 222A/223A, Federal Emergency Management Agency, Washington, D.C., 1994. Vol. 1 (Provisions) and Vol. 2 (Commentary).

[56] FEMA 273. NEHRP guidelines for the seismic rehabilitation of buildings. FEMA Report 273, Federal Emergency Management Agency, Washington, D.C., 1997.

[57] FEMA 350. Recommended seismic design criteria for new steel moment-frame buildings. FEMA Report 350, SAC Joint Venture, a partnership of SEAOC, ATC and CUREE, Washington, D.C., 2000.

[58] FEMA 356. Prestandard and commentary for the seismic rehabilitation of buildings. FEMA Report 356, Federal Emergency Management Agency, Washington, D.C., 2000.

[59] A. Filiatrault. 2-D modeling of the MCEER WC70 hospital. Multidisciplinary Center for Earthquake Engineering Research, 2006.

[60] A. Filiatrault, M. Bruneau, D. Alesch, M. Constantinou, G. Dargush, M. Grigoriu, G. Lee, E. Maragakis, G. Mosqueda, W. Petak, A. Reinhorn, and D. von Winterfeldt. Enhancing the seismic resilience of acute care facilities: An overview of mceer research. In *Proceedings of the Eight National Conference on Earthquake Engineering (8NCEE)*, San Francisco, CA, 2006.

[61] A. Frankel, C. Mueller, T. Barnhard, D. Perkins, E. Leyendecker, N. Dickman, S. Hanson, and M. Hopper. National seismic hazard maps. Open-File Report 96-532, United States Geological Survey, Denver, CO, 1996.

[62] D. L. Garcia and T. T. Soong. Seismic fragility of block type non-structural components. Part 1: Unrestrained components. *Earthquake Engineering and Structural Dynamics*, 32:111–129, 2003.

[63] D. L. Garcia and T. T. Soong. Seismic fragility of block type non-structural components. Part 2: Restrained components. *Earthquake Engineering and Structural Dynamics*, 32:131–149, 2003.

[64] P. Gardoni, A. Der Kiureghian, and K. Mosalam. Probabilistic models and fragility estimates for bridge components and systems. Technical Report PEER 2002/13, Pacific Earthquake Engineering Research Center, U.C. Berkeley, CA, 2002.

[65] P. Gardoni, A. Der Kiureghian, and K. M. Mosalam. Probabilistic capacity models and fragility estimates for reinforced concrete columns based on experimental observations. *ASCE Journal of Engineering Mechanics*, 128(10):1024–1038, 2002.

[66] P. Gardoni, K. M. Mosalam, and A. Der Kiureghian. Probabilistic seismic demand models and fragility estimates for RC bridges. *Journal of Earthquake Engineering*, 7(Special Issue 1):79–106, 2003.

[67] D. Gasparini and E. H Vanmarcke. Simulated earthquake motions compatible with prescribed response spectra. Technical Report R76-4, Massachusetts Institute of Technology, Boston, MA, 1976.

[68] E. Goodwin. Experimental evaluation of the seismic performance of hospital piping subassemblies. Master's thesis, University of Nevada, Reno, NV, 2004.

[69] M. Grigoriu. *Applied Non-Gaussian Processes*. PTR Prentice-Hall, Englewood Cliffs, NJ, 1995.

[70] M. Grigoriu and C. Kafali. Response of linear systems to stationary bandlimited gaussian and non-Gaussian processes. *Probabilistic Engineering Mechanics*, February 2007. (submitted).

[71] R. A. W. Haddon. Earthquake source spectra in Eastern North America. *Bulletin of the Seismological Society of America*, 86:1300–1313, 1996.

[72] R. A. W. Haddon. Use of empirical Green's functions, spectral ratios, and kinematic source models for simulating strong ground motion. *Bulletin of the Seismological Society of America*, 86(3):597–615, 1996.

[73] B. Halldorsson. *Calibration of the Specific Barrier Model to Earthquakes of Different Tectonic Regions and Synthesis of Strong Ground Motions for Earthquake Engineering Applications*. PhD thesis, The State University of New York at Buffalo, Buffalo, NY, 2004.

[74] B. Halldorsson, G. Dong, and A. S. Papageorgiou. Earthquake motion input and its dissemination via the internet. *Journal of Engineering and Engineering Vibration*, 1(1):20–26, 2002.

[75] B. Halldorsson and A. S. Papageorgiou. Calibration of the specific barrier model to earthquakes of different tectonic regions. *Bulletin of the Seismological Society of America*, 95(4):1276–1300, 2005.

[76] T. C. Hanks and R. K. McGuire. The character of high-frequency strong ground motion. *Bulletin of the Seismological Society of America*, 71(6):2071–2095, 1981.

[77] H. Hao, C. S. Oliveira, and J. Penzien. Multiple station ground motion processing and simulation based on SMART-I array data. *Nuclear Engineering and Design*, 111:293–310, 1989.

[78] R. S. Harichandran and E. H. Vanmarcke. Stochastic variation of earthquake ground motion in space and time. *ASCE Journal of Engineering Mechanics*, 112(2):154–175, 1986.

[79] HAZUS 97. *Earthquake Loss Estimation Methodology*. Federal Emergency Management Agency, Washington, D.C., 1997.

[80] HAZUS-MH. *Multi-Hazard Loss Estimation Methodology - Earthquake Model*. Department of Homeland Security, Federal Emergency Management Agency, Washington, D.C., hazus-mh mr2 edition, 2006.

[81] J. P. Heaney, J. Petarka, and L. T. Wright. Research needs for engineering aspects of natural disasters. *Journal of Infrastructure Systems*, 6(1):4–14, 2000.

[82] R. B. Herrmann. An extension of random vibration theory estimates of strong ground motion to large distances. *Bulletin of the Seismological Society of America*, 75:1447–1453, 1985.

[83] J. Holmes. Vulnerability curves for buildings in tropical-cyclone regions. In *Proceedings of Seventh ASCE Specialty Conference on Probabilistic Mechanics and Structural Reliability*, pages 78–81, Rochester, NY, 1996.

[84] G. Housner and P. C. Jennings. Generation of artificial earthquakes. *ASCE Journal of the Engineering Mechanics Division*, 90:113–150, 1964.

[85] L. R. Husid. Caracteristicas de terremotos. Analisis general. In *Revista del IDIEM 8*, pages 21–42, 1969.

[86] H. H. M. Hwang and J.-R. Huo. Generation of hazard-consistent fragility curves. *Soil Dynamics and Earthquake Engineering*, 13:345–354, 1994.

[87] H. H. M. Hwang and J. W. Jaw. Probabilistic damage analysis of structures. *ASCE Journal of Structural Engineering*, 116(7):1992–2007, 1990.

[88] H. H. M. Hwang, H. Lin, and J.-R. Huo. Seismic performance evaluation of fire stations in Shelby County, Tennessee. *Earthquake Spectra*, 13(4):759–772, 1997.

[89] ICBO. *Uniform Building Code*. International Conference of Building Officials, 1997.

[90] ICC. *International Building Code*. International Code Council, 2000.

[91] Pinelli. J.-P., E. Simiu, K. Gurley, C. Subramanian, L. Zhang, A. Cope, J.J. Filliben, and S. Hamid. Hurricane damage prediction model for residential structures. *ASCE Journal of Structural Engineering*, 130(11):1685–1691, 2004.

[92] J. D. Jarrell, M. Mayfield, E. N. Rappaport, and C. W. Landsea. The deadliest, costliest, and most intense United States hurricanes from 1900 to 2000, 2001. NOAA Technical Memorandum NWS TPC-1, Miami, Florida.

[93] D. L. Johnson. Hurricane katrina service assessment report, 2006.

[94] C. Kafali and M. Grigoriu. Fragility analysis for nonstructural systems in critical facilities. In *Proceedings of Seminar on Seismic Design, Performance, and Retrofit of Nonstructural Components in Critical Facilities (ATC-29-2)*, pages 375–385, Newport Beach, CA, 2003.

[95] C. Kafali and M. Grigoriu. Seismic fragility analysis. In *Proceedings of the Ninth ASCE Specialty Conference on Probabilistic Mechanics and Structural Reliability (PMC2004)*, Albuquerque, NM, 2004.

[96] C. Kafali and M. Grigoriu. Rehabilitation decision analysis. In *Proceedings of the Ninth International Conference on Structural Safety and Reliability (ICOSSAR'05)*, Rome, Italy, 2005.

[97] C. Kafali and M. Grigoriu. Rehabilitation decision analysis toolbox. In *Proceedings of the Convention of Structural Engineers Association of California (SEAOC 2005)*, San Diego, CA, 2005.

[98] C. Kafali and M. Grigoriu. Application of fragility-based decision support methodologies. Technical Report In Preparation, Multidisciplinary Center for Earthquake Engineering Research, Buffalo, NY, 2007.

[99] C. Kafali and M. Grigoriu. Seismic fragility analysis: Application to simple linear and nonlinear systems. *Earthquake Engineering and Structural Dynamics*, May 2007. (in press).

[100] C. Kafali, E. Mo, and M. Grigoriu. Seismic fragility of linear systems subjected to non-Gaussian ground acceleration processes. In *Proceedings of the Eight National Conference on Earthquake Engineering (8NCEE)*, San Francisco, CA, 2006.

[101] J. C. Kaimal, J. C. Wyngaard, Y. Izumi, and O. R. Cote. Spectral characteristics of surface-layer turbulence. *Quarterly Journal of the Royal Meteorological Society*, 98:563–589, 1972.

[102] K. Kanai. An empirical formula for the spectrum of strong earthquake motions. *Bulletin of the Earthquake Research Institute*, 39:85–95, 1961.

[103] F. Katagiri and Y. Izutani. Empirical green's function corrected for source effect. *Earthquake Engineering and Structural Dynamics*, 21:341–349, 1992.

[104] H. Kawakami and P. De Jesus Bidon. A simplified input output relation method using AR model for earthquake wave propagation analysis. *Earthquake Engineering and Structural Dynamics*, 26:1041–1057, 1997.

[105] G. Kjell. Predicting response spectra for earthquake signals generated as filtered noise. *Probabilistic Engineering Mechanics*, 17:241–252, 2002.

[106] R. D. Knabb, J. R. Rhome, and D. P. Brown. Tropical cyclone report: Hurricane Katrina: 23Ű30 August 2005, 2006.

[107] P. Kranz. Aftershocks in Taiwan. *News Week*, 3649:62, October 1999.

[108] L. Kristensen and N. O. Jensen. Lateral coherence in isotropic turbulence and in the natural wind. *Boundary Layer Meteorology*, 17:353–373, 1979.

[109] L. Kristensen, H. A. Panofsky, and S. D. Smith. Lateral coherence in longitudinal wind components in strong winds. *Boundary Layer Meteorology*, 21:199–205, 1981.

[110] C. W. Landsea. A climatology of intense (or major) Atlantic hurricanes. *Monthly Weather Review*, 121:1703–1713, 1993.

[111] D. L. Lau, A. Tang, and J. R. Pierre. Performance of lifelines during the 1994 Northridge Earthquake. *Canadian Journal of Civil Engineering*, 22(2):438–451, 1995.

[112] Y. K. Lin. *Probabilistic Theory of Structural Dynamics*. McGraw–Hill, New York, 1967.

[113] H. Liu. *Wind Engineering: A Handbook for Structural Engineers*. Prentice Hall, Englewood Cliffs, NJ, 1991.

[114] C. H. Loh. Analysis of spatial variation of seismic waves and ground movements from SMART-I data. *Earthquake Engineering and Structural Dynamics*, 13:561–581, 1985.

[115] C. H. Loh and Lin S. G. Directionality and simulation in spatial variation of seismic waves. *Engineering Structures*, 12:134–143, 1990.

[116] C. H. Loh and Y. T. Yeh. Spatial variation and stochastic modeling of seismic differential ground movement. *Earthquake Engineering and Structural Dynamics*, 16:583–596, 1988.

[117] N. Luco, L. Manuel, S. Baldava, and P. Bazzurro. Correlation of damage of steel moment-resisting frames to a vector-valued set of ground motion parameters. In *Proceedings of the Ninth International Conference on Structural Safety and Reliability (ICOSSAR'05)*, pages 2719–2726, Rome, Italy, 2005.

[118] G. R. Martin and R. Dobry. Earthquake site response and seismic code provisions. *NCEER Bulletin*, 8(4):1–6, 1994.

[119] MCEER. Rehabilitation Decision Analysis Toolbox (RDAT) version 1, 2004. URL: http://civil.eng.buffalo.edu/users_ntwk/index.htm.

[120] K. M. McMullin and D. Merrick. Seismic performance of gypsum walls - Experimental test program. CUREE Woodframe Project Report W-15, Consortium of Universities for Research in Earthquake Engineering, Richmond, CA, 2002.

[121] J. R. Morison, M. P. O'Brien, J. W. Johnson, and S. A. Schaff. The force exerted by surface waves on piles. *AIME Petroleum Transactions*, 189:149–154, 1950.

[122] NIST. National Institute of Standards and Technology, Extreme wind speed data sets: Hurricane wind speeds, 2007. URL: http://www.itl.nist.gov/div898/winds/hurricane.htm.

[123] M. J. O'Connor and B. R. Ellingwood. Reliability of nonlinear structures with seismic loading. *ASCE Journal of Structural Engineering*, 113(5):1011–1028, 1987.

[124] M. J. O'Connor and B. R. Ellingwood. Site-dependent models of earthquake ground motion. *Earthquake Engineering and Structural Dynamics*, 21:573–589, 1992.

[125] C. S. Oliveira, H. Hao, and J. Penzien. Ground motion modeling for multiple input structural analysis. *Structural Safety*, 10:79–93, 1991.

[126] G. B. Ou and R. B. Herrmann. A statistical model for ground motion produced by earthquakes at local and regional distances. *Bulletin of the Seismological Society of America*, 80(6):1397–1417, 1990.

[127] A. S. Papageorgiou. On two characteristic frequencies of acceleration spectra: Patch corner frequency and f_{max}. *Bulletin of the Seismological Society of America*, 78:509–528, 1988.

[128] A. S. Papageorgiou. Engineering seismology, advances in earthquake engineering 3. In *Computational Mechanics Publications*, pages 153–201. Southampton, UK, 1997.

[129] A. S. Papageorgiou. The barrier model and strong ground motion. *Pure and Applied Geophysics*, 160:603–634, 2003.

[130] A. S. Papageorgiou and K. Aki. A specific barrier model for the quantitative description of the inhomogeneous faulting and the prediction of strong ground motion. Part I. Description of the model. *Bulletin of the Seismological Society of America*, 73:693–722, 1983.

[131] A. S. Papageorgiou and K. Aki. A specific barrier model for the quantitative description of the inhomogeneous faulting and the prediction of strong ground motion. Part II. Applications of the model. *Bulletin of the Seismological Society of America*, 73:953–978, 1983.

[132] Y. J. Park. New conversation method from response spectrum to psd function. *ASCE Journal of Engineering Mechanics*, 121(12):1391–1392, 1995.

[133] PEER. Pacific Earthquake Engineering Research Center strong motion database, 2003. URL: http://peer.berkeley.edu/smcat.

[134] D. D. Pfaffinger. Calculation of power spectra from response spectra. *ASCE Journal of Engineering Mechanics*, 109(1):357–372, 1983.

[135] W. J. Pierson and L. Moskowitz. A proposed spectral form for fully developed wind seas based on the similarity theory of s. a. kitaigorodskii. *Journal of the Geophysical Research*, 69:5181–5190, 1964.

[136] S. T. Quek, Y. P. Teo, and T. Balendra. nonstationary structural response with evolutionary spectra using seismological input model. *Earthquake Engineering and Structural Dynamics*, 19:275–288, 1990.

[137] T. Rashed. Seismic vulnerability of megacities. In *Seismic Design Practice into the Next Century: Research and Application*. Balkema, Rotterdam, 1998.

[138] T. Rashed. Geospatial technologies, vulnerability assessment, and sustainable

hazards mitigation in cities. In M. Campagna, editor, *GIS for Sustainable Development: Bringing Geographic Information Science into Practice towards Sustainability*, pages 287–309. Taylor and Francis (CRC Press), New York, 2006.

[139] L. R. Russell. Probability distributions for hurricane effects. *ASCE Journal of Waterways, Harbours, and Coastal Engineering Division*, 97:139–154, 1971.

[140] E. Safak. Analytical approach to calculation of response spectra from seismological models of ground motion. *Earthquake Engineering and Structural Dynamics*, 16:121–134, 1988.

[141] E. Safak, C. Mueller, and J. Boatwright. A simple model for strong ground motions and response spectra. *Earthquake Engineering and Structural Dynamics*, 16:203–215, 1988.

[142] G. R. Saragoni and G. C. Hart. Simulation of artificial earthquakes. *Earthquake Engineering and Structural Dynamics*, 2:249–267, 1974.

[143] T. Sarpkaya and M. Isaacson. *Mechanics of Wave Forces on Offshore Structures*. Van Nostrand Reinhold Company, New York, NY, 1981.

[144] M. I. J. Schotanus, P. Franchin, A. Lupoi, and P. E. Pinto. Seismic fragility analysis of 3D structures. *Structural Safety*, 26:421–441, 2004.

[145] M. Shinozuka. Monte carlo simulation of structural dynamics. *Computers and Structures*, 2:855–873, 1972.

[146] M. Shinozuka and G. Deodatis. Stochastic wave models for stationary and homogeneous seismic ground motion. *Structural Safety*, 10:235–246, 1991.

[147] M. Shinozuka, G. Deodatis, R. Zhang, and A. S. Papageorgiou. Modeling, synthetics and engineering applications of strong earthquake wave motion. *Soil Dynamics and Earthquake Engineering*, 18:209–228, 1999.

[148] M. Shinozuka, M. Q. Feng, H. Kim, T. Uzawa, and T. Ueda. Statistical analysis of fragility curves. Technical Report MCEER-03-0002, Multidisciplinary Center for Earthquake Engineering Research, Buffalo, NY, 2003.

[149] M. Shinozuka, M. Q. Feng, J. Lee, and T. Naganuma. Statistical analysis of fragility curves. *ASCE Journal of Engineering Mechanics*, 126(12):1224–1231, 2000.

[150] M. Shinozuka, H. Hwang, and M. Reich. Reliability assessment of reinforced concrete containment structures. *Nuclear Engineering and Design*, 80:247–267, 1984.

[151] M. Shinozuka and Y. Sato. Simulation of nonstationary random processes. *ASCE Journal of the Engineering Mechanics Division*, 93:11–40, 1967.

[152] N. Shome, C. A. Cornell, P. Bazzurro, and J. E. Carballo. Earthquakes, records, and nonlinear responses. *Earthquake Spectra*, 14(3):469–500, 1998.

[153] R. Sigbjorusson and M. Morch. Spectral analysis of nonlinear wave load effects on offshore platforms. *Engineering Structures*, 4:29–36, 1982.

[154] E. Simiu and R. H. Scanlan. *Wind Effects on Structures*. John Wiley & Sons, New York, NY, 2 edition, 1986.

[155] R. H. Simpson. The hurricane disaster potential scale. *Weatherwise*, 27:169–186, 1974.

[156] A. Singhal and A. S. Kiremidjian. Method for probabilistic evaluation of seismic structural damage. *ASCE Journal of Structural Engineering*, 122(12):1459–1467, 1996.

[157] A. Singhal and A. S. Kiremidjian. Bayesian updating of fragilities with application to RC frames. *ASCE Journal of Structural Engineering*, 124(8):922–929, 1998.

[158] V. Sokolov, C. H. Loh, and K. L. Wen. Empirical model for estimating Fourier amplitude spectra of ground acceleration in Taiwan region. *Earthquake Engineering and Structural Dynamics*, 29:339–357, 2000.

[159] V. Sokolov, C. H. Loh, and K. L. Wen. Site-dependent design input ground motion estimation for the Taipei area: A probabilistic approach. *Probabilistic Engineering Mechanics*, 16:177–191, 2001.

[160] P. Somerville, N. Smith, S. Punyamurthula, and Joseph Sun Woodward-Clyde Federal Services. Development of ground motion time histories for phase 2 of the FEMA/SAC steel project. SAC Background Report SAC/BD-97/04, SAC Joint Venture, a partnership of SEAOC, ATC and CUREE, Sacramento, CA, 1997.

[161] J. Song and B. R. Ellingwood. Seismic reliability of special moment steel

frames with welded connections: I. *ASCE Journal of Structural Engineering*, 125(4):357–371, 1999.

[162] J. Song and B. R. Ellingwood. Seismic reliability of special moment steel frames with welded connections: II. *ASCE Journal of Structural Engineering*, 125(4):372–384, 1999.

[163] T. T. Soong. *Random Differential Equations in Science and Engineering*. Academic Press, New York, NY, 1973.

[164] T. T. Soong and M. Grigoriu. *Random Vibration of Mechanical and Structural Systems*. PTR Prentice-Hall, Englewood Cliffs, NJ, 1993.

[165] L. J. Steinberg and A. M. Cruz. When natural and technological disasters collide: Lessons from the Turkey Earthquake of August 17, 1999. *Natural Hazards Review*, 5(3):121–130, 2004.

[166] R. H. Stewart. Introduction to physical oceanography. Open Source Textbook, Department of Oceanography, Texas A&M University, 2007. http://oceanworld.tamu.edu/resources/ocng_textbook/contents.html.

[167] H. Tajimi. A statistical method of determining the maximum response of a building structure during an earthquake. In *Proceedings of the Second World Conference on Earthquake Engineering*, Tokyo and Kyoto, Japan, 1960.

[168] A. K. Tang, editor. *Izmit (Kocaeli) Earthquake of August 17, 1999 Including Duzce Earthquake of November 12, 1999: Lifeline Performance*. ASCE Technical Council on Lifeline Earthquake Engineering, 2000. Monograph No. 17.

[169] P. Thoft-Christensen. Deterioration of concrete structures. In *Proceedings of 1st International Conference on Bridge Maintenance, Safety and Management*, Barcelona, Spain, 2002.

[170] J.-C. Thouret. Urban hazards and risks; consequences of earthquakes and volcanic eruptions: An introduction. *GeoJournal*, 49:131–135, 1999.

[171] G. R. Toro and R. K. McGuire. An investigation into earthquake ground motion characteristics in Eastern North America. *Bulletin of the Seismological Society of America*, 77(2):468–489, 1987.

[172] M. D Trifunac. A method for synthesizing realistic strong motion. *Bulletin of the Seismological Society of America*, 61(6):1739–1753, 1971.

[173] M. D. Trifunac and A. G. Brady. A study on the duration of strong earthquake ground motion. *Bulletin of the Seismological Society of America*, 65:581–626, 1971.

[174] J. F. Unruh and D. D. Kana. An iterative procedure for generation of consistent power/response spectrum. *Nuclear Engineering and Design*, 66:427–435, 1981.

[175] J. F. Unruh and D. D. Kana. Power/response spectrum transformation in equipment qualification. *Journal of Pressure Vessel Technology*, 107(2):197–202, 1985.

[176] USGS. Measuring earthquakes, 1997. URL: http://pubs.usgs.gov/gip/earthq1/measure.html.

[177] USGS. Understanding plate motions, 1999. URL: http://pubs.usgs.gov/publications/text/understanding.html.

[178] USGS. Implications for earthquake risk reduction in the United States from the Kocaeli, Turkey, Earthquake of August 17, 1999, 2000. U. S. Geological Survey Circular 1193.

[179] USGS. Earthquake rates and probabilities in the United States: A PSHA perspective, 2006. URL: http://eqint.cr.usgs.gov/eq-men/html/Earthquake_Rates_and_Probability.html.

[180] USGS. National seismic hazard mapping project, Earthquake probability mapping, United States Geological Surveys, 2006. URL: http://eqint.cr.usgs.gov/eq-men/html/neweqprob-06.html.

[181] D. Veneziano, M. Grigoriu, and A. Cornell. Vector process models for system reliability. *ASCE Journal of the Engineering Mechanics Division*, 103:441–460, 1977.

[182] A. Wanitkorkul and A. Filiatrault. Simulation of strong ground motions for seismic fragility evaluation of nonstructural components in hospitals. Technical Report MCEER-05-0005, Multidisciplinary Center for Earthquake Engineering Research, Buffalo, NY, 2005.

[183] Y. K. Wen. Method for random vibration of hysteretic systems. *ASCE Journal of the Engineering Mechanics Division*, 102(2):249–263, 1976.

[184] Y. K. Wen. Statistical combination of extreme loads. *ASCE Journal of the Structural Division*, 103(ST5):1079–1093, 1977.

[185] Y.-K. Wen. *Structural Load Modeling and Combination for Performance and Safety Evaluation*. Elsevier, New York, 1990.

[186] P. H. Wirsching, T. L. Paez, and K. Ortiz. *Random Vibrations, Theory and Practice*. Wiley, New York, 1995.

[187] Y. T. Yuan and A. Whittaker. MCEER demonstration hospitals. Multidisciplinary Center for Earthquake Engineering Research, 2002.

[188] A. Zerva. Seismic ground motion simulations from a class of spatial variability models. *Earthquake Engineering and Structural Dynamics*, 21:351–361, 1992.

[189] A. Zerva and Zervas V. Spatial variation of seismic ground motions: An overview. *Applied Mechanics Reviews*, 55:271–297, 2002.